Novel calcium-regulating mechanism of barium-doped material for the treatment of neuropathic pain

Thesis submitted in partial fulfilment for the Award of Degree

Doctor of Philosophy

By

Shreyasi Majumdar

DEPARTMENT OF PHARMACEUTICAL ENGINEERING & TECHNOLOGY
INDIAN INSTITUTE OF TECHNOLOGY
(BANARAS HINDU UNIVERSITY) VARANASI–
221005
INDIA

Roll No.18161005

2024

CERTIFICATE

It is certified that the work contained in the thesis titled "**Novel calcium-regulating mechanism of barium-doped material for the treatment of neuropathic pain**" by **Ms. Shreyasi Majumdar** has been carried out under my supervision and that this work has not been submitted elsewhere for a degree.

It is further certified that the student has fulfilled all the requirements of Comprehensive Examination, Candidacy, and SOTA for the award of Ph.D. Degree.

17/3/25

Date:

Place: IIT (BHU), Varanasi

Prof. Sairam Krishnamurthy

(Supervisor)

Prof. SAIRAM KRISHNAMURTHY
Dept. of Pharm. Engg. & Tech.
Indian Institute of Technology
(Banaras Hindu University)
Varanasi-221005 (U.P.)

DECLARATION BY THE CANDIDATE

I, **Shreyasi Majumdar**, certify that the work embodied in this Ph.D. thesis is my own bonafide work and carried out by me under the supervision of **Prof. Sairam Krishnamurthy** from **July, 2018 to June, 2024** at the **Department of Pharmaceutical Engineering & Technology, Indian Institute of Technology (Banaras Hindu University), Varanasi.** The matter embodied in this Ph.D. thesis has not been submitted for the award of any other degree/diploma.

I declare that I have faithfully acknowledged and given credit to the research workers wherever their works have been cited in my work in this thesis. I further declare that, I have not willfully copied any other's work, paragraphs, text, data, results, etc. reported in the journals, books, magazines, reports, dissertations, theses, etc., or available at websites and have not included them in this Ph.D. thesis and have not cited as my own work.

Date: 17·3·25

Place: IIT (BHU), Varanasi

(Shreyasi Majumdar)

CERTIFICATE BY THE SUPERVISOR AND HEAD OF THE DEPARTMENT

It is certified that the above statement made by the student is correct to the best of our knowledge.

Prof. Sairam Krishnamurthy

(Supervisor)

Prof. SAIRAM KRISHNAMURTHY
Dept. of Pharm. Engg. & Tech.
Indian Institute of Technology
(Banaras Hindu University)
Varanasi-221005 (U.P.)

Head of the Department

विभागाध्यक्ष / Head
भैषजकीय अभियांत्रिकी एवं प्रौद्योगिकी विभाग /
Department of Pharmaceutical Engineering & Technology
भारतीय प्रौद्योगिकी संस्थान / INDIAN INSTITUTE OF TECHNOLOGY
(बनारस हिन्दू विश्वविद्यालय) / (BANARAS HINDU UNIVERSITY)
वाराणसी–२२१००५ / Varanasi-221005

COPYRIGHT TRANSFER CERTIFICATE

Title of the Thesis: "Novel calcium-regulating mechanism of barium-doped material for the treatment of neuropathic pain"

Candidate's Name: Ms. Shreyasi Majumdar

Copyright Transfer

The undersigned hereby assigns to the Indian Institute of Technology (Banaras Hindu University), Varanasi all rights under copyright that may exist in and for the above thesis submitted for the award of the "***Doctor of Philosophy***".

Date: 17·3·25

Place: IIT (BHU), Varanasi

Shreyasi Majumdar

Note: However, the author may reproduce or authorize others to reproduce material extracted verbatim from the thesis or derivative of the thesis for author's personal use provided that the source and University's copyright notice are indicated.

ACKNOWLEDGEMENTS

This work represents the culmination of years of unwavering dedication, wherein numerous individuals generously extended their support and guidance. Above all, I express my profound gratitude to Lord Shiva for providing me with this remarkable opportunity to express my deepest appreciation to all those who played an instrumental role in assisting and guiding me throughout my research journey. Their unwavering assistance and guidance have been invaluable, and I am truly grateful for their contributions.

At the outset, I would like to pay my tribute to the father and founder of the Banaras Hindu University respected ***Mahamana Pt. Madan Mohan Malviya Ji***, because of whom thousands of students every year put their step towards a bright and prosperous future.

I want to express my heartfelt gratitude to my supervisor, ***Prof. Sairam Krishnamurthy,*** for grooming me not only to conduct independent research but also for acquainting me with other areas affiliated with scientific pursuits. His vast knowledge and logical way of thinking have been of great value to me. This work would not have been possible without his guidance, support and encouragement. His unflinching courage and conviction will always inspire me, and I hope to continue to work with his noble thoughts.

I convey my profound gratitude to my esteemed R.P.E.C members, ***Dr. P.K. Nayak*** and ***Dr. Abha Mishra***, for their invaluable suggestions throughout my Ph.D. tenure.

I am also grateful to ***Prof. S. Hemalatha***, Head, Department of Pharmaceutical Engineering & Technology, Indian Institute of Technology (Banaras Hindu University) and ***Prof. S.K. Srivastava*** (Former Head) for permitting me to utilize the department's resources for my research endeavours.

I want to express my sincere gratitude to all the teachers of the department; ***Prof. B. Mishra, Prof. S.K. Singh, Prof. Sanjay Singh, Dr. A.K. Srivastava, Prof. M.S. Muthu, Prof. Senthil Raja, Dr. Alakh N. Sahu, Dr. Ruchi Chawla, Dr. G. P. Modi, Dr. S.K. Mishra, Dr. A. K. Maurya , Dr. Vinod Tiwari, Dr. S. K. Jain, Dr. Rajnish, Dr. A.K.***

Agrawal, Dr. Deepak Kumar, Dr. Dinesh Kumar and ***Dr. Jairam Meena*** for their valuable suggestion and guidance throughout the course of my research.

I also want to thank the ***Department of Science and Technology*** for providing me with financial support through the DST INSPIRE Fellowship.

A special thanks to ***Prof. S.K. Trigun*** and ***Dr. Debasmit Mallick***, from the Department of Zoology, Institute of Science, Banaras Hindu University, India for their help and guidance in molecular analysis.

I wish to express my sincere appreciation to the Sophisticated Analytical & Technical Help Institute (SATHI), Central Discovery Centre (CDC)-BHU, Varanasi, and Central Instrument Facility, IIT (BHU), Varanasi, for their provision of diverse spectroscopic and microscopic techniques utilized in my research work.

It gives me great pleasure to acknowledge the support of my respected seniors and lab mates ***Dr. Dhananjay, Dr. Pankaj Paliwal, Dr. Sukesh K. Gupta, Dr. Akanksha Mishra, Dr. Santosh K. Prajapati, Dr. Ramakrishna Kakarla, Dr. Qadir Alam, Dr. Prabha Rajput, Dr. Pratigya Tripathi, Aquib, Gajendra T.A., Neha Singh, Asha, Neeraj, and Swagata*** for their stimulating discussion and brilliant suggestions. I would also like to thank my juniors; ***Rajesh, Vilas, Shital, Priya, and Kirti*** whose moral support always inspired me.

I extend my heartfelt gratitude and indebtedness to my beloved friends ***Dr. Poonam Bhadoria and Dr. Parul Rawat*** for their affection, love and moral support whenever I was in need.

I pay my sincere thanks to ***Mr. Nandlal, Mr. Rafeeq, Mr. Tabrej, Mr. Upadhyay, Mr. Atul Kumar Gupta, Mr. Yashwant Singh, Mr. Anand Kumar, Mr. Jamil, Mr. Virendra,*** and all other non-teaching staff of the department for providing all the necessities required for my research.

Most importantly, I would like to express my deepest gratitude to my parents, ***Mrs. Ruma Majumdar*** and ***Mr. Prabir Kumar Majumdar***, for their unwavering blessings, invaluable contributions, and unconditional support at every stage of my life. I am also immensely grateful to my brother, ***Pratyaya Majumdar***, for his constant support throughout my journey.

Table of Contents

Certificate **ii**

Declaration by the Candidate **iii**

Copyright Transfer Certificate **iv**

Acknowledgements **v**

Table of Contents **vii**

List of Tables **xv**

List of Figures **xxvii**

List of Abbreviations **xxix**

Preface **xxxiii**

1. Introduction **1**

1.1. The Genesis of Idea: From Concept to Cure 1

1.2. The background of bioactive glass 2

1.3. Role of therapeutic ions in soft tissue repair and regeneration 3

1.4. Diverse Applications of Bioactive Glass: Innovations in Medicine and Beyond 5

1.4.1. Bioactive glasses exhibit wound healing property 5

1.4.2. Bioactive glasses facilitate angiogenesis 8

1.4.3. Bioactive glasses in gastrointestinal tissue regeneration 9

1.4.4. Bioactive glasses in myocardial tissue engineering 9

1.4.5. Bioactive glass aids in the peripheral nerve regeneration 10

1.5. Innovation in Biomaterials: The Development of Barium-Doped Bioactive Glass (BaBG) 11

1.6. Understanding Neuropathic Pain: An Introduction 12

1.7. Symptoms of Neuropathic pain 13

1.8. Epidemiology of Neuropathic pain 14

1.9. The physiology of pain perception 15

1.10. Pathophysiology and molecular mechanism of Neuropathic pain 18

1.10.1. Peripheral sensitization: 18

1.10.2. Central sensitization: 20

1.11. Clinical pharmacotherapy for the treatment of Neuropathic pain 23

1.11.1. Calcium channel blockers/ anticonvulsants 23

1.11.2. Nonsteroidal anti-inflammatory drugs (NSAIDs) 24

1.11.3. Antidepressants 25

1.11.4. Opioids 26

1.11.5. Additional pharmacotherapy 27

1.12. Role of ion channels in the development and progression of Neuropathic pain 28
1.12.1. Voltage-Gated Sodium Channels 29
1.12.2. Transient receptor potential (TRP) channels 29
1.12.3. Calcium channels and their role in the development of Neuropathic pain 30
1.13. Role of calcium ions in the pathophysiology of Neuropathic pain 31
1.14. Significance of glial cells in Neuropathic pain 33
1.14.1. Calcium -binding protein: S100 proteins 34
1.14.2. S100 proteins: A key player in the pathophysiology of various diseases 35
1.15. Hypothesis 38
1.16. Objectives: 40
2. Introduction 41
2.1. Materials and Methods 44
2.1.1. Synthesis of the bioactive glasses 44
2.1.1.1. Barium doped Bioactive glass (BaBG) 44
2.1.1.2. 45S5 45
2.1.2. Characterization of the bioactive glass samples 45
2.1.2.1. Particle size and surface area determination 45
2.1.2.2. X-Ray Diffraction (XRD) 46
2.1.2.3. Fourier Transform Infrared (FTIR) Spectroscopy 46
2.1.2.4. Transmission electron microscopy (TEM) 47
2.1.3. Preparation of SBF (Simulated Body Fluid) 47
2.1.4. pH behavior of 45S5 and BaBG in SBF 47
2.1.5. In vitro hydroxyapatite forming ability of BaBG and 45S5 47
2.1.6. Surface characterization and quantitative elemental analysis of BaBG and 45S5 48
2.1.7. Hemolysis assay 48
2.1.8. Cell line and cell culture 49
2.1.9. In vitro cytotoxicity assay 49
2.1.10. Apoptosis assay (AO/EtBr) 50
2.1.11. In vitro cell growth/proliferation assay 50
2.1.12. Scratch-wound healing assay 51
2.1.13. Evaluation of the anti-inflammatory activity of bioactive glasses against LPS-induced inflammation 51
2.1.14. Data Analysis 52
2.2. Results and Discussion 52

2.2.1. Particle size and surface area analysis 52
2.2.2. X-ray diffraction (XRD) analysis of BaBG & 45S5 53
2.2.3. FTIR analysis of the bioactive glasses 56
2.2.4. Transmission electron microscopy (TEM) analysis 58
2.2.5. pH behavior of the bioactive glass samples in the SBF solution 58
2.2.5. SEM and EDX analysis of BaBG and 45S5 62
2.2.6. BaBG and 45S5 shows biocompatibility in hemolysis assay 64
2.2.7. BaBG and 45S5 exhibit cytocompatibility during in vitro cell proliferation and cytotoxicity assay 65
2.2.8. BaBG and 45S5 exhibits cytocompatibility during acridine orange/ethidium bromide staining 68
2.2.9. BaBG and 45S5 shows regeneration during the scratch assay 70
2.2.10. BaBG and 45S5 exhibits anti-inflammatory properties 72
2.3. Conclusion 74
3. Introduction 76
3.1. Materials and Methods 78
3.1.1. Materials 78
3.1.2. Preparation of Simulated body fluid (SBF) 78
3.1.3. *In vitro* pharmacokinetic study of BaBG 78
3.1.4. Animals 79
3.1.5. Experimental design for single dose oral in-vivo pharmacokinetic study 79
3.1.6. Pharmacokinetic Analysis 80
3.1.7. Analysis of Ca, Si, and Ba in urine and feces 81
3.1.8. Experimental design for in-vivo biodistribution study after single dose oral administration of BaBG 81
3.1.9. Scanning electron microscopy (SEM) of vital organs 82
3.1.10. Digestion of the biological samples for ICP-MS 82
3.1.11. Inductively coupled plasma-mass spectroscopy (ICP-MS) 83
3.1.12. Body weight and organ coefficient 84
3.1.13. Statistical analysis 84
3.2. Results and discussion 84
3.2.1. Temporal *in vitro* release of Ca, Si, and Ba from BaBG in SBF solution 84
3.2.2. *In vivo* oral pharmacokinetic study 87
3.2.2.1. The plasma concentration of Ca, Ba, and Si released from BaBG in rats during the *in vivo* pharmacokinetic study 87

3.2.2.2. *In vivo* oral pharmacokinetic profile of Ca, Ba, and Si released from BaBG 91
3.2.3. Urinary and fecal excretion 95
3.2.4. Changes in body weight and organ coefficient after oral administration of BaBG 100
3.2.5. *In vivo* biodistribution of Ca, Ba, and Si in vital organs and their scanning electron microscopical analysis 100
3.3. Summary 107
4. Introduction **108**
4.1. Materials and Methods 109
4.1.1. Materials 109
4.1.2. Animals 109
4.1.3. Acute oral toxicity study 110
4.1.4. Subacute oral toxicity study 111
4.1.5. Behavioral assessments 112
4.1.5.1. Rotarod test 112
4.1.5.2. Open field test (OFT) 113
4.1.5.3. Grip strength test 114
4.1.5.4. Spontaneous locomotor activity (Actophotometer) 114
4.1.6. Organ coefficient 114
4.1.7. Preclinical pathology 115
4.1.8. Hematology 115
4.1.9. Biochemical analysis 115
4.1.10. Histological analysis 116
4.1.11. Statistical analysis 116
4.2. Results and discussion 116
4.2.1. Acute toxicity study 116
4.2.1.1. General observation and behavioral analysis 116
4.2.1.2. Effect of BaBG on the body weight during the acute toxicity study 118
4.2.1.3. Effect of BaBG on the organ coefficient during the acute toxicity study 119
4.2.1.4. Effect of BaBG on various enzymes during the acute toxicity study 121
4.2.1.5. Histological analysis of various organs of BaBG-treated rats during the acute toxicity study 124
4.2.2. Sub-acute toxicity study 129
4.2.2.1. General observations 129

4.2.2.2. Effect of BaBG on the body weight and food consumption during the sub-acute toxicity study 131
4.2.2.3. Effect of BaBG on hematological parameter during the sub-acute toxicity study 132
4.2.2.4. Effect of BaBG on organ-coefficient during the sub-acute toxicity study 132
4.2.2.5. Effect of BaBG on various enzymes during the sub-acute toxicity study 134
4.2.2.6. Effect of BaBG on the neurobehavioral activity during sub-acute toxicity study 137
4.2.3.7. Histological analysis of various organs of BaBG treated rats during the sub-acute toxicity study 139
4.3. Summary 148
5. Introduction **149**
5.1. Materials and methods 154
5.1.1. Materials 154
5.1.2. Experimental animals and their ethical statement 154
5.1.3. Chronic constriction injury (CCI) model of Neuropathic pain 155
5.1.4.1. Animal experimental design for the temporal study to measure the changes in the intercellular calcium $(Ca^{2+})_i$ and S100b level 156
5.1.4.2. Animal experimental design for validation of the role of S100b in the pathogenesis/progression of NP 157
5.1.5. Behavioral analysis: 159
5.1.5.1. Thermal hyperalgesia (hot-plate test) 159
5.1.5.2. Cold allodynia (acetone drop test) 159
5.1.5.3. Mechanical hyperalgesia (Randall Selitto test) 159
5.1.5.4. Dynamic mechanical allodynia (Cotton swab test) 160
5.1.5.5. Rota rod 160
5.1.5.6. Sciatic functional index (SFI) 161
5.1.5.7. BBB (Basso, Beattie, and Bresnahan) locomotor test 161
5.1.6. Gastrocnemius muscle mass assessment 162
5.1.7. Real Time quantitative PCR 162
5.1.8. Assessment of S100b, TNF-α, and IL-6 protein level in sciatic nerve and spinal cord 165
5.1.9. Immunofluoresence 165
5.1.10. Golgi–Cox Staining 166
5.1.10.1. General Precautions 166
5.1.10.2. Preparation of Solutions 166

5.1.10.3. Procedure for staining 167
5.1.10.4. Quantification of dendritic branching and spine density 168
5.1.11 Measurement of intracellular calcium level 169
5.1.12. Histological analysis of gastrocnemius muscle 169
5.1.13. Statistical analysis 169
5.2. Results and Discussion 170
5.2.1. Temporal study to evaluate the development of NP phenotypes and changes in the intracellular calcium and S100b protein level 170
5.2.1.1. Effect of CCI on the development of NP phenotypes during the temporal study 170
5.2.1.2. Temporal changes in the intracellular calcium, S100b, and pro-inflammatory cytokine (TNF-α) level post-CCI of sciatic nerve 172
5.2.2. Validation of the role of S100b in the pathogenesis/progression of NP in rat CCI model 176
5.2.2.1. Effect of pentamidine on the CCI-induced sensory and motor deficits 176
5.2.2.2. Effect of pentamidine on the CCI-induced motor coordination 179
5.2.2.3. Effect of pentamidine on the intracellular calcium $(Ca^{2+})_i$ and S100b level in SN and SC 181
5.2.2.4. Effect of pentamidine on the $Ca_V2.2$ and TRPV1 mRNA expression in SN and SC 184
5.2.2.5. Effect of pentamidine on the expression of S100b in SN and SC 186
5.2.2.6. Effect of pentamidine on the CCI-induced microglial activation in SN and SC 187
5.2.2.7. Effect of pentamidine on the CCI-induced astrocytes activation in SN and SC 188
5.2.2.8. Effect of pentamidine on the CCI-induced neuroinflammation 192
5.2.2.9. Effect of pentamidine on the neuronal morphology post-CCI injury 193
5.2.2.10. Effect of pentamidine on the gastrocnemius muscle post-CCI injury 196
5.2.2.11. Effect of pentamidine on the gastrocnemius muscle post-CCI injury 197
5.3. Conclusion 199

6. Introduction **202**
6.1. Materials and methods 207
6.1.1. Materials 207
6.1.2. Experimental animals and their ethical statement 207
6.1.3. *Ex vivo* electrophysiological assessment of calcium channel blocking effects of BaBG 208
6.1.3.1. Preparation of physiological fluid (PF) 208
6.1.3.2. *Ex vivo* electrophysiological assessment 208
6.1.4. Chronic constriction injury (CCI) model of Neuropathic pain 210
6.1.5. Experimental design for pharmacological evaluation of BaBG for the treatment of NP 210
6.1.6. Behavioral analysis: 212
6.1.6.1. Thermal hyperalgesia (hot-plate test) 212
6.1.6.2. Cold allodynia (acetone drop test) 212
6.1.6.3. Mechanical hyperalgesia (Randall Selitto test) 213
6.1.6.4. Dynamic mechanical allodynia (Cotton swab test) 213
6.1.6.5. Rota rod 213
6.1.6.6. Sciatic functional index (SFI) 214
6.1.6.7. BBB (Basso, Beattie, and Bresnahan) locomotor test 215
6.1.7. Electrophysiological measurement of action potential 215
6.1.8. Electromyogram (EMG) recordings 216
6.1.9. Gastrocnemius muscle mass assessment 217
6.1.10. Real Time quantitative PCR 217
6.1.11. Assessment of S100b, TNF-α, IL-6, and IL-10 protein level in sciatic nerve and spinal cord 218
6.1.12. Immunofluoresence analysis 218
6.1.13. Golgi–Cox Staining 218
6.1.14. Measurement of intracellular calcium level 218
6.1.15. Histological analysis of gastrocnemius muscle 218
6.1.16. Histological analysis of sciatic nerve (SN) using luxol fast blue staining 219
6.1.17. In silico docking of S100b proteins with metal ions (Ca^{2+} and Ba^{2+}) 219
6.1.17.1. Preparation of Ligand and Protein 219
6.1.17.2. Analysis and Visualization 220
6.1.18. Statistical analysis 220
6.2. Results and Discussion 220

6.2.1. Effect of calcium channel blocking (CCB) properties of BaBG in the *ex vivo* setup 220
6.2.2. Effect of BaBG on mechanical /thermal hyperalgesia and allodynia 226
6.2.3. Effect of BaBG on the CCI-induced alterations in motor functions 228
6.2.4. Effect of BaBG on the mRNA expression of TRPV1 and CaV 2.2 along with the intracellular calcium level $(Ca^{2+})_i$ in the SN and SC post-CCI 231
6.2.5. Effect of BaBG on the expression of S100b in SN and SC 234
6.2.6. Effect of BaBG on the CCI-induced astrocytes activation in SN and SC 237
6.2.7. Effect of BaBG on the CCI-induced neuroinflammation 239
6.2.8. Effect of BaBG on the neuronal morphology post-CCI injury 244
6.2.9. Effect of BaBG on the CCI-induced axonal degeneration 247
6.2.10. Effect of BaBG on the electrophysiological response upon stimulating the sciatic nerve 250
6.2.11. Effect of BaBG on the muscle functioning in response to the cold-stimulus-evoked allodynia 251
6.2.12. Effect of BaBG on the gastrocnemius muscle post-CCI injury 252
6.3. Conclusion 255
7. Summary and Conclusion **258**
7.1. Important outcomes 262
7.2. Scope for Further Work 263
Bibliography **264**
List of Publications **289**

LIST OF FIGURES

Figure 1.1	The primary afferent pathways and its connections in the dorsal horn of spinal cord	17
Figure 1.2	The ascending pathway of the pain perception	18
Figure 1.3	The peripheral changes in the primary afferent neuron after the peripheral nerve injury	20
Figure 1.4	The mechanisms of central sensitization of WDR neurons. Diagram showing the various mechanisms involved in neuropathic pain at different sites in the nociceptive pathway	22
Figure 1.5	The proposed hypothesis of pharmacological evaluation of BaBG in the experimental model of neuropathic pain	38
Figure 2.1	Nitrogen adsorption-desorption isotherm of (A) 45S5 and (B) BaBG at STP (standard temperature and pressure)	53
Figure 2.2	XRD pattern of BaBG & 45S5 bioactive glass samples before SBF treatment (A) and XRD pattern of 45S5 (B) and BaBG (C) after soaking them in SBF for 1, 3, 7, and 14days	58
Figure 2.3	FTIR transmittance spectra of the bioactive glasses before soaking it in SBF solution (A) and FTIR spectra of 45S5 (B) and BaBG (C) after immersion in the SBF solution for 1, 3, 7, and 14 days	60
Figure 2.4	The morphology and phase analysis of the synthesized BaBG and 45S5. (A) TEM image and (B) SAED pattern of 45S5 and BaBG	61
Figure 2.5	The changes in the pH of the SBF solution after soaking BaBG and 45S5 for 30 days	61
Figure 2.6	SEM micrographs of (i) 45S5 (A) and BaBG (B) before immersion in SBF, (ii) 45S5 and (iii) BaBG after the SBF treatment for 1 (A), 3 (B), and 14 (C) days respectively	63
Figure 2.7	EDX analysis of (i) 45S5 and (ii) BaBG after 1 (A) and 14 (B) days of SBF treatment	64
Figure 2.8	Effect of BaBG & 45S5 sample on hemolysis at different concentrations (i) and micrographs of RBC cells after incubation with negative control (A), positive control (B), 45S5 (C) and BaBG (D) respectively. All values are mean ± SD (n=4). $^{a}p<0.05$, $^{b}p<0.05$, $^{c}p<0.05$ and $^{d}p<0.05$ compared to 5, 10.25 and 50 mg respectively. (Two-way ANOVA followed by Bonferroni post hoc test)	67
Figure 2.9	Effect of BaBG & 45S5 on percentage proliferation (A), percentage cytotoxicity of K562 cells at different concentrations (B) and percentage cell proliferation of the C6 cells at various time intervals (C). All values are mean ± SD (n=4). $^{a}P<0.05$, $^{b}P<0.05$, $^{c}p<0.05$ and $^{d}p<0.05$ compared to 5, 10, 25 and 50 µg/ml of bioactive glass sample (BaBG and 45S5), $^{x}p<0.05$, $^{y}p<0.05$ compared to 24 and 48 h of	69

	incubation with BaBG and 45S5 and $^{\$}p<0.05$ and $^{@}p<0.05$ compared to control (culture medium treated) and 45S5 treated group (Two-way ANOVA followed by Bonferroni post hoc test)	
Figure 2.10	Apoptosis assay of C6 cells following treatment with BaBG (A) and 45S5 (B) with Acridine orange/ Ethidium bromide. Green color staining with Acridine orange suggests the living and healthy cells and the Ethidium bromide is staining for nucleic acid. Bright-field (i), Acridine orange staining (ii), Ethidium bromide staining (iii), the merge of ii over iii (iv), overlay of iv over i (v). Arrow indicates early apoptotic cells	70
Figure 2.11	Scratch/wound healing assay in C6 cells following treatment with BaBG, 45S5, or Temozolomide (TMZ) (A), time-dependent percentage wound recovery in C6 cells treated with the above formulations (B) and comparison of time-dependent percent wound area recovery to wound area created in the presence of culture medium, BaBG, 45S5 or TMZ (C-F). All values are mean ± SD (n=3). $^{a}P<0.05$, $^{b}P<0.05$ and $^{c}p<0.05$, compared to culture media, 45S5 and BaBG treatment and $^{@}p<0.05$, $^{\#}p<0.05$ and $^{\$}p<0.05$ compared to 4, 8 and 16 h of incubation of C6 cells (Two-way ANOVA followed by Bonferroni post hoctest)	72
Figure 2.12	Effect of BaBG and 45S5 on IL-6 (A), TNF-α (B) and IL-10 (C) level in C6 cells. All values are mean ± SD (n=3). $^{a}P<0.05$, $^{b}P<0.05$ and $^{x}p<0.05$ compared to vehicle (culture media treated), LPS, and 45S5 treatment groups (Two-way ANOVA followed by Bonferroni post hoc test)	74
Figure 3.1	Schematic representation of the experimental protocol of the in-vivo single-dose oral pharmacokinetics study of BaBG	80
Figure 3.2	Schematic representation of the experimental protocol of the in-vivo biodistribution study after single-dose oral administration of BaBG	82
Figure 3.3	The release pattern of Ca (A), Si (B), and Ba (C) in SBF solution at pH 7.4 from BaBG at various time intervals for 7 days using ICP-MS and their representation by heatmap(D)	86
Figure 3.4	Plasma concentration profile of Ca (i), Ba (ii), and Si (iii) released from BaBG administered orally with the heatmap representation of the plasma concentration of Ca, Ba, and Si (iv). All values are in mean ± SD (n=7 rats/ group). $^{@}p<0.05$, $^{a}p<0.05$, and $^{b}p<0.05$ compared to control, dose 1mg/kg and 5 mg/kg of BaBG respectively. $^{w}p<0.05$, $^{x}p<0.05$, and $^{y}p<0.05$compared to 1, 24, 48 h respectively (Two-way ANOVA followed by Bonferroni post-hoc test)	90-91
Figure 3.5	Representative scanning electron microscopy image of the stomach of the control and BaBG-treated rat exhibiting the deposition of abundant hydroxyapatite (HA) crystals on the gastric epithelium layer of the stomach without any abrasion	106

of the protective layer qualitatively. The macroscopic photographs of the stomach of both the groups are also showing normal morphology. Magnification: 5k X; scale bars: 2 µm

Figure 3.6 Representative photograph of the scanning electron microscopy of liver (i), spleen (ii), kidney (iii), heart (iv), lungs (v), and brain (vi) section of control (A) and orally treated BaBG rat (B). The liver section of the treated rat exhibited the presence of normal hepatocytes (H) surrounding the sinusoids (S) and central vein (CV). The deposition of hydroxyapatite (HA) along with the presence of erythrocytes (RBC; shown in red arrow) is seen. The spleen of BaBG-treated rat exhibiting abundant hydroxyapatite (HA) deposition and the lungs of control and BaBG rats also exhibited normal alveoli (A) and alveolar duct (Ad). Similarly, the cross-section of the kidneys of treated rat exhibited normal architecture of the Bowman's capsule (B; yellow arrow) along with the glomerular tuft. There are also podocytes (P) and erythrocytes (RBC) visible along with the deposition of crystals of HA. The SEM analysis of heart exhibited intact myofibres (Myo) with the presence of loose connective tissue and collagen fibers (CF). BaBG rats exhibited normal surface morphology in brain section similar to the control rats without any deposition of HA. Magnification of liver, spleen, lung, and heart: 550X and 5 kX; scale bars: 40 µm and 4 µm respectively. Magnification of kidneys: 450 X and 1.5 kX; scale bars: 50 µm and 10 µm respectively. Magnification of brain: 1 kX and 5 kX; scale bars: 20 µm and 4 µm respectively 106

Figure 4.1 Schematic representation of the experimental protocol for single-dose acute toxicity study (OECD 423) to determine the LD50 cut-off (mg/kg b.w.) value. The starting dose of 300 mg/kg b.w. was selected. If 2-3 animals die, a lower test dose (i.e., 50 mg/kg) was tested and if no or one animal dies, the next higher dose (i.e., 2000 mg/kg) was tested. Black arrow indicates the test procedure followed in our study 111

Figure 4.2 Schematic representation of the repeated 28-day oral toxicity study as per OECD 407 guidelines. In the subacute toxicity study, rats (n=10/group) were administered BaBG (dose: 50, 500, and 1000 mg/kg b.w.) and were observed daily for any sign of toxicity 113

Figure 4.3 Representative macroscopic photographs showing normal morphology of (i) 45S5 [liver (A), brain (B), kidneys (C), spleen (D), and lungs (E)] and (ii) BaBG [liver (F), brain (G), kidneys (H), spleen (I), and lungs (J)] treated rats after single-dose administration of highest dose (i.e., 2000 mg/kg b.w.) at the end of day 14 118

Figure 4.4	Effect of single-dose oral administration of BaBG and 45S5 on body weight of rats at various time points during the experimental protocol. All values are in mean ± SD (n=6 female rats/ group). (Two-way ANOVA followed by Bonferroni post hoc test)	119
Figure 4.5	Effect of single-dose oral administration of BaBG and 45S5 on organ coefficient of the brain (A), heart (B), lung (C), kidneys (D), liver (E), and spleen (F) at the end of the experimental protocol. All values are in mean ± SD (n=6 female rats/ group). (One-way ANOVA followed by Tukey's multiple comparison post hoc test)	121
Figure 4.6	Effect of single-dose oral administration of BaBG and 45S5 on serum concentration of AST (A), ALT (B), ALP (C), creatinine (D), CK-MB (E), and calcium (F) at the end of the experimental protocol. All values are in mean ± SD (n=6 female rats/ group). (One-way ANOVA followed by Tukey's multiple comparison post hoc test)	126
Figure 4.7	Effect of single-dose oral administration of BaBG and 45S5 (dose of 300 and 2000 mg/kg b.w.) on highly perfused organs like brain, heart, lung, liver, kidney, and spleen tissue stained with hematoxylin and eosin	129
Figure 4.8	Effect of repeated-dose 28 days oral administration of BaBG and 45S5 (50, 500, and 1000 mg/kg) on body weight of male (A) and female (C) rats along with their food intake (B and D, respectively) during the experimental protocol. All values are in mean ± SD (n=5 rats/ group). (Two-way ANOVA followed by Bonferroni post -hoc test)	131
Figure 4.9	Schematic representation of the track plot of (i) male and (ii) female rats respectively divided into following groups: control (A), 45S5 (B, C, D; dose: 50, 500, and 1000 mg/kg b.w. respectively), and BaBG (E, F, G; dose: 50, 500, and 1000 mg/kg b.w. respectively) recorded during 5 min test sessions on day 28 (ANYMAZE)	139
Figure 4.10	Histological analyses of the brain tissue of control (A), 45S5, and BaBG (B and C respectively; dose: 1000 mg/kg b.w.) treated male and female rats after repeated 28 days oral administration. Bar: 50 µm and 20 µm. Hematoxylin and eosin staining	142
Figure 4.11	Histological analyses of the lungs of control (A), 45S5, and BaBG (B and C respectively; dose: 1000 mg/kg b.w.) treated male and female rats in subacute toxicity study. 45S5 and BaBG treated rats exhibited normal appearance of alveoli with thin epithelial walls surrounded by capillaries similar to the control rats. Edema or alveolar hemorrhage in the alveolar cavities was also not observed in the treatment groups. Bar: 100 µm. Hematoxylin and eosin staining	143

Figure 4.12	Histological analyses of the heart of control (A), 45S5, and BaBG (B and C respectively; dose: 1000 mg/kg b.w.) treated male and female rats. The heart of 45S5 and BaBG treated rats exhibited normal morphology with oval and centrally located nuclei in cardiomyocytes regularly arranged in myofibres. No vacuolar degeneration of the myofibrils was observed in 455S5 and BaBG rats. Bar: 50 µm. Hematoxylin and eosin staining	144
Figure 4.13	Effect of repeated-dose 28 day oral administration of BaBG and 45S5 on microstructure of liver (dose: 1000 mg/kg b.w.) in male and female rats. (A) Control and (B) 45S5 treated male and female rats exhibited normal hepatocytes with intact vesicular nucleus radiating from the central vein surrounding the portal tract. No congestion of the central vein or dilation of the sinusoid was observed. (C) The female BaBG treated rats showed mild lymphoid infiltration in the portal areas without any sinusoid dilation. Bar: 100 µm. Hematoxylin and eosin staining	145
Figure 4.14	Effect of repeated-dose 28 day oral administration of BaBG and 45S5 on microstructures of kidney (dose: 1000 mg/kg b.w.) in male and female rats. The cross-section of (A) control, (B) 45S5, and (C) BaBG treated male and female rats exhibited normal architecture of glomeruli, bowman's capsule, and renal corpuscles with intact proximal and distal convulated tubules. Bar: 50 µm. Hematoxylin and eosin staining	146
Figure 4.15	Effect of repeated-dose oral administration of BaBG and 45S5 (dose: 1000 mg/kg b.w.) on spleen of male and female rats. The cross-section of (A) control, (B) 45S5, and (C) BaBG treated male and female rats showed normal appearance of the lymphatic nodules of white pulp, splenic cords of red pulp, and the spleen trabecula. Bar: 50 µm. Hematoxylin and eosin staining	147
Figure 5.1	Presents a graphical representation depicting the schematic diagram outlining the proposed hypothesis concerning the molecular mechanism underlying the pathogenesis of NP in a CCI-induced NP rat model. The injury to the sciatic nerve (SN) leads to the development of central sensitization due to upregulation in the expression of calcium channels (Cav2.2) in the dorsal horn of spinal cord (SC). Besides, there are also enhanced expression of heat-sensing TRPV1 channels in the SC. Upregulation in the expression of these channel results increase in the influx of calcium ions leading to hyperexcitation of the nociceptive neurons and development of NP phenotypes. In addition, the resident immune cells of CNS i.e., glial cells (astrocytes and microglia) get activated post-CCI leading to increase in release of calcium-binding	153

	proteins i.e., S100b. S100b gets activated in presence of calcium ions causing release of pro-inflammatory cytokines and progression of NP. Therefore, the temporal changes in the intracellular calcium and S100b protein level will help to identify the pharmacological window of opportunity. Besides, to validate the role of S100b in the pathogenesis and progression of NP in this model, we have used specific S100b inhibitor i.e., pentamidine to evaluate its effect on NP phenotypes	
Figure 5.2	Schematic representation of the experimental protocol followed for the CCI-induced neuropathic pain model and the behavioral assessment of the symptoms developed post-surgery	156
Figure 5.3	Schematic representation of the experimental protocol followed for the temporal study performed to measure the intracellular calcium and S100b level in the CCI-induced neuropathic pain model	157
Figure 5.4	Schematic representation of the experimental protocol followed for validation of the role of S100b in the pathogenesis/progression of NP in the CCI-induced NP model in rats	158
Figure 5.5	Sensory and motor deficit due to chronic constriction injury in rats. The effect of CCI on the development of (A) thermal hyperalgesia, (B) cold allodynia, (C) mechanical hyperalgesia, and (D) changes in the BBB score. All values are in mean ± SD (n=4 rats/ group). $^{a}p<0.05$, $^{b}p<0.05$, and $^{c}p<0.05$ compared to D-0, D-3, and D-7 respectively. (One-way ANOVA followed by Tukey multiple comparison post-hoc test)	172
Figure 5.6	Temporal changes in the intracellular calcium, S100b and TNF-α level in SN and SC post-CCI injury. All values are in mean ± SD (n=4 rats/ group). $^{a}p<0.05$, $^{b}p<0.05$, $^{c}p<0.05$, $^{d}p<0.05$, $^{e}p<0.05$, and $^{f}p<0.05$ compared to 0, 0.25, 0.5, 1, 3, and 7 days post-injury. (One-way ANOVA followed by Tukey's multiple comparison post-hoc test)	175
Figure 5.7	(A) A correlation between intracellular calcium level, S100b, and TNF-α level on D-21 post-CCI. (B) A correlation between S100b level and NP phenotypes on D-21 post-CCI	175
Figure 5.7	(B) A correlation between S100b level and NP phenotypes on D-21 post-CCI of peripheral nerve.	176
Figure 5.8	Sensory and motor deficit due to chronic constriction injury in rats. Effect of pentamidine on (A) thermal hyperalgesia, (B) cold allodynia, (C) mechanical hyperalgesia, (D) dynamic mechanical allodynia, and (E) retention time on the rota-rod. All values are in mean ± SD (n=12 rats/ group). $^{a}p<0.05$, $^{b}p<0.05$, $^{c}p<0.05$, and $^{d}p<0.05$ compared to control, sham, CCI, and pentamidine respectively. (Two-way ANOVA followed by Bonferroni post-hoc test)	179

Figure 5.9	Representative images of the (i) paw of the ipsilateral side and (ii) footprints of control, CCI, pentamidine and pregabalin treated rats. (ii) Effect of pentamidine on SFI and BBB score. All values are in mean ± SD (n=12 rats/ group). $^{a}p<0.05$, $^{b}p<0.05$, $^{c}p<0.05$, and $^{d}p<0.05$ compared to control, sham, CCI, and pentamidine respectively. (Two-way ANOVA followed by Bonferroni post-hoc test)	181
Figure 5.10	Effect of pentamidine on (i) intracellular calcium and (ii) S100b level in SN and SC. All values are in mean ± SD (n=4 rats/ group). $^{a}p<0.05$, $^{b}p<0.05$, $^{c}p<0.05$, and $^{d}p<0.05$ compared to control, sham, CCI, and pentamidine respectively. (Two-way ANOVA followed by Bonferroni post-hoc test for Fura 2-AM assay) (One-way ANOVA followed by Tukey's multiple comparison post-hoc tests for S100b level)	183
Figure 5.11	A correlation between S100b and NP phenotypes after the pentamidine treatment (10mg/kg b.w.)	183
Figure 5.12	Effect of pentamidine on $Ca_V2.2$ and TRPV1 mRNA expression in the SN (A and C respectively) and SC (B and D respectively). All values are in mean ± SD (n=4 rats/ group). $^{a}p<0.05$, $^{b}p<0.05$, $^{c}p<0.05$, and $^{d}p<0.05$ compared to control, sham, CCI, and pentamidine respectively. (One-way ANOVA followed by Tukey's multiple comparison post-hoc test)	186
Figure 5.13	Effect of pentamidine on S100b expression in the SN. Scale bar was set at 50 μM with 20X magnification. All values are in mean ± SD (n=3 rats/ group). $^{a}p<0.05$, $^{b}p<0.05$, $^{c}p<0.05$, and $^{d}p<0.05$ compared to control, sham, CCI, and pentamidine respectively. (One-way ANOVA followed by Tukey's multiple comparison post-hoc test)	189
Figure 5.14	Effect of pentamidine on S100b expression in the SC. Scale bar was set at 50 μM with 20X magnification. All values are in mean ± SD (n=3 rats/ group). $^{a}p<0.05$, $^{b}p<0.05$, $^{c}p<0.05$, and $^{d}p<0.05$ compared to control, sham, CCI, and pentamidine respectively. (One-way ANOVA followed by Tukey's multiple comparison post-hoc test)	190
Figure 5.15	Effect of pentamidine on Iba-1 expression in the SC. Scale bar was set at 50 μM with 20X magnification. All values are in mean ± SD (n=3 rats/ group). $^{a}p<0.05$, $^{b}p<0.05$, and $^{c}p<0.05$ compared to control, sham, and CCI respectively. (One-way ANOVA followed by Tukey's multiple comparison post-hoc test)	190
Figure 5.16	Effect of pentamidine on GFAP expression in the SN. Scale bar was set at 50 μM with 20X magnification. All values are in mean ± SD (n=3 rats/ group). $^{a}p<0.05$, $^{b}p<0.05$, and $^{c}p<0.05$ compared to control, sham, and CCI respectively. (One-way ANOVA followed by Tukey's multiple comparison post-hoc test)	191

Figure 5.17	Effect of pentamidine on GFAP expression in the SC. Scale bar was set at 50 μM with 20X magnification. All values are in mean ± SD (n=3 rats/ group). $^{a}p<0.05$, $^{b}p<0.05$, and $^{c}p<0.05$ compared to control, sham, and CCI respectively. (One-way ANOVA followed by Tukey's multiple comparison post-hoc test)	191
Figure 5.18	Effect of pentamidine on (i) NF- κB mRNA expression and (ii) TNF-α and IL-6 levels in the SN and SC. All values are in mean ± SD (n=4 rats/ group). $^{a}p<0.05$, $^{b}p<0.05$, $^{c}p<0.05$, and $^{d}p<0.05$ compared to control, sham, CCI, and pentamidine respectively. (One-way ANOVA followed by Tukey's multiple comparison post-hoc test)	193
Figure 5.19	Representative images of Golgi-cox impregnated spinal cord slice of control, sham, CCI, pentamidine, and pregabalin treated rats. Scale bar was set at 200, 100, and 50 μM	195
Figure 5.20	(i) Representative image of the camera lucida drawing of neuron of SC which is superimposed over concentric circles using Sholl analysis. (ii) Effect of pentamidine on (A) number of branching points across the soma, (B) dendrite length at radial distance from the soma and (C) the total length of dendrites. All values are in mean ± SD (n=4 / group). $^{a}p<0.05$ and $^{b}p<0.05$ compared to control and sham respectively. (One-way ANOVA followed by Tukey's multiple comparison post-hoc test)	195
Figure 5.21	Effect of pentamidine on NF-L expression in the SN. Scale bar was set at 50 μM with 20X magnification. All values are in mean ± SD (n=3 rats/ group). $^{a}p<0.05$, $^{b}p<0.05$, and $^{c}p<0.05$ compared to control, sham, and CCI respectively. (One-way ANOVA followed by Tukey's post-hoc test)	198
Figure 5.22	(A) Representative images of the gastrocnemius muscle of the contralateral and ipsilateral side of the leg. (B) Representative image of the histological analyses of gastrocnemius muscle stained with hematoxylin and eosin at the end of 21st day post-surgery. (C and D) Effect of pentamidine on gastrocnemius muscle weight and cross-section area of muscle fiber. All values are in mean ± SD (n=5 rats/ group). $^{a}p<0.05$, $^{b}p<0.05$, $^{c}p<0.05$, and $^{d}p<0.05$ compared to control, sham, CCI, and pentamidine respectively. (One-way ANOVA followed by Tukey's multiple comparison post-hoc test)	199
Figure 5.23	Showcases the specific objective's outcome in exploring the molecular mechanism behind neuropathic pain (NP) in a CCI-induced rat NP model. It suggests that the development and progression of NP is associated temporal increase in the intracellular calcium and calcium-binding protein i.e., S100b. Treatment with pentamidine, a specific S100B inhibitor, significantly reversed the neuropathic pain phenotypes induced by CCI. Besides, CCI of peripheral nerve caused	201

	hyperactivation of astrocytes and microglia that was induced by S100B and pentamidine attenuated these observed changes. Treatment with pentamidine also lowered the S100B-induced increase in pro-inflammatory markers, specifically TNF-α and IL-6, in both the SC and SN post-injury. Therefore, these findings highlight that S100b is involved in progression and development of NP phenotypes in the CCI-induced NP model and could be the essential factor for an analgesic drug for better management of NP	
Figure 6.1	Presents a graphical representation depicting the schematic diagram outlining the proposed hypothesis concerning the molecular mechanism underlying the pathogenesis of NP in a CCI-induced NP rat model. The injury to the sciatic nerve (SN) leads to central sensitization due to upregulation in the expression of calcium channels ($Ca_V2.2$) in the dorsal horn of spinal cord (SC). Besides, there are also enhanced expression of heat-sensing TRPV1 channels in the SC. Enhanced expression of these channel results increase in the influx of calcium ions leading to hyperexcitation of the nociceptive neurons and development of NP phenotypes. In addition, the glial cells get activated post-CCI leading to increase in release of calcium-binding proteins i.e., S100b that further triggers the release of pro-inflammatory cytokines and contributes to the progression of NP. Barium-doped bioactive glass (BaBG) leaches barium ion from its framework after coming in contact with the physiological fluid. BaBG, due to its calcium modulating effects may alleviate sensory and motor deficits observed in the CCI-induced NP in rats. It may also prevent the activation of calcium-binding protein i.e., S100b, reduce neuroinflammation, and concurrently cause axonal repair and remodelling; hence may have disease modifying effects	206
Figure 6.2	Schematic representation of the Plexiglas nerve bath chamber nerve apparatus with the ground, stimulating, and recording electrode used in the experiment. The isolated sciatic nerve (SN) is placed over the platform of nerve chamber in presence of physiological fluid containing the test compounds is stimulated and the compound nerve action potential (CAP) generated is recorded	209
Figure 6.3	Schematic representation of the experimental protocol followed for the pharmacological evaluation of BaBG for the treatment of NP in rat CCI model	211
Figure 6.4	Representative images of the EMG recording from the gastrocnemius muscle in response to the cold-stimulus-evoked allodynia in the experimental rats	216
Figure 6.5	Effect of BaBG on the generation of CAP. All values are mean ± SD (n=4). $^{a}p<0.05$, $^{b}p<0.05$, $^{c}p<0.05$, $^{d}p<0.05$, $^{e}p<0.05$, and $^{f}p<0.05$ compared to groups i.e., in the PF, in the PF containing	224-225

	Pregabalin, in the PF containing BaBG, in the PF containing BaCl2, in the PF containing 45S5, in the PF containing reduced calcium ions and BaBG, and in the PF containing BaBG and Pregabalin respectively. (One-way ANOVA followed by Tukey's post hoc test)	
Figure 6.6	Effect of BaBG on (A) mechanical hyperalgesia, (B) thermal hyperalgesia, (C) cold allodynia, and (D) dynamic mechanical allodynia. All values are in mean ± SD (n=12 rats/ group). $^{a}p<0.05$, $^{b}p<0.05$, $^{c}p<0.05$, $^{d}p<0.05$, $^{e}p<0.05$, and $^{f}p<0.05$ compared to control, CCI, BaBG-1, BaBG-5, BaBG-10, and 45S5-10 respectively (Two-way ANOVA followed by Bonferroni post-hoc test)	228
Figure 6.7	Effect of BaBG on (A) SFI, (B) BBB score, and (C) time spent on rota rod. All values are in mean ± SD (n=12 rats/ group). $^{a}p<0.05$, $^{b}p<0.05$, $^{c}p<0.05$, $^{d}p<0.05$, $^{e}p<0.05$, and $^{f}p<0.05$ compared to control, CCI, BaBG-1, BaBG-5, BaBG-10, and 45S5-10 respectively (Two-way ANOVA followed by Bonferroni post-hoc test)	230
Figure 6.8	Effect of BaBG on the (i) mRNA expression of TRPV1 and Cav2.2, and on (ii) the intracellular calcium level in the SN and SC. (ii). All values are in mean ± SD (n=4 / group). $^{a}p<0.05$, $^{b}p<0.05$, $^{c}p<0.05$, $^{d}p<0.05$, $^{e}p<0.05$, and $^{f}p<0.05$ compared to control, CCI, BaBG-1, BaBG-5, BaBG-10, and 45S5-10 respectively. (One-way ANOVA followed by Tukey's multiple comparison post-hoc test)	233-234
Figure 6.9	Effect of BaBG on S100b expression in the SN. Scale bar was set at 50 μM with 20X magnification. All values are in mean ± SD (n=3 rats/ group). $^{a}p<0.05$, $^{b}p<0.05$, $^{c}p<0.05$, $^{d}p<0.05$, $^{e}p<0.05$, and $^{f}p<0.05$ compared to control, CCI, BaBG-1, BaBG-5, BaBG-10, and 45S5-10 respectively. (One-way ANOVA followed by Tukey's multiple comparison post-hoc test)	236
Figure 6.10	Effect of BaBG on S100b expression in the SC. Scale bar was set at 50 μM with 20X magnification. All values are in mean ± SD (n=3 rats/ group). $^{a}p<0.05$, $^{b}p<0.05$, $^{c}p<0.05$, $^{d}p<0.05$, $^{e}p<0.05$, and $^{f}p<0.05$ compared to control, CCI, BaBG-1, BaBG-5, BaBG-10, and 45S5-10 respectively. (One-way ANOVA followed by Tukey's multiple comparison post-hoc test)	236
Figure 6.11	Effect of BaBG on GFAP expression in the SN. Scale bar was set at 50 μM with 20X magnification. All values are in mean ± SD (n=3 rats/ group). $^{a}p<0.05$, $^{b}p<0.05$, $^{c}p<0.05$, $^{d}p<0.05$, $^{e}p<0.05$, and $^{f}p<0.05$ compared to control, CCI, BaBG-1, BaBG-5, BaBG-10, and 45S5-10 respectively. (One-way ANOVA followed by Tukey's multiple comparison post-hoc test)	238

Figure 6.12 Effect of BaBG on GFAP expression in the SC. Scale bar was set at 50 μM with 20X magnification. All values are in mean ± SD (n=3 rats/ group). $^{a}p<0.05$, $^{b}p<0.05$, $^{c}p<0.05$, $^{d}p<0.05$, $^{e}p<0.05$, and $^{f}p<0.05$ compared to control, CCI, BaBG-1, BaBG-5, BaBG-10, and 45S5-10 respectively. (One-way ANOVA followed by Tukey's multiple comparison post-hoc test) 239

Figure 6.13 Effect of BaBG in the mRNA expression of GFAP, S100b, and NF-kB expression in the SN (i) and SC (ii). All values are in mean ± SD (n=4 / group). $^{a}p<0.05$, $^{b}p<0.05$, $^{c}p<0.05$, $^{d}p<0.05$, $^{e}p<0.05$, and $^{f}p<0.05$ compared to control, CCI, BaBG-1, BaBG-5, BaBG-10, and 45S5-10 respectively. (One-way ANOVA followed by Tukey's multiple comparison post-hoc test) 242

Figure 6.14 Effect of BaBG on TNF- α, IL-6, and IL-10 levels in the SN and SC. All values are in mean ± SD (n=4 / group). $^{a}p<0.05$, $^{b}p<0.05$, $^{c}p<0.05$, $^{d}p<0.05$, $^{e}p<0.05$, and $^{f}p<0.05$ compared to control, CCI, BaBG-1, BaBG-5, BaBG-10, and 45S5-10 respectively. (One-way ANOVA followed by Tukey's multiple comparison post-hoc test) 243

Figure 6.15 Molecular docking showing interaction of calcium (Ca^{2+}) and barium (Ba^{2+}) against S100b protein. 3D docking diagram of S100b bound to (i) Ca^{2+} and (ii) Ba^{2+} along with their (iii) binding potential 244

Figure 6.16 Representative images of Golgi-Cox impregnated SC slice of control, CCI, BaBG-10, 45S5-10 and pregabalin treated rats. Scale bar was set at 200, 100, and 50 μM with 4, 10, and 20X magnification 246

Figure 6.17 (i) Representative image of the camera lucida drawing of neuron of SC which is superimposed over concentric circles using Sholl analysis. (ii) Effect of BaBG on (A), number of branching points (B) dendrite length across the soma, and (C) total length of dendrites. All values are in mean ± SD (n=4 / group). $^{a}p<0.05$, $^{b}p<0.05$, and $^{c}p<0.05$ compared to control, CCI, and BaBG-10 respectively. (One-way ANOVA followed by Tukey's post-hoc test) 247

Figure 6.18 Effect of BaBG on NF-L expression in the SN. Scale bar was set at 50 μM with 20X magnification. All values are in mean ± SD (n=3 rats/ group). $^{a}p<0.05$, $^{b}p<0.05$, $^{c}p<0.05$, $^{d}p<0.05$, $^{e}p<0.05$, and $^{f}p<0.05$ compared to control, CCI, BaBG-1, BaBG-5, BaBG-10, and 45S5-10 respectively. (One-way ANOVA followed by Tukey's multiple comparison post-hoc test) 249

Figure 6.19 Representative image of the histological analyses of SN stained with luxol fast blue at the end of 28th day post-surgery. The arrangement of nerve fibre is disrupted (shown in black 249

	arrow) with high degree of myelin vacuolation (red star) in the disease group	
Figure 6.20	Effect of BaBG on (A) amplitude, (B) latency of CAP, and (C) MNCV. All values are in mean ± SD (n=5 rats/ group). $^{a}p<0.05$, $^{b}p<0.05$, $^{c}p<0.05$, $^{d}p<0.05$, $^{e}p<0.05$, and $^{f}p<0.05$ compared to control, CCI, BaBG-1, BaBG-5, BaBG-10, and 45S5-10 respectively. (One-way ANOVA followed by Tukey's multiple comparison post-hoc test)	251
Figure 6.21	Representative images of the EMG recording in response to the cold-stimulus-evoked allodynia in control, CCI, BaBG-1, BaBG-5, BaBG-10, 45S5-10, and pregabalin treated rats	254
Figure 6.22	Representative images of the gastrocnemius muscle of the contralateral and ipsilateral side of the leg along with the histological analyses of gastrocnemius muscle stained with hematoxylin and eosin at the end of experimental protocol. Effect of BaBG on gastrocnemius muscle weight and cross-section area of muscle fiber. All values are in mean ± SD (n=5 rats/ group). $^{a}p<0.05$, $^{b}p<0.05$, $^{c}p<0.05$, $^{d}p<0.05$, $^{e}p<0.05$, and $^{f}p<0.05$ compared to control, CCI, BaBG-1, BaBG-5, BaBG-10, and 45S5-10 respectively. (One-way ANOVA followed by Tukey's multiple comparison post-hoc test)	254
Figure 6.23	Showcases the specific objective's outcome in exploring the molecular mechanism behind the effect of BaBG in attenuating neuropathic pain (NP) in a CCI-induced NP rat model. It suggests that the development and progression of NP is associated with the enhanced calcium channel and TRPV1 expression that caused increase in the intracellular calcium and calcium-binding protein i.e., S100b level. These events led to glial cell activation that releases cytokine storm, thus exaggerating NP sensation. BaBG exhibited novel calcium regulating mechanism as it prolonged the repolarization phase of action potential. The Treatment with BaBG significantly reversed the NP phenotypes induced by CCI. Besides, CCI of peripheral nerve caused glial cell hyperactivation that was attenuated by BaBG. BaBG also lowered the S100B-induced increase in pro-inflammatory markers, specifically TNF-α and IL-6, in both the SC and SN post-injury	256
Figure 7.1	Summary and conclusion of the study	261

LIST OF TABLES

Table 1.1	Definition of the negative and positive symptoms observed clinically in patients suffering from neuropathic pain	14
Table 1.2	Clinical pharmacomanagement of neuropathic pain	25
Table 2.1	The chemical composition (mol %) of 45S5 and BaBG	45
Table 2.2	Brunauer–Emmett–Teller (BET) analysis results of 45S5 and BaBG	53
Table 2.3	Comparison of the important properties of 45S5 and BaBG	75
Table 3.1	Pharmacokinetic parameters for Ca released after single-dose oral administration of BaBG	94
Table 3.2	Pharmacokinetic parameters for Ba released after single-dose oral administration of BaBG	95
Table 3.3	Pharmacokinetic parameters for Si released after single-dose oral administration of BaBG	95
Table 3.4	Urinary and fecal excretion of Ca post-oral administration of BaBG in rats	98
Table 3.5	Urinary and fecal excretion of Ba post-oral administration of BaBG in rats	98
Table 3.6	Urinary and fecal excretion of Si post-oral administration of BaBG in rats	99
Table 3.7	Tissue concentration of Ca, Ba, and Si in the brain, heart, lungs, liver, kidneys, and spleen after single-dose oral administration of BaBG at doses 1, 5, and 10 mg/kg b.w. at days 1, 3, 5, and 7	104
Table 4.1	General observation and behavioral analysis during the first 4 h and 24 h after single-dose administration of BaBG and 45S5 (300 and 2000 mg/kg b.w.) in rats	118
Table 4.2	General observation and behavioral analysis after repeated-day administration of BaBG and 45S5 (50, 500, and 1000 mg/kg b.w.) in rats	130
Table 4.3	The organ coefficient of male and female rats after repeated 28 days oral administration of BaBG and 45S5 (50, 500, and 1000 mg/kg b.w.)	134

Table 4.4 The effect of repeated-dose 28 days oral administration of BaBG and 45S5 (50, 500, and 1000 mg/kg b.w.) on serum concentration of calcium, creatinine, CK-MB, ALP, ALT, and AST of male and female rats at the end of the experimental protocol. 136

Table 5.1 Primer sequences used for qRTPCR 164

Table 6.1 Primer sequences used for qRTPCR 217

LIST OF ABBREVIATIONS

ACC	:	Anterior cingulate cortex
ACN	:	Acetonitrile
ALP	:	Alkaline phosphatase
ALT	:	Alanine transaminase
AMY	:	Amygdala
AST	:	Aspartate transaminase
ASTM	:	American society for testing and materials
AUC	:	Area under curve
$Ba(NO_{3)2}$	:	Barium nitrate
BaBG	:	Barium-doped bioactive glass
BBB	:	Basso, Beattie, and Bresnahan
BCA	:	Bicinchoninic acid
BET	:	Brunauer–Emmett–Teller
BJH	:	Barrett-Joyner-Halendra
$Ca(NO_3)_2.4H_2O$	:	Calcium nitrate tetrahydrate
CCBs	:	Calcium channel blockers
CCI	:	Chronic constriction injury
CCSEA	:	Committee for the Control and Supervision of Experimentals on Animals
CL	:	Clearence
C_{max}	:	Maximum plasma concentration
CMC	:	Carboxymethyl cellulose
CNS	:	Central nervous system
CRE	:	Creatinine
D	:	Day
EDTA	:	Ethylene diamine tetra acetic acid
EDX	:	Energy dispersive Xray
ETS	:	Experimental toe spreading
FBS	:	Fetal bovine serum
FDA	:	Food and Drug Administration
FTIR	:	Fourier transform infrared spectroscopy
GFAP	:	Glial fibrillary acidic protein
GIT	:	Gastro intestinal tract
HA	:	Hydroxyapatite
Hb	:	Haemoglobin
HCA	:	Hydroxy carbonated appetite
HCT	:	Haematocrit
Iba-1	:	Ionized calcium-binding adapter molecule 1
ICG	:	International Commission on glass
ICP-MS	:	Inductively coupled plasma mass spectrometry

IL 10	:	Interleukin 10
IL-6	:	Interleukin 6
IR	:	Infrared
IUPAC	:	International Union of pure and applied Chemistry
KBr	:	Potassium Bromide
kV	:	Kilo volt
LD_{50}	:	Lethal dose
LDH	:	Lactate dehydrogenase
LPS	:	Lipopolysaccharide
LTP	:	Long term potentiation
mA	:	Milli ampere
MBP	:	Myelin basic protein
MCHC	:	Mean cell haemoglobin concentration
MCV	:	Mean corpuscle volume
MHC	:	Major histocompatibility complex
MRT	:	Mean Residence Time
$NaNO_3$	:	Sodium nitrate
NBO	:	Non bridging oxygen
NF	:	Neurofilament
NF-κB	:	Nuclear factor kappa B
NOAEL	:	No observed adverse effect level
NP	:	Neuropathic pain
NPL	:	Normal foot print length
NTS	:	Normal toe spreading
OECD	:	Organization for Economic Cooperation and Development
OFT	:	Open field test
PBS	:	Phosphate buffer saline
PL	:	Print length
PNS	:	Peripheral nervous system
PPM	:	Parts per million
qRT-PCR	:	Quantitative Real-Time polymerase chain reaction
RAGE	:	Receptor for advanced glycated end product
RBC	:	Red blood corpuscle
RDW	:	Red blood cell distribution
RVM	:	Rostroventral medulla
SAED	:	Selected area electron diffraction
SBF	:	Simulated body fluid
SC	:	Spinal cord
SD	:	Standard deviation
SEM	:	Scanning electron microscopy
SFI	:	Sciatic functional index
SN	:	Sciatic nerve

$t_{1/2}$	:	Half life
TBI	:	Traumatic brain injury
TCO4	:	Technical committee 4
TEM	:	Transmission electron microscopy
TEOS	:	Tetraethyl orthosilicate
TEP	:	Triethyl phosphate
TH	:	Thalamus
TLR 4	:	Toll like receptor 4
T_{max}	:	Total time required to reach maximum plasma concentration
TMZ	:	Temozolomide
TNF-α	:	Tumour necrosis factor-alpha
TRIS	:	Trihydroxy methyl aminomethane
TRPV1	:	Transient receptor potential Vanilloid-1
TS	:	Total spreading
TT	:	Distance between intermediary toes
VEGF	:	Vascular endothelial growth factor
VGCC	:	voltage-gated calcium channel
V_z	:	Volume of distribution
WBC	:	White blood cells
XRD	:	X-ray diffractometry

PREFACE

The thesis's research work entitled "**Novel calcium-regulating mechanism of barium-doped material for the treatment of neuropathic pain**" is based on the assessment of the calcium-regulating mechanism of barium-doped biomaterial and its pharmacological potential for the treatment of neuropathic pain (NP) using chronic constriction injury (CCI) model. NP is a prominent clinical illness that arises as a consequence of injury to the somatosensory nervous system leading to either spontaneous or evoked pain. Globally, NP affects 7-10 % of people worldwide. Despite over a century of studies on nociception, the current treatments for chronic pain have limited effectiveness with adverse effects, leading to withdrawal and poor quality of life. Currently, calcium channel blockers (CCBs) are the first-line treatment for NP. The clinically prescribed CCBs include pregabalin and gabapentin which are organic in nature. Unlike inorganic compounds, organic compounds have various protein interactions which are linked to significant adverse effects. Therefore, it is imperative to develop novel therapeutic strategies that would work on calcium channels. We have selected an inorganic compound i.e., barium-doped bioactive glass (BaBG) that may have certain advantages over the organic compounds as barium that is doped in BaBG are endogenously present in the body so they may not pose any undesired effects. Besides, barium is present in exoplanets so we have evolved containing barium within us. Thus, BaBG was synthesized using the wet chemistry method i.e., sol-gel method. By using the *ex vivo* electrophysiological technique, the calcium-regulating properties of BaBG via its action on the calcium channel were assessed. Further, to examine its potential regenerative and anti-inflammatory properties, cell line-based studies were performed. To assess the therapeutic potential of BaBG for the treatment of NP, a

comprehensive calcium-modulating molecular mechanism was performed in CCI-induced NP in rats. In extension, the sensory and motor abnormalities developed post-CCI was evaluated using a variety of pain behavioral assessment tests. The synaptic rewiring occurring post-BaBG treatment was also examined by tracing the neurons. Furthermore, the *in vivo* biodistribution of the dopants leached from BaBG was determined using quantitative analytical techniques such as inductively coupled plasma mass spectrometry (ICP-MS) as BaBG not only contains barium under the permissible physiological limits but also has other elements that are involved in various physiological activities. By employing a multidisciplinary approach encompassing materials science, pharmacology, and toxicology, we strived to harness the unique properties of BaBG for the development of therapeutic interventions for NP. The entire work has been compiled into seven chapters**: Chapter 1** describes the introduction and significance of the present study. **Chapter 2** describes the synthesis and characterization of barium-doped bioactive glass (BaBG), investigating it's *in vitro* regenerative and anti-inflammatory potential. **Chapter 3** describes the *in vivo* pharmacokinetics, biodistribution, and excretion of dopants released from BaBG following oral administration. **Chapter 4** describes the oral acute and sub-acute toxicity study of BaBG according to the OECD guidelines. **Chapter 5** describes the temporal changes in the intracellular calcium and S100b protein levels in the pathophysiology of CCI-induced NP in rats. **Chapter 6** describes the pharmacological evaluation of BaBG in the treatment of NP. **Chapter 7** summarizes the entire study completed with its essential outcomes.

Chapter 1
Introduction

1. Introduction

1.1. The Genesis of Idea: From Concept to Cure

The discovery of Bioglass® (45S5) in 1971 has led to numerous developments in tissue engineering applications (Hench, Splinter et al. 1971). Bioglass® owing to its bioactivity and osteogenic properties (i.e., osteoconduction and osteostimulation) led to its clinical use for the first time as middle ear prosthetics (MEP®) in 1985 to treat the otomastoiditis-induced hearing loss (Wilson, Clark et al. 1994). Later on, the soft connective tissue bonding of bioactive glass (BG) was first observed in 1981 (Hench 2013). Since then, numerous studies have reported the beneficial interaction of BGs with the non-osseous tissues (Tan, Romanska et al. 2003, Saravanapavan, Verrier et al. 2004, Verrier, Blaker et al. 2004, Wang, Wu et al. 2007, Dai, Yuan et al. 2009, Mao, Lin et al. 2014, Pires, Bonan et al. 2018). BGs, the bioceramic biomaterial, exhibit enormous biological functions due to leaching out of various therapeutic ions that are doped in its framework after coming in contact with the physiological fluid which induces specific intrinsic cellular responses (Perez, Singh et al. 2017). Growing evidence suggests that various trace metals like Cu^{2+}, Mg^{2+}, Zn^{2+}, and Sr^{2+} are doped in the structural framework of BGs purposefully to target specific physiological functions (Dai, Yuan et al. 2009, Zhang, Park et al. 2015, Dziadek, Zagrajczuk et al. 2018, Majumdar, Hira et al. 2021). Consequently, we have incorporated barium into the BGs (BaBG). In the previous study from our lab, it was demonstrated that the oral administration of BaBG exhibited anti-ulcer properties in various gastric ulcer models in rats because of its ability to form a protective layer in the stomach (Paliwal, Kumar et al. 2018) and it also acts like an antacid. Further, previously, fewer reports indicated that the presence of Ba^{2+} in the extracellular fluid resulted in prolonged action potential

plateaus observed in the growth cone of the regenerating axon of lamprey (Macvicar's and Llinas 1985). Barium is also reported to generate a barium spike in the growth cone of the regenerating axon (Macvicar's and Llinas 1985). Besides, the calcium channels exhibit greater selectivity for Ba^{2+} ions compared to Ca^{2+} ions (Hagiwara and Byerly 1981). In light of the aforementioned facts, we have synthesized inorganic barium-doped bioactive glass (BaBG) and performed some preliminary studies where the BaBG scaffold (Indian patent No.: 484408) had exhibited the ability to regenerate the deafferented nerve in the complete transection model of neuropathic pain (NP). So, this gave us the confidence that BaBG has the potential to be used for the treatment of NP which would probably act on the calcium channels and calcium channel blockers (CCBs) are widely used for the management of NP. Moreover, according to reports, barium is found in exoplanets, indicating that all living organisms have developed with barium in their bodies (Silva, Demangeon et al. 2022). In addition, barium is found in rocks, soil, and water (Myrvang, Gjengedal et al. 2016), meaning that every living organism is inevitably exposed to barium. Thus, our body has mechanisms to utilize as well as eliminate it, unlike the organic compounds that are foreign to the body. Therefore, we rationalized using BaBG for the treatment of NP.

1.2. The background of bioactive glass

The journey to a new era of tissue replacement and regeneration started on a bus ride in July 1967, when a U.S. army colonel projected the major agony of mankind after the loss of a limb and offered a major task of developing an artificial bone that the body does not reject. The need for the discovery was based to address the issues associated with then applicable materials for bone regeneration: a) foreign body reaction, b) lack of osseointegration, and bioactivity. This led to an arduous quest to research at the

University of Florida, leading to the discovery of 45S5 Bioglass® ($45SiO_2$–$24.5Na_2O$–$24.5CaO$–$6P_2O_5$ wt%) in November 1969 (Hench 2006).

45S5 Bioglass® synthesized by Professor Larry Hench in 1969 was the evolutionary step paving the way towards a benefic liaison of ceramic engineering and biomedical applications (Hench 2006). Being the first of a third-generation biosynthetic material that could bond to the living tissue like bone and soft tissues; 45S5 Bioglass® was soon discovered to produce *in vivo* activity through a process called osteostimulation, whereby in situ bone regeneration is controlled by the release of ionic dissolution products (IDPs) from the BG particulates leading to up-regulation of genes affecting the production of several growth factors, cytokines, osteoblast differentiation factors, etc. (Hench 2013). Ever since its discovery in 1969, the researches for clinical applications have exploded; from being used for conductive hearing loss (Bioglass Ossicular Reconstruction Prosthesis in 1985), traumatic bone repair, to arthroplasty, spine fusion, cranioplasty, the ocular implant (for fibrovascularization) to fixing oral, dental and periodontal defects to the treatment of dentinal hypersensitivity (Majumdar, Gupta et al. 2022) and metastatic colorectal carcinoma of the liver by radioactive glass TheraSphere® (by Nordion Inc. in 2018)comprising Yttrium-90 (^{90}Y) radionuclide (Baino, Hamzehlou et al. 2018, Majumdar, Gupta et al. 2022).

1.3. Role of therapeutic ions in soft tissue repair and regeneration

BGs, the bioceramic biomaterial, exhibits enormous biological functions by inducing specific intrinsic cellular response due to leaching out of various therapeutic cargoes (ions) after coming in contact with the physiological fluid (Perez, Singh et al. 2017). Various metallic ions (Ag^+, Ba^{2+}, Zn^{2+}, Cu^{2+}, Co^{2+}) are incorporated in the structural framework of BGs purposefully to target specific physiological functions (Dai, Yuan et

al. 2009, Zhang, Park et al. 2015, Dziadek, Zagrajczuk et al. 2018, Majumdar, Hira et al. 2021). Studies have reported that the ions doped in the BGs modifies the physicochemical properties of BGs and hence controls the degradation rates with subsequently better biocompatibility (Gupta, Majumdar et al. 2021). As previously reported, the trace metallic elements are toxic for the cells and tissues at a higher concentration, so to achieve desired biological actions, the leaching of ions should be in an optimum concentration in a controlled manner (Baino, Hamzehlou et al. 2018). For instance, the trace elements (Zn, Cu, Co, Sr) are reported to have anabolic effects in the hard tissue metabolism, and the doping of Co^{2+} reportedly promoted osteogenesis by activating angiogenesis-related genes (Kargozar, Lotfibakhshaiesh et al. 2016). Similarly, silicon (Si) is another important bioactive cation in biomedicine that is essential for the formation and calcification of bones and teeth. It also activates the blood clotting factor XII (Gryshchuk and Galagan 2016, Chen, Han et al. 2018) that further activate different downstream cascades of blood coagulation. Moreover, the optimum release of Ga^{3+} from the BGs matrices exhibited enhanced thrombus formation and platelet adhesion along with whole blood clotting (Pourshahrestani, Zeimaran et al. 2017). Li^{+} incorporated in the BGs activated the Wnt/β-catenin signaling pathway and enhanced the secretion of insulin-like growth factor 1, and promoted angiogenesis (Haro Durand, Vargas et al. 2017). Therefore, BGs have an excellent hemostatic property and promote vascularization of the tissue-engineered construct required for tissue regeneration.

Further, many therapeutic ions doped in the BGs act as enzyme co-factors that stimulate various biochemical pathways, essential for soft tissue repair and regeneration (Lapa, Cresswell et al. 2020). Zinc (Zn^{2+}), a co-factor of many metalloenzymes, is essential for the proliferation, differentiation, and mineralization of osteoblasts (Della Pepa and

Brandi 2016). Besides, studies have also reported that Zn^{2+} eluted from the zinc-doped BGs upregulated the expression of VEGF mRNA, angiopoietin-1, and fibroblast growth factor-2; hence have angiogenic properties required for tissue regeneration (Zhang, Park et al. 2015). Similarly, series of studies have highlighted that copper (Cu^{2+}) ions activate hypoxia-inducible factor-alpha (HIF-α), adaptive response of the human body in hypoxic conditions that aids in angiogenesis and skeletal muscle regeneration (Wan, Gilbert et al. 2008). Another important soft tissue application of the therapeutic ion (Zn^{2+}) doped in the structural framework of BGs includes peripheral nerve regeneration (Sabbatini, Boccafoschi et al. 2014). Sabbatini et al. (Sabbatini, Boccafoschi et al. 2014) explored and reported that Zn^{2+}-doped BGs favored the adhesion and proliferation of the neuronal cell line with enhanced expression of GAP-43, a protein associated with nerve growth and a major component of the growth cones of the elongating axon. Apart from this, the therapeutics ions like Ag^{+} (Pratten, Nazhat et al. 2004, Dai, Yuan et al. 2009) also have anti-bacterial properties, so they are used to coat the catheters and treat urinary tract infections. Based on this scientific evidence, it can be said that BGs have the potential to be used in soft tissue regenerative medicine due to the doped therapeutic ions. Apart from this, BGs are less risky than gene therapy and cost-effective than growth factors.

1.4. Diverse Applications of Bioactive Glass: Innovations in Medicine and Beyond

1.4.1. Bioactive glasses exhibit wound healing property

Wound healing is the dynamic and well-orchestrated physiological process involving the overlapping of four different mechanisms: hemostasis, inflammation, proliferation, and tissue remodeling. It requires an optimal environment to heal, but the extreme loss of blood increases the chance of hypothermia, acidosis, infections and causes multiple

organ failure (Heckbert, Vedder et al. 1998). The existing treatment strategies mainly involve palliative wound dressings, which otherwise are incompetent; thus, there is a need for safe and biocompatible biomaterials to stop arterial and venous bleeding. Current research has paved the way for BGs as an effective hemostatic agent due to the release of ions simulating various processes involved in different stages of wound healing (Naseri, Lepry et al. 2017, Majumdar, Gupta et al. 2022). A study has investigated the silver exchanged mesoporous silica sphere (AgMSS) for its antibacterial properties for uncontrollable hemorrhage control (Dai, Yuan et al. 2009). The thromboelastographic analysis reported the thrombotic property of AgMSS. The time for the fibrin formation in the silver-doped mesoporous silica sphere (2.9 ± 0.2 min) was significantly lower than the control (9.1 ± 2.5 min). The prothrombin (PT) and activated partial thromboplastin time (aPTT) are critical parameters for predicting the hemostatic properties of a biomaterial. AgMSS treatment reduced PT, and aPTT, supporting the fascinating role of BG in hemostasis. Similarly, silver-doped nanoporous BG (n-BGS) prepared using the sol-gel process possessed significantly greater hemostatic and antibacterial properties compared to the BG without nanopores (BGS) (Hu, Xiao et al. 2012). Further, due to the high surface area of the nonporous n-BGS, complete *in vivo* hemostasis in substantially less time, i.e., 27 ± 2.0 seconds, than BGS and control (86 ± 3 and193 ± 8 sec, respectively) was observed.

More recently, BGs were explored in diseases like diabetes, where the wound healing ability is primarily compromised and hence causes a greater risk of infection. Diabetic foot ulcer (DFU), one of the severe complications of diabetes mellitus, was treated using the rubidium-doped BG nanospheres (Rb-BGNs) (He, Ding et al. 2019). The *in vitro* study reported that the ionic dissolution products (IDPs) of Rb-BGMs induced the

proliferation of fibroblasts (FBs) and human immortal keratinocytes (HaCaTs) along with cell migration in the scratch assay, gold standard for repair of the injured tissues. The consolidated findings support the role of Rb-BGMs in wound healing as FBs and HaCaTs are primarily associated with the re-epithelialization and collagen deposition, vital steps of wound healing. Besides, Rb-BGMs increased the expression of various growth factors essential for wound healing (i.e., VEGF (vascular endothelial growth factor), EGF (epidermal growth factor), and PDGF (platelet-derived growth factor)). Based on the effectiveness of growth factor on wound closure, EF was loaded into Rb-BGM and produced a synergistic effect with improved hemostasis and collagen deposition compared to unloaded Rb-BGMs. A further study by Cong et al. (Mao, Lin et al. 2014) established the potential of BGs in accelerating the healing of full-thickness diabetes wounds in rodents. Bioglass® ointment significantly improved the fibroblast proliferation and formation of the granulation tissue compared to the saline-treated diabetic rats. Hence, BGs can heal wounds by incorporating various other ions to elicit several different cellular responses.

The US-FDA has approved a melt-derived borate-based Bioglass® matrix as a wound dressing (MIRRAGEN™, ETS Wound Care LLC, USA) to treat acute and chronic deep wounds (http://etissuesolutions.com/ 2017). The preclinical study data reported MIRRAGEN® advanced wound matrix to exhibit the slightest inflammation and healed deep wounds in less time. There was significantly more granulation tissue than synthetic polymer fiber and silver-doped collagen fiber (http://etissuesolutions.com/ 2017). Following these seminal results, BGs can serve as an advanced material system for faster wound healing. However, more preclinical and clinical research is required to translate BGs efficiently.

1.4.2. Bioactive glasses facilitate angiogenesis

The beneficial role of 45S5 in promoting endothelial cell proliferation and tubule formation suggestive of angiogenesis was first evidenced in 2004 (Day 2005). The study reported the stimulatory role of IDPs of 45S5 on de novo release and expression of VEGF and bFGF in human intestinal fibroblasts (CCD-18Co) (Day 2005). The same research group (Day, Boccaccini et al. 2004) also reported that composite scaffolds of polyglycolic acid (PGA)/45S5 after 28 and 42 days of subcutaneous (s.c.) implantation in Lewis rats promoted neovascularization without any inflammatory response. In another study, sintered 45S5 promoted angiogenesis using a model of an arteriovenous loop formed between the contralateral sides of the femoral artery and vein in the medial thigh of the Lewis rats (Arkudas, Balzer et al. 2013). The loop placed in a Teflon isolation chamber and embedded in a sintered 45S5 granular matrix filled with fibrin gel showed axial vascularization and dense sprouting angiogenesis three weeks post-operation. The authors suggested that the intrinsic type of vascularization with an equal number of blood vessels in the arterial and venous parts could allow transplantation of the entire construct using the AVL pedicle to confer neovascularization in larger soft tissues.

Moreover, the IDP of BGs stimulates fibroblasts to secrete angiogenic growth factors, which activates endothelial cells to form a vascular network on the scaffolds, thereby enhancing *ex vivo* pre-vascularization of the scaffolds (Gorustovich, Roether et al. 2010, Yu, Peng et al. 2016, Balasubramanian, Hupa et al. 2017, Qazi, Berkmann et al. 2018). Furthermore, Co^{2+} ions also produce chemical hypoxia and induce HIF-1α with further activation of the downstream hypoxic pathway. In a study (Wu, Zhou et al. 2012), sustained release of Co^{2+} ions from a Co-doped BG scaffold has been shown to

upregulate the gene expression of VEGF and HIF-1α, leading to vascularized tissue regeneration

1.4.3. Bioactive glasses in gastrointestinal tissue regeneration

Peptic Ulcer Disease (PUD) is said to have a worldwide prevalence of 4% and have a high recurrence rate despite long-term chronic drug treatment and its associated adverse effects (Lanas and Chan 2017, Paliwal, Kumar et al. 2018). Moosvi et al. (Moosvi and Day 2009) reported that 45S5 promotes healing of injured superficial intestinal mucosa through a mechanism involving epithelial restitution, which involves epithelial cell migration adjacent to the denuded basal lamina. 45S5 affected paracrine mucosal signaling, promoting rapid epithelial repair modulating intestinal epithelial cell growth and migration without causing cell proliferation in a dose-dependent manner.

1.4.4. Bioactive glasses in myocardial tissue engineering

The most versatile application of BGs lies in the possibility of regenerating tissues with inferior regenerative potentials like that of the heart and the lungs. Chen et al. (Chen, Jin et al. 2010) developed a cardiac patch using elastomeric poly(glycerol sebacate) (PGS) with nanoparticles of the melt-derived 45S5 to provide mechanical support to the damaged tissues. However, PGS has limited applicability due to the cytotoxicity of the acidic degradation products, which the alkaline BGs neutralize. In an *in vitro* study, PGS-BG exhibited reduced cytotoxicity to the hESC-CM compared to PGS and even promoted cell proliferation. BG incorporated hydrogel has also been investigated in myocardial TE (Li and Guan 2011). Barabadi et al. (Barabadi, Azami et al. 2016) fabricated gelatin-COL (G/C) hydrogel containing sol-gel-derived BG (G/C/BG). The G/C/BG scaffold-treated cells showed significantly higher viability than the G/C

hydrogel after 72 h of incubation. In addition, cell attachment assay showed more significant infiltration of cells through the pores of the scaffold (G/C/BG) along with increased expression of cardiac tissue-specific proteins like Desmin and α-Actin.

1.4.5. Bioactive glass aids in the peripheral nerve regeneration

Traumatic injury, surgery, chemotherapy, and diseases like diabetes, hypothyroidism, and rheumatoid arthritis lead to motor and sensory deprivation of the affected area due to peripheral nerve damage. Treatment of damaged nerves involves allografts or autografts, with the implicit drawbacks of finding the matching donor and blunted complete functional recovery (Grinsell and Keating 2014). Thus, the other possible alternatives preferred nowadays to bridge the gaps between the damaged peripheral nerves include the nerve guide conduits (NGC). Based on the importance of directional guidance to the regenerating axons, Kim et al. (Kim, Lee et al. 2012) designed a biocompatible and biodegradable scaffold filled with phosphate glass fibers (PGf). The *in vitro* study reported that the length of the neurites of the DRG (dorsal root ganglion) grew to 1220.8 ±168.4 μm length that was significantly larger compared to the control group (875.1±185.1 μm) after incubating for three days. Further, in the *in vivo* experimental model, the sciatic nerve was transected, and the gap was bridged using the conduits. Interestingly, the *in vivo* study results were similar to the *in vitro* data regarding neurite length and number. Similarly, in a very recent study, PGf formulated into gelatin methacrylate (GeIMA) hydrogel (GeIMA-PGf) exhibited significantly more aligned directional growth and spreading of C6 cells over its surface after 14 days incubation compared to GeIMA (Keskin-Erdogan, Patel et al. 2021). This observed growth of C6 cells might be due to the biophysical cues provided by the PGf for neural

growth. Hence, BGs can be considered an essential biomaterial for nerve conduits, guiding regenerated fibers and supporting further nerve regeneration.

1.5. Innovation in Biomaterials: The Development of Barium-Doped Bioactive Glass (BaBG)

Barium (Ba^{2+}) is a trace alkaline earth metal present in the human body (22 mg in a 70 kg adult) (Schroeder, Tipton et al. 1972), mainly in the bones and also in muscle, skin, connective tissue, and the lungs and elicits various physiological functions (Satoh, Kubota et al. 1987, Majumdar, Gupta et al. 2021, Majumdar, Hira et al. 2021). The enrichment of barium in the bone of rodents is also reported and is essential for their calcification (Moore Jr 1964). There are various reports on the use of barium as radiocontrast agents as well as in radio-osteometric analysis (Madanat, Moritz et al. 2009). Barium causes concentration-dependent contraction of the smooth muscle (Satoh, Kubota et al. 1987) but there is a paucity of information on the pharmacological potential of barium. According to reports, barium is found in exoplanets, indicating that all living organisms have developed with barium in their bodies (Silva, Demangeon et al. 2022). In addition, barium is found in rocks, soil, and water (Myrvang, Gjengedal et al. 2016), meaning that every living organism is inevitably exposed to barium. Thus, our body has mechanisms to utilize as well as eliminate it, unlike the organic compounds that are foreign to the body. In light of the aforementioned facts, we had incorporated in the BGs to elicit specific physiological functions. In our laboratory, we have reported that barium-doped BGs possess anti-ulcer properties (Paliwal, Kumar et al. 2018). Additionally, we have reported that Ba^{2+} released from BaBG possesses anti-inflammatory properties (Majumdar, Hira et al. 2021). Previously, fewer reports indicated that the presence of Ba^{2+} ions in the extracellular fluid resulted in prolonged

action potential plateaus observed in the growth cone of regenerating axon of lamprey (Macvicar's and Llinas 1985). The calcium channels also exhibit greater selectivity for Ba^{2+} ions compared to Ca^{2+} ions (Hagiwara and Byerly 1981). Therefore, we presumed that BaBG has the potential to be used as a therapeutic strategy for the treatment of neuropathic pain (NP) by acting on the calcium channels.

1.6. Understanding Neuropathic Pain: An Introduction

Neuropathic pain (NP) is a persistent pain condition that occurs due to injury or lesion to the central or peripheral nervous system (Baron, Maier et al. 2017). The International Association for the Study of Pain (IASP) has defined pain as "an unpleasant sensory and emotional experience associated with, or resembling that associated with, actual or potential tissue damage" (Raja, Carr et al. 2020). It mostly arises as a direct consequence of a lesion or diseases affecting the somatosensory system (Gierthmühlen and Baron 2016). The somatosensory nerves mostly originate in the skin, muscles, joints, and fascia and comprise thermoreceptors, mechanoreceptors, chemoreceptors, and nociceptors (Colloca, Ludman et al. 2017). These nerves transmit the sensory signals from the periphery to the spinal cord (SC) and subsequently to the brain for perception of "sensations" such as touch, pain, pressure, vibrations, and temperature. Therefore, any lesions or disorders affecting the somatosensory nervous system can cause abnormal and disrupted transmission of sensory information to the spinal and supraspinal regions which results in the emergence of sensory anomalies (Colloca, Ludman et al. 2017). The identification of distinct sensory abnormalities is essential for accurately diagnosing NP and differentiating it from other types of pain. The damage to bodily tissues leads to the occurrence of acute pain which serves as a warning signal for the body and plays a crucial role in safeguarding its well-being. Nevertheless, acute pain has the potential to progress into a chronic state in the presence

of a disease, as a result of maladaptive changes in the neural pathways within the SC and regions above it. The International Classification of Disease (ICD) given by World Health Organization (WHO) defines chronic pain as the pain that persists for more than three months of duration (Nicholas, Vlaeyen et al. 2019). The emergence of chronic NP has a significant impact on an individual's physical capabilities, psychological state, and interpersonal engagements and imposes a huge burden on the healthcare system. Further, the global epidemiological studies suggested that NP affects around 7-10 % of people worldwide (Colloca, Ludman et al. 2017, Bannister, Sachau et al. 2020) with greater rates documented in individuals with metabolic diseases like diabetes mellitus (up to 26 %) or in case of spinal cord injury (around 40%) (Widerström-Noga 2017, Smith, Hébert et al. 2020). Besides, it is anticipated that the number of patients suffering from NP will rise in the years to come. Therefore, NP is a serious clinical illness that necessitates further investigation to comprehend its pathogenesis and to devise effective treatment of persistent pain.

1.7. Symptoms of Neuropathic pain

The peripheral nerve injury normally induces the NP which may either be spontaneous pain or the stimulus evoked pain (Van Hecke, Austin et al. 2014) as represented in **Table 1.1**. The spontaneous pain is stimulus independent which can be either shooting electrical attacks (paroxysmal pain) or the painful ongoing burning sensation (superficial pain) occurring due to spontaneous ectopic activity in the nociceptive C-fibers thus causing central sensitization of the dorsal horn neurons (Baron, Maier et al. 2017). The second category of the NP is the stimulus evoked pain which may either be allodynia or hyperalgesia (Loeser and Treede 2008). According to the International Association for the Study of Pain (IASP), allodynia refers to the experience of pain in response to a stimulus that that is normally non painful and is caused due to the action

of the Aβ fibers on the CNS. Similarly, hyperalgesia is increased response to a stimulus that is normally painful due to decrease in the threshold of the nociceptive nonmyelinated C-fibers (Buonocore, Demartini et al. 2016). Further, the evoked pain can easily be stimulated by touch, vibration, hot, cold and pin prick (Loeser and Treede 2008).

Table 1.1: Definition of the negative and positive symptoms observed clinically in patients suffering from neuropathic pain

Negative symptoms and signs	
Hypoaesthesia	Reduced sensation to non-painful stimuli
Pall-hypoaesthesia	Reduced sensation to vibration
Hypoalgesia	Reduced sensation to painful stimuli
Thermal hypoaesthesia	Reduced sensation to cold or warm stimuli
Spontaneous sensations or pain	
Paraesthesia	Non-painful ongoing sensation (skin crawling sensation)
Paroxysmal pain	Shooting electrical attacks for seconds
Superficial pain	Painful ongoing sensation, often a burning sensation
Evoked pain	
Mechanical dynamic allodynia	Pain from normally non-painful light moving stimuli on skin
Cold hyperalgesia	Pain from normally non-painful cold stimuli
Heat hyperalgesia	Pain from normally non-painful heat stimuli
Mechanical punctate, pin-prick hyperalgesia	Pain from normally stinging but non-painful stimuli

1.8. Epidemiology of Neuropathic pain

The prevalence rates of persistent pain range from 11 % to 40 % worldwide, and according to a study conducted by the US Centers for Disease Control and Prevention (CDC), 20.4 % of people suffers from chronic pain in United States (Dahlhamer 2018, Cohen, Vase et al. 2021). Similarly, a comprehensive analysis of research conducted in

the UK found that the overall prevalence rate of chronic pain was 43.5 %, with the incidence of moderate-to-severe debilitating pain ranging from 10.4 % to 14.3 % (Fayaz, Croft et al. 2016). In Asia, the prevalence rate of chronic pain ranges from 13 to 51 % (Bhattarai, Pokhrel et al. 2007, Sá, Moreira et al. 2019). Specifically, as per the meta-analysis study performed, the data collected from India revealed that around 19.3 % of people are experiencing NP (Bhattarai, Pokhrel et al. 2007, Dureja, Jain et al. 2014, Saxena, Jain et al. 2018). Additionally, it was more prevalent in the older population i.e., beyond the age of 65 (Saxena, Jain et al. 2018). In the older population, the prevalence of NP was reported to be 23.5 % compared to 15.5 % in the younger population in India (Saxena, Jain et al. 2018). The Global Burden of Disease Study 2019 has confirmed once again that pain and pain-related disorders are the primary cause of disability and disease burden worldwide (Mills, Nicolson et al. 2019, Shin, Shin et al. 2022). Hence, the substantial worldwide burden of chronic pain necessitates addressing the origin and consequences of NP, with a focus on both individual and population-based interventions.

1.9. The physiology of pain perception

The primary afferent fibers of the somatosensory nervous system are comprised of the nociceptive non-myelinated C-fibers that generally terminate at the spino-thalamic projection neuron in the upper laminae as depicted in **Figure 1.1** (highlighted in red). In addition, there are non-nociceptive myelinated A-fibres that are projected into the deeper laminae of the spinal cord (indicated in blue color). Aβ fibers are responsible for perceiving delicate sensations such as touch, while the C and Aδ fibers detect more intense stimuli including mechanical and thermal sensations. (Meyer, Ringkamp et al. 2005). Further, there is second order projection neuron of wide dynamic range (WDR)

type (marked in orange in **Figure 1.1**) that directly receives input from the nociceptive C-fiber terminals. However, there is multisynaptic input from the A-fiber. The WDR neuron also receives inhibitory input from the GABAergic interneurons (colored green). Injury to the sensory peripheral fibres (A and C fibers) causes activation of the nociceptors in response to the external stimulus like temperature, pressure, touch, vibration, etc. which are relayed to the dorsal horn of SC via the generation of action potential (Peirs and Seal 2016). After a peripheral nerve lesion, the nociceptive neurons become abnormally sensitive and develop pathological spontaneous activity (Colloca, Ludman et al. 2017). The hyperactivity of nociceptors causes secondary neuroplastic changes in the spinothalamic tract and modulates the synaptic transmission at the spinal level leading to central sensitization (D'Mello and Dickenson 2008).

The spinal projections then carry the nociceptive information via the spinothalamic and spinoreticulothalamic tract to the supraspinal areas including the periaqueductal grey (PAG) and thalamus (TH) that acts as a central relay station for sensory information (Tracey and Mantyh 2007, Peirs and Seal 2016). Projections to the posterolateral thalamus convey specific information about the stimulus and originate from the endpoints of the column/medial lemniscus route. On the other hand, the medial thalamic nuclei get information related to the emotional aspect of pain (Peirs and Seal 2016). Subsequently, the signals reaches the complex "pain neuromatrix" located in the cortical regions i.e., somatosensory cortex (SC), prefrontal cortex (PFC), insular (INS), and anterior cingulated cortex (ACC) (Tracey and Mantyh 2007). SC is reported to encode the sensory-discriminative aspects of pain while INS, ACC, and PFC is implicated to regulate the affective (emotional) and interoceptive aspects of pain along

with the pain-related decision making by PFC (Apkarian, Bushnell et al. 2005, Tracey and Mantyh 2007) as shown in **Figure 1.2**.

Normally, the descending efferent pathways from the PAG and rostroventral medulla (RVM) runs downward to the dorsal horn of the SC through the dorsal section of the lateral funiculus (Peirs and Seal 2016) which regulate the pain signal and effectively block its facilitation (Wood 2020). However, in case of chronic pain like NP, here is loss of descending analgesic pathway (Baron, Maier et al. 2017). Additionally, there is impairment of the inhibitory input from the GABAergic interneurons into the SC, hence causes hyper excitation of nociceptors that enhances the pain sensation.

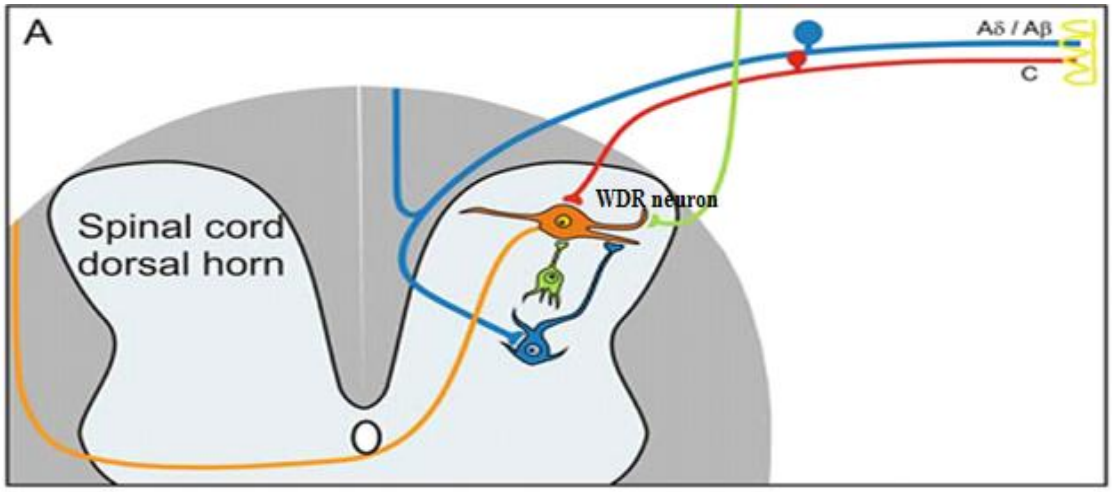

Figure 1.1. The primary afferent pathways and its connections in the dorsal horn of spinal cord. Reprinted with permission from Elsevier (Baron, Binder et al. 2010).

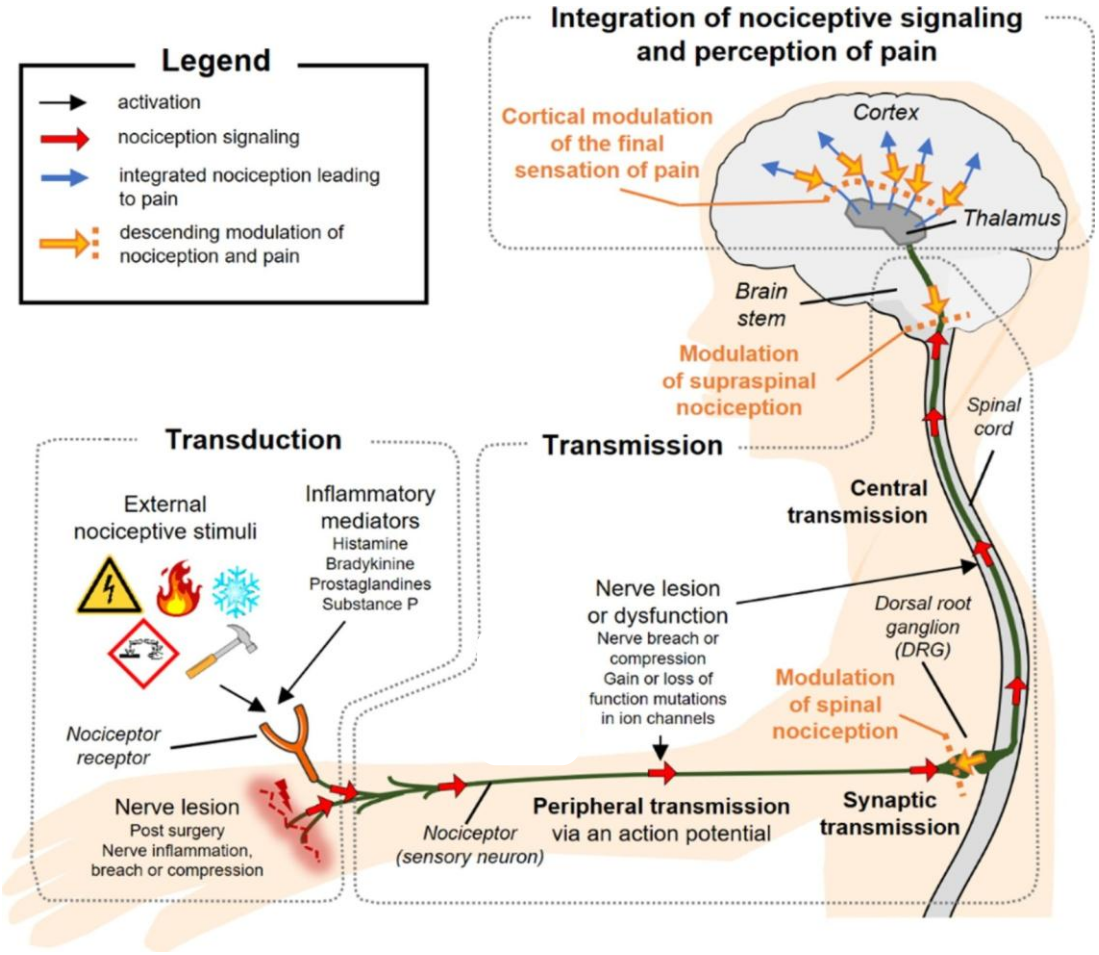

Figure 1.2. The ascending pathway of the pain perception. Reprinted with permission from Elsevier (da Silva, Lepetre-Mouelhi et al. 2022).

1.10. Pathophysiology and molecular mechanism of Neuropathic pain

1.10.1. Peripheral sensitization:

Peripheral sensitization is the ectopic activity developed in the primary afferent nociceptors after partial peripheral nerve lesion or damage (Baron 2006). Typically, following an injury, certain axons get damaged and disintegrate, while others stay intact and connected to the organ, as depicted in as depicted in **Figure 1.3**. This leads to the activation of voltage-gated sodium channels ($Na_v1.7$, $Na_v1.8$ & $Na_v1.9$) on both the damaged and intact sections of the nociceptive C fiber axon (Woolf and Mannion 1999, Waxman, Merkies et al. 2014)**,** which results in a decrease in the threshold for action

potential generation in the injured nerve and consequently leads to increased nerve activity and excruciating pain sensations (Lai, Hunter et al. 2003). Additionally, research has indicated a mutation in the SCN9A gene, responsible for encoding the sodium channel $Na_V1.7$. This mutation results in a change in the gating properties of the channel, causing a shift in its activation towards hyper polarization. As a result, the channel becomes easier to activate, leading to a rapid generation of action potential (Yang, Wang et al. 2004).

Additionally, the peripheral nerve injury induces an upregulation of TRPV 1 expression on the intact A-fibers and C-fibers, which leads to thermal sensitivity (Hudson, Bevan et al. 2001, Hong, Morrow et al. 2004). Out of all the members of the TRP family, the receptor TRPV1 has been extensively researched and is responsible for detecting heat beyond 42°C, which is near the threshold where pain is sensed (Julius 2013). Further, other temperature-sensitive ion channels, such as TRPV2, become active at temperatures exceeding 52°C and TRPV3 and TRPV4 are activated at temperatures ranging from 25°C to 35°C (Julius 2013). In addition, the TRPV2 and TRPA1 receptors are involved in the perception of mechanosensation, indicating their ability to detect multiple types of stimuli (Baron, Maier et al. 2017). Even after peripheral nerve loss or lesion, there is evidence of over expression of the TRPM 8 receptor, which sensitizes cold-sensitive C-fibers and causes cold hyperalgesia (Wasner, Schattschneider et al. 2004).

Moreover, several signaling pathways are involved in the development of peripheral sensitization in NP conditions. Calcitonin gene related peptide and substance P are examples of inflammatory mediators that are released from nociceptive terminals following injury. These mediators enhance the vascular permeability, which in turn

causes localized edema and allows the byproducts of injury, including as prostaglandins, bradykinin (Wang, Ehnert et al. 2006), growth factors, and cytokines, to escape (Cohen and Mao 2014). These mediators stimulate the ion channels that are present on the nociceptive terminal by either direct processes (phosphorylation) or indirect mechanisms (the prostaglandin pathway) which have the ability to sensitize them, which can lead to decreased firing thresholds and more discharges (Fornasari 2012).

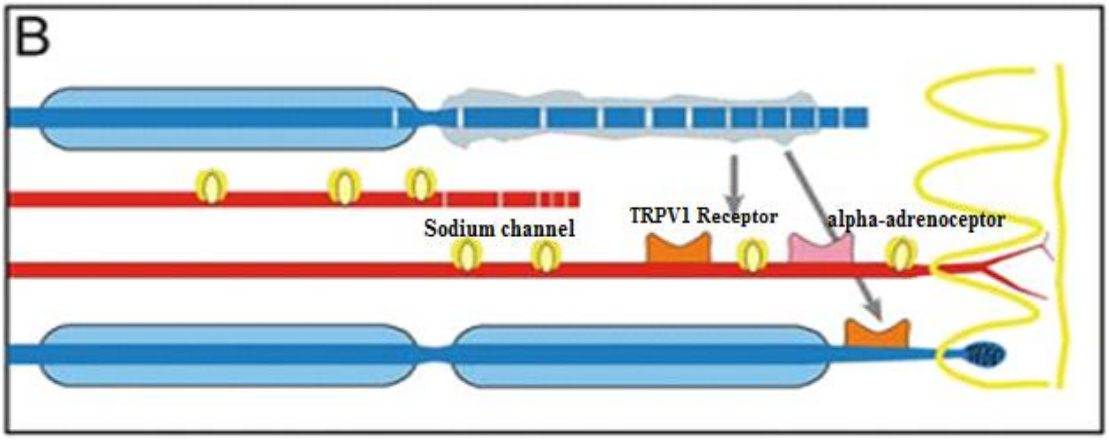

Figure 1.3. The peripheral changes in the primary afferent neuron after the peripheral nerve injury. Reprinted with permission from Elsevier (Baron, Binder et al. 2010).

1.10.2. Central sensitization:

Peripheral sensitization of the afferent C nociceptive fibers causes neuroplastic changes in the spinothalamic tract, which enhances the synaptic excitability of neurons in the SC, brainstem, and brain This ultimately leads to central sensitization (Baron, Maier et al. 2017). Spinal cord dorsal horn neurons are sensitized by primary afferent sensory fibers through the release of glutamate. The glutamate then acts on post-synaptic N-methyl-D-aspartate (NMDA) receptors, which play an integral part in the development and maintenance of central sensitization (Baron 2006). In addition, there is an abnormal rise in the upregulation of calcium channels, leading to an enhanced inflow of calcium

ions (Cui, Wu et al. 2021). The influx of calcium ions removes the Mg^{2+} block from the NMDA receptors, resulting in the further entry of calcium. These events trigger different intracellular cascade pathways, including MAPK, PKA, PKC, extracellular signal-related kinase (ERK), and Src. This contributes to an increased sensitivity of the central nervous system, causing normal inputs to elicit exaggerated responses (Woolf 2007). In addition to all of these various cytokines, prostaglandin, BDNF, and substance P also stimulate NMDA receptors and contribute to increased sensitivity to heat and mechanical stimuli (Baron 2006). All of these physiological alterations contribute to, or uphold, the presence of persistent pain as represented in **Figure 1.4**.

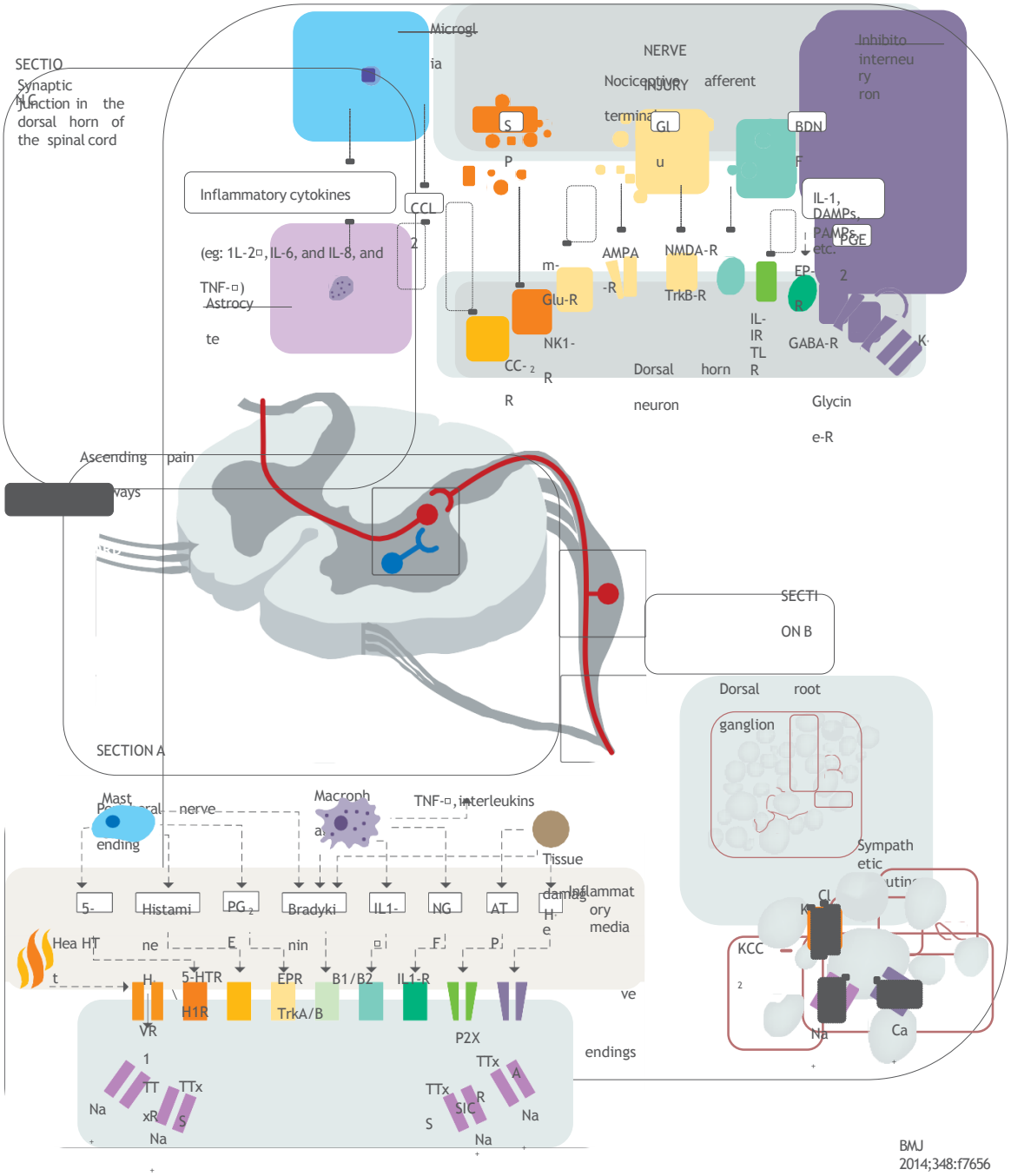

Figure 1.4. The mechanisms of central sensitization of WDR neurons. Diagram showing the various mechanisms involved in neuropathic pain at different sites in the nociceptive pathway. AMPA=α-amino-3-hydroxy-5-methyl- 4-isoxazolepropionic acid; ASIC=acid sensing ion channel; B1/B2=bradykinin receptor 1/2; BDNF=brain derived neurotrophic factor; CCL=chemokine (C-C motif) ligand; CC-R2=CC-chemokine receptor; DAMPs=danger associated molecular patterns; EPR=prostaglandin E2 sensitive receptor; GABA: γ-aminobutyric acid; Glu=glutamate; H1R=histamine receptor; 5-HT=5-hydroxytryptamine; IL=interleukin; KCC=potassium-chloride cotransporter; m-Glu=metabatropic glutamate; NGF=nerve

growth factor; NK=neurokinin; NMDA=N-methyl-D-aspartate; PAMPs: pathogen associated molecular patterns; PG=prostaglandin; P2X=purinergic receptor channel; -R=receptor; SP=substance P; TLR=toll-like receptor; TNF=tumor necrosis factor; Trk=tyrosine kinase; TTxR=tetrodotoxin resistant sodium channel; TTxS=tetrodotoxin sensitive sodium channel; VR=vanilloid receptor (transient receptor potential cation channel subfamily V member 1 TRPV-1). Reprinted with permission from BMJ Publishing Group Ltd. (Cohen and Mao 2014).

1.11. Clinical pharmacotherapy for the treatment of Neuropathic pain

The management of neuropathic pain mostly involves addressing symptoms, and only in certain pathological conditions, the underlying reasons can be treated to alleviate pain. Treating neuropathic pain entails using a range of drugs with the goal of alleviating pain and enhancing overall quality of life. However, around 35% of NP patients do not respond to classical analgesics and even exhibit substantial side-effects (Dworkin, O'connor et al. 2007, Kamerman, Wadley et al. 2015). This is mostly owing to the fact that there is complex overlaying of the molecular and cellular mechanisms contributing to NP which are not entirely comprehended.

1.11.1. Calcium channel blockers/ anticonvulsants

Anticonvulsants are used for the treatment of a wide range of chronic pain conditions, particularly those that are of a neuropathic origin. Within the context of neuropathic pain, activation of many ion channels takes place, including the voltage-gated calcium channel, which is responsible for modulating neuronal firing (Zamponi, Lewis et al. 2009, Alles and Smith 2021). Carbamazepine, oxcarbazepine, topiramate, gabapentin, pregabalin, and lamotrigine are the anticonvulsants that are most frequently used in the management of chronic pain, which includes the treatment of medical conditions such as diabetic neuropathy, trigeminal neuralgia, and other similar conditions (Guy, Mehta et al. 2014). Gabapentin and pregabalin are currently the first-line treatment for the

management of chronic pain (Saxena, Jain et al. 2018, Cavalli, Mammana et al. 2019). Both of these medications have the ability to control the levels of intracellular Ca^{2+}, and they also have active effects on substance P, involved in sensitization of the pain pathways (Gilron and Flatters 2006). Gabapentinoids are reported to bind to the auxiliary unit of calcium channel i.e., α2δ and regulates the calcium influx and aberrant synaptic transmission (Patel and Dickenson 2016). However, the clinical drawbacks of them includes increased risk of atrial fibrillation (Afib) along with somnolence, dizziness, and peripheral edema (10 % to 15 %) (Park, Hunter et al. 2023). Further, the withdrawal rate for pregabalin is 19 % which is mainly due to dizziness and somnolence (Moore, Straube et al. 2009).

1.11.2. Nonsteroidal anti-inflammatory drugs (NSAIDs)

NSAIDs are the analgesics that are used the most frequently by people of varying ages, with the elderly being the most likely to use them for treating acute painful conditions (Vo, Rice et al. 2009). They are usually used frequently for conditions like sprains, headaches, menstrual cramps, surgical pain, and so forth. Additionally, these medications are utilized to treat chronic pain conditions, such as rheumatoid arthritis and osteoarthritis due to their ability to diminish inflammation and other mediators of peripheral sensitization (Crofford 2013). Cyclooxygenase (COX) inhibition is the primary mechanism of action for this class of medicines, which also inhibits the production of prostaglandins that are involved in the progression of NP. The use of these medications is being restricted in clinics, despite the fact that they are effective. This is because there have been worries raised about the contraindications and side effects that they may cause (Paglia, Silva et al. 2021). Acetaminophen, a strong and safer nonsteroidal anti-inflammatory drug (NSAID) analgesic, works by inhibiting COX-3

in the acute therapy paradigm. Acetaminophen poses the dangers of liver damage and nephropathy. Therefore, patients with a history of alcohol and tobacco use are administered lower dosages of this medication (Gloor, Schvartz et al. 2019).

Table 1.2. Clinical pharmacomanagement of neuropathic pain

	Class	Drugs	Dose
First-line therapy	Calcium channel α2-δ ligands	Gabapentin	100–1800 mg/day
		Pregabalin	50–450 mg/day
	Tricyclic antidepressants (TCAs)	Amitriptyline	10–150mg/day
	Serotonin–norepinephrine reuptake inhibitors (SNRI)	Duloxetine	20–120mg/day
		Venlafaxine	37.5–225mg/day
Second-line therapy	Opioids	Tramadol	25–100mg/day
	Topical treatment	Lidocaine	5% patches or gel
		Capsaicin	8% patches
Third-line therapy	Strong opioids	Morphine	10–120mg/day
		Oxycodone	10–120mg/day
	Neurotoxin	Botulinum toxin	25–300 U BTX-A 0.9% saline

(Saxena, Jain et al. 2018, Cavalli, Mammana et al. 2019)

1.11.3. Antidepressants

The analgesic action of tricyclic antidepressants (TCA) is a result of their ability to prevent the reuptake of norepinephrine at the synapses in the spinal dorsal region. The analgesic effect of TCA is attributed to their ability to prevent the reuptake of norepinephrine at the synapses in the spinal dorsal region (Zilliox 2017). Additionally, they also exhibit secondary activity via affecting sodium channels. Amitriptyline has a moderate level of inhibition in both norepinephrine and serotonin reuptake. On the other hand, nortriptyline, which is equally effective but has lesser side effects, demonstrates a higher level of inhibition specifically in norepinephrine reuptake. TCA are efficacious

in treating several forms of neuropathic pain, including severe diabetic neuropathy and postherpetic neuralgia (Park and Moon 2010). TCA are deemed efficacious in the treatment of central pain; nonetheless, there is a scarcity of data about their effectiveness in particular central pain causes. The primary issue associated with the utilization of tricyclic antidepressants is the occurrence of adverse effects. Typical adverse reactions consist of drowsiness and anticholinergic symptoms, such as dry mouth, impaired vision, constipation, urine retention, and postural hypotension. These medications should be taken carefully in individuals who have a history of heart illness. It is advisable to do a screening electrocardiogram (ECG) to check for any abnormalities in the heart's conduction before starting treatment. Additionally, attention should be exercised in patients with glaucoma, urinary retention, or autonomic neuropathy (Park and Moon 2010). Similarly, serotonin norepinephrine reuptake inhibitors (SNRIs) such as venlafaxine, duloxetine, milnacipran are also prescribed for pain management but they carry serious side effects including suicidal tendencies, liver damage, weight gain, withdrawal symptoms, etc. (Park and Moon 2010).

1.11.4. Opioids

Opioids, which are highly strong and effective pain relievers, have recently been relegated to a third-line treatment option for chronic pain in medical clinics, despite their well-established therapeutic benefits (Park and Moon 2010). Morphine, methadone, tramadol, tapentadol, and buprenorphine are frequently used for pain management purposes (Nadeau, Wu et al. 2021). Opioids tolerance is the primary element that restricts the effectiveness of treatment, resulting in the need for higher doses, the occurrence of severe adverse effects, and in rare cases, even death of patients (Nadeau, Wu et al. 2021). Tramadol exhibits a dual mode of action, functioning both as

a central opioid agonist at the mu receptor and as an inhibitor of norepinephrine and serotonin reuptake (da Rocha, Mizzaci et al. 2020). It has demonstrated efficacy in several neuropathic pain situations, such as severe diabetic neuropathy and mixed neuropathic pain syndromes. Despite being regarded as a safer option compared to other narcotic painkillers, this medication is classified as a schedule IV prohibited substance and is experiencing a growing problem of misuse and abuse. The negative consequences of tramadol usage encompass dizziness, nausea, constipation, somnolence, and orthostatic hypotension. Further, codeine, morphine, oxycodone, and fentanyl are examples of potent opioids commonly used for chronic pain management. Their efficacy in managing various neuropathic pain syndromes is a subject of debate, and the utilization of opioids for the treatment of persistent noncancerous pain is a matter of public health concern due to the increasing number of fatalities associated with prescription opioids in the United States (Dowell 2022).

1.11.5. Additional pharmacotherapy

Additional approaches for managing chronic pain include the use of low dose naltrexone, topical medications such as diclofenac, lidocaine, and capsaicin, skeletal muscle relaxants like baclofen, tizanidine, and cyclobenzaprine, as well as botulinum toxin A and cannabinoids (Dowell 2022). However, further research is needed to determine the most effective therapeutic approach, such as combination therapy. Divalproex sodium has also demonstrated success in the treatment of painful diabetic neuropathy and trigeminal neuralgia. However, it does not effectively reduce overall pain or enhance quality of life (Muresanu, Verisezan Rosu et al. 2021).

1.12. Role of ion channels in the development and progression of Neuropathic pain

Modifications in the expression, trafficking, and functioning of ion channels in primary sensory neurons can elicit neuronal hyperexcitability and spontaneous activity, thus leading to the development and maintenance of NP (Aurilio, Pota et al. 2008, Bouali-Benazzouz, Landry et al. 2021). As previously stated, the expression and function of ion channels have been reportedly altered in the primary afferent of animals with neuropathic pain (Tibbs, Posson et al. 2016). Besides, remodeling caused by alterations to the membrane-bound proteins comprising ion channels, might also alter the electrical characteristics of the damaged neuron. Preclinical research on NP indicate that membrane modification leads to increased neuronal excitability due to decrease in the threshold of action potential generation because of disruption in the ionic homeostasis (Bouali-Benazzouz, Landry et al. 2021). The hyper excitability of the nociceptors is observed both at the specific location of nerve damage as well as farther away in the dorsal root ganglia and dorsal horn of the SC. These patterns of anomalous and excessive discharge are considered to be the main reasons for the positive symptoms (paresthesia, dysesthesia, hyperalgesia, and allodynia) experienced by people with NP (Markman and Dworkin 2006). Hence, ion channels have a crucial function in the development and maintenance of NP by regulating the neuronal excitability, the release of neurotransmitters, and the activation of glial cells. The intricate pathophysiology of NP involves voltage-gated sodium and calcium channels, transient receptor potential (TRP) channels, potassium channels, hyperpolarization-activated cyclic nucleotide (HCN) channels, and acid-sensing ion channels (ASICs) (Tibbs, Posson et al. 2016).

1.12.1. Voltage-Gated Sodium Channels

Neuronal action potentials depend on voltage-gated sodium channels (Na_v). $Na_v1.3$, $Na_v1.7$, $Na_v1.8$, and $Na_v1.9$ subcategories of Na_v channels have been implicated of causing NP (Tibbs, Posson et al. 2016). $Na_v1.3$ is reportedly upregulated in sensory neurons after nerve injury. This particular subtype is typically not present in the fully developed sensory neurons, but it reemerges after nerve injury leading to heightened activity and spontaneous firing of the neurons, which ultimately contributes to the perception of pain (Liu, Zhong et al. 2020). Further, hereditary pain syndromes have also been linked to $Na_v1.7$ gene mutations (Niu, Liu et al. 2021). This mutation results in a change in the gating properties of the channel, causing a shift in its activation towards hyper polarization. As a result, the channel becomes easier to activate, leading to a rapid generation of action potential (Yang, Wang et al. 2004). $Na_v1.7$ is highly expressed in PNS sensory neurons and regulates pain sensitivity in erythromelalgia and paroxysmal severe pain condition (Niu, Liu et al. 2021). Similarly, $Na_v1.8$ and $Na_v1.9$ channels are mostly found in nociceptive neurons and plays a role in producing action potentials when the body is exposed to painful stimuli leading to allodynia (Niu, Liu et al. 2021).

1.12.2. Transient receptor potential (TRP) channels

The lesion to the peripheral nerve causes an increase in the expression of TRPV 1 on the A-fibers and C-fibers that are still intact, which ultimately results in a heightened sensitivity to heat (Hudson, Bevan et al. 2001, Hong, Morrow et al. 2004). Among all the members of the TRP family, the receptor TRPV1 has been the subject of substantial investigation. It is the receptor that is responsible for detecting heat that is higher than

42 °C, which is near the threshold where pain is perceived (Julius 2013). Further, other temperature-sensitive ion channels that are reportedly upregulated aberrantly and are involved in the pathophysiology of NP includes TRPV2 which become active at temperatures exceeding 52°C, and TRPV3 and TRPV4 that are activated at temperatures ranging from 25°C to 35°C (Julius 2013). In addition, the TRPV2 and TRPA1 receptors are also reported to be involved in the perception of mechanosensation, indicating their ability to detect multiple types of stimuli (Baron, Maier et al. 2017). TRPA1 is expressed in nociceptive neurons and has been implicated in the development of mechanical allodynia and hyperalgesia following nerve injury (Souza Monteiro de Araujo, Nassini et al. 2020). Even after peripheral nerve loss or lesion, there is evidence of over expression of the TRPM 8 receptor, which sensitizes cold-sensitive C-fibers and causes cold hyperalgesia clinically and preclinically (Wasner, Schattschneider et al. 2004). TRP family receptors are calcium-permeable receptors and their upregulation following peripheral nerve injury leads to an increase in intracellular calcium levels, which in turn promotes neuronal hyperexcitability (Liu, Miao et al. 2023). These mechanisms synergistically amplify synaptic transmission and increase sensitivity, resulting in persistent pain.

1.12.3. Calcium channels and their role in the development of Neuropathic pain

Voltage-gated calcium channels (VGCC) open when the membrane depolarizes and are involved in both generating the action potential and triggering a variety of downstream physiological cytoplasmic cascades. However, under pain-inducing pathological circumstances there is abnormal upregulation of the VGCC which probably enhances the synaptic vesicle release of pain-inducing transmitters like glutamate, substance P, and calcitonin gene-related peptide, thus altering the sensory excitability and leading to

heightened pain sensations. (Altier and Zamponi 2004). Alteration in the voltage-gated calcium channel (VGCC) expression, leads to an elevation in the inflow of Ca^{2+}, which in turn mediates a variety of neuronal processes, including membrane excitability, neurotransmitter release, synaptic plasticity along with the release of pro-inflammatory cytokines, resulting in an exacerbation of pain sensation following sciatic nerve damage (Berridge, Lipp et al. 2000, Yaksh 2006). Further, The N-type VDCC α1β subunit immunoreactivity expression has been reported to rise in the dorsal root ganglion (DRG) cells and lamina II of the spinal cord in 5 to 20 days after nerve CCI (Yaksh 2006) that contribute to neuronal firing and development of NP (Nowycky, Fox et al. 1985, Bourinet, Francois et al. 2016, Hoppanova and Lacinova 2022). Moreover, the CCI model demonstrated that the density of T-type current increases in response to injury of the SN (Jagodic, Pathirathna et al. 2008). This finding was further supported by Yue and colleagues, who observed an increase in both T-current density and amplitude following spinal nerve ligation (Watanabe, Ueda et al. 2015). Ca_V3 channels not only have a role in neuropathic pain caused by nerve injury, but also contribute to the development of painful diabetic neuropathy (Todorovic and Jevtovic-Todorovic 2014). Therefore, it is worth mentioning that CCBs are the first-line therapeutic strategies for the treatment of NP.

1.13. Role of calcium ions in the pathophysiology of Neuropathic pain

According to studies performed on the pathophysiology of NP, one of the most important factors that lead to the development and maintenance of neuropathy is the dysregulation of calcium homeostasis that occurs after neurons have been injured (Siau and Bennett 2006, Cui, Wu et al. 2021). There are reports that demonstrated an alteration in the voltage-gated calcium channel (VGCC) expression, leading to an

elevation in the inflow of Ca^{2+} (Berridge, Lipp et al. 2000, Yaksh 2006). This, in turn, mediates a variety of neuronal processes, such as membrane excitability, neurotransmitter release, and synaptic plasticity along with the release of pro-inflammatory cytokines, which ultimately leads to an intensification of the pain sensation following sciatic nerve (SN) damage (Kawamata and Omote 1996, Berridge, Lipp et al. 2000, Yaksh 2006, Tilley, Cedeño et al. 2022). In addition, the activation of calcium-permeable receptors, such as TRPV1, also results in an increase in the levels of $(Ca^{2+})i$, which in turn promotes neuronal hyperexcitability (Liu, Miao et al. 2023). The increase in the $(Ca^{2+})_i$ has been reported to further facilitate the increase in the influx of calcium through various ion channels leading to neuroplastic changes in the primary afferent fibres and glial cell-induced neuroinflammation that exacerbates pain (Kawamata and Omote 1996). These mechanisms synergistically amplify synaptic transmission and increase sensitivity, resulting in persistent pain. Moreover, the elevated $(Ca^{2+})_i$ also stimulate many calcium-binding proteins that activate glial cells and trigger the production of pro-inflammatory cytokines and chemokines, which further heighten the sensitivity of pain pathways (Cho and Huh 2020, Jager, Goodwin et al. 2024). Additionally, the sustained elevation of intracellular calcium levels can activate various calcium-dependent enzymes, such as proteases and kinases, which modify neuronal function and enhance pain signaling. As $(Ca^{2+})_i$ ions contribute to membrane depolarization and also act as a second messenger, therefore an aberrant increase in the calcium ion post-injury triggers a wide range of cellular processes including the release of neurotransmitters such as glutamate, substance P, and calcitonin gene-related peptides and increasing the chronicity of pain (Smith, Cabot et al. 2002, Takasusuki and Yaksh 2011). Therefore, calcium ions play a pivotal role in the

development and persistence of NP and clinically CCBs are considered as the first-line therapy for the management of NP conditions.

1.14. Significance of glial cells in Neuropathic pain

Glia encompasses a wide range of specialized cell types that exist in both the peripheral nervous system (including Schwann cells, satellite glia, and perineural glia) and the central nervous system (including astrocytes, oligodendrocytes, microglia, and perivascular glia). These cells make up 70% of the total cell population in brain and spinal cord. When activated, both astrocytes and microglia emit several signaling molecules that can have either protective or harmful effects (Jha, Jeon et al. 2012). Glia have lately been recognized as significant contributors to the mechanisms of chronic pain (Mika, Zychowska et al. 2013), and are now being considered as a promising target for therapeutic research (Pocock and Kettenmann 2007). After the peripheral nervy injury, studies have reported an increase in the number of activated microglia (DH) on the ipsilateral side of the dorsal horn of SC (Jergová and Čížková 2007), leading to systemic release of cytokines that mediate pain hyper sensitization (McGinnis and Ji 2023). Further, studies have also indicated microglia to have an pivotal role in the initial stages of NP, while astrocytes are responsible for maintaining NP phenotypes (Zhuo, Wu et al. 2011). Similarly, following neuronal damage, interleukins was found to be elevated in various NP models that induces allodynia and hyperalgesia in rats (Khan, Noboru et al. 2018). The role of glial cells were further confirmed using fluorocitrate, an anti-metabolic drug that disrupts the Krebs cycle via the inhibition of glia-specific aconitase which mitigated NP phenotypes in NP model (Clark, Gentry et al. 2007). Moreover, in a recent study, elevated levels of S100b was observed that reflect the activation of glial cells, which in turn stimulates inflammatory responses, hence

contributing to the chronic nature of NP (Michetti, Di Sante et al. 2021). In addition, prolonged activation of astroglia following neuronal injury is reported to be associated with the maintenance of a prolonged state of chronic neuroinflammation, contributing to the persistence of NP (Fan, Zhang et al. 2023). The aforementioned compiled evidence underscores the significance of glial cell activation as a pivotal element in the progression and endurance of NP. In the light of this, we have elucidated the temporal changes in the glial-cell associated neuroinflammation following the CCI of SN in rats.

1.14.1. Calcium -binding protein: S100 proteins

S100 proteins are a group of small, acidic calcium-binding proteins that are involved in both intracellular and extracellular functions (Kligman and Hilt 1988). Initially, these proteins were isolated from a sub cellular fraction of a bovine brain and the name S100 denotes its 100% solubility in saturated neutral ammonium sulfate solution (Moore 1965). The S100 protein family is one of the largest Ca^{2+} binding protein subfamilies having an EF-hand motif, which was originally grown from two members (S100A1 and S100b) and is expressed only in vertebrates (Moore 1965). A distinguishing feature of these proteins is that the individual members are confined to particular cellular compartments and can migrate on Ca^{2+} activation, and Ca^{2+} signal transduction in spatial as well as temporal manner by interacting with target-specific S100 proteins (Heizmann 2022). Further, the S100 are cytosolic proteins carrying a wide range of functions by regulations of calcium balance, cell growth, cell proliferation, apoptosis, inflammation, and energy metabolism (Marenholz, Heizmann et al. 2004, Xia, Braunstein et al. 2018). While the intracellular function comprises membrane protein transportation, recruitment, intracellular receptor interaction, transcriptional regulation, its integration with nucleic acids or enzymes, and DNA repair. When S100 binds to

calcium they trigger a cascade of downstream pathways by binding to various cellular proteins (Leclerc, Fritz et al. 2009). The receptor for advanced glycation end products (RAGE) or the cytokine-activated Toll-like receptor (TLR) mediated innate immunity pathways are triggered depending upon the type of S100 protein released by monocytes and neutrophils, which further elevates the levels of interleukin-6 (IL-6), interleukin-1β (IL-1β) and tumor necrosis factor (TNF-α) (Leclerc, Fritz et al. 2009). The increased levels of these inflammatory cytokines further starts a vicious inflammatory cycle (Sims, Rowe et al. 2009). Moreover, the activated S100 proteins tends to modulate glial cells activation, triggering inflammatory responses due to the release pro-inflammatory cytokines and chemokines via NF- κB or calcium-dependent pathway, contributing to pathogenesis of inflammatory diseases (Michetti, Di Sante et al. 2021).

1.14.2. S100 proteins: A key player in the pathophysiology of various diseases

S100 proteins have been observed to serve as a reliable indicator of neuroinflammation or glial activation in several neurodegenerative disorders, such as Parkinson's disease (PD). The notion that S100b may have a role in the development of PD arose from the findings of preclinical investigations, which revealed increased levels of S100B expression in the glial cells of mice exposed to MPTP (Muramatsu, Kurosaki et al. 2003). Further, the clinical findings showed a correlation between neuroinflammation and degeneration, and higher expression of S100b in the substantia nigra of the six patients with PD (Sathe, Maetzler et al. 2012). Studies have also reported a direct relationship exists between the levels of serum S100 and the severity of motor dysfunctions in PD patients (Schaf, Tort et al. 2005). Moreover, five years post-diagnosis, the level of serum auto antibodies against the S100B proteins was found to be almost four times higher in PD patients as compared to the controls (Gruden, Sewell

et al. 2011). Similarly, there is scientific evidence from preclinical studies that demonstrates an elevated level of S100b protein being produced and released in a culture of C6 rat glioma cells that were exposed to MPTP. The elevation in S100 release is associated with heightened glial activation, resulting in decreased neuronal viability (Iuvone, Esposito et al. 2007).

Furthermore, the levels of S100B are elevated in CSF as well as sera, in both chronic active and active demyelinating multiple sclerosis plaques (Petzold, Eikelenboom et al. 2002). Previous studies have demonstrated that when demyelination occurs in *ex vivo* demyelinating models, there is a significant rise of astrocytic S100B; however, when S100B action is inhibited, demyelination is reduced and the expression of inflammatory markers is downregulated (Barateiro, Afonso et al. 2016). A recent study has shown that Pentamidine, an approved antiprotozoal drug, inhibits S100b activity. This leads to improvements in biomolecular and neuropathological parameters, as well as the clinical disease score, in the relapsing-remitting experimental autoimmune encephalomyelitis SJL/J mouse model of MS (Di Sante, Amadio et al. 2020).

Traumatic brain injury is a pathological condition caused by an external force or physical impulse that disrupts brain function and physiology (Timofeev, Santarius et al. 2012). Clinically, the cohort study demonstrated the association between the neurological outcome post-severe head injury and the serum S100b levels (Netto, Conte et al. 2006). Moreover, the sudden increase in the serum S100b followed by brain injury has been reported to be due to the disintegrated blood-brain barrier or the systematic inflammatory reaction in the brain (Netto, Conte et al. 2006). Similarly, rheumatoid arthritis is a complex systemic autoimmune pathology characterized by chronic

inflammation and the inflammation associated with it is believed to be linked with the S100 proteins (Croia, Bursi et al. 2019).

Compelling clinical evidences have highlighted increased levels of calcium-binding proteins i.e., S100 in the cerebrospinal fluid of patients suffering from sciatica pain (Brisby, Olmarker et al. 1999, Skouen, Brisby et al. 1999). In parallel, a recent study also found that S100b was elevated in individuals suffering from trigeminal neuralgia, representing all of the symptoms observed in people suffering from NP (Ito, Seki et al. 2023). Similarly, preclinically, there are reports on enhanced expression of S100b in the SC post-spinal nerve transection with the rodents displaying behavioral hypersensitivity (Tanga, Raghavendra et al. 2006, Chen, Huang et al. 2020). Besides, S100b induces the aberrant release of pro-inflammatory cytokines that are involved in the development and progression of NP phenotypes (Tanga, Raghavendra et al. 2006, Stefani, Leite et al. 2019). Based on the above clinical and preclinical consolidated evidences, S100b is recognized as a pathophysiological marker for persistent pain caused by nervous system damage. However, there is no information on the time-dependent changes in S100b in NP conditions. Hence, the aim of the present study was to evaluate the temporal changes in calcium-binding protein (S100b) level in rats with CCI-induced NP. This analysis will provide valuable insights into the dynamics of disease pathophysiological progression and also will assist in identifying the optimal timing for interventions. In addition, prior research has shown that the presence of Ba^{2+} inhibits the release of S100b from primary astrocyte cultures (Vizuete, Hansen et al. 2019). Consequently, we believe that barium leached from the BaBG has the potential to mitigate the S100-induced neuroinflammation, a crucial factor involved in the persistence of NP.

1.15. Hypothesis

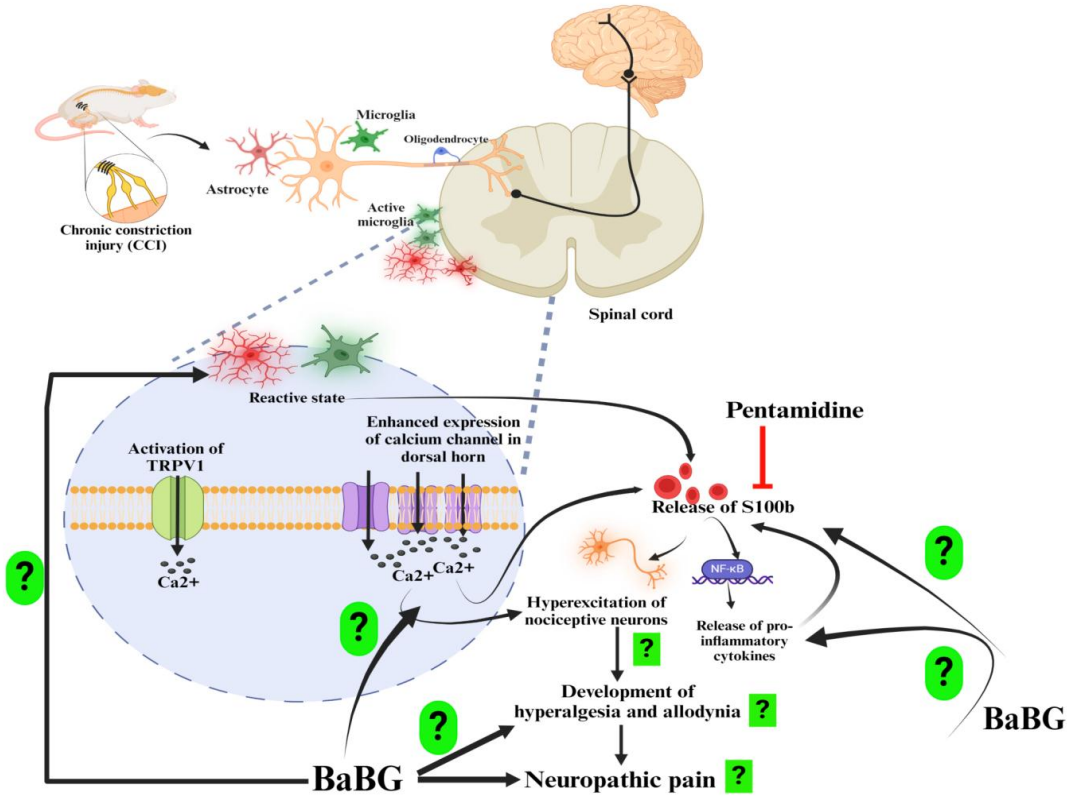

Figure 1.5: The proposed hypothesis of pharmacological evaluation of BaBG in the experimental model of neuropathic pain. Red and Green arrow denotes inhibition and unknown.

The injury to the sciatic nerve (SN) leads to the development of central sensitization due to the upregulation in the expression of calcium channels ($Ca_v2.2$) in the dorsal horn of spinal cord (SC). Besides, there are also enhanced expression of heat-sensing TRPV1 channels in the SN and SC following neuronal injury that leads to the development of thermal hyperalgesia. Upregulation in the expression of these channel results in an increase in the influx of calcium ions leading to hyper excitation of the nociceptive neurons and development of core neuropathic pain (NP) phenotypes i.e., hyperalgesia and allodynia (Kawamata and Omote 1996, Tilley, Cedeño et al. 2022). In addition, the resident immune cells of the central nervous system i.e., glial cells (astrocytes and microglia) get activated post-CCI (chronic constriction injury) leading

to increase in the release of calcium-binding proteins i.e., S100b. Further, S100b gets activated in presence of calcium ions causing release of pro-inflammatory cytokines that further exaggerates the NP conditions (Tanga, Raghavendra et al. 2006, Chen, Huang et al. 2020). However, there is lack of comprehensive knowledge on the temporal changes in the ionic concentration post-injury that causes the development of NP. Therefore, our study's major aim was to evaluate the temporal changes in the intracellular calcium and S100b protein level in the CCI model of NP which will help to identify the pharmacological window of opportunity. CCI model holds clinical relevance and presents face validity as the animal exhibits similar painful and abnormal peripheral neuropathies as observed clinically like the spontaneous pain, hyperalgesia to heat and mechanical stimuli along with the development of allodynia (Bennett and Xie 1988). Further, in terms of the predictive validity, CCI model is preferred widely for drug discovery as the pain symptoms persists for a longer time (Whiteside, Adedoyin et al. 2008). Further, to validate the role of S100b in the pathogenesis and progression of NP in this model, our next objective involved the use of specific S100b inhibitor i.e., pentamidine to access its effect on NP phenotypes. This analysis will offer vital insights into the dynamics of disease pathophysiological progression and also will assist in identifying the optimal timing for interventions.

Inorganic biomaterials like the barium-doped bioactive glass (BaBG) has the tendency to leach the pharmacologiaclly active ions from its framework into the physiological milieu, which impart various biological effects (Majumdar, Gupta et al. 2021). Since, barium has calcium-modulating effects and calcium channels also exhibit greater selectivity for Ba^{2+} ions compared to Ca^{2+} ions (Hagiwara and Byerly 1981). Therefore, we have hypothesized that BaBG has the potential to be used for the treatment of NP that would probably act on the calcium channels and calcium channel blockers (CCBs)

are widely used clinically for the management of NP. Barium released from BaBG may also prevent the activation of calcium-binding protein i.e., S100b, reduce neuroinflammation, and concurrently cause axonal repair and remodeling; hence may have disease-modifying effects. Therefore, the use of BaBG in CCI model of NP would provide new insight into pathophysiology and pharmacotherapy of NP. Hence, our specific objectives are to evaluate the pharmacological effects of BaBG in alleviating the sensory and motor deficits observed in NP condition.

Furthermore, the clinical translation of BaBG necessitates investigating the release kinetic profile and biodistribution of the dopants leached from BaBG. Besides, the understanding of the fate of dopants released after the oral administration is highly important for optimizing the dose regimens therefore; another aim of our study was to determine the *in vivo* pharmacokinetic parameters of the leached ions from BaBG and its biodistribution and excretion profile.

1.16. Objectives:

Objective 1: Synthesis and characterization of barium-doped bioactive glass (BaBG) and its in vitro regenerative potential.

Objective 2: Evaluation of the *in vivo* pharmacokinetics, biodistribution and excretion of dopants released from BaBG after the oral administration.

Objective 3: Acute and sub-acute oral toxicity study of BaBG and 45S5 according to the OECD guidelines.

Objective 4: To evaluate the temporal changes in the intracellular calcium and S100b protein levels in the pathophysiology of the CCI-induced neuropathic pain in rats.

Objective 5: Pharmacological effect of BaBG in the treatment of Neuropathic pain.

Chapter 2

Synthesis and characterization of barium-doped bioactive glass (BaBG) and it's *in vitro* regenerative potential

2. Introduction

Bioactive glasses (BGs) are orthobiologic materials which are widely employed as a bone graft for the regeneration of bone defects caused as a result of trauma or various diseases (Hoppe, Güldal et al. 2011). 45S5 is the FDA-approved BG which is mostly used as a coating over orthopedic implants for bone joining (Ajita, Saravanan et al. 2015). They are also preferred as dental fillings as they increase the pH which imparts bactericidal properties (Earl, Leary et al. 2011, Jones 2015). Normally, traumatic injuries like bone fractures and tissue damage are associated with inflammation which is considered to be the primary pathological hallmark (Lonergan, Baker et al. 2003). Therefore, there is a need to develop a novel BG with minimum immunogenic response for improved biological application. Further, some of the studies suggested the orthobiologic biomaterials that are employed as a bone graft are associated with inherent limitations of immune rejection and inflammation (Kneser, Schaefer et al. 2006, Mariani, Lisignoli et al. 2019). This immune response is mediated due to the activation of calcium-dependent immunogenic pathways even in the absence of immune-stimulating signals due to their physiochemical properties (Andorko and Jewell 2017). Hence, it we have investigated the effectiveness of BG on various inflammatory mediators.

BG is mostly limited to orthopedic and dental purposes as it stimulates osteoblast proliferation but there are some reports on its use in healing damaged soft tissues (Rahaman, Day et al. 2011). Basically, acute inflammation, an initial step during the healing of any injury, facilitates tissue remodeling (Dong, Chang et al. 2017) which subsides within a few days after the insult. However, biomaterials induce excessive expression of pro-inflammatory cytokines due to the activation of the resting immune

cells of the brain i.e. M1 phenotype of microglia has a deleterious effect on tissue regeneration and limits their use (Boehler, Graham et al. 2011). So, there is a need to develop a bioactive material that would have minimal effect on the release of inflammatory mediators from the glial cells without causing cytotoxicity.

Growing evidence suggests that doping of various trace metals like Cu^{2+}, Mg^{2+}, Zn^{2+}, and Sr^{2+} has various pharmacological effects that enhance the biological performances of BGs. Similarly, previous reports from our laboratory highlighted that doping barium in the BG framework has the potential to treat ulcers by forming a protective layer in the stomach against abrasive luminal acids (Paliwal, Kumar et al. 2018). Barium is also reported to generate a barium spike in the growth cone of the regenerating axon (Macvicar's and Llinas 1985). Like calcium, barium is one of the trace alkaline earth metals found in the human body and is enriched in the enamel of the teeth (Austin, Smith et al. 2013). The enrichment of barium in the bone of rodents is also reported and is essential for their calcification (Moore Jr 1964). There are various reports on the use of barium as a radiocontrast agents as well as in radio-osteometric analysis (Madanat, Moritz et al. 2009). Moreover, barium causes concentration-dependent contraction of the smooth muscle (Satoh, Kubota et al. 1987) but there is a paucity of information on the pharmacological potential of barium. However, there is constrained information on the use of barium-doped bioglass on pro and anti-inflammatory markers which are generally released during tissue injury. Based on the consolidated evidence on barium, in the present study, we incorporated barium in BG (BaBG) and investigated its effects on the pro-inflammatory cytokines released during traumatic events.

BGs are mostly prepared using the traditional method of melting or quenching silica and alkali oxides at very high temperatures (Hench 2006). However, these alkali

ingredients pick up other impurity cations at a very high temperature which reduces the binding of the bone tissues with the bioglass and sometimes causes hypersensitivity (Li, Clark et al. 1991). The final steps of grinding, polishing, and sieving the bioglass add further contaminants to it. Therefore, there is a need to use an alternate method which can reduce impurity and enhance its biocompatibility and application. The sol-gel method is a wet-chemistry process that produces porous bioglass with an increased surface area that makes bioglass to be used as a carrier of drugs for controlled release (Zheng and Boccaccini 2017). The sol-gel-derived BG has a faster rate of dissolution in the body fluid that stimulates the formation of the hydroxyapatite (HA) on the surface of BGs (Li, Clark et al. 1991, Pereira and Hench 1996). Moreover, the release of various ions upon dissolution elicits local therapeutic action and thus has the potential to be used in soft tissue engineering (Baino, Fiume et al. 2018). In the light of above-mentioned facts, the BaBG was prepared using the sol-gel method.

To validate our hypothesis, BaBG and 45S5 were prepared in the nanometer range following the sol-gel method. 45S5 being the FDA-approved biomaterial, was used as a positive control for all the biological *in vitro* experiments and also to investigate the effect of barium on various biological activities. The structure of BGs was characterized using Fourier transform infrared spectroscopy (FTIR) and X-ray diffractometry (XRD) and the surface phenomenon was assessed using scanning electron microscopy (SEM). The cytotoxicity of BaBG and 45S5 was assessed by MTT on the C6 and K562 cell lines. The cell-cell interaction was checked by the scratch assay which is an *in vitro* transection model of neurotrauma. Further, the biocompatibility was confirmed by the hemolysis test and the *in vitro* bioactivity by immersing the BGs samples in SBF. In addition, the immune response of BaBG and 45S5 was evaluated by measuring the pro-

inflammatory cytokines like interleukin (IL-6) and tumor necrosis factor (TNF-α) as well as the anti-inflammatory IL-10. As BaBG has never been considered before as a reinforcing compound to bind with the peripheral tissue, the BG developed in the present study is a newer bioactive material for biomedical engineering applications.

2.1. Materials and Methods

2.1.1. Synthesis of the bioactive glasses

2.1.1.1. Barium doped Bioactive glass (BaBG)

BaBG (44.85SiO_2-2.6P_2O_5-24.3Na_2O-26.9CaO-1.35BaO) (mol%) was prepared using the analytical grade chemicals through the sol-gel method (Long, Yang et al. 2015). To prepare 10 g of glass, 15.97 ml tetraethyl orthosilicate (TEOS) and 1.41 ml triethyl phosphate (TEP) (from SRL Pvt. Ltd., India) were weighed and stirred for 45 minutes for homogenous mixing. Then to induce catalytic hydrolysis, 10.21 g calcium nitrate tetrahydrate ($Ca(NO_3)_2.4H_2O$, 99%), 6.64 g sodium nitrate ($NaNO_3$, 99%) and 0.58 g barium nitrate ($Ba(NO_3)_2$, 99%) (all from Loba Chemie, Mumbai, India) are dissolved in 150 ml of water/ethanol mixture in acidic pH. Then the above-nitrated solution was gradually added into the silica-phosphate solution and constantly stirred for 2 h at 40°C. The solution was then aged for a period of 24 h at room temperature. The aged gel was dried at a temperature of 60°C for 24 h and further at 120°C for another 24 h to remove excess water. The dried sample was grounded and thermally treated at 550°C for 6 h in an oxidizing environment at 3°C/ min in an electric furnace to remove residual nitrates from precursors of calcium, sodium, and barium. At last, the sintered samples were pulverized in a zirconia planetary ball mill (VB ceramics, India) for 15 min at 500 rpm to make a fine powder.

2.1.1.2. 45S5

The sol-gel method was used to synthesize 45S5 (46.1SiO_2-2.6P_2O_5-24.4Na_2O-26.9CaO) (mol%) involving hydrolysis and the polycondensation reactions (Pirayesh and Nychka 2013). 10 g of the sol-gel derived bioglass was prepared by magnetic stirring 16.75 ml TEOS and 1.44 ml TEP (from Otto chemika) in the presence of ethanolic solution containing 1(M) nitric acid for 45 min. Subsequently, the following reagents were added to the above reaction mixture: 10.42 g calcium nitrate tetrahydrate and 6.81 g sodium nitrate (Loba Chemie, Mumbai, India) at an interval of 30 min with constant stirring. Now the above mixture was aged for 24 h and dried at 120°C for another 24 h to remove excess water. The dried gel was grounded and stabilized in an electric furnace at 550°C for 6 h to eliminate the residual nitrates from precursors of calcium and sodium. Finally, the fine powdered sample was obtained using a planetary ball mill (VB Ceramics, India).

Table 2.1. The chemical composition (mol %) of 45S5 and BaBG

Composition (Mol %)	**45S5**	**BaBG**
SiO_2	46.1	44.85
P_2O_5	2.6	2.6
Na_2O	24.4	24.3
CaO	26.9	26.9
BaO	0.0	1.35

2.1.2. Characterization of the bioactive glass samples

2.1.2.1. Particle size and surface area determination

The mean particle size of the synthesized bioactive glass samples was analyzed based on the principle of dynamic light scattering using distilled water as a dispersant at 25°C (Delsa™Nano C, Beckman Coulter, USA) (Patel, Surekha et al. 2019). The N_2

adsorption-desorption measurements were carried out (Quantachrome Instruments NOVA 1000, USA) and the BET-specific surface area, pore diameter, and pore volume were calculated using the Brunauer–Emmett–Teller (BET) and Barrett-Joyner-Halendra (BJH) methods (de Souza Balbinot, Leitune et al. 2020).

2.1.2.2. X-Ray Diffraction (XRD)

The phase analysis of the BG samples before and after the SBF (simulated body fluid) treatment was determined by X-ray diffraction (Ali, Ershad et al. 2018). The bioactive glass samples before and after 1, 3, 7, and 14 days of the bioactivity test were finely grounded and were subjected to X-Ray source to produce diffraction (RIGAKU-Miniflex II diffractometer). The source of radiation is Cu-Kα of wavelength (λ) =1.540 Å at 40 kV and 35 mA. The entire analysis was performed in 2θ ranging from 20° to 80° with a step size of 0.02° and the scanning speed was set at 1° per min. In this experiment, the interpretation of the XRD pattern obtained was referred using the JCPDS-International Centre for Diffraction Data cards.

2.1.2.3. Fourier Transform Infrared (FTIR) Spectroscopy

The analysis of the HCA developed over the bioactive glass samples which confirms the *in vitro* bioactivity was analyzed through FTIR spectrophotometer (FTIR-8400S, SHIMADZU) in the range of 400-4000 cm^{-1}. The finely powdered bioactive glass samples both before and after the SBF treatment for 1, 3, 7, and 14 days were mixed with the spectroscopic grade KBr in the ratio of 1:100 and were transferred to the die cavity. Then a pressure of around 10 MPa was applied to form a clear homogenous disc. This disc was then immediately placed inside the FTIR spectrophotometer, and the IR absorption spectra were recorded (Yadav, Singh et al. 2020).

2.1.2.4. Transmission electron microscopy (TEM)

The morphologies of 45S5 and BaBG were observed using a transmission electron microscope (TEM) (Tecnai G2, FEI Company, USA), and the phases present in the samples were detected by selected area electron diffraction (SAED).

2.1.3. Preparation of SBF (Simulated Body Fluid)

The *in vitro* bioactivity of the BG samples was checked using the SBF having a similar ionic concentration as the human plasma (Kokubo and Takadama 2006). NaCl, $NaHCO_3$, KCl, K_2HPO_4, $MgCl_2$, $CaCl_2$, and Na_2SO_4 were weighed and dissolved in the distilled water and the pH was adjusted to 7.4 using TRIS (trihydroxy methyl aminomethane) and 1N HCl at 37°C.

2.1.4. pH behavior of 45S5 and BaBG in SBF

The SBF treatment of the BG stimulates the formation of the hydroxyapatite (HA) and leaching out of the ions. BaBG and 45S5 were soaked in SBF in an airtight container held at 37°C at a concentration of 1.5 mg/ml for a period of 30 days. The changes in the pH of the SBF were measured in accordance with the method of Technical Committee 4 (TCO4) of the International Commission on Glass (ICG) (Macon, Kim et al. 2015).

2.1.5. *In vitro* hydroxyapatite forming ability of BaBG and 45S5

The BGs prepared can be assessed *in vitro* for their bioactivity (HA or HCA formation) by treating them with the SBF at a fixed concentration of 1.5 mg/ml and incubating it at 37°C according to Technical Committee 4 (TCO4) of the International Commission on Glass (ICG) (Macon, Kim et al. 2015). After the samples were soaked in the SBF for various periods up to 14 days, they were washed with deionized water and dried in the

hot air oven at 50°C for 5 h. The hydroxyl carbonated apatite (HCA) thus formed over the surface of BaBG and 45S5 are assessed by FTIR, XRD, and SEM-EDX (Tripathi, Kumar et al. 2016).

2.1.6. Surface characterization and quantitative elemental analysis of BaBG and 45S5

The change in the surface characteristics and elemental composition of the BG both before and after dispersing in the SBF can be analyzed by SEM and EDX (Energy-dispersive X-Ray) respectively. At first, the bioactive glass samples were treated with SBF for 1, 3, and 14 days at 37°C. Then the samples were rinsed thoroughly, dried at 50°C for 4 h and gold-coated using a sputter coating instrument. The changes in the composition of elements and surface morphology were assessed using the EVO/18 Research, ZEISS (Shahrbabak, Sharifianjazi et al. 2019).

2.1.7. Hemolysis assay

The blood compatibility of the BaBG and 45S5 can be evaluated by determining the percentage of hemolysis occurring when the heparinized blood is treated with bioactive glass samples. The hemolysis assay was performed as per the standard protocol (ASTM F 756-00) (ASTM 2000). 7 ml of PBS was taken in a test tube to which 5-100 mg of the powder (5, 10, 25, 50, and 100 mg) was added. Then 1ml of the heparinized blood was added to the above and incubated at 37 °C for 3 h. Positive and negative control was prepared by adding 7 ml of distilled water and 7ml of PBS to the heparinized blood respectively. Then the above solution was centrifuged at 10^4 rpm for 15min, and the optical densities of the supernatant were measured at 540 nm using a Micro-plate reader (BioTek, USA). The percentage of the hemolytic index was calculated by the following

formulae:

$$\text{Hemolytic index (\%)} = \frac{(\text{OD of sample} - \text{OD of negative control})}{(\text{OD of positive control} - \text{OD of negative control})} \text{ X } 100$$

2.1.8. Cell line and cell culture

Human erythromyeloma cells (K562; suspension type) were purchased from ATCC, Manassas, USA and the C6 (Rat glioblastoma; adherent type) cells were procured from NCCS, India. The cell lines were grown in a complete media containing RPMI 1640 (Invitrogen, Carlsbad, CA) supplemented with 10 % FBS (HiMedia, India), 100 U/ml penicillin and 100 µg/ml streptomycin (HiMedia, India).

2.1.9. *In vitro* cytotoxicity assay

Cytotoxicity assays are mostly performed with the aim to evaluate the cytocompatibility of the biomaterials for their biological use. The cytotoxic effect of BaBG and 45S5 was first assessed on the human leukemic suspension-type cells i.e. K562 cells to check their biocompatibility with the blood cells. The assay is based on the lytic activity of BaBG and 45S5 using CytoTox assay kit (Promega, USA) (Ali, Ershad et al. 2018). K562 cells tumor cells (5×10^3) were co-cultured with different range of concentrations (5-100 µg/mL) of BaBG and 45S5 in a 96-well culture plate and were incubated for 18 h at 37 °C, 5 % CO_2. The percentage of cytotoxicity was calculated from the undermentioned formula:

$$\%\ \text{Cytotoxity} = \frac{(\text{Experimental} - \text{Effector Spontaneous} - \text{Target Spontaneous})}{(\text{Target Maximum} - \text{Target Spontaneous})} \text{X} 100$$

The Target maximum refers to the positive control for cytotoxicity, Target spontaneous indicates negative control and the effector spontaneous is the treatment with bioactive glass.

2.1.10. Apoptosis assay (AO/EtBr)

The *in vitro* cytotoxicity of BaBG and 45S5 was further assessed on the adherent-type cells i.e. C6 cells by the apoptotic cell death assay using Acridine orange/Ethidium bromide staining under a fluorescence microscope (NikonEclipse80i, Nikon, Japan). The C6 cells are the glioblastoma cell line and were used as glial cells are the resting immune cells of the brain and their activation secretes various pro-inflammatory cytokines.

2.1.11. *In vitro* cell growth/proliferation assay

To access the growth inhibitory potential of BaBG and 45S5, the MTT assay was performed on both suspension as well as adherent-type cells i.e. K562 and C6 cells respectively. K562 cells (5×10^3 cells) were cultured in a 96-well culture plate and were treated with serial concentrations (5-100 µg/mL) of the BaBG and 45S5 and incubated for 48 hours at 37 °C in humidified condition (5 % CO_2). In the case of the C6 cells, 50 µg/mL of BaBG and 45S5 were plated in a 96-well plate and incubated for 24, 48, 72, and 96 hours followed by cell MTT assay using CellTiter 96 kit (Promega, USA). The absorbance (OD values) was measured at 570 nm using a microplate reader (BioTek, USA) (Hira, Mishra et al. 2014). The percent growth inhibition of the tumor cells was calculated using the mentioned formula:

$$\%\ \text{Growth Inhibition} = \left[1 - \frac{\text{Experimental OD570}}{\text{Target OD570}}\right] \text{X } 100$$

The Experimental OD value refers to 45S5 and BaBG-treated tumor cells while the Target OD indicates the corresponding values of the cells cultured in the absence of BaBG and 45S5.

2.1.12. Scratch-wound healing assay

Scratch assay, *in vitro* transection model for neurotrauma was performed on the C6 cells that were grown in the serum-free media and the wound was created by scratching the confluent layer of cells using the sterile microtip and the image was captured (0 h) (Zeng, Han et al. 2015). Then the cells were grown in the presence of BaBG, 45S5 (50µg/mL), and Temozolomide (TMZ) for 24 h and the wound images were photographed in a time-dependent manner (magnification 100X). The wound area was calculated automatically by CellProfiler™ image analysis software which quantifies the area occupied by the cell sample. The closure percentage increased as the cells migrated over time:

$$\text{Wound Closure } \% = \left[\frac{\text{A(t = 0h)} - \text{A(t = }\Delta\text{h)}}{\text{A(t = 0h)}}\right] \text{X100}$$

Where, A(t=0h) is the wound area at t=0 h and A(t=Δh) is the wound area measured hours after the scratch was performed.

2.1.13. Evaluation of the anti-inflammatory activity of bioactive glasses against LPS-induced inflammation

The anti-inflammatory effects of the BaBG were performed specifically on C6 cells as microglia mostly produce pro-inflammatory mediators in response to traumatic stimuli. The inflammation was induced in C6 cells (5×10^3) by incubating them with LPS (10 µg/mL) for 24 h at 37 °C, 5 % CO_2. In order to evaluate the anti-inflammatory effect of

BaBG and 45S5 against LPS-induced inflammation, the tumor cells were co-cultured with increasing concentrations of BaBG and 45S5 in a 96-well culture dish (0.1-100 µg/mL). The levels of IL-6, TNF-α and IL-10 were assessed through ELISA kit (Cat. No. E-EL-R0015, R0019, and R0016 respectively, Elabscience, USA) as per the manufacturer's guidelines.

2.1.14. Data Analysis

All the data was analyzed by Graph Pad Prism software (San Diego, CARRID: SCR_002798). The parameters performed on the cell lines and the hemolysis assay were analyzed by two-way ANOVA. Bonferroni post hoc test was performed on the significant data to observe the within and between group interaction. $P<0.05$ was considered to be significant in all the analyses and the values were presented as mean ± SD.

2.2. Results and Discussion

2.2.1. Particle size and surface area analysis

The prepared batches of BaBG and 45S5 bioactive glass had particle size in the nanometer range of 508 ± 39.3 nm and 430 ± 41.9 nm respectively. **Figure 2.1** represents the nitrogen adsorption-desorption isotherm plots of BaBG and 45S5 based on the amount of nitrogen physioabsorbed on the bioactive glass samples at varying relative pressure. The isotherm exhibited the presence of a hysteresis loop as previously observed (Taherkhani and Moztarzadeh 2016). The BET results are summarized in **Table 2.2** and the BET-specific surface area of 45S5 and BaBG are 20.271 and 18.029 m^2g^{-1} respectively that corroborated by their particle size. Further, the pore diameter of 45S5 and BaBG was 3.455 and 3.451 nm respectively. Therefore, according to the

IUPAC classification, it can be inferred that the pore size of the synthesized BGs is in the mesoporous range (pore diameter in between 2 to 50 nm). Thus, owing to its smaller particle size in the nanometer range these glass samples have a larger surface area which increases its biomedical applications.

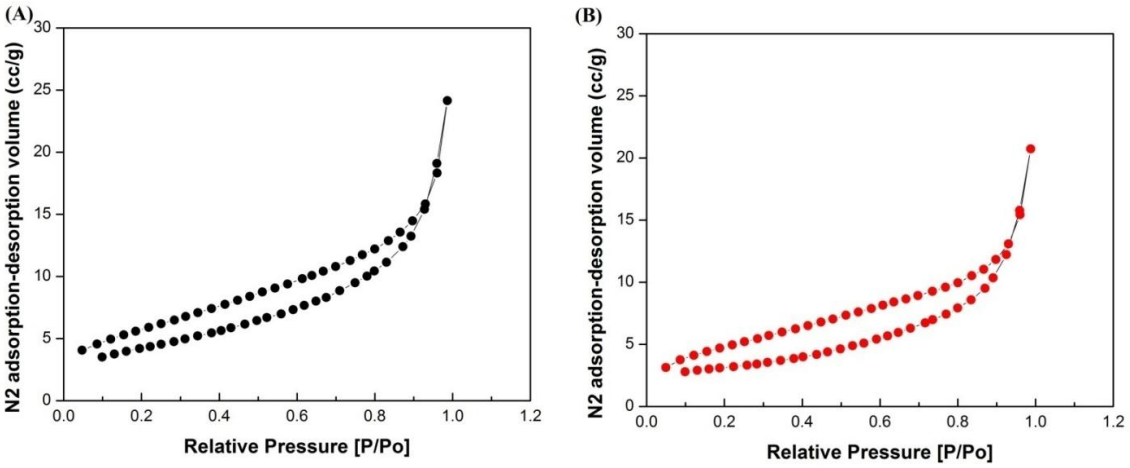

Figure 2.1: Nitrogen adsorption-desorption isotherm of (A) 45S5 and (B) BaBG at STP (standard temperature and pressure)

Table 2.2: Brunauer–Emmett–Teller (BET) analysis results of 45S5 and BaBG.

Material	BET-specific surface area (m^2/g)	Total pore volume (cc/g)	Pore diameter (nm)
45S5	20.371	In adsorption: 0.031	In adsorption: 3.455
		In desorption: 0.034	In desorption: 3.350
BaBG	18.029	In adsorption: 0.027	In adsorption: 3.457
		In desorption: 0.030	In desorption: 3.616

2.2.2. X-ray diffraction (XRD) analysis of BaBG & 45S5

The XRD patterns of 45S5 and BaBG before and after treating the samples in SBF for various time periods are shown in **Figure 2.2(A) and 2.2(B&C)** respectively. From **Figure 2.2(A)**, the amorphous nature of the bioactive glasses can be elucidated by the presence of a broad hump for both samples (45S5 and BaBG) in 2θ ranging from 20° to 30° which may be attributed to the Si-O-Si network (Fredholm, Karpukhina et al.

2010). Further, there are no prominent sharp peaks detected which confirms the amorphous nature of the samples. The SBF treatment of BaBG and 45S5 for 1, 3, 7 and 14 days shows a clear indication of crystalline peaks in the XRD patterns as depicted in **Figure 2.2 (B&C)**. This confirms the ability of the glasses to form hydroxyapatite (calcium phosphate hydroxide) in the presence of the body fluids which affirms the bioactivity of these samples (Ali, Ershad et al. 2018). In the present study, it is evident from the XRD pattern that in 45S5, there is presence of a prominent sharp peak of high intensity at $2\theta = 29.5°$ (PDF # 85-1108) which corresponds to calcite ($CaCO_3$) formation. Further, other sharp intense peaks that correspond to HA are formed at 2θ = 31.9°, 33.18°, 39.69°, 45.72 and 48.4° of *hkl* planes (211), (112), (212), (203) and (222) respectively (PDF # 74-0566) (Arepalli, Tripathi et al. 2016). This finding is supported by previous reports, where 45S5 favored the formation of calcite as the major phase during the HA layer growth due to the reaction of the excess calcium ions released with the carbonate ions present in the SBF (Kansal, Goel et al. 2011, Tulyaganov, Makhkamov et al. 2013). The calcite layer formed in 45S5 hampered the formation of HA but has the equal ability to bind to the bones and aid in its regeneration (El-Gohary, Tohamy et al. 2013). A series of studies reported various factors facilitating the formation of calcite, including the glass composition, particle size and porosity of the bioactive glasses (Mozafari, Banijamali et al. 2019). It is reported that highly porous bioactive glasses allow easy diffusion of Ca^{2+} ions that may ease the precipitation of calcite. Further, the bioactive glasses with increased surface area also promote greater leaching out of Ca^{2+} ions and thus facilitate the formation of calcite. Moreover, in our study, though calcite retarded the HA formation but this did not affect the biocompatibility of the bioglass as corroborated by the hemolysis and cytotoxicity

studies (**Figures 2.7 & 2.8**). Further, after 3 days of treatment with SBF, the diffraction pattern shows the formation of two prominent peaks at 2θ = 31.84 and 45.72 as depicted in **Figure 2.2(B)**.

Similarly in BaBG, the treatment with SBF led to the formation of the peak at a 2θ = 22.8°, 25.9°, 32°, 39° and at around 47.3° that corresponds to the precipitation of the hexagonal crystalline hydroxyapatite ($Ca_{10}(PO_4)_6(OH)_2$) (PDF #74-0566) (Arepalli, Tripathi et al. 2015). The intensity of the HA peak increased gradually with the increasing time duration of SBF treatment which corroborates the SEM result (**Figure 2.5**) and thus demonstrated the gradual increase in the HA formation. The above-mentioned peaks are associated with *hkl* (111), (002), (211), (212), and (222) reflecting planes. In addition, there was a formation of rhombohedral calcite in BaBG with a diffraction peak at 2θ = 29.5° matched with PDF #85-1108 (**Figure 2.2(C)**) (Tulyaganov, Makhkamov et al. 2013). The formation of calcite may be due to the addition of modifier cations of larger radii in the glass composition (Ba^{2+}; ionic radius = 135 pm) substituting for Ca^{2+} (ionic radius = 100 pm) (Mozafari, Banijamali et al. 2019). It is reported that ions of larger ionic radius tend to make the glass network less compact and hence the higher dissolution rate and more release of ions. Moreover, this trend was also observed by Arepalli et al., (Arepalli, Tripathi et al. 2015) but the inclusion of increasing concentration of barium ion reduced the calcite formation. Nevertheless, calcite is biocompatible and is reported to treat bone defects that emerge due to traumatic conditions or congenital defects (Monchau, Hivart et al. 2013) and the HA formed also facilitates the rapid proliferation of the osteoblast cells by initiating the production of ostegenin, a protein which helps in bone reconstruction (Ripamonti, Ma et al. 1992).

2.2.3. FTIR analysis of the bioactive glasses

Fourier transform infrared transmission spectra (in the range of 400-4000 cm^{-1}) of 45S5 and BaBG before and after immersion in the SBF solution for different time periods are shown in **Figure 2.3(A)** and **2.3 (B&C)** respectively. The transmittance spectra of BaBG and 45S5 illustrate bands centered at around 470 cm^{-1} and 793 cm^{-1} which corresponds to Si-O-Si symmetric bending and Si–O–Si symmetric stretching of non-bridging oxygen atoms between SiO_4 tetrahedral networks of the bioactive glasses respectively with very little differences in it (Tripathi, Hira et al. 2015). This also confirms that the bioactive glass samples have a tetragonal Si-O-Si group formed as a result of the polymerization of the silanol groups as reported previously (De Oliveira, De Souza et al. 2013). The peak observed at around 1096 cm^{-1} is associated with Si–O–Si asymmetric stretching [35]. The small band at around 1386 cm^{-1} is affirmed to the stretching mode of C–O vibration of CO_3 groups which may be formed due to the contact of the BaBG and 45S5 with CO_2 of the atmosphere (Yadav, Singh et al. 2020). The band centered at around 3489 cm^{-1} is mainly attributed to the OH group present on the surface of the bioactive glass samples.

Moreover, the *in vitro* bioactivity of the synthesized BaBG and 45S5 was assessed after soaking the bioactive glass samples in SBF for a period of 1, 3, 7, and 14 days. It is evident from **Figure 2.3(B)** that when the 45S5 sample was soaked in the SBF solution, newer divided vibrational bands were visible at around 571 and 616 cm^{-1}. This corresponds to the P–O bending mode of vibrations which corroborates the XRD and SEM results (**Figure 2.5**) and hence proves the precipitation of crystalline apatite (Deliormanlı 2016). An additional peak was observed at around 974 cm^{-1} which is

attributed to the symmetrical stretching of the P-O bond (Tripathi, Kumar et al. 2016). The bands at around 1492 and 1631 cm^{-1} correspond to the (carbonate) C–O stretching mode of the CO_3^{2-} group formed due to exposure of bioglass sample to the environmental CO_2 or precipitation of the crystalline phase of calcite as confirmed by XRD (Pazarçeviren, Tahmasebifar et al. 2018). A very broad peak at around 3467 cm^{-1} was observed which can be attributed to the O-H stretching mode of vibrations thus confirming the formation of hydroxy carbonated apatite (HCA) (Ravarian, Moztarzadeh et al. 2010). Similarly, BaBG after the SBF treatment showed two divided vibrational bands at around 573 and 623 cm^{-1} which corresponds to P-O bending (De Oliveira, De Souza et al. 2013) (**Figure 2.3(C)**) that confirms the formation of crystalline calcium phosphate (hydroxyapatite) layer on the surface as supported by SEM & XRD results. The band observed at around 1095 cm^{-1} is due to PO_4^{3-} bending and 1639 cm^{-1} corresponds to the carbonate groups CO_3^{2-} indicating the precipitation of carbonated apatite (HCA) similar to the apatite formed in the bones (Macon, Kim et al. 2015). Even the band observed at 3448 cm^{-1} is due to the presence of a hydroxy group on the surface of BaBG. Hence, based on the FTIR study we can conclude that BaBG and 45S5 favor the formation of hydroxy carbonated apatite layer following treatment with SBF.

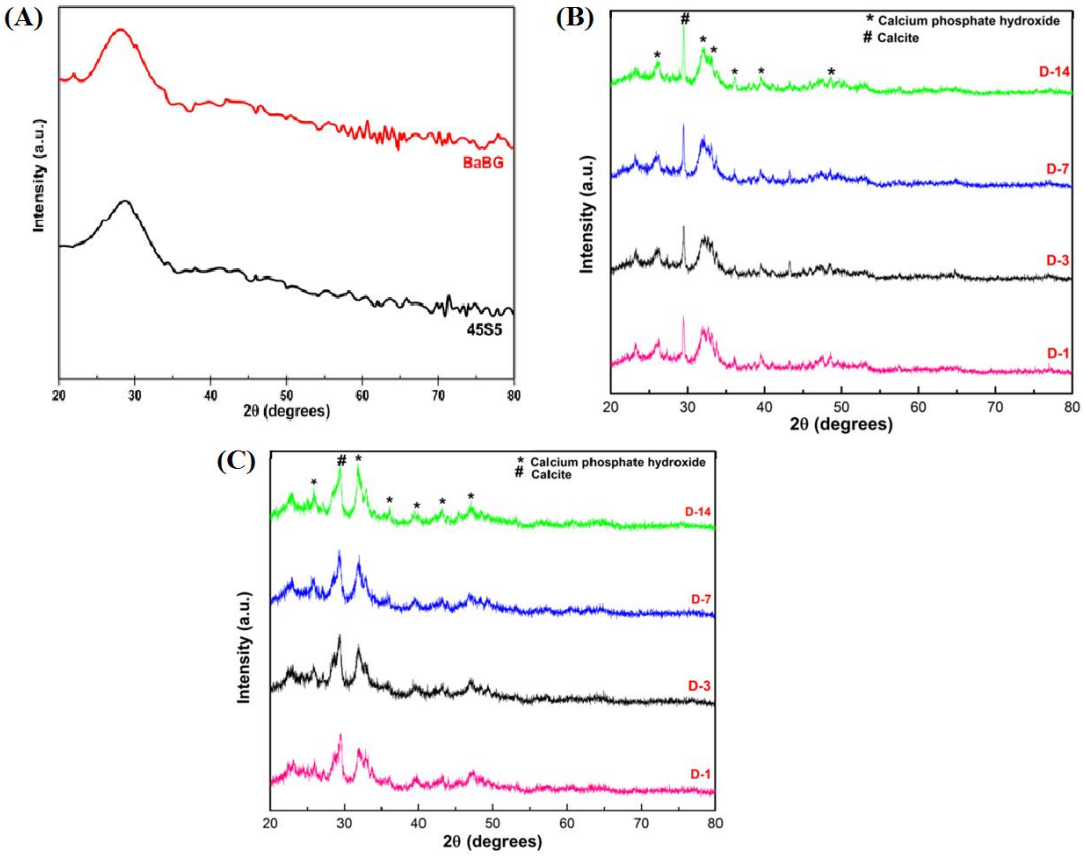

Figure 2.2: XRD pattern of BaBG & 45S5 bioactive glass samples before SBF treatment (A) and XRD pattern of 45S5 (B) and BaBG (C) after soaking them in SBF for 1, 3, 7, and 14 days.

2.2.4. Transmission electron microscopy (TEM) analysis

The TEM image of 45S5 and BaBG samples showed heterogeneous nanosized spherical particles (**Fig. 2.4A**), and their corresponding SAED patterns obtained exhibited diffused rings without diffraction spots or well-defined diffraction rings, suggesting that the synthesized BGs are amorphous (depicted in **Fig. 2.4B**).

2.2.5. pH behavior of the bioactive glass samples in the SBF solution

The pH of the SBF solution altered after treatment with bioactive glasses for a period of 30 days which is depicted in the **Figure 2.5**. In the present study, the pH of the solution at 37°C increased gradually till the first three days, attained maxima and then

declined. It was observed that on the fourth day, the pH of the solution after immersion with 45S5 and BaBG was found to be 9.02 and 9.91 respectively in comparison to the initial pH of 7.4. Surprisingly, in the case of BaBG, the pH of SBF increased again after 12 days till day 17, followed by a gradual decrease in the pH. However, this increment in the pH was not found in the case of 45S5.

The initial increase in pH value was due to the rapid leaching out of the Na^{+}, Ca^{2+}, and Ba^{2+} ions from the glass sample in exchange with H^{+} or H_3O^{+} ions that are present in the SBF solution similarly as suggested previously (Hench 2006). The released Ca^{2+} ions stimulate the release of various growth factors like VEGF (Vascular endothelial growth factor) and FGF (fibroblast growth factor) which stimulate angiogenesis (Ajita, Saravanan et al. 2015). The acidic H^{+} ions are then replaced by various cations present in the bioactive glasses which increase the level of hydroxyl ions in the SBF solution. The hydroxyl ion attacks the silica network, resulting in silanol formation through hydrolysis. However, the pH of the solution decreased after 3 days as the concentration of cations gradually decreased on the surface of the sample. This decrease in the pH may also be caused due to the precipitation of Ca^{2+} ions as calcium phosphates which form the crystalline apatite layer as seen in SEM images (**Figure 2.6**). It has been previously reported that the apatite formed on the surface of the bioactive glass samples prevents the direct contact of the glass surface with the SBF that may hinder the ionic exchange so the pH decreases (Tripathi, Rath et al. 2019).

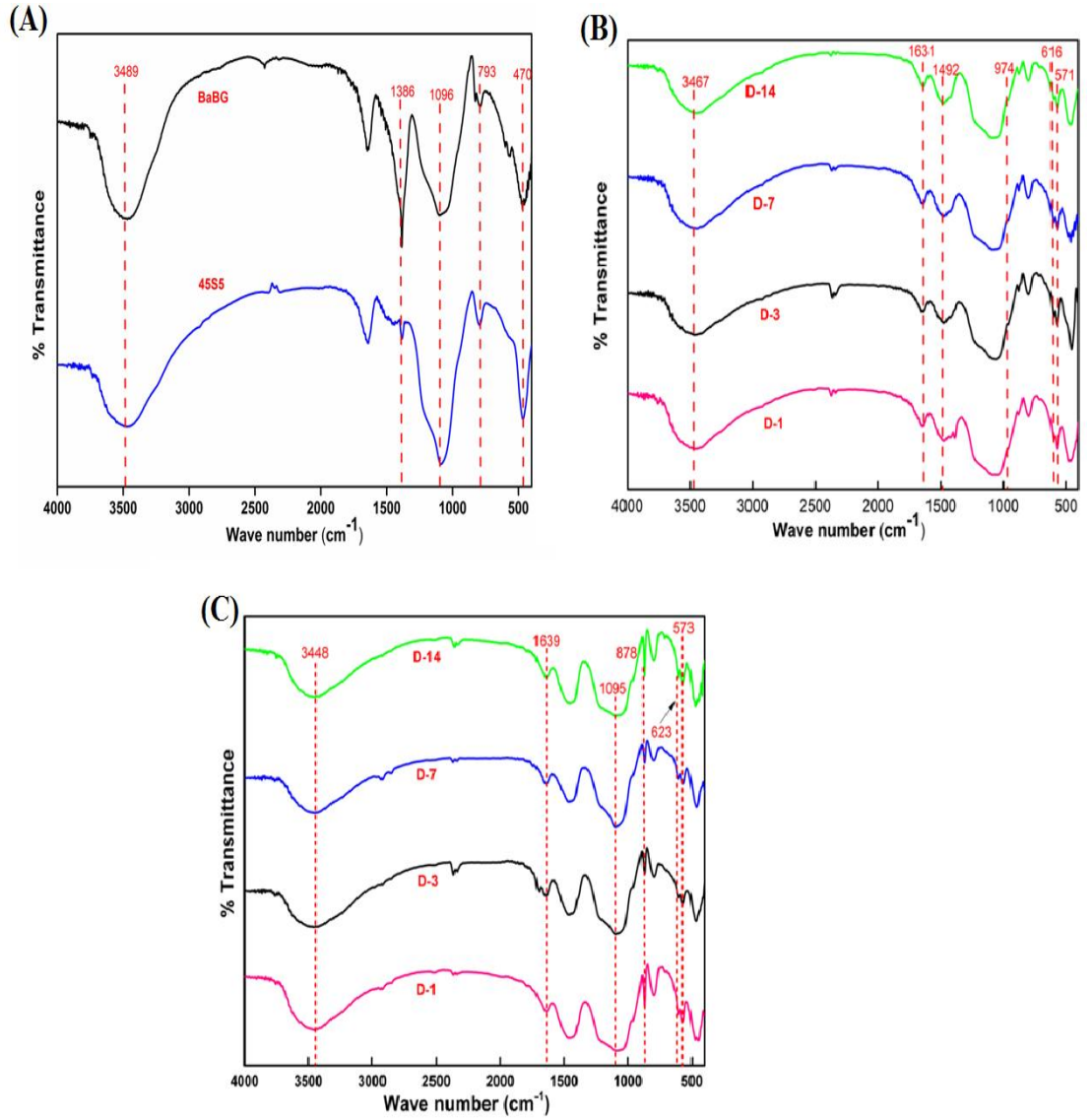

Figure 2.3: FTIR transmittance spectra of the bioactive glasses before soaking it in SBF solution (A) and FTIR spectra of 45S5 (B) and BaBG (C) after immersion in the SBF solution for 1, 3, 7, and 14 days.

In BaBG, the rise in pH of the SBF was more compared to 45S5 due to higher NBO (nonbridging oxygen) to which the protons from SBF bind to form silanol groups, thus enhancing the faster deposition of hydroxycarbonate apatite (Ali, Ershad et al. 2018). Earlier studies have also reported that the substitution of barium oxide at the expense of silica possesses a higher rate of dissolution (Arepalli, Tripathi et al. 2015) and hence greater bioactivity (Leenakul, Kantha et al. 2013). Brukner et al., (Brückner, Tylkowski

et al. 2016) investigated the effects of substitution of alkali ions of varying ionic radius in the basic glass structure and reported that substituting with ions of the larger ionic radius caused expansion of the glass network and hence decreased oxygen density. Thus, the incorporation of Ba^{2+} (ionic radius = 135 pm) substituting for Ca^{2+} (ionic radius = 100 pm) in bioactive glass enhances ion exchange which raises the pH of SBF.

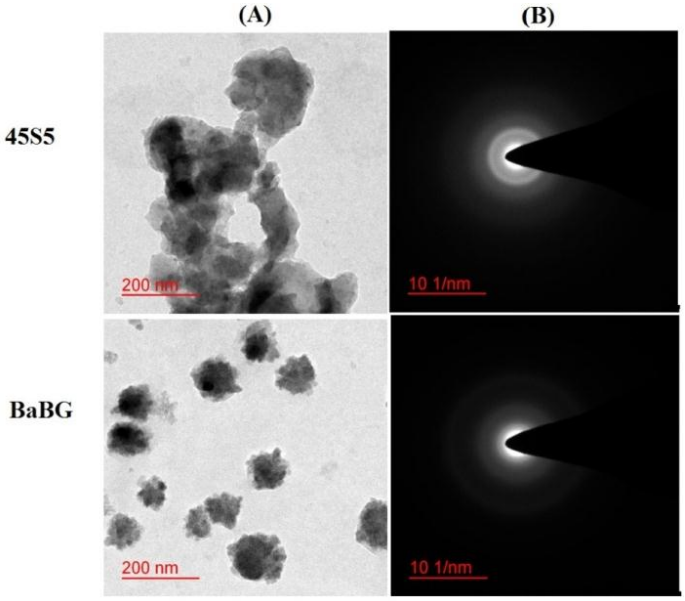

Figure 2.4: The morphology and phase analysis of the synthesized BaBG and 45S5. (A) TEM image and (B) SAED pattern of 45S5 and BaBG

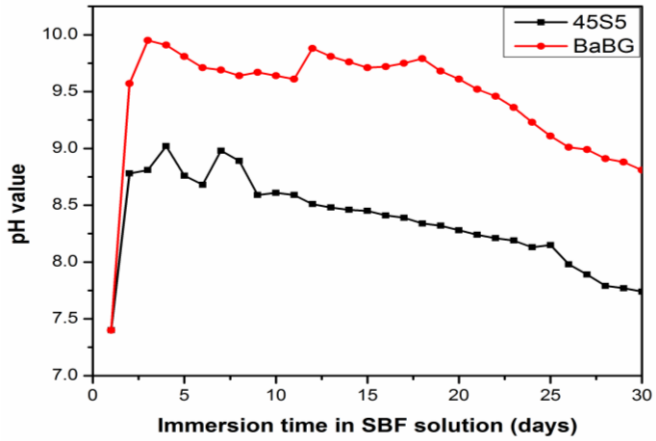

Figure 2.5: The changes in the pH of the SBF solution after soaking BaBG and 45S5 for 30 days

2.2.5. SEM and EDX analysis of BaBG and 45S5

The SEM micrograph displays the surface morphology of the bioactive glass before and after the SBF treatment for 1, 3, and 14 days at 37°C as shown in **Figure 2.6**. 45S5 and BaBG bioactive glasses showed very fine scattered grains on their surface before their treatment with SBF (**Figure 2.6(i)**) which was similarly observed by Beherei et al., (Beherei, Mohamed et al. 2009) with no existence of HA particles. Moreover, the elemental analysis by EDX confirms the substitution of Ba in the BaBG along with the presence of other elements like Ca, Si, and P in both the bioactive glasses as shown in **Figure 2.7(iA & iiA)** respectively. Subsequently, the surface of the SBF-treated 45S5 was covered with a layer of irregular crystals of various shapes and sizes that continued to grow with increasing time duration (**Figure 2.6(ii)**). The crystals formed are due to the deposition of HA which was also confirmed by the XRD and FTIR results. Similarly, **Figure 2.6(iii)** shows the partial formation of needle-shaped crystals after 1 day on BaBG following treatment with SBF. Gradually the entire surface was covered by a layer of the *in-situ* formed HA (Shahrbabak, Sharifianjazi et al. 2019). The EDX analysis also confirmed the formation of HA on the surface of 45S5 and BaBG (**Figure 2.7(iB & iiB)**). Recent studies have demonstrated that the formation of HA largely relies on the exchange of cations of the bioactive glasses that act as network-modifying agents and the H^+ from the SBF (Baino 2019). Further, there is adsorption of ions (Ca^{2+} and PO_4^{3-}) from SBF. Hence, we may conclude that both the bioactive glasses favor the growth of HCA upon SBF treatment as also confirmed by the FTIR as well as XRD.

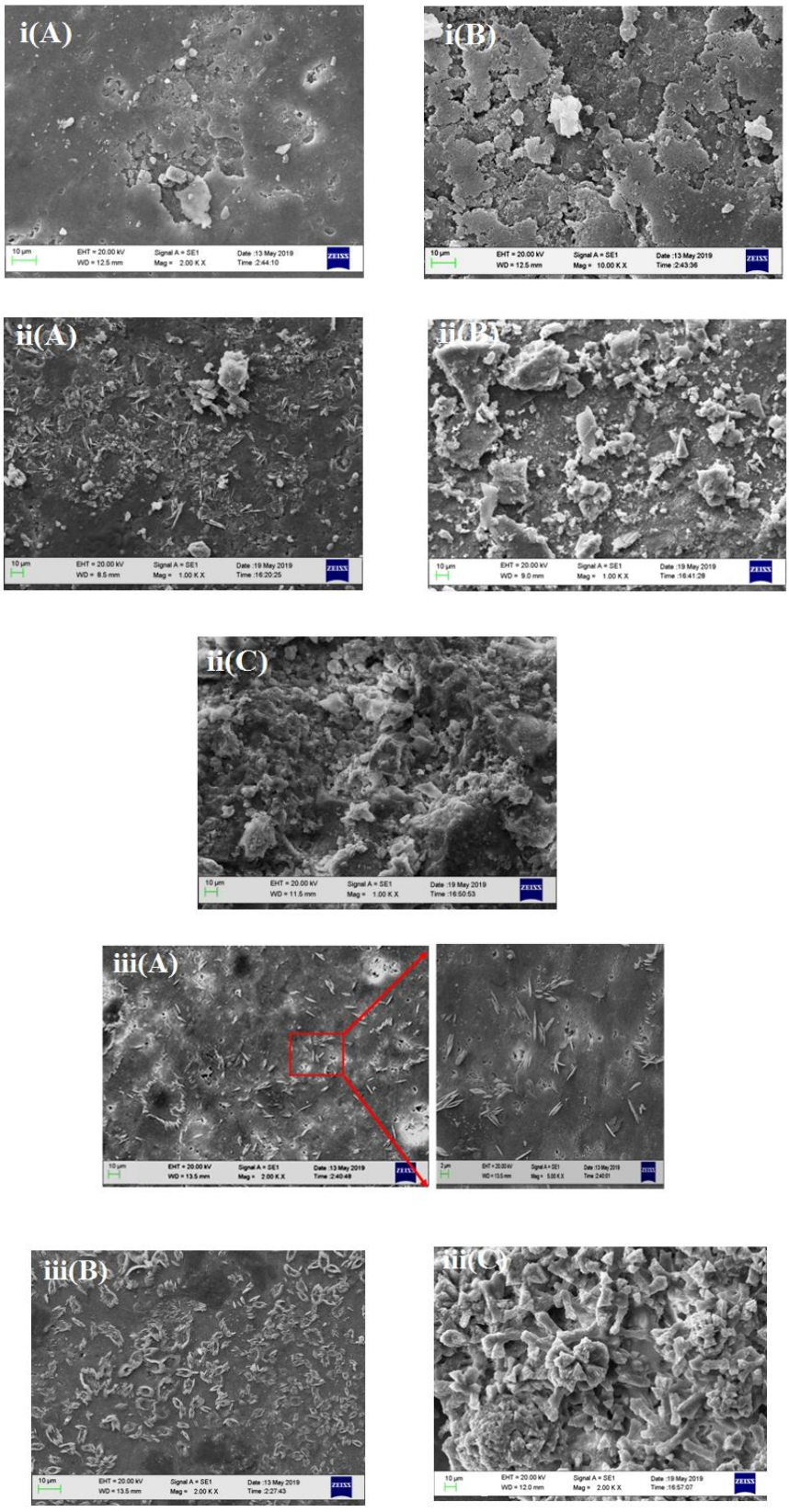

Figure 2.6: SEM micrographs of (i) 45S5 (A) and BaBG (B) before immersion in SBF, (ii) 45S5 and (iii) BaBG after the SBF treatment for 1 (A), 3 (B), and 14 (C) days respectively

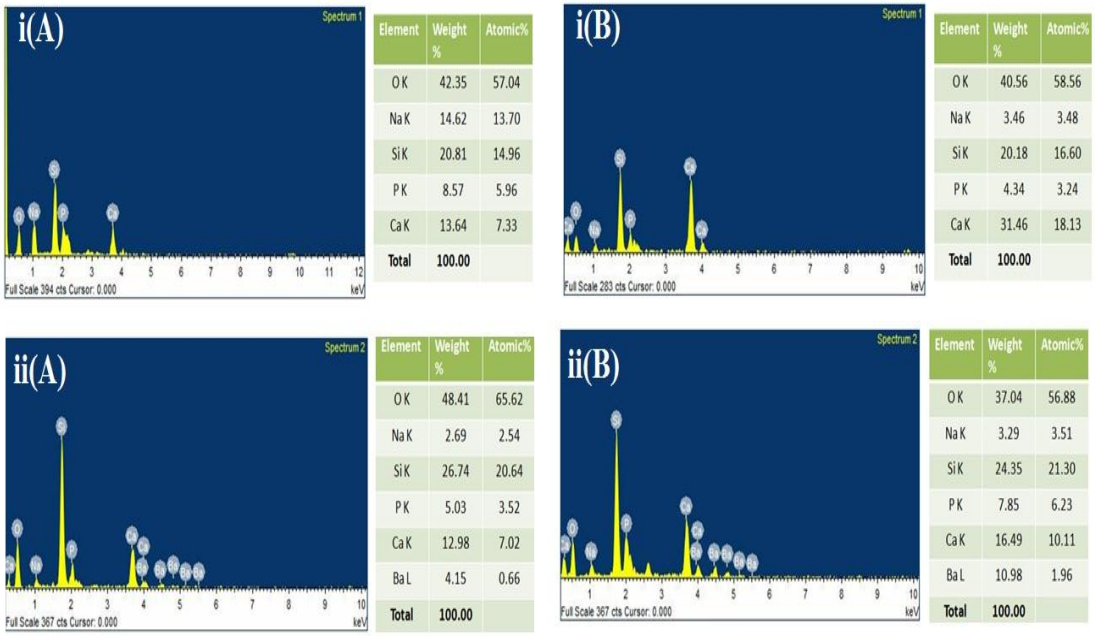

Figure 2.7: EDX analysis of (i) 45S5 and (ii) BaBG after 1 (A) and 14 (B) days of SBF treatment.

2.2.6. BaBG and 45S5 shows biocompatibility in hemolysis assay

Hemolysis is the lysis of the cytoplasmic membrane of RBC and the release of oxygen-containing protein i.e. hemoglobin into the blood plasma. It is an indicative phenomenon which occurs when any toxic foreign material comes in contact with the blood (Seyfert, Biehl et al. 2002). Thus, hemolysis assay is an important parameter to analyze the biocompatibility of any synthesized material with blood so that it can be used as an implant material. The percentage of hemolysis of the blood caused by the treatment of BaBG and 45S5 is represented in **Figure 2.8**. It was observed that the hemolysis index increased with the increase in the amount of BaBG and 45S5. However, 45S5 causes maximum hemolysis of 3.21 ± 0.28% while BaBG caused hemolysis of 2.91± 0.39% when 100 mg was used which is under the permissible limit of 5% (Rathinam, Sivakumar et al. 1994). Thus, the hemolysis assay ascertains the

biocompatibility and non-hemolytic nature of the bioactive glass samples. Hence, BaBG and 45S5 have medically high potential to be used as a regenerative biomaterial.

2.2.7. BaBG and 45S5 exhibit cytocompatibility during *in vitro* cell proliferation and cytotoxicity assay

In the present study, the glioblastoma (C6 cells) cells that are adherent in nature were used to evaluate the cytocompatibility while human leukemic suspension-type cells of granulocytic origin (K562 cells) were used to assess the biocompatibility of the bioactive glasses. These cells are immortal, unlike the primary glial cells that have a limited life. Normally, the majority of the synthesized biomaterials exhibit cytocompatibility with various cell lines but their effects at higher concentrations need longer incubation to obtain better knowledge about cell proliferation and viability. Thus, the above cancerous cell lines were used which have uncontrolled cell division.

The concentration-dependent effect of BaBG and 45S5 on the *in vitro* proliferation and cytotoxicity were performed on the K562 cells and are represented in **Figure 2.9(A, B)**. The cells were incubated with different concentrations of BaBG and 45S5 ranging from 5 µg/ml to 100 µg/ml. In the case of the *in vitro* cytotoxicity test, K562 cells were incubated for 18 h as this time period is considered optimum, neither short nor too long (Decker and Lohmann-Matthes 1988). Studies have reported that longer incubation makes the specific release of lactate dehydrogenase (LDH) less significant (Wiltrout, Frost et al. 1978). Further, longer incubation is required to observe long-term effects like growth inhibition so the K562 cells were incubated for 48 h in case of an *in vitro* proliferation study. Statistical analysis by two-way ANOVA revealed significant differences in proliferation and cytotoxicity among the groups ([F (2, 45)=95.15;

P<0.05]) and ([F (2, 45)=1398; P<0.05]) respectively, concentration ([F (4, 45)=6.420; P<0.05]) and ([F (2, 45)=115; P<0.05]) respectively, and between group and concentration ([F (8, 45)=2.382; P<0.05]) and ([F (8, 45)=27.53; P<0.05]) respectively. Post hoc analysis revealed that there was a significant decrease in the percentage proliferation of K562 cells compared to the control group after treatment with 45S5. Similarly, to further confirm the tolerability of BaBG and 45S5, the concentration-dependent cytotoxicity test was performed which showed an increase in the % cytotoxicity with the increase in BaBG and 45S5 (**Figure 2.9B**). However, the increase in the % cytotoxicity is less than 10% for both glasses which is within the acceptable limit. In support of our result, previous studies have shown that barium did not impart any toxicity on the osteoblast cell (MG63) (Ball, Mound et al. 2014). Even Loza et al., (Loza, Föhring et al. 2016) reported barium sulfate to be an inert compound with no cytotoxic response on the alveolar macrophages. Therefore, BaBG prepared using the sol-gel method is biocompatible and tolerant to K562 cells which corroborate with the non-hemolytic nature as observed in the hemolysis assay.

Further, the time-dependent effect of BaBG and 45S5 on the percentage cell proliferation was assessed on the C6 cells at different time intervals (24, 48, 72, and 96 h) shown in **Figure 2.9C**. The incubation of the C6 cell line with BaBG and 45S5 at a fixed concentration of 50 µg/ml showed a significant increase in percentage cell proliferation among the group ([F (2, 24) = 23.90; P<0.05]) but not with time ([F (3, 24) = 1.323; P<0.05]). However, there was a significant interaction between group and time ([F (6, 24) = 4.111; P<0.05]). Post hoc analysis revealed that BaBG induced an increase in percentage proliferation in the C6 cell line compared to the control from 72 h onwards. This increase in percentage proliferation may be due to the doping of barium

as this effect was not observed with the 45S5 treatment. In support of our findings, previous reports demonstrated that the incorporation of divalent ion promotes cell proliferation by enhancing cellular activity (Zhu, Lu et al. 2019). Overall, BaBG showed biocompatibility and cytocompatibility in concentration and time-dependent manner for K652 and C6 cell lines respectively. Surprisingly, the increased proliferating effect of BaBG was more specific to C6 glial cells. This may be due to the barium ion as the activity of glial cells is largely influenced by the ion exchange mechanism (Kivi, Lehmann et al. 2000).

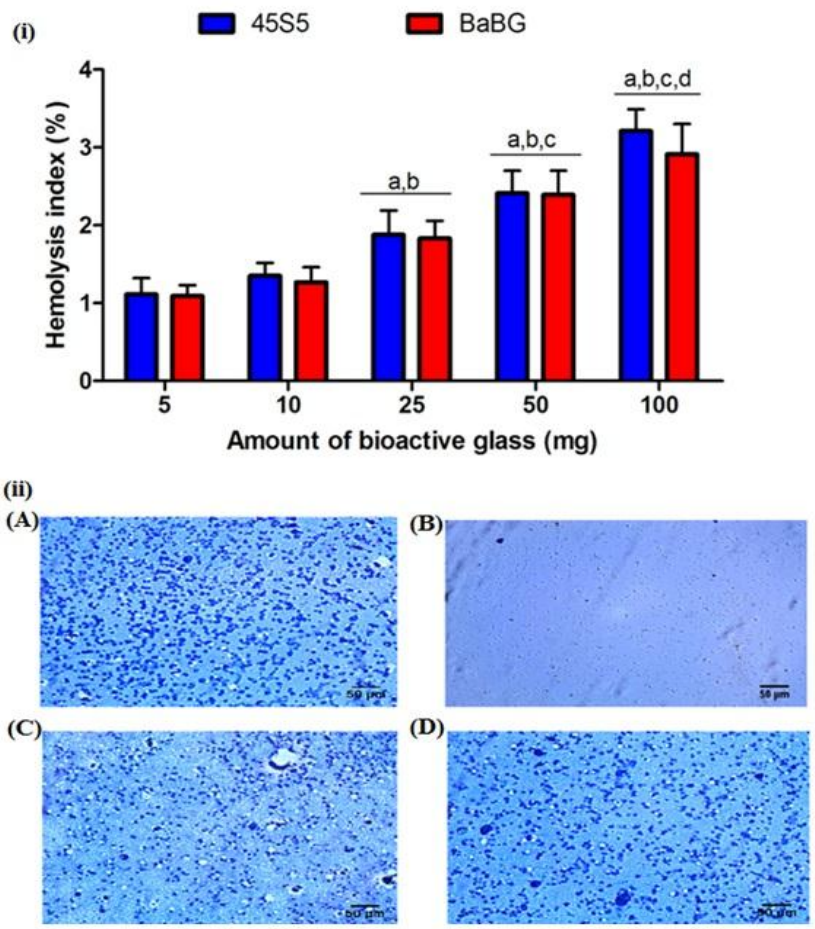

Figure 2.8: Effect of BaBG & 45S5 sample on hemolysis at different concentrations (i) and micrographs of RBC cells after incubation with negative control (A), positive control (B), 45S5 (C) and BaBG (D) respectively. All values are mean ± SD (n=4). $^{a}p<0.05$, $^{b}p<0.05$, $^{c}p<0.05$ and $^{d}p<0.05$ compared to 5, 10.25 and 50 mg respectively. (Two-way ANOVA followed by Bonferroni post hoc test)

2.2.8. BaBG and 45S5 exhibits cytocompatibility during acridine orange/ethidium bromide staining

The use of biomaterials at higher concentrations always increases the chances of cytotoxicity so the *in vitro* cytocompatibility of BaBG and 45S5 was further elucidated in the adhered cell line i.e. C6 through the apoptotic assay (acridine orange/ethidium bromide) (**Figure 2.10**). Apoptosis is one of the crucial parameters for the assessment of the cytocompatibility of novel compounds. In this study, the apoptosis was determined by the differential uptake of acridine orange and ethidium bromide by the C6 cells. Acridine orange is a nucleic acid intercalating fluorescent dye that emits uniform green fluorescence by both viable and nonviable cells. Since apoptosis causes chromatin condensation followed by its fragmentation so when the cells enter the early apoptotic phase, they emit green central fluorescence (nucleus) surrounded by green patches due to the cleaved DNA. In the late apoptotic phase, the condensed DNA emits orange fluorescence as the cytoplasmic membrane of the cells is compromised so the uptake of ethidium bromide is more than the acridine orange (Baskić, Popović et al. 2006). Treatment with BaBG and 45S5 showed that most of the cells are viable as the cells emit uniform bright green fluorescence after 18h of incubation with fewer cells in the early apoptotic phase. This result substantiates the increased proliferation of C6 cells by BaBG treatment (**Figure 2.9C**). Similarly, in the previous study, it was reported that the addition of barium in porous

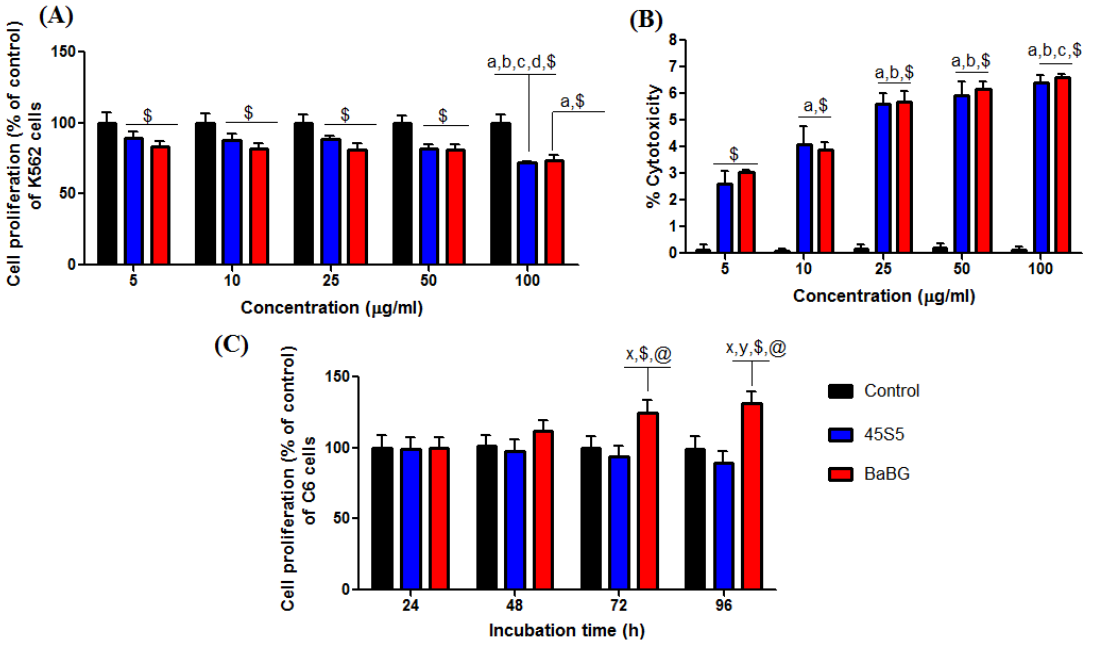

Figure 2.9: Effect of BaBG & 45S5 on percentage proliferation (A), percentage cytotoxicity of K562 cells at different concentrations (B) and percentage cell proliferation of the C6 cells at various time intervals (C). All values are mean ± SD (n=4). $^{a}P<0.05$, $^{b}P<0.05$, $^{c}p<0.05$ and $^{d}p<0.05$ compared to 5, 10, 25 and 50 µg/ml of bioactive glass sample (BaBG and 45S5), $^{x}p<0.05$, $^{y}p<0.05$ compared to 24 and 48 h of incubation with BaBG and 45S5 and $^{\$}p<0.05$ and $^{@}p<0.05$ compared to control (culture medium treated) and 45S5 treated group (Two-way ANOVA followed by Bonferroni post hoc test)

ceramic foam did not impart any toxic properties to the osteoblast cells (Ball, Mound et al. 2014). Yajima et al., (Yajima, Uemura et al. 2012) also investigated the antiapoptotic role of barium where it was found that barium increases the expression of X-linked inhibitors of apoptosis proteins (XIAP). XIAP inhibits the activation of caspase-3 and hence imparts anti-apoptotic effects. Therefore, both BaBG and 45S5 are cytocompatible.

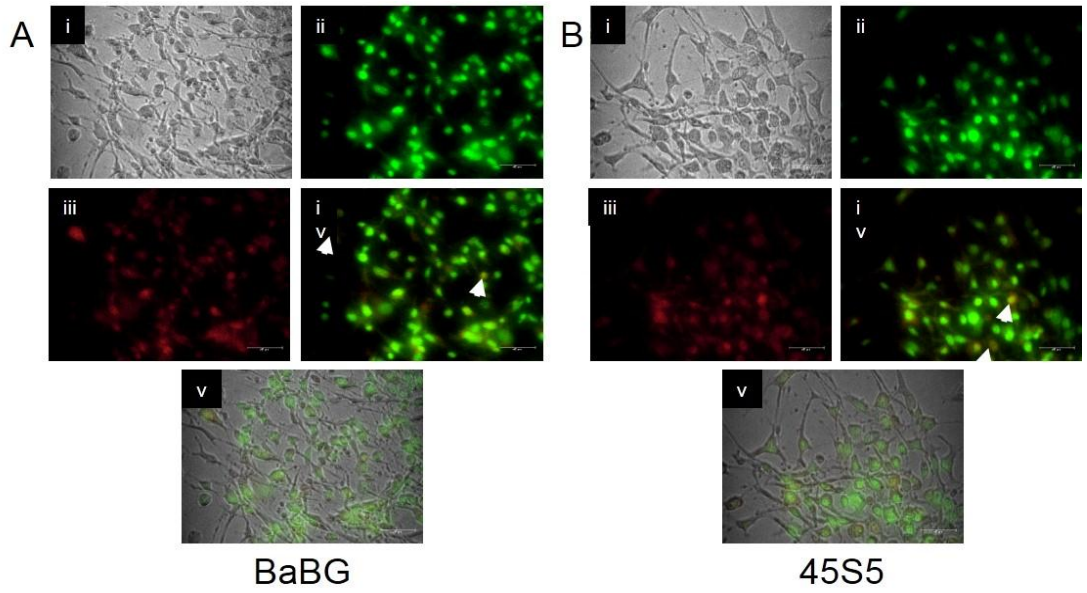

Figure 2.10: Apoptosis assay of C6 cells following treatment with BaBG (A) and 45S5 (B) with Acridine orange/ Ethidium bromide. Green color staining with Acridine orange suggests the living and healthy cells and the Ethidium bromide is staining for nucleic acid. Bright-field (i), Acridine orange staining (ii), Ethidium bromide staining (iii), the merge of ii over iii (iv), overlay of iv over i (v). Arrow indicates early apoptotic cells

2.2.9. BaBG and 45S5 shows regeneration during the scratch assay

Scratch assay is the *in vitro* technique used to analyze the effect of any synthesized compounds on cell migration. It is also an *in vitro* transection model for neurotrauma i.e. traumatic brain injury (TBI) that is the main cause of mortality in all age groups (Kumaria 2017). In this study, the wound was induced by scratching the monolayer of cells and the treatment with BaBG and 45S5 caused coordinated horizontal cell movement (**Figure 2.11A**). Statistical analysis by repeated measure two-way ANOVA revealed significant differences in percentage wound area recovery among groups [$F(3, 32)=1299$; $P<0.05$], time [$F(3, 32)=328.7$; $P<0.05$] and a significant interaction between groups and time [$F(9, 32)=135.6$; $P<0.05$]. Post-hoc analysis showed that 45S5 treatment ameliorated the percentage wound area recovery significantly compared to the culture media treated group after 4h incubation whereas BaBG

exhibited significant recovery after 16 h (**Figure 2.11B**). However, the extent of the percentage wound area recovery of 45S5 and BaBG was comparable after 24 h incubation. In support of our observation, previous reports showed that 45S5 enhances the migration of epithelial cells and also causes vascularization which aids in wound healing (Zeng, Han et al. 2015). The horizontal cell migration is considered as gold standard for the repair and regeneration of the injured tissues (Grada, Otero-Vinas et al. 2017). In addition, Zhang et al., (Zhang, Niu et al. 2018) also demonstrated that the ionic products of bioglass enhanced the proliferation of stem cells which aids in tissue regeneration. For the first time, it is reported that the inclusion of barium in bioglass showed time-dependent wound area recovery that is comparable to 45S5. In support of our finding, previously, it has been demonstrated that the combination of ions activates various extracellular signaling pathways which facilitates the migration of cells and hence helps in regeneration (Yamaguchi‐Ueda, Akazawa et al. 2019). It is also reported that the ionic product of biomaterials influences the osteoblast proliferation and recovery of tissue injury through various cytokines released from immune cells (Chen, Wu et al. 2014). Moreover, Temozolomide (TMZ), a negative control that was used in our study on C6 cells showed a significant reduction in the percentage of wound area recovery compared to the groups treated with culture media and the bioactive glass samples as it is the alkylating agent and the first-line treatment for glioblastoma.

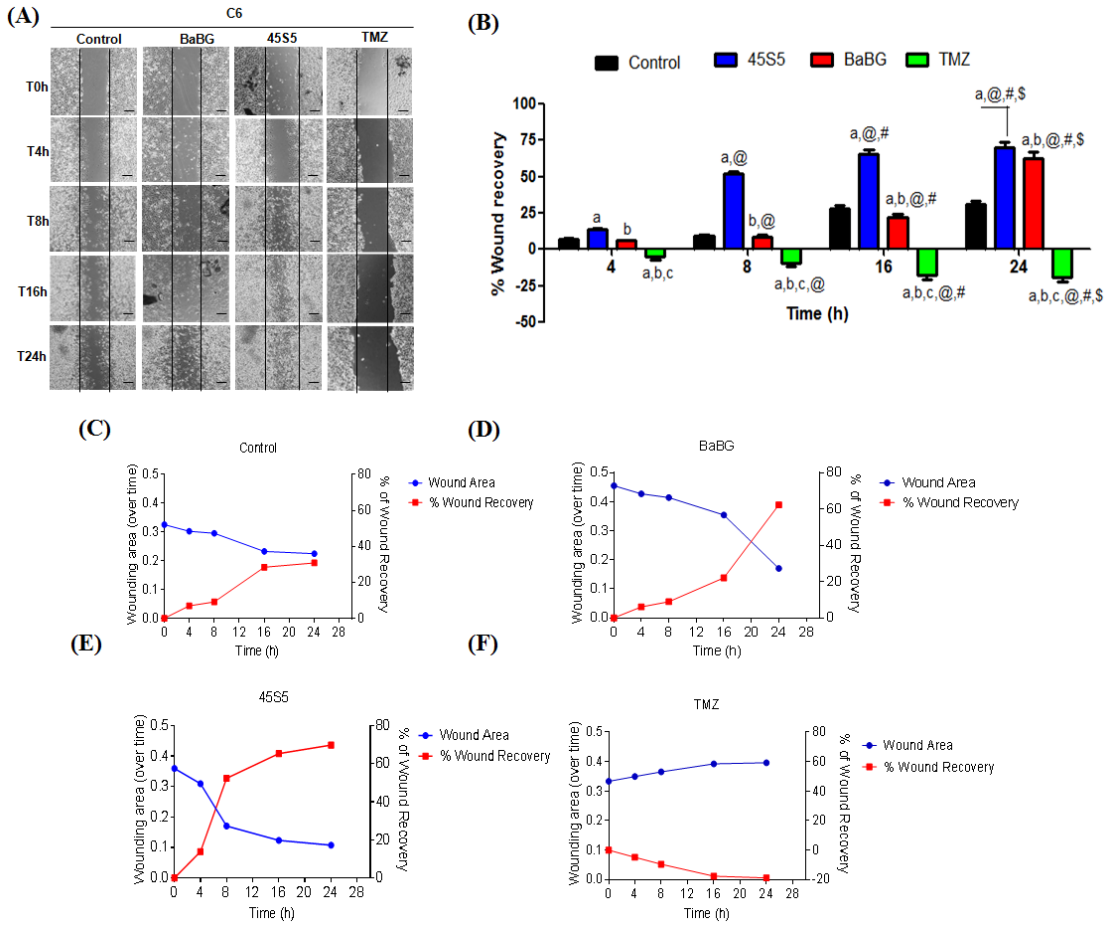

Figure 2.11: Scratch/wound healing assay in C6 cells following treatment with BaBG, 45S5, or Temozolomide (TMZ) (A), time-dependent percentage wound recovery in C6 cells treated with the above formulations (B) and comparison of time-dependent percent wound area recovery to wound area created in the presence of culture medium, BaBG, 45S5 or TMZ (C-F). All values are mean ± SD (n=3). $^{a}P<0.05$, $^{b}P<0.05$ and $^{c}p<0.05$, compared to culture media, 45S5 and BaBG treatment and $^{@}p<0.05$, $^{\#}p<0.05$ and $^{\$}p<0.05$ compared to 4, 8 and 16 h of incubation of C6 cells (Two-way ANOVA followed by Bonferroni post hoc test)

2.2.10. BaBG and 45S5 exhibits anti-inflammatory properties

Chronic and acute inflammatory diseases are associated with elevated pro-inflammatory cytokines like IL-6 and TNF-α as an inflammatory response which leads to neurodegeneration (Smith, Das et al. 2012). Since the microglia are the resident immune cells of the brain and that is activated in response to traumatic events or stimuli leading to the production of pro-inflammatory mediators (Boehler, Graham et al. 2011).

Therefore, in our present study, we investigated the anti-inflammatory effects of BaBG and 45S5 in LPS-stimulated C6 cells (**Figure 2.12)**. Statistical analysis by two-way ANOVA revealed significant differences in IL- 6, TNF-α and IL- 10 level among groups ([F (1, 56)=138.3; P<0.05], [F (1, 56)=70.03; P<0.05] and [F (1, 56)=179.7; P<0.05] respectively), with different concentration of BaBG and 45S5 ([F (13, 56)=228.9; P<0.05], [F (13, 56)=513.5; P<0.05] and [F(13, 56)=279.0; P<0.05] respectively) and a significant interaction between groups and different concentration ([F (13, 56)=12.31; P<0.05], [F (13, 56)=3.797; P<0.05] and [F (13, 56)=6.839; P<0.05] respectively). Post-hoc analysis showed that LPS treatment significantly increased the levels of IL-6 and TNF-α, while it decreased the level of IL-10 as compared to vehicle (culture media) treated cells (shown in Fig. 11). The LPS-induced release of the inflammatory cytokines may be due to the activation of the microglia which leads to the progression of various chronic inflammatory diseases (Xing, He et al. 2018). Therefore, the elevation of the inflammatory mediators is a key marker for the traumatic insult of the tissues. In this regard, previously it has been reported that IL-6 and TNF-α prevent osteoblast proliferation and thus have a deleterious effect on osteogenesis as well as caused cognitive deficits in rats (Lorenzo 2000). Interestingly, treatment with BaBG and 45S5 ameliorated the LPS-induced increase in inflammatory cytokines like IL-6 and TNF-α with subsequent elevation in the anti-inflammatory cytokine i.e. IL-10 in C6 cells. However, BaBG-induced amelioration of the inflammatory response was more significant compared to 45S5. For the first time, we reported that BaBG maintained the cytokine homeostasis by alleviating the pro-inflammatory cytokines with a simultaneous increase in the anti-inflammatory mediators. Thus, BaBG can be used as a disease-modifying agent for traumatic injury.

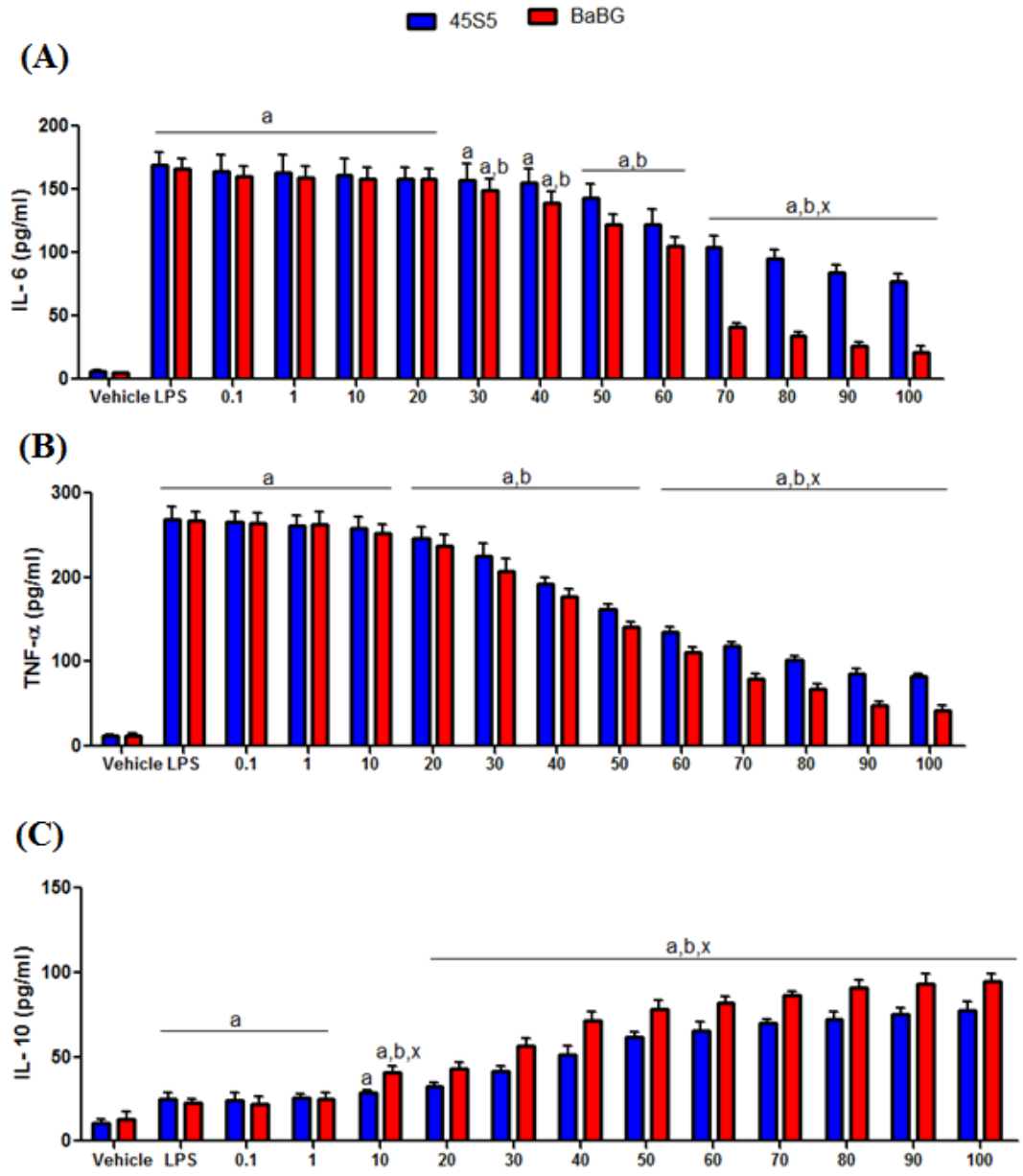

Figure 2.12: Effect of BaBG and 45S5 on IL-6 (A), TNF-α (B) and IL-10 (C) level in C6 cells. All values are mean ± SD (n=3). $^{a}P<0.05$, $^{b}P<0.05$ and $^{x}p<0.05$ compared to vehicle (culture media treated), LPS, and 45S5 treatment groups (Two-way ANOVA followed by Bonferroni post hoc test)

2.3. Conclusion

In the current investigation, a comparative study of the barium-doped bioactive glass (BaBG) and 45S5 was performed as represented in **Table 2.3**. Both the samples were prepared using the sol-gel method and characterized by XRD, SEM, EDX, and FTIR

analysis. The bioactive glasses were amorphous in nature and showed a higher tendency to form hydroxyapatite which affirms the bioactivity of the biomaterials. Further, BaBG and 45S5 were biocompatible as confirmed by the hemolysis assay. Additionally, both the bioactive glasses increased the horizontal cell migration in the scratch assay which is a gold standard for the repair and regeneration of the injured tissues. BaBG and 45S5 increased the percentage of cell proliferation without producing any cytotoxic effects on C6 and K562 cells. Moreover, BaBG exhibited prominent anti-inflammatory effects compared to 45S5. Therefore, BaBG shows potential to be used as a regenerative biomaterial in traumatic injuries.

Table 2.3: Comparison of the important properties of 45S5 and BaBG.

Sl. No.	Properties	45S5	BaBG
1	Composition (mol%):		
	SiO_2	46.1	44.85
	P_2O_5	2.6	2.60
	Na_2O	24.4	24.30
	CaO	26.9	26.90
	BaO	0.0	1.35
2	Particle size (nm)	430±41.9	508±39.3
3	BET-specific surface area (m^2/g)	20.371	18.029
4	Hemolytic index (%) of 100 mg sample	3.21±0.28	2.91±0.39
5	Cytotoxicity (%) of K562 cells at 100 µg/ml	6.39±0.27	6.62±0.08
6	Proliferation (%):		
	• K562 cells after 18 h incubation at 100 µg/ml	72.35±0.712	73.83±3.89
	• C6 cells after 96 h incubation at 50 µg/ml	89.16±8.120	131.231±8.37
7	Wound closure (%) in scratch assay after 24 h incubation	69.80±4.073	62.36±4.73
8	Inflammatory markers (pg/ml):		
	• IL-6	77.27±5.85	21.40±4.96
	• TNF- α	82.19±4.038	42.21±5.46
9	Anti-inflammatory marker (pg/ml):		
	• IL-10	77.81±4.71	94.72±4.36

Chapter 3

Evaluation of the *in vivo* pharmacokinetics, biodistribution and excretion of dopants released from BaBG after the oral administration

3. Introduction

Bioactive glasses (BGs) are bio and cytocompatible third-generation silica-based inorganic compounds that have tremendous tissue regenerative potential (Majumdar, Gupta et al. 2022) and are mostly used as implants or as drug delivery systems due to their mesoporous nature (Gupta, Majumdar et al. 2021). Their bioactivity is attributed to the various therapeutic dopants present in its silica network that are leached into the physiological environment (Majumdar, Gupta et al. 2021, Taye 2022) which activates a cascade of proteins or ion channels required for physiological activity. Recently, the pharmacological efficacy of BGs has also been explored and the orally administered barium-doped BG (BaBG) exhibited an anti-ulcer effect in various gastric ulcer models in rats (Paliwal, Kumar et al. 2018). Therefore, the clinical translation for systemic use necessitates investigating the release kinetic profile and biodistribution of the dopants leached from BGs. Further, due to the inherent osteogenic and bactericidal properties, BGs are used clinically as orthopedic implants for extremely serious orthopedic deformities (Schepers, Ducheyne et al. 1993, Jones, Brauer et al. 2016). The clinical implants for osseous tissues are required to be present *in situ* throughout the patient's life. So, these implants must have higher stability with a low leaching tendency. Hence, determining the preclinical release kinetic profile of the dopants of BGs will confer light on their chemical and biological stability when used as implants.

In general, the therapeutic ions that are doped in the silica network of BGs are an integral part of the normal physiology of the body where the ionic homeostasis is maintained (Majumdar, Gupta et al. 2021). These physiologically and pharmacologically active dopants produce therapeutic efficacy if the leaching ionic concentrations are within the physiological limits. However, if this physiological ionic

set-point is broken due to excessive leaching of doped elements it may lead to various physiochemical, pharmacokinetic, and pharmacodynamic interactions (Rivadeneira, Luz et al. 2015, Zheng, Kapp et al. 2019). Additionally, the release of dopants from BGs causes an increase in the pH as described in **Chapter 1** which may alter the bioavailability of weak acidic drugs whose absorption is pH-dependent (Akula and PK 2018) and hence may affect their onset of action and bioavailability. Moreover, BGs may even cause increased accumulation of dopants in excretory organs which will change the *in situ* ionic homeostasis (Mao, Chen et al. 2016). This may alter the excretion of drugs that may remain in the body even after their normal washout periods. Hence, this makes it necessary to perform the biodistribution and excretion of the leached elements before using them as a therapeutic strategy.

Further, understanding the fate of the dopants released after oral administration is highly important for optimizing the dose regimens which can be determined from the *in-vivo* pharmacokinetic study (Schwartz and Pateman 2021). It will also help in the context of determining the absorption, tissue distribution, metabolism, and excretion of the released dopants. Moreover, since the kinetic profile of the dopants indirectly determines their residence time in the body, it can also be used to predict the potential adverse effects that they might produce if used for a longer duration (Schwartz and Pateman 2021). Hence, this is the first investigational preclinical study performed to explore the release kinetics of therapeutic ions leached from BG, their pharmacokinetic parameters, biodistribution, and excretion when administered orally in rats. Administration of drugs via the oral route is preferred clinically because of patient compliance and performing oral pharmacokinetic and biodistribution studies will help to elucidate the effects of gastric contents and food on release kinetics.

Therefore, in the present study, the *in-vitro* release kinetics of various dopants from BaBG in SBF and alteration in pH of the solution were accessed using an inductively coupled plasma mass spectrometer (ICP-MS). Further, the changes in plasma concentration of Ca, Ba, and Si after single-dose oral administration of BaBG were studied in rats at various time points and the pharmacokinetic parameters were calculated using the PKSolver software. The distribution of therapeutic dopants from BaBG in various organs and their route of excretion were also investigated in urine and feces. In addition, SEM analysis of the tissue sections of the brain, heart, lungs, liver, kidneys, and spleen of the BaBG-treated rats was performed to analyze the topographical and surface morphological changes in the organs post-BaBG treatment.

3.1. Materials and Methods

3.1.1. Materials

Carboxymethyl cellulose (CMC), paraformaldehyde, glutaraldehyde, and chemicals used to prepare phosphate buffer solution were obtained from SRL, India.

3.1.2. Preparation of Simulated body fluid (SBF)

The *in-vitro* leaching of doped elements from the BG samples was carried out in the SBF solution that was prepared following the procedure mention in section 2.1.3.

3.1.3. *In-vitro* pharmacokinetic study of BaBG

The leaching of dopants from the BG network with respect to time was evaluated in SBF according to the technique suggested by Technical Committee 4 (TC04) of the International Commission on Glass (ICG) (Macon, Kim et al. 2015). The *in vitro* pharmacokinetic study was performed by incubating the glass sample in SBF at a

concentration of 1.5 mg/mL in an airtight polyethylene container to prevent any loss of media; hence avoiding any change in the ratio of glass/SBF. Throughout the experiment, the container was kept in an incubating orbital shaker maintained at 37 °C at 120 rpm. After 0.25, 0.5, 1, 2, 3, 6, 12, 24, 48, 72, 120, and 168 h, 5mL of the solution was removed using a syringe. The solution was then passed through a 0.22 µm Millipore filter and the concentrations of Si, Ca, and Ba were measured with ICP-MS and expressed in ppm.

3.1.4. Animals

The animal experiment was carried out on the adult healthy male albino Wistar rats (200±20 g) that were procured from the Institutional Animal House, IMS- BHU, Varanasi, India. All the experimental rats were acclimatized for 7 days to the laboratory environmental conditions in a controlled temperature of 25 ± 1°C and 45-55 % relative humidity. All throughout the experimental protocol, the experimental animals were kept in a 12:12h light: dark cycle with an *ad libitum* food (Paramount Laboratory Animal feed, Lanka, India) and water supply. During the experimental design, the National Institute of Health Guidelines (publication number 85-23, revised 2013) on animal care experimentation were followed to abridge the number of animals used. The entire experiment was accredited by the Central Animal Ethical Committee of the Indian Institute of Technology (Banaras Hindu University), Varanasi, India (Ref No. IIT(BHU)/IAEC/2022/039).

3.1.5. Experimental design for single dose oral *in-vivo* pharmacokinetic study

The *in-vivo* oral pharmacokinetic study of BaBG was performed in the Wistar rats that were divided into four groups: naïve control, BaBG (1 mg/kg b.w.), BaBG (5 mg/kg

b.w.), and BaBG (10 mg/kg b.w.) (**Figure 3.1**) using the randomization technique. Each group in the study had seven rats. BaBG was suspended in 0.5 % CMC and administered orally to the overnight fasted experimental rats. Subsequently, blood was collected at 1, 24, 48, 72, 120, and 168 h post administration of BaBG from the lateral tail-vein of mildly anaesthetized rats (anaesthetized using diethyl ether) in heparinized centrifuge tubes. Plasma was collected immediately by centrifuging the blood samples at 4000 g (Remi Centrifuge, model number C-24BL, India) for 10 min at 4 °C (Prajapati and Krishnamurthy 2021). The supernatant was decanted and stored at -80 °C until further analysis.

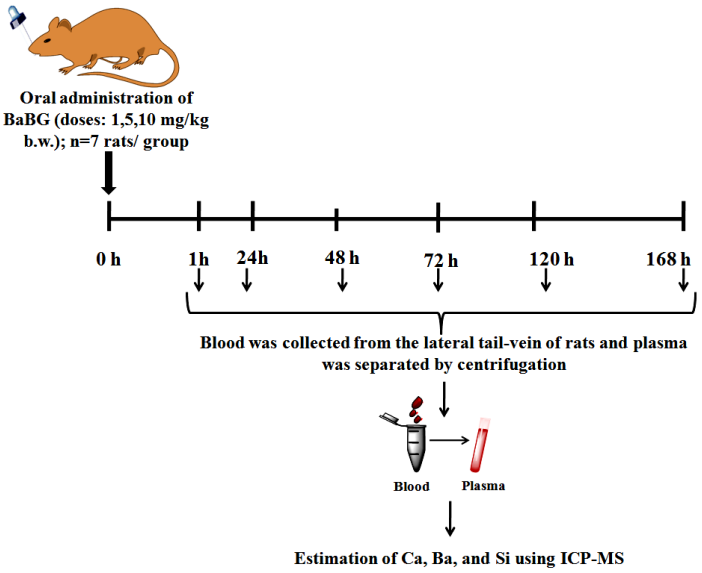

Figure 3.1: Schematic representation of the experimental protocol of the in-vivo single-dose oral pharmacokinetics study of BaBG. The image has been drawn using ChemDraw 15.0.

3.1.6. Pharmacokinetic Analysis

Pharmacokinetic parameters like maximum plasma concentration (C_{max}) and the total time required to reach C_{max} (i.e., T_{max}) of BaBG were obtained from the plasma concentration-time curve (AUC) of BaBG. Similarly, the mean residence time (MRT),

half-life ($t_{1/2}$), volume of distribution (V_z), and clearance (CL) of BaBG were calculated via non-compartmental analysis using the PK Solver software, an 'add-on' for the Microsoft Excel (Zhang, Huo et al. 2010). All the pharmacokinetic parameters are expressed as mean ± SD.

3.1.7. Analysis of Ca, Si, and Ba in urine and feces

To estimate the excretion of Ca, Si, and Ba into urine and feces, the experimental animals during the oral pharmacokinetic study were housed in metabolic cages for sample collection. The urine and fecal samples from each group were collected at the same time points of the pharmacokinetic experimental protocol for evaluating the urinary and fecal excretion of elements (i.e., 0-1, 1-24, 24-48, 48-72, 72-120, 120-168, and 168-192 h). They were weighed immediately, chemically digested, and analyzed by ICP-MS for the presence of Ca, Si, and Ba.

3.1.8. Experimental design for *in-vivo* biodistribution study after single dose oral administration of BaBG

To estimate the distribution of dopants released from BaBG in various organs, the rats were randomly divided into four groups: naïve control, BaBG (1 mg/kg b.w.), BaBG (5 mg/kg b.w.), and BaBG (10 mg/kg b.w.) (n=6 rats/group). The same dose of BaBG that was used during the *in-vivo* pharmacokinetic study was selected and administered orally in the rats (**Figure 3.2**). Post-dosing, at distinct time points (days 1, 3, 5, and 7), the rats of each group were anesthetized using 3 % v/v isoflurane inhalation. Then the animals were sacrificed by cervical dislocation and vital organs like the brain, heart, lungs, liver, kidneys, and spleen were dissected. The organs were weighed and processed for digestion and ICP-MS. The SEM analysis was performed to assess the formation of HA

as well as the surface morphological changes of all the organs collected from the rats of the highest dose group (i.e., 10 mg/kg b.w.) at day 7 post-dosing.

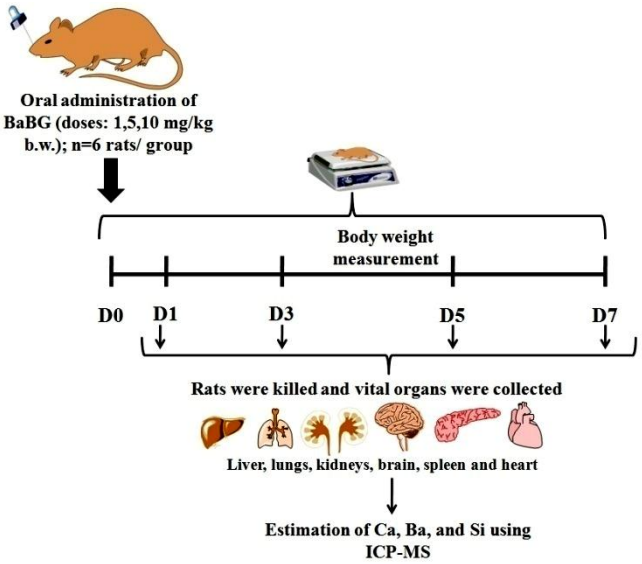

Figure 3.2: Schematic representation of the experimental protocol of the in-vivo biodistribution study after single-dose oral administration of BaBG. The image has been drawn using ChemDraw 15.0

3.1.9. Scanning electron microscopy (SEM) of vital organs

The vital organs like the brain, heart, lungs, kidneys, liver, and spleen collected were fixed in 2.5 % glutaraldehyde solution overnight at 4 °C followed by washing in PBS thrice. Then the tissue samples were dehydrated in a graded series of acetone and dried thoroughly. Subsequently, the dried tissue samples were gold-palladium coated (EMITECH SC 7620) and viewed under the scanning electron microscope (Zeiss EVO LS 10, Carl Zeiss Ltd., Germany) at 10 kV.

3.1.10. Digestion of the biological samples for ICP-MS

Tissue samples of around 300 mg of the vital organs (brain, heart, lungs, kidneys, liver, and spleen) were pre-digested in an acidic condition by incubating the biological samples in a 3 mL mixture of nitric acid and perchloric acid (9:1) for 24 hours. Then

the above mixture was heated at 80 °C for 10 h and again at 140 °C for 30 min. Later on, 2-3 ml of a mixture of nitric acid and perchloric acid was added to the reacting vessel to digest the residue and was further heated at 145 °C till the samples were evaporated to dryness. Finally, 2 % v/v nitric acid solution was added to dissolve the residues and filtered with Whatman filter paper (grade 1, pore size of 11 μm). The filtrate obtained was then diluted to make up the volume up to 5 mL. Similarly, the plasma (300 μL), urine (300 μL), and fecal samples (300 mg) were collected and digested as per the protocol followed for the tissue samples (Dumala, Mangalampalli et al. 2019).

3.1.11. Inductively coupled plasma-mass spectroscopy (ICP-MS)

The concentration of Ca, Si, and Ba present in the digested solutions was performed using ICP-MS which is a single quadrupole type [iCAP-RQ (Thermofisher Scientific, USA)]. The external calibration technique was followed for the quantitative analysis of the samples. The calibration curves for all the analytes were built on 8 different concentrations (0.5-100 ppb), from the limit of detection (LOD) of the corresponding element with the intention that concentrations of all analytes in the samples were within the linear range of the calibration curve. The calibration standards were analyzed at regular intervals during analysis to monitor the instrument drift. Also, ultrapure deionized water blanks were frequently used in the study alongside the samples to check for any loss or cross-contamination. All the measurements were carried out using the full quantitative analysis mode.

3.1.12. Body weight and organ coefficient

During the biodistribution study, the body weight of the animals in each group was weighed before and after BaBG administration. Similarly, at the end of biodistribution experiment for each time-point, the organ (brain, heart, lungs, liver, kidneys, and spleen) weight was recorded and the organ coefficient for every time point was calculated using the following formulae:

$$\text{Organ coefficient} = \left[\frac{\text{Weight of the organ (g)}}{\text{Total body weight (g)}}\right] \text{X}100$$

3.1.13. Statistical analysis

All the data were analyzed statistically by GraphPad Prism Version 8.0 (San Diego, CA, RRID: SCR_002798). The *in-vivo* pharmacokinetic parameters for the released ions were assessed statistically by one-way ANOVA followed by Tukey's multiple comparison tests. The two-way ANOVA followed by the Bonferroni post-hoc test was used to statistically analyze the plasma concentration profile, urinary and fecal excretion, body weight, organ coefficients, and biodistribution of Ca, Ba, and Si. We have considered $p < 0.05$ to be statistically significant in all the analyses, and all the values were presented as mean ± SD.

3.2. Results and discussion

3.2.1. Temporal *in-vitro* release of Ca, Si, and Ba from BaBG in SBF solution

Normally, when BGs react with any physiological fluid like SBF, structural and chemical changes occur and it progresses as a function of time, leading to the accumulation of dissolution products. This series of events ultimately causes alteration in the ionic composition and thus the pH of the reacting fluid. The release of Ca, Si,

and Ba from BaBG post-immersion in SBF solution with respect to time is shown in **Figure 3.3**. After the incubation of BaBG in SBF, the Ca level increased significantly (i.e., 106 ppm) compared to the initial concentration (i.e., 80 ppm) within 30 mins (**Figure 3.3A**). Further, at 1 h, the Ca concentration was 164 ppm and then it increased to 275 ppm at 24 h. According to the theory proposed by Hench et al. (Hench 2006) on the biomineralization of BGs, the increase in the level of Ca is due to the dissolution of the silica framework that leads to rapid leaching of cationic alkali/alkaline earth elements present as oxide network modifiers in the glasses in exchange with H^+ / H_3O^+ from SBF solution. Subsequently, there is a sharp reduction in the Ca concentration from day 3 (72 h) onwards and the Ca level was estimated to be around 148 ppm on day 7 (168 h). This indicates the migration of leached calcium along with phosphate from SBF to the silanol-rich layer on the surface of BaBG. The migration of the elements is considered essential as it leads to nucleation to form calcium phosphate, the precursor of amorphous HA.

Similarly, the concentration of Si was increased and then it gradually decreased as shown in **Figure 3.3B** and reaching maxima at 24 h (i.e., 51 ppm). The composition of SBF as proposed by Kokubo et al. (Kokubo and Takadama 2006) has no Si present in it thus the appearance of Si after immersion of BaBG would have come from the degradation of silica networks in BaBG in a time-dependent manner. However, after 24 h, the level of Si fell steadily until the last day of immersion (i.e., day 7). This reduction in Si may be due to the fact that the leached Si in the SBF solution condenses and repolymerizes to form negatively charged silanol (Hench 2006). Additionally, the amorphous HA layer also starts to deposit on the surface of BaBG, acting as a barrier between the BG surface and SBF; hence, preventing further degradation of the silica

network. Likewise, the leaching profile of the network modifiers in BaBG i.e., Ba is represented in its release curve i.e., **Figure 3.3C** and it exhibited a slow increase within the first few hours, reaching the maximum concentration followed by a reduction in their concentration. The initial phase of release can be attributed to the surface Ba or the isolated Ba species trapped in the vitreous matrix and therefore it does not require extra energy to break the bonds and leach immediately. Further, the later phase of ionic release is due to the incorporated dopants inside the glass matrix. Ba^{2+} has a larger ionic radius (135 p.m.) compared to Ca^{2+} (ionic radius is 100 p.m.) which causes an expanded glass network and decreased oxygen density (Majumdar, Hira et al. 2021). Thus, there is more leaching of the cationic ions from doped BGs than the parent 45S5. Previously, it has also been reported that the incorporation of barium in BaBG has increased the pH of SBF solution compared to the undoped 45S5, thus confirming the dissolution of the silica matrix and release of Ca, Si, and Ba (Majumdar, Hira et al. 2021).

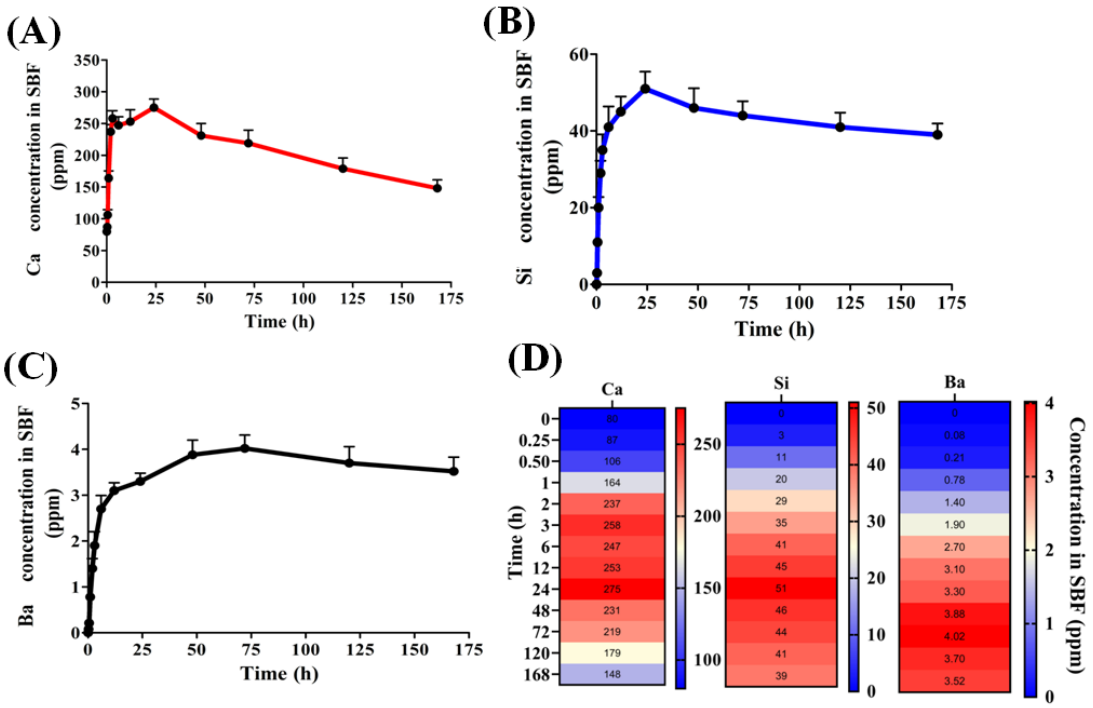

Figure 3.3: The release pattern of Ca (A), Si (B), and Ba (C) in SBF solution at pH 7.4 from BaBG at various time intervals for 7 days using ICP-MS and their representation by heatmap (D).

3.2.2. *In-vivo* oral pharmacokinetic study

3.2.2.1. The plasma concentration of Ca, Ba, and Si released from BaBG in rats during the *in-vivo* pharmacokinetic study

The plasma concentration of the leached Ca, Ba, and Si from BaBG after the oral administration at doses 1, 5, and 10 mg/kg were determined and is represented in **Figure 3.4 (i, ii, and iii)** respectively. The leaching profile of network modifiers is an essential parameter that needs to be evaluated before using inorganic biomaterials therapeutically as they tend to leach dopants that produce several biological effects at the physiological level. However, an increase in their level in the body beyond the physiological level can produce various physiochemical, pharmacokinetic and pharmacodynamic interactions. For instance, antibiotics like tetracycline have been reported to form insoluble metal ion chelation with Ca that reduces its absorption which can affect the bioavailability (Wanner, Walker et al. 1991). Further, the presence of excessive Ca may produce major drug interactions with calcium channel blockers and antiepileptic drugs (Kim, Kim et al. 2022). Therefore, the *in-vivo* release kinetics of the leached dopants from the matrix of BaBG was evaluated. In the present study, the plasma concentration-time curve of Ca and Ba exhibited a dose-dependent increase in their concentration in the plasma from the first hours, reaching maxima at 24 h and then slowly decreasing to the basal level by the end of the experimental protocol (shown in **Figures 3.4i and 3.7ii**). The plasma level of Ba increased maximum to 1.38 ppm at a dose of 10 mg/kg b.w. BaBG (reference level of Ba in the serum of control rats is reported to be around 0.6 ppm (Bligh and Taylor 1963)). Similarly, the calcium level in the plasma of BaBG-treated rats was increased to 55.6 ppm at the highest dose of 10 mg/kg b.w. Statistical analysis by two-way ANOVA revealed significant changes in calcium and barium

concentration in the plasma among the groups ([$F_{(3,144)}$ = 78.84; $p < 0.05$]) and $F_{(3,144)}$ = 164.8; $p < 0.05$]) respectively, time ([$F_{(5,144)}$ = 103.8; $p < 0.05$]) and ([$F_{(5,144)}$ = 244.1; $p < 0.05$]) respectively and, their interaction ([$F_{(15,144)}$ = 15.49; $p < 0.05$]) and([$F_{(15,144)}$ = 53.57; $p < 0.05$]) respectively. The Bonferroni post-hoc analysis revealed a significant increase in the level of both Ca and Ba at 24 h and 48 h at all the doses tested compared to the control rats. The above-observed result suggests that the cations doped in the BG framework were leached in exchange with the H^+ from the acidic gastric fluid in the stomach (Paliwal, Kumar et al. 2018). These released ions are considered to activate a cascade of proteins required for cellular activity over a period of time which may be one of the reasons for the regenerative properties of BaBG in the *in-vitro* model of neurotrauma (Majumdar, Hira et al. 2021). Further, every element in our body has a physiological and pharmacological limit and an uncontrolled and unchecked release of therapeutic dopants from BGs may lead to adverse effects. In this case, the increase in the level of Ba is within the safety limits and is also considered non-toxic as per the acute and sub-acute oral toxicity study performed in rats (Majumdar and Krishnamurthy 2022).

The network modifiers i.e., Ca and Ba, after their uphill increment till 24h showed a gradual dip in their concentration in the plasma. The gradual decrease in calcium concentration in plasma after 24 h maybe due to its accumulation over the silanol-rich layer form an amorphous HA layer (as observed in XRD and FTIR during *in vitro* study). Additionally, since Ca is an endogenous element in the body, therefore; an increase in its level is re-established naturally to the basal level through various physiological pathways. There are many calcium homeostasis-maintaining mechanisms that include its influx and efflux by the activation of various calcium transporter/

channels, hormonal regulation through calcitonin, parathyroid hormone, and Vitamin D3, and also by deposition in various organs and bones (Matikainen, Pekkarinen et al. 2021). Similarly, the decrease in the level of Ba after 24 h may be because it is rapidly excreted out of the body mainly through the fecal matter as observed during the excretion studies (**Table 3.6**). Moreover, there was a dose-dependent increase in the clearance (CL) of Ba from the plasma and at a dose 10 mg/kg, CL increased by around 3-fold compared to 1 mg/kg (**Table 3.2**). Ba accumulated mainly in the metabolizing and excretory organs like the liver and kidneys (**Table 3.7**). Ba has also been reported to get deposited mostly in the hard osseous tissues like the skeleton and teeth and also in fats (Kravchenko, Darrah et al. 2014, Kovrlija, Locs et al. 2021), which may have caused the decrease in Ba plasma level after the observed C_{max} at 24 h (**Table 3.2**).

Similarly, after the oral administration of BaBG, there was a statistically significant increase in the level of Si in plasma at all doses compared to the control rats followed by a gradual decrease (as shown in **Figure 3.4iii**). The reference level of the reported Si level in control rats is 3 ppm (Du, Chen et al. 2019). The initial phase of increased Si in the plasma of treated rats may be due to the dissolution of the silicate networks of BaBG in the presence of physiological fluid (Hench 2006). Then the leached Si is absorbed into the systemic circulation through the gastrointestinal epithelium. However, by the end of day 3, the elevated level of Si was found to be statistically insignificant and at the end of day 7, it was similar to the basal level of Si present in the plasma of control rodents. This reduction in the level of Si may be due to the biodistribution of Si to various tissue compartments. Meanwhile, after the oral administration of BaBG, Si was remarkably higher in the spleen and liver which may be due to the uptake by the reticuloendothelial system (RES) and kuffer cells

respectively (as represented in **Table 3.7**) as similarly reported by Lee et al. (Lee, Kim et al. 2014).

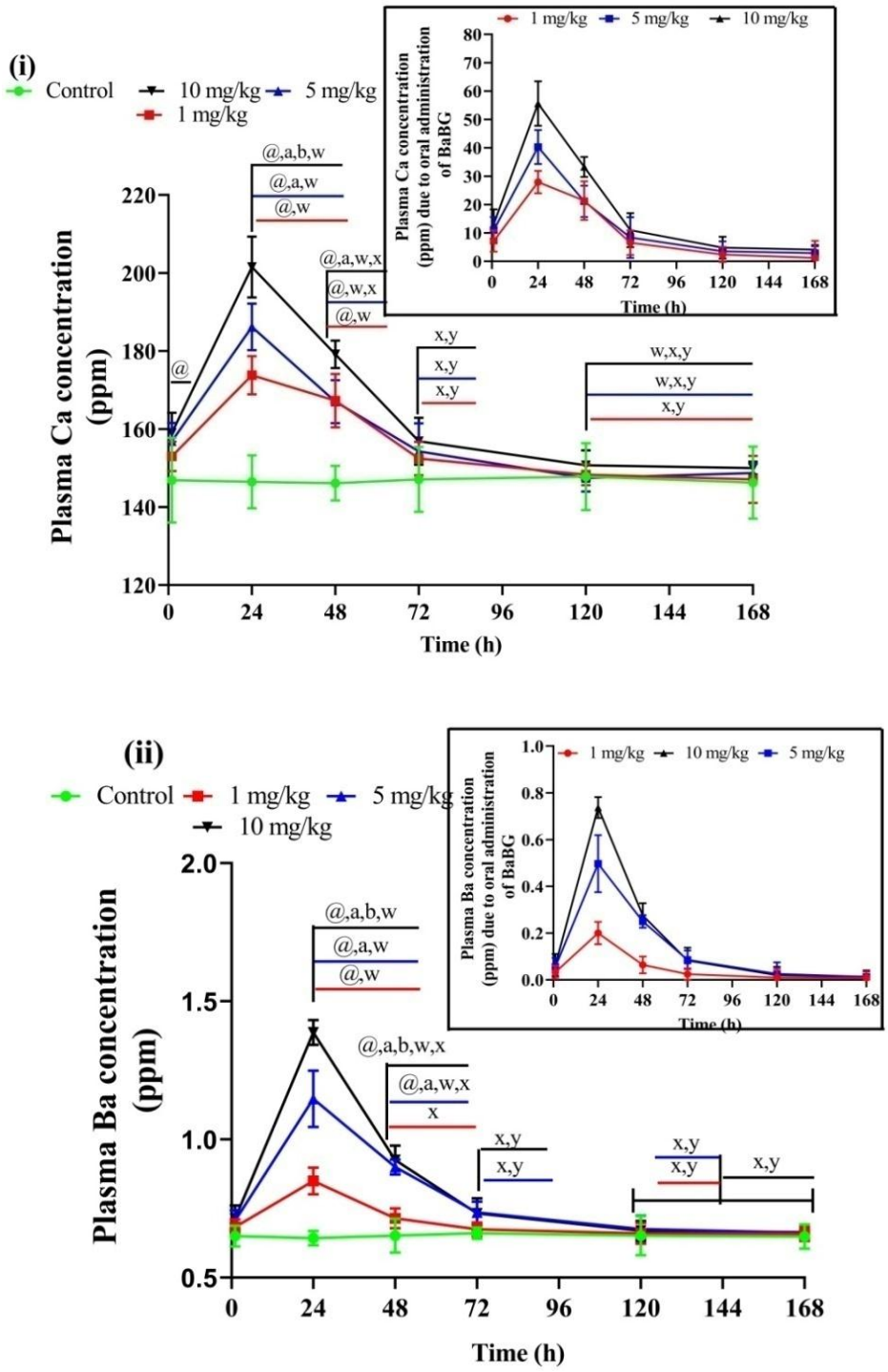

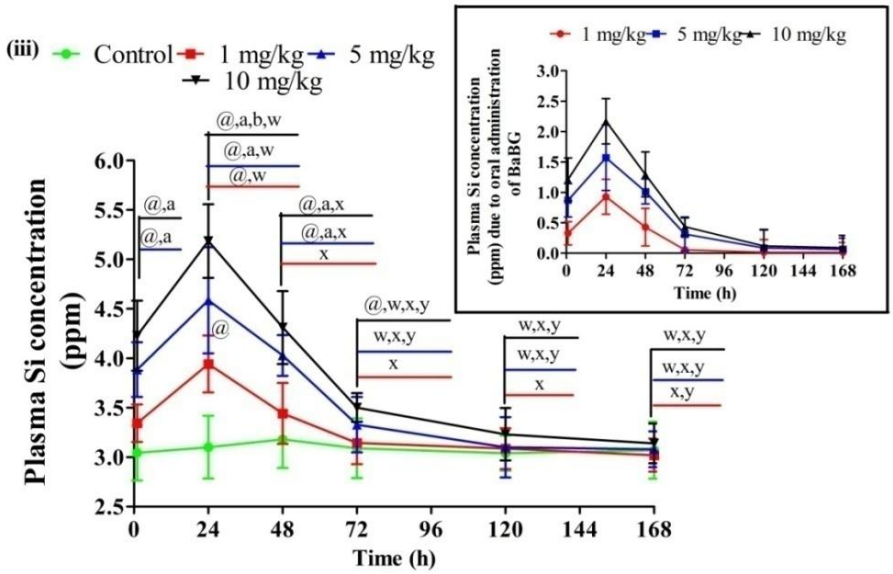

Figure 3.4: Plasma concentration profile of Ca (i), Ba (ii), and Si (iii) released from BaBG administered orally. All values are in mean ± SD (n=7 rats/ group).). $^{@}p<0.05$, $^{a}p<0.05$, and $^{b}p<0.05$ compared to control, dose 1mg/kg and 5 mg/kg of BaBG respectively. $^{w}p<0.05$, $^{x}p<0.05$, and $^{y}p<0.05$compared to 1, 24, 48 h respectively (Two-way ANOVA followed by Bonferroni post-hoc test).

3.2.2.2. *In-vivo* oral pharmacokinetic profile of Ca, Ba, and Si released from BaBG

The addition of network modifiers like CaO and BaO into the silica network of BGs tends to change the framework of BaBG which may alter the dissolution kinetics and hence the pharmacokinetic parameters. Therefore, the pharmacokinetic parameters of the released therapeutic ions (Ca, Ba, and Si) from BaBG after its oral administration were estimated and are reported in **Tables 3.1, 3.2, and 3.3** respectively. The maximum concentration of Ca observed in the plasma (C_{max}) after the oral administration at doses 1, 5, and 10 mg/kg was 27.93 ± 3.02, 40.28 ± 5.19, and 55.62 ± 4.48 ppm respectively and statistical analysis by one-way ANOVA followed by Tukey's post-hoc test revealed significant differences between them. However, the time taken to reach C_{max} (i.e., T_{max}) was the same for all the doses and was observed at 24 h. Moreover, the time taken for the concentration of Ca in plasma to reduce by 50% (i.e., $t_{1/2}$) was found to be 39.27 ± 3.72, 37.08 ± 2.99, and 36.85 ± 3.08 h for 1, 5, and 10 mg/kg respectively and was

statistically insignificant ($p > 0.05$). We also observed that the volume of distribution (V_z) and mean residence time (MRT) for Ca was increased in a dose-dependent manner (as shown in **Table 3.1**). Since $t_{1/2}$ is a composite pharmacokinetic parameter which is determined by V_z, hence, it can be ascertained that Ca in the blood circulation is biodistributed and is more concentrated in tissue compartments than in the vascular compartment of the body after its release from BaBG which corroborated the biodistribution study results (**Table 3.7**). Further, with an increase in dose, Ca leached from BaBG exhibited longer MRT. This may be due to the reason that around 98 % of filtered Ca gets reabsorbed by the renal tubules of kidneys (Blaine, Chonchol et al. 2015) by passive diffusion or solvent drag under normal physiological conditions. Additionally, the increased Ca are also removed from the blood circulation by binding to serum albumin non-covalently (Blaine, Chonchol et al. 2015); hence, longer MRT with the increase in the dose of BaBG.

Similarly, after the oral administration of BaBG, Ba ions are leached from the BG framework and enter the systemic circulation by absorption through the biological membrane. The course of movement of the leached dopants throughout the body before their excretion is essential to elucidate the extent of therapeutic effects as well as the toxic effects they might produce. Hence, the pharmacokinetic parameters of Ba released from BaBG were determined and are represented in **Table 3.2**. In the present study, after the leaching of Ba in the GIT, they are absorbed which caused a significant increase in the C_{max} of Ba in a dose-dependent manner similar to Ca in plasma. The T_{max} was observed at 24 h for all the doses. The C_{max} increased to more than double at a dose of 5 mg/kg b.w. (i.e. 0.49 ± 0.0488 ppm) compared to 1 mg/kg (0.22 ± 0.0189 ppm). Similarly, at dose 10 mg/kg, C_{max} increased significantly to 1.38 ppm compared to both

doses (1 and 5 mg/kg b.w.; $p<0.05$). The increased C_{max} for Ba in plasma with dose sheds light on the fact that the leached barium was absorbed through the gastrointestinal epithelium and has reached the blood circulation. However, on the contrary to Ca, the $t_{1/2}$ and MRT for Ba decreased in a dose-dependent manner and the specific reason explaining this trend remains unclear. The biodistribution pattern of the divalent Ba after their absorption from the GIT may help to explain this unusual trend. From the above results, it can also be presumed that after reaching the highest plasma concentration at 24 h, the physiological hemostasis set-point for barium is broken. As a result, irrespective of increased C_{max} with an increase in dose, there is a decrease in $t_{1/2}$ and MRT for doses 5 and 10 mg/kg compared to the lowest dose (i.e., 1 mg/kg b.w.). In general, the body tries to maintain homeostasis by distributing it to other body compartments or by excreting it. It has been observed that biologically non-essential elements like Ba have the tendency to get rapidly deposited mainly in less perfused mineralized organs like the skeleton systems (Bligh and Taylor 1963, Panahifar, Chapman et al. 2019). Ba having larger ionic radii than Ca gets more readily adsorbed in the form of colloidal particles on the surface of bones that help in the calcification process. Additionally, Ba was rapidly excreted in the feces since the body has the tendency to reduce the load of non-essential elements from the body as evidenced by the increased clearance (as represented in **Table 3.5**) with the increased dose which was statistically significant ($p<0.05$). Therefore, from the above-mentioned results, we can say that the increased level of Ba in blood circulation is normalized by physiological homeostatic pathways including biodistribution and excretion.

Further, in the case of Si, the C_{max} increased with dose and was found to be 0.93 ± 0.073, 1.57 ± 0.184, and 2.18 ± 0.206 ppm for 1, 5, and 10 mg/kg b.w. respectively and the

T_{max} was observed at 24 h for all the doses (as shown in **Table 3.3**). Furthermore, another important pharmacokinetic parameter is Vz which was also found to be augmented by approx. 2.8 and 4.2-fold at doses 5 and 10 mg/kg compared to 1mg/kg. Higher Vz indicates that the absorbed Si in the vascular compartment has a high tendency to escape the blood circulation and enter the extravascular compartments as observed during the biodistribution study (**Table 3.7**). Similarly, the MRT of Si in the body for doses 5 and 10 mg/kg was significantly higher compared to 1 mg/kg ($p<0.05$) which can be due to enhanced distribution in various tissues. Studies have reported that Si accumulation in various organs mainly the liver and spleen was observed for 3 days in rats (Lee, Kim et al. 2014). As per the previous study, there was no accumulated organ toxicity of BaBG in rats when administered orally at a dose up to 1000 mg/kg b.w. (Majumdar and Krishnamurthy 2022).

Table 3.1: Pharmacokinetic parameters for Ca released after single-dose oral administration of BaBG

Pharmacokinetic parameters	1 mg/kg BaBG	5 mg/kg BaBG	10 mg/kg BaBG
Half life ($t_{1/2}$) (h)	39.27± 3.72	37.08± 2.99	36.85± 3.08
T_{max}(h)	24	24	24
C_{max}(ppm)	27.93± 3.02	40.28± 5.19[a]	55.62± 4.48[a,b]
AUC $_{0-t}$ (ppm.h)	1636.01± 32.98	2127.17± 27.38[a]	2989.02± 40.96[a,b]
Vz (mg/kg)/(ppm)	0.0332± 0.002	0.1171± 0.003[a]	0.1657±0.021[a,b]
CL (mg/kg)/(ppm)/h	0.00058± 0.000071	0.00219± 0.00025[a]	0.00311± 0.00039[a,b]
MRT (h)	53.72 ± 5.34	59.12± 4.90	59.59± 4.16

All data are expressed as mean ± SD (n = 7 male rats/ group). [a]$p<0.05$ and [b]$p < 0.05$ compared to 1 and 5 mg/kg b.w. respectively. (One-way ANOVA followed by Tukey's multiple comparison post-hoc tests)

Table 3.2: Pharmacokinetic parameters for Ba released after single-dose oral administration of BaBG

Pharmacokinetic parameters	1 mg/kg BaBG	5 mg/kg BaBG	10 mg/kg BaBG
Half life ($t_{1/2}$) (h)	31.62± 2.88	26.47 ± 2.05[a]	24.72 ± 2.71[a]
T_{max}(h)	24	24	24
C_{max}(ppm)	0.22± 0.0189	0.49 ± 0.0488[a]	0.73±0.064[a,b]
AUC $_{0-t}$ (ppm.h)	8.804± 0.65	23.67 ± 1.93[a]	28.97 ±2.52[a,b]
Vz (mg/kg)/(ppm)	4.961± 0.37	7.904 ± 0.84[a]	12.101 ±0.99[a,b]
CL(mg/kg)/(ppm)/h	0.109± 0.0078	0.207 ± 0.0154[a]	0.339 ±0.0316[a,b]
MRT (h)	48.26± 3.91	46.79 ± 4.05	41.51 ± 3.98[a]

All data are expressed as mean ± SD (n = 7 male rats/ group).[a]$p<0.05$ and [b]$p < 0.05$ compared to 1 and 5 mg/kg b.w. respectively. (One-way ANOVA followed by Tukey's multiple comparison post-hoc tests)

Table 3.3: Pharmacokinetic parameters for Si released after single-dose oral administration of BaBG

Pharmacokinetic parameters	1 mg/kg BaBG	5 mg/kg BaBG	10 mg/kg BaBG
Half life ($t_{1/2}$) (h)	22.31 ± 2.51	29.24 ±1.96[a]	29.95 ± 3.04[a]
T_{max}(h)	24	24	24
C_{max}(ppm)	0.93 ± 0.073	1.57 ± 0.184[a]	2.18 ±0.206[a,b]
AUC $_{0-t}$ (ppm.h)	39.24 ± 4.26	88.73 ± 7.21[a]	120.32 ±9.13[a,b]
Vz (mg/kg)/(ppm)	0.812 ± 0.071	2.305 ±0.181[a]	3.432 ±0.244[a,b]
CL(mg/kg)/(ppm)/h	0.0252 ± 0.0019	0.054 ± 0.0043[a]	0.081 ±0.0075[a,b]
MRT (h)	35.33 ±3.04	46.13 ± 4.13[a]	47.17 ± 3.86[a]

All data are expressed as mean ± SD (n = 7 male rats/ group).[a]$p<0.05$ and [b]$p < 0.05$ compared to 1 and 5 mg/kg b.w. respectively. (One-way ANOVA followed by Tukey's multiple comparison post-hoc tests)

3.2.3. Urinary and fecal excretion

The inorganic biomaterials are considered biologically safe and can be translated clinically only if they have a controlled rate of elimination and metabolism. Therefore, the excretion kinetics of Ca, Ba, and Si released from BaBG after the oral administration were evaluated and are represented in **Tables 3.4, 3.5, and 3.6** respectively. The clearance of any inorganic compound from the body follows two

major eliminating routes i.e., hepatobiliary and fecal excretion and urinary excretion, hence, we temporally measured the level of Ca, Ba, and Si in urine and feces. It was observed that the cumulative amount of Ca excreted in urine and feces increased with the dose of BaBG (**Table 3.4**). Statistical analysis by two-way ANOVA exhibited significant changes in Ca level in the urine and feces among the groups ([$F_{(3,168)}$ = 271.5; $p < 0.05$] and $F_{(3,168)} = 162.5$; $p < 0.05$] respectively), time ([$F_{(6,168)} = 1434$; $p < 0.05$] and [$F_{(6,168)} = 2031$; $p < 0.05$] respectively) and, their interaction ([$F_{(18,168)} = 7.664$; $p < 0.05$] and [$F_{(18,168)} = 5.606$; $p < 0.05$] respectively). The post-hoc analysis revealed a significant increase in the level of Ca in the urine and feces from 24 h onwards at doses 5 and 10 mg/kg compared to the control group. The above-observed results have been similar to the previous report where calcium is excreted mainly through urine and feces to maintain the body's homeostasis (Ross, Taylor et al. 2012). However, after the glomerular filtration of Ca by kidneys, 80% of the filtered Ca is reabsorbed via passive diffusion or solvent drag in the proximal tubule (Ross, Taylor et al. 2012). It is also noteworthy that, in our study, the cumulative excretion of Ca was more in feces than in urine. We speculate that BaBG tends to get adsorbed into the mucous layer of the stomach after oral administration (**Figure 3.7**). This protective layer (mucus) has the tendency to continuously renew itself and is removed from the site, travels to the lower GIT and is excreted in feces. Therefore, Ca released into the lower GIT from the trapped BaBG in mucus has the lesser opportunity to get absorbed, leading to increased Ca levels in feces.

Similarly, in the excretion kinetic study of Ba, there was an increase in the level of Ba in both the urine and feces dose-dependently like Ca (shown in **Table 3.5)**. Normally, Ba released from BaBG are absorbed into the blood through the biological membrane

of GIT and then the body tries to restore homeostasis by distributing it to the bones and excretion through urine and feces (Moffett, Smith-Simon et al. 2007, Kravchenko, Darrah et al. 2014). Likewise, in our study, we observed that the plasma level of Ba after the oral administration of BaBG followed a downhill fall after the observed T_{max} at 24 h (**Figure 3.4ii**). The fall in the level of Ba may be due to increased clearance dose-dependently (**Table 3.2**) as Ba is a non-essential element and the body tries to eliminate it to restore homeostasis. We also observed that the fecal excretion of Ba exceeded the urinary excretion. In support of our observation, a study published indicated feces to be the primary route of excretion of Ba in rats that were exposed to barium chloride in their diet (Stoewsand, Anderson et al. 1988). Similarly, in the biodistribution study, the Ba level was higher in the liver compared to the kidneys (**Table 3.7**). The deposited Ba in the liver is most likely to get secreted in bile and thereby excreted out in feces.

The elimination kinetics of Si leached from BaBG after the single dose oral administration is represented in **Table 3.6** and statistical analysis by two-way ANOVA followed by post-hoc test exhibited significant elevation in the level of Si in urine and feces compared to the control rats. The detection of Si in urine implies that the kidneys are one of the excreting organs and even in the biodistribution study of BaBG, Si was detected more in the kidneys and liver compared to other organs (**Table 3.7**). Normally, Si that enters the systemic circulation after absorption through the intestinal mucosa follows the renal route of excretion without affecting the microstructure of the kidneys (Majumdar and Krishnamurthy 2022).

Table 3.4: Urinary and fecal excretion of Ca post-oral administration of BaBG in rats

Doses of BaBG (mg/kg b.w.)	Cumulative amount excreted in urine (ppm)						
	0-1h	**1-24 h**	**24-48 h**	**48-72 h**	**72-120 h**	**120-168 h**	**168-192h**
Control	20.48±3.78	38.88±3.26	56.10±4.91	77.49 ±5.15	105.54 ±6.84	120.37 ±9.79	139.39 ±3.27
1	22.19±2.15	50.26±4.26	75.65±8.35$^{@}$	98.76 ±7.84$^{@}$	118.69 ±4.12$^{@}$	138.90±7.23$^{@}$	154.94±9.91$^{@}$
5	25.44±2.03	59.57±7.07$^{@}$	89.78 ±6.07$^{@,a}$	112.26±10.52$^{@,a}$	129.70±10.83$^{@,a}$	147.78±3.68$^{@,a}$	167.39±5.38$^{@,a}$
10	26.32±4.11	66.34±5.73$^{@,a}$	101.14±8.72$^{@,a,b}$	127.47±5.37$^{@,a,b}$	157.58±13.42$^{@,a,b}$	167.61±7.71$^{@,a,b}$	181.87±6.22$^{@,a,b}$
	Cumulative amount excreted in feces (ppm)						
Control	35.82±1.45	74.13±8.82	114.14±13.20	146.19±8.81	181.76±14.49	220.47±15.35	254.70±18.02
1	33.03±3.89	79.05±9.16	121.32±10.26	152.41±6.78	192.63±5.24	235.07±6.16	275.45±12.52$^{@}$
5	40.16±4.19	93.67±7.90$^{@}$	144.71±11.33$^{@,a}$	175.38±10.04$^{@,a}$	201.72±10.72$^{@,a}$	251.57±10.73$^{@,a}$	292.84±9.75$^{@,a}$
10	37.54±5.28	102.71±12.23$^{@,a}$	161.82±4.04$^{@,a,b}$	192.27±5.27$^{@,a,b}$	235.25±8.06$^{@,a,b}$	279.73±11.47$^{@,a,b}$	310.80±17.79$^{@,a,b}$

Data are expressed as mean ± SD (n = 7 male rats/group). $^{@}p<0.05$, $^{a}p<0.05$ and $^{b}p<0.05$ compared to control, 1, and 5 mg/kg b.w. respectively (Two-way ANOVA followed by Bonferroni post-hoc test).

Table 3.5: Urinary and fecal excretion of Ba post-oral administration of BaBG in rats

Doses of BaBG (mg/kg b.w.)	Cumulative amount excreted in urine (ppm)						
	0-1h	**1-24 h**	**24-48 h**	**48-72 h**	**72-120 h**	**120-168 h**	**168-192h**
Control	0.41 ±0.083	0.78 ±0.052	1.08 ±0.28	1.35 ±0.34	1.70 ±0.20	2.12 ±0.36	2.43 ±0.42
1	0.39 ±0.051	0.79 ±0.094	1.41 ±0.35	1.89±0.19$^{@}$	2.15 ±0.37$^{@}$	2.42 ±0.28	2.80 ±0.3
5	0.43 ±0.037	0.96 ±0.046	1.45 ±0.18	1.92±0.22$^{@}$	2.21 ±0.41$^{@}$	2.69 ±0.23$^{@}$	3.11±0.28$^{@,a}$
10	0.48 ±0.066	1.12 ±0.18	1.70 ±0.28$^{@}$	2.20 ±0.39$^{@}$	2.67 ±0.18$^{@,a,b}$	3.15 ±0.41$^{@,a,b}$	3.61 ±0.42$^{@,a,b}$
	Cumulative amount excreted in feces (ppm)						
Control	0.38 ±0.016	0.68±0.092	1.08 ±0.15	1.48 ±0.17	1.83 ±0.37	2.24 ±0.14	2.68 ±0.28
1	0.40 ±0.025	0.84 ±0.056	1.42 ±0.21	1.91 ±0.27$^{@}$	2.33 ±0.18$^{@}$	2.72 ±0.35$^{@}$	3.06 ±0.31
5	0.42 ±0.073	0.89 ±0.12	1.61±0.17$^{@}$	2.03 ±0.29$^{@}$	2.61 ±0.39$^{@}$	3.03 ±0.44$^{@}$	3.49 ±0.46$^{@,a}$
10	0.37 ±0.028	1.12±0.19	1.98±0.24$^{@,a,b}$	2.71 ±0.35$^{@,a,b}$	3.08±0.42$^{@,a,b}$	3.85 ±0.41$^{@,a,b}$	4.25 ±0.57$^{@,a,b}$

Data are expressed as mean ± SD (n = 7 male rats/group).$^{@}p<0.05$, $^{a}p<0.05$ and $^{b}p<0.05$ compared to control, 1, and 5 mg/kg b.w. respectively (Two-way ANOVA followed by Bonferroni post-hoc test).

Table 3.6: Urinary and fecal excretion of Si post-oral administration of BaBG in rats

Doses of BaBG (mg/kg b.w.)	Cumulative amount excreted in urine (ppm)						
	0-1h	**1-24 h**	**24-48 h**	**48-72 h**	**72-120 h**	**120-168 h**	**168-192h**
Control	1.03±0.12	2.11±0.27	2.64±0.34	3.17±0.18	3.75±0.27	4.14±0.28	4.73±0.32
1	1.65±0.19	2.36±0.16	3.09±0.32	3.68±0.29$^{@}$	4.22±0.21$^{@}$	4.81±0.41$^{@}$	5.32±0.28$^{@}$
5	1.51±0.11	2.62±0.23$^{@}$	3.19±0.39$^{@}$	3.89±0.24$^{@}$	4.38±0.13$^{@}$	5.08±0.51$^{@}$	5.75±0.41$^{@}$
10	1.72±0.17$^{@}$	2.83±0.24$^{@,a}$	3.67±0.40$^{@,a,b}$	4.17±0.38$^{@,a}$	4.82±0.36$^{@.a}$	5.69±0.33$^{@,a,b}$	6.37±0.74$^{@,a,b}$
	Cumulative amount excreted in feces (ppm)						
Control	0.72±0.17	1.72±0.27	2.72±0.35	3.78±0.31	4.76±0.64	5.89±0.66	6.62±0.85
1	1.01±0.23	2.89±0.15$^{@}$	4.15±0.39$^{@}$	5.21±0.27$^{@}$	6.13±0.46$^{@}$	7.09±0.37$^{@}$	7.74±0.43$^{@}$
5	0.94±0.084	3.19±0.28$^{@}$	4.39±0.45$^{@}$	5.84±0.53$^{@,a}$	7.01±0.32$^{@,a}$	7.81±0.40$^{@,a}$	8.88±0.74$^{@,a}$
10	0.88±0.26	3.66±0.13$^{@,a}$	5.27±0.35$^{@,a,b}$	7.62±0.49$^{@,a,b}$	8.85±0.61$^{@,a,b}$	9.39±0.54$^{@,a,b}$	10.03±0.52$^{@,a,b}$

Data are expressed as mean ± SD (n = 7 male rats/group).$^{@}p<0.05$,$^{a}p<0.05$, and $^{b}p<0.05$ compared to control, 1mg/kg, and 5 mg/kg b.w. dose of BaBG respectively (Two-way ANOVA followed by Bonferroni post-hoc test).

3.2.4. Changes in body weight and organ coefficient after oral administration of BaBG

In the temporal biodistribution study of BaBG at different doses, the body weight and the organ coefficient of the treated rats were measured as they are the essential parameters to ascertain the normal physiological functioning of the internal organs. Therefore, the body weight of the rats treated with BaBG at doses 1, 5, and 10 mg/kg were measured (data not shown). Statistical analysis by two-way ANOVA showed no significant differences between the body weights of rats in every group ($p > 0.05$). Moreover, the organ coefficients of various vital organs like the brain, heart, lungs, liver, kidneys, and spleen were also statistically insignificant ($p > 0.05$) compared to the control group. This confirms that the doses selected for the pharmacokinetic and biodistribution study were safer and these findings are in agreement with our previous report (Majumdar and Krishnamurthy 2022) where BaBG was found to be non-toxic as per the OECD acute and sub-acute toxicity study performed on rats.

3.2.5. *In-vivo* biodistribution of Ca, Ba, and Si in vital organs and their scanning electron microscopical analysis

When any inorganic-based biomaterials are designed to be used systemically for therapeutic purposes and have a longer MRT, their organ accumulation and biodistribution in the body is an essential parameter that needs to be studied. This will help in optimizing the dosage regimen including the route of administration, dose, dosing interval and the duration of treatment. Biodistribution studies also assist in elucidating the potential organ toxicity or cumulative toxicity that the test compounds might produce. During the *in-vivo* pharmacokinetic study, the circulation half-life of

Ca, Ba, and Si was found to be 36.85 ± 3.08, 24.71 ± 2.71, and 29.95 ± 3.04 h respectively (**Table 3.1, 3.2, and 3.3**) at the highest dose tested, thus demonstrating a longer circulation in the body. Hence, the biodistribution of BaBG after oral administration was evaluated in vital organs. As shown in **Table 3.7** and **Figure 3.6**, there was a dose-dependent increase in the level of Ca, Ba, and Si in the vital organs (brain, liver, heart, kidneys, lungs, and spleen). At day 1 (D 1) post-administration of BaBG, there was a statistically significant level of calcium detected in the liver, kidneys, and spleen at a dose of 5 mg/kg compared to the control group. However, at the highest dose, a statistically significant level of Ca was detected in all the organs compared to the control rats ($p < 0.05$). As time progressed, at D 3, the amount detected in all the organs increased further and at 10 mg/kg, the increase was almost 1.2-fold compared to D 1. One possible reason may be that after the absorption of leached Ca from BaBG into the systemic circulation, the body tries to maintain homeostasis. There are various physiological calcium stores in the body where the surplus of calcium is stored (CHENG, Wei et al. 2006, Patel and Docampo 2010). Additionally, the rapid increase in Ca level was drastically reduced through urine as a statistically significant amount of Ca was detected in the kidneys (**Table 3.7**). In the SEM of the kidney tissue sections of BaBG-treated rats (10 mg/kg), there was the presence of HA (as represented in **Figure 3.6iii**). HA are biocompatible endogenous substances which are biodegradable and their deposition did not affect the microarchitecture or physiological functioning of kidneys during sub-acute toxicity study performed in rats (Majumdar and Krishnamurthy 2022). Furthermore, we also observed a higher percentage of Ca accumulation in the spleen compared to other organs from D 1 along with the deposition of HA (**Figure 3.6ii**). The reason may be that the body has normal physiological

phenomena to eliminate foreign particles that enter the systemic circulation by phagocytosis into the spleen through the splenic artery. So, either BaBG of smaller size would have been absorbed into the blood from GIT or HA formed *in situ* in the stomach (as observed in the SEM of the stomach tissue in **Figure 3.5**) may have migrated to the splenic tissue. Similarly, the liver is also involved in the endocytosis of foreign entities (BaBG) via the resident mononuclear macrophages of the RES that are abundantly present (Bhandari, Larsen et al. 2021). Subsequently, from D 5 onwards, the Ca level followed a downhill pattern and after day 7, we did not find statistically elevated levels of Ca in any of the major organs.

After the dissolution of the glass network, there is simultaneous leaching of Si and Ba in the *in-vitro* dissolution study in SBF (**Figure 3.3**). Similarly, in the *in-vivo* study, there was early detection of these elements in the liver and spleen on D 1 (**Table 3.7**). Their presence may be due to the opsonization of glass particles by the sinusoidal endothelial cells and Kupffer cells of the liver and phagocytes of the spleen, the major organs for removing the circulating exogenous entities. Statistical analysis by two-way ANOVA exhibited significant elevation in the level of Siand Ba at doses 5 and 10 mg/kg compared to the control group at D 1. Ba increased to 2.53 and 1.28 fold in the spleen and liver respectively at the highest dose while Si was elevated by approx. 1.5 fold in these eliminating organs. A previous study based on the silica-based nanoparticle showed that they were absorbed from the intestin eepithelium and are reportedly redistributed mainly in the liver and spleen (Fu, Liu et al. 2013). Normally, after the oral administration of any inorganic biomaterials, they are absorbed into the portal vein from the intestine and reache the liver. This could be one possible reason for the presence of HA in the liver (as represented in **Figure 3.6i**). Similarly, Ba and Si content

were also elevated significatly in the kidneys from D 1 after oral exposure compared to the control group. For Si, there was a more than 2-fold increase in its level in the kidneys. On the other hand, Ba and Si were in relatively lower concentration in the brain and lungs (**Table 3.7**). The Ba and Si concentrations reached the peak at D 3 like Ca in a dose-dependent manner followed by a reduction and levelling off to the basal level. It reflects that there is a dose-dependent elevation in the concentration of elements leached from BaBG. Therefore, dose selection should be done cautiously when employing BG for oral or systemic administration during therapeutic intervention.

Table 3.7: Tissue concentration of Ca, Ba, and Si in the brain, heart, lungs, liver, kidneys, and spleen after single-dose oral administration of BaBG at doses 1, 5, and 10 mg/kg b.w. at days 1, 3, 5, and 7

(i)	Concentration of Ca (ppm) in Brain				Concentration of Ba (ppm) in Brain			
	D1	D3	D5	D7	D1	D3	D5	D7
Control	9.61±1.78	10.23±0.93	10.17±1.22	9.74±0.90	0.0067±0.00014	0.0062±0.00084	0.0060±0.0011	0.0068±0.0007
BaBG-1	10.28±0.85	11.89±1.43	9.92±0.75^{y}	9.87±1.07^{y}	0.0063±0.0013	0.0072±0.0006	0.0068±0.0017	0.0066±0.0005
BaBG-5	10.94±1.71	12.27±1.02$^{@}$	10.01±1.46^{y}	9.63±1.21^{y}	0.0067±0.0007	0.0078±0.0012$^{@}$	0.0070±0.0004	0.0065±0.0007
BaBG-10	11.53±2.03$^{@}$	12.92±0.96$^{@}$	10.38±0.37^{y}	10.11±0.89^{y}	0.0069±0.0011	0.0081±0.0003$^{@}$	0.0071±0.0012	0.0062±0.0016^{y}
(ii)	Concentration of Ca (ppm) in Lungs				Concentration of Ba (ppm) in Lungs			
	D1	D3	D5	D7	D1	D3	D5	D7
Control	157.62±14.12	160.02±13.98	151.91±10.12	159.21±16.04	0.045±0.0068	0.050±0.0044	0.049±0.0086	0.044±0.0071
BaBG-1	163.07±12.17	171.11±7.77	160.48±9.83	158.96±7.51	0.056±0.0061	0.063±0.0059$^{@}$	0.050±0.0028^{y}	0.047±0.0067^{y}
BaBG-5	170.50±6.91	180.56±9.09$^{@}$	161.23±17.15^{y}	163.60±10.89	0.061±0.0078$^{@}$	0.072±0.0034$^{@}$	0.058±0.0060^{y}	0.049±0.0054^{y}
BaBG-10	177.68±15.98$^{@}$	191.78±10.13$^{@,a}$	167.41±8.03^{y}	160.70±13.68^{y}	0.070±0.0044$^{@,a}$	0.083±0.0061$^{@,a,x}$	0.061±0.0081^{y}	0.053±0.023^{x,y}
(iii)	Concentration of Ca (ppm) in Heart				Concentration of Ba (ppm) in Heart			
	D1	D3	D5	D7	D1	D3	D5	D7
Control	81.03±10.93	84.35±7.01	89.16±8.80	80.99±11.27	0.014±0.0034	0.014±0.0047	0.012±0.0024	0.015±0.0061
BaBG-1	89.02±6.59	96.19±10.11	80.22±4.48^{y}	84.41±5.87	0.019±0.0026	0.021±0.0016	0.015±0.0010	0.013±0.0057^{y}
BaBG-5	94.48±12.03	100.39±9.87$^{@}$	90.78±7.42	86.29±6.26^{y}	0.023±0.0067$^{@}$	0.034±0.0073$^{@,a,x}$	0.019±0.0035^{y}	0.015±0.0072^{x,y}
BaBG-10	101.66±8.13$^{@,a}$	113.01±13.17$^{@,a}$	96.97±10.39$^{@,y}$	82.72±9.94^{x,y,z}	0.030±0.0051$^{@,a}$	0.041±0.0039$^{@,a,x}$	0.021±0.0060$^{@,x,y}$	0.017±0.0028^{x,y}
(iv)	Concentration of Ca (ppm) in Liver				Concentration of Ba (ppm) in Liver			
	D1	D3	D5	D7	D1	D3	D5	D7
Control	9.36±1.21	9.19±1.09	9.40±0.72	9.03±0.83	0.072±0.0081	0.078±0.0093	0.074±0.0055	0.080±0.0123
BaBG-1	10.73±1.25	11.85±0.82$^{@}$	9.18±1.04^{y}	9.41±1.82^{y}	0.096±0.0230	0.119±0.0207$^{@}$	0.102±0.0148$^{@}$	0.088±0.0038
BaBG-5	12.43±1.09$^{@,a}$	13.71±0.91$^{@,a,x}$	10.42±0.96^{x,y}	9.82±0.52^{x,y}	0.120±0.0141$^{@}$	0.148±0.0209$^{@,a}$	0.117±0.0091$^{@}$	0.095±0.0106
BaBG-10	15.86±1.31$^{@,a,b}$	16.90±1.19$^{@,a}$	11.14±0.61^{y}	9.25±0.68^{x,y}	0.132±0.0357$^{@,a}$	0.169±0.0258$^{@,a}$	0.121±0.0179$^{@}$	0.098±0.0128^{y}
(v)	Concentration of Ca (ppm) in Kidneys				Concentration of Ba (ppm) in Kidneys			
	D1	D3	D5	D7	D1	D3	D5	D7
Control	93.42±7.89	92.12±4.12	95.19±8.04	97.89±6.43	0.038±0.0041	0.042±0.0063	0.034±0.0048	0.041±0.0069
BaBG-1	98.78±10.82	109.83±2.13$^{@,x}$	94.28±9.15^{y}	95.93±8.45^{y}	0.044±0.0076	0.056±0.0092$^{@,x}$	0.043±0.0070^{y}	0.038±0.002^{y}
BaBG-5	106.13±2.91$^{@}$	118.01±2.24$^{@,x}$	102.59±10.27^{y}	93.50±4.98^{x,y}	0.051±0.0047$^{@}$	0.069±0.0103$^{@,a,x}$	0.050±0.0031$^{@,y}$	0.044±0.0050^{y}
BaBG-10	115.70±6.04$^{@,a}$	132.33±4.08$^{@,a,b,x}$	106.86±5.99$^{@,a,x,y}$	95.57±7.34^{x,y}	0.060±0.0089$^{@,a}$	0.081±0.0116$^{@,a,b,x}$	0.061±0.0064$^{@,a,b,y}$	0.045±0.0028^{x,y,z}
(vi)	Concentration of Ca (ppm) in Spleen				Concentration of Ba (ppm) in Spleen			
	D1	D3	D5	D7	D1	D3	D5	D7
Control	26.18±3.45	25.03±1.89	23.44±2.25	26.12±3.01	0.051±0.0078	0.048±0.0051	0.045±0.0041	0.050±0.0029
BaBG-1	30.67±4.09	37.12±3.58$^{@,x}$	27.84±3.18^{y}	25.78±2.26^{x,y}	0.070±0.0036	0.091±0.0061$^{@}$	0.073±0.0082$^{@}$	0.058±0.0053^{y}
BaBG-5	33.13±4.03$^{@}$	39.93±1.34$^{@,x}$	29.36±1.47$^{@,y}$	24.95±2.01^{x,y}	0.082±0.015$^{@}$	0.147±0.0294$^{@,a,x}$	0.088±0.0162$^{@,y}$	0.060±0.0075^{x,y,z}
BaBG-10	38.26±4.15$^{@,a,b}$	43.09±5.18$^{@,a,x}$	31.21±3.89$^{@,x,y}$	26.41±3.55^{x,y}	0.091±0.025$^{@}$	0.231±0.0336$^{@,a,b,x}$	0.094±0.0102$^{@,y}$	0.062±0.0058^{x,y,z}

(vii)	Concentration of Si (ppm) in Brain			
	D1	**D3**	**D5**	**D7**
Control	0.63±0.055	0.59±0.045	0.61±0.058	0.56±0.071
BaBG-1	0.60±0.045	0.71±0.074$^{@}$	0.68±0.126	0.59±0.070^{y}
BaBG-5	0.67±0.082	0.80±0.093$^{@,x}$	0.71±0.068^{y}	0.62±0.103^{y}
BaBG-10	0.63±0.062	0.88±0.120$^{@,a,x}$	0.68±0.053^{y}	0.65±0.067^{y}
(viii)	**Concentration of Si (ppm) in Lungs**			
	D1	**D3**	**D5**	**D7**
Control	1.46±0.26	1.62±0.13	1.59±0.22	1.48±0.094
BaBG-1	2.67±0.31$^{@}$	3.38±0.25$^{@,x}$	1.92±0.14^{x,y}	1.65±0.23^{x,y}
BaBG-5	2.91±0.28$^{@}$	4.04±0.36$^{@,a,x}$	2.17±0.18$^{@,x,y}$	1.73±0.14^{x,y,z}
BaBG-10	3.12±0.27$^{@,a}$	4.31±0.52$^{@,a,x}$	2.38±0.31$^{@,a,x,y}$	1.71±0.12^{x,y,z}
(ix)	**Concentration of Si (ppm) in Heart**			
	D1	**D3**	**D5**	**D7**
Control	0.83±0.059	0.92±0.172	0.85±0.390	0.89±0.114
BaBG-1	1.49±0.182$^{@}$	1.78±0.161$^{@,x}$	1.23±0.171$^{@,y}$	0.96±0.083^{x,y}
BaBG-5	1.74±0.096$^{@}$	1.96±0.234$^{@}$	1.54±0.201$^{@,a,y}$	1.01±0.160^{x,y,z}
BaBG-10	2.05±0.272$^{@,a,b}$	2.15±0.177$^{@,a}$	1.78±0.103$^{@,a,y}$	1.19±0.184^{x,y,z}
(x)	**Concentration of Si (ppm) in Liver**			
	D1	**D3**	**D5**	**D7**
Control	2.08±0.11	2.17±0.34	2.10±0.16	2.02±0.35
BaBG-1	9.19±1.42$^{@}$	14.08±1.31$^{@,x}$	8.44±1.03$^{@,y}$	3.21±0.47^{x,y,z}
BaBG-5	12.48±1.78$^{@,a}$	19.16±2.62$^{@,a,x}$	10.61±1.76$^{@,y}$	4.01±0.48^{x,y,z}
BaBG-10	17.62±2.49$^{@,a,b}$	24.67±3.26$^{@,a,b,x}$	10.99±2.07$^{@,a,x,y}$	4.96±0.24$^{@,x,y,z}$
(xi)	**Concentration of Si (ppm) in Kidneys**			
	D1	**D3**	**D5**	**D7**
Control	2.51±0.27	2.98±0.31	2.33±0.20	2.80±0.37
BaBG-1	3.61±0.39$^{@}$	8.21±0.66$^{@,x}$	5.03±0.39$^{@,x,y}$	3.04±0.19^{y,z}
BaBG-5	4.01±0.44$^{@}$	11.04±1.34$^{@,a,x}$	6.14±0.48$^{@,a,x,y}$	3.97±0.23$^{@,y,z}$
BaBG-10	6.88±0.71$^{@,a,b}$	14.27±1.45$^{@,a,b,x}$	8.88±0.92$^{@,a,b,x,y}$	4.02±0.46$^{@,a,x,y,z}$
(xii)	**Concentration of Si (ppm) in Spleen**			
	D1	**D3**	**D5**	**D7**
Control	4.71±0.48	4.37±0.30	4.58±0.56	4.19±0.25
BaBG-1	5.42±0.97	9.93±1.64$^{@,x}$	6.02±0.48^{y}	5.03±0.41^{y}
BaBG-5	7.56±0.53$^{@,a}$	13.35±1.16$^{@,a,x}$	8.15±0.97$^{@,a,y}$	5.89±0.83$^{@,x,y,z}$
BaBG-10	10.97±1.51$^{@,a,b}$	17.09±2.31$^{@,a,b,x}$	10.21±1.35$^{@,a,b,y}$	6.61±0.39$^{@,a,x,y,z}$

Data are expressed as mean ± SD (n = 6 male rats/group).$^{@}p<0.05$, $^{a}p<0.05$, and $^{b}p<0.05$ compared to control, 1mg/kg, and 5 mg/kg BaBG b.w. respectively. $^{x}p<0.05$, $^{y}p<0.05$, and $^{z}p<0.05$compared to days after the oral treatment of BaBG (D1, D3, and D5of the individual group respectively). (Two-way ANOVA followed by Bonferroni post-hoc test)

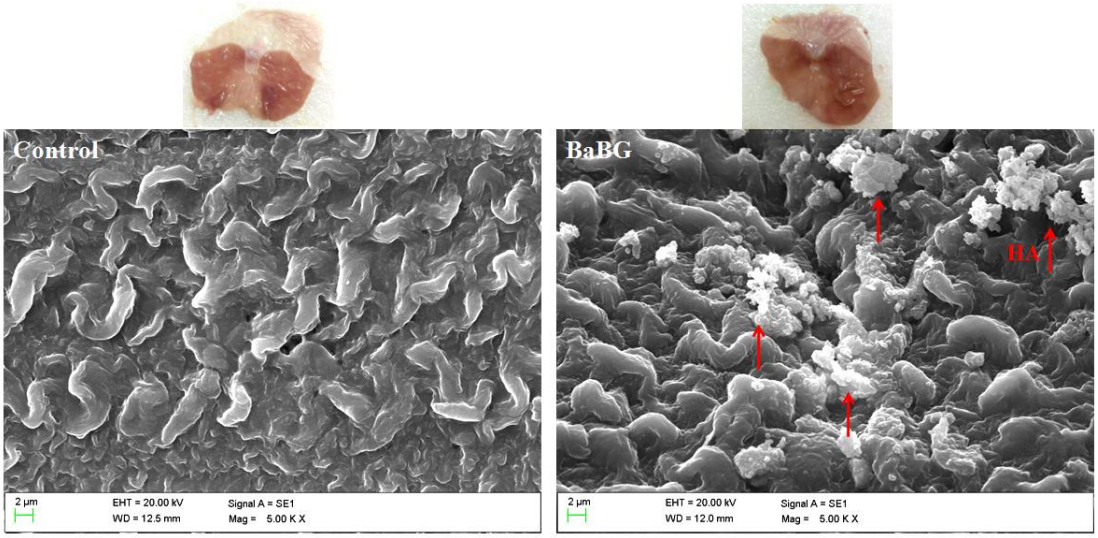

Figure 3.5: Representative scanning electron microscopy image of the stomach of the control and BaBG-treated rat exhibiting the deposition of abundant hydroxyapatite (HA) crystals on the gastric epithelium layer of the stomach without any abrasion of the protective layer qualitatively. The macroscopic photographs of the stomach of both the groups are also showing normal morphology. Magnification: 5k X; scale bars: 2 µm

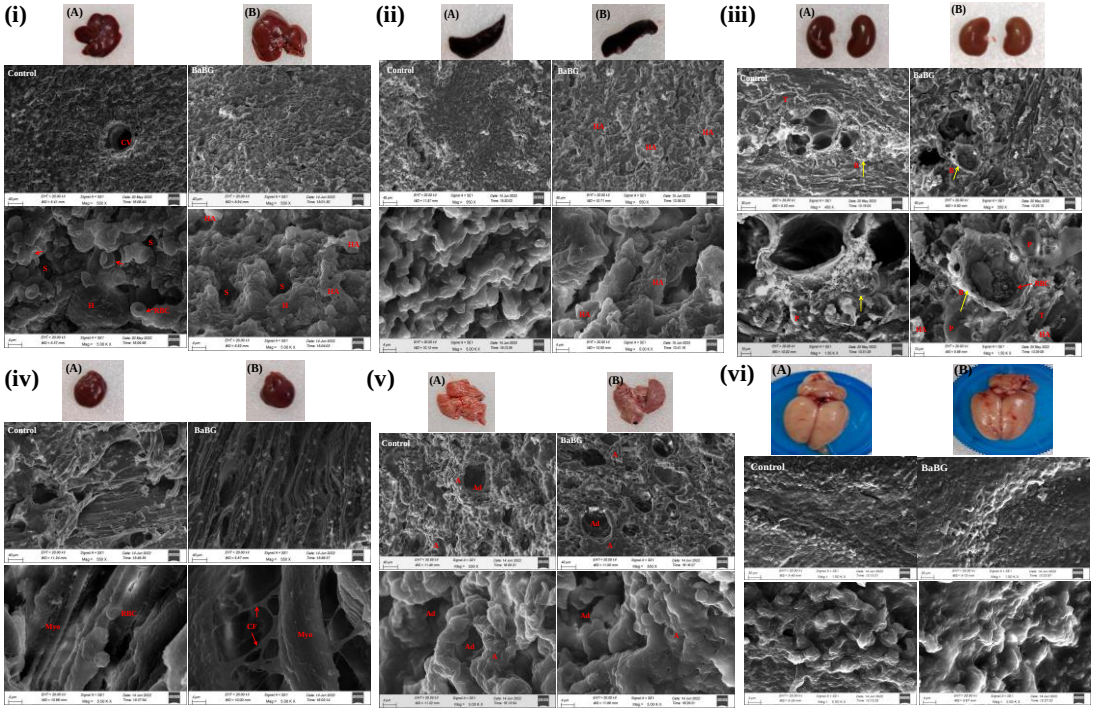

Figure 3.6: Representative photograph of the scanning electron microscopy of liver (i), spleen (ii), kidney (iii), heart (iv), lungs (v), and brain (vi) section of control (A) and orally treated BaBG rat (B). The liver section of the treated rat exhibited the presence of normal hepatocytes (H) surrounding the sinusoids (S) and central vein (CV). The deposition of hydroxyapatite (HA) along with the presence of erythrocytes (RBC; shown in red arrow) is seen. The spleen of BaBG-treated rat exhibiting abundant hydroxyapatite (HA) deposition and the lungs of control and BaBG rats also exhibited

normal alveoli (A) and alveolar duct (Ad). Similarly, the cross-section of the kidneys of treated rat exhibited normal architecture of the Bowman's capsule (B; yellow arrow) along with the glomerular tuft. There are also podocytes (P) and erythrocytes (RBC) visible along with the deposition of crystals of HA. The SEM analysis of heart exhibited intact myofibres (Myo) with the presence of loose connective tissue and collagen fibers (CF). BaBG rats exhibited normal surface morphology in brain section similar to the control rats without any deposition of HA. Magnification of liver, spleen, lung, and heart: 550X and 5 kX; scale bars: 40 µm and 4 µm respectively. Magnification of kidneys: 450 X and 1.5 kX; scale bars: 50 µm and 10 µm respectively. Magnification of brain: 1 kX and 5 kX; scale bars: 20 µm and 4 µm respectively.

3.3. Summary

In the current study, the pre-clinical single-dose oral release kinetics, biodistribution and excretion of dopants from sol-gel derived BaBG were evaluated. BaBG was amorphous and mesoporous in nature and its bioactivity was affirmed by its ability to form HA in SBF. The *in-vitro* release profile for Si, Ca and Ba from the BaBG framework in the simulated physiological milieu exhibited controlled release of the dopants with the maximum concentration observed at 24 h for Ca and Si. Similarly, the *in-vivo* oral pharmacokinetics study demonstrated the dose-dependent release of network modifiers into the plasma and the T_{max} was observed at 24 h for Si, Ca and Ba at all doses. There was dose-dependent elevation in the half-life of Si and Ca and the Vz increased by 4.2 and 4.99-fold respectively at 10 mg/kg. However, the half-life for Ba decreased with an increase in dose. The clearance (CL) of Ba increased 1.90 and 3.11-fold at doses 5 and 10 mg/kg respectively compared to 1 mg/kg BaBG. Further, the excretion study demonstrated feces to be the prime excretory route for Ba and Si. The biodistribution study indicated that Ca, Ba, and Si accumulated mainly in the excretory organs of the body such as the liver, spleen, and kidneys. Moreover, we have observed that barium leached from BaBG was detected in the peripheral organs as well as in the central nervous system i.e., the brain. Therefore, this study provides information on the fate of the released elements from orally administered BaBG, their release pattern, biodistribution and excretion.

Chapter 4

Acute and sub-acute oral toxicity study of BaBG and 45S5 according to the OECD guidelines

4. Introduction

Bioactive glasses (BGs) have immense hard tissue clinical applications (Hench, Splinter et al. 1971) and have received several FDA approvals for periodontal (Stanley, Hall et al. 1997), orthopedic (Jones, Brauer et al. 2016), and cranio-maxilo-facial applications (Bernardeschi, Nguyen et al. 2015). Later on, with improvement in the field of inorganic biomaterials, BGs have found their way to regenerating and repairing non-osseous and non-calcified tissues (Pires, Bonan et al. 2018, He, Ding et al. 2019, Qi, Zhu et al. 2020). Similarly, in **Chapter 2,** the anti-inflammatory and tissue regenerative potential of barium leached from BaBG was demonstrated. We also observed that there was dose-dependent release of network modifiers into the plasma after oral administration of BaBG (reported in **Chapter 3**). Despite the tremendous potential regenerative properties of BGs observed preclinically, there are no clinically translated products of BGs for oral and systemic administration. This is mainly due to inadequate preclinical toxicity studies that could prove their efficacy and safety. So, there is a need to perform oral toxicity studies of BGs to ascertain the therapeutic range for future pharmacological applications.

Further, the bioactivity of BGs is mainly due to the leaching of various doped ions from its framework which may enter the systemic circulation through the sublingual or buccal cavity and cross the blood-brain barrier, affecting the central nervous system (CNS) (i.e., brain), which controls most of the bodily functions. If BGs are used as implants then they are intended to remain *in situ* throughout the patient's life, so it is essential to perform long-term toxicity studies to assess their possible toxic effects on various vital organs, including the neurotoxic effects. Therefore, the toxicity study is essential for new drug discovery as it helps envisage the lethal dose (LD_{50}), a crucial

criterion for dose selection during systemic administration. Hence, an oral acute and sub-acute toxicity study for BaBG was performed according to the OECD (Organization for Economic Co-operation and Development) guidelines. Since 45S5 is the FDA-approved and commercialized BG for tissue engineering, it was used to compare the safety profile of BaBG in this study. In the present study, changes in the body weight and organ coefficients, hematological parameters, neuro-behavioral tests, biochemical estimation of various enzymes, and histological analysis were performed. Hence, the preclinical oral toxicity studies performed will help establish the safety and efficacy and will also help to estimate the dose of the developed BG when used for various pharmacological applications in not-too-distant future.

4.1. Materials and Methods

4.1.1. Materials

AUTOSPAN® Liquid Gold Calcium and MBK Alkaline Phosphatase Assay kit were purchased from ARKRAY Healthcare Pvt. Ltd., India. AST (GOT) and ALT (GPT)-Modified IFCC kits were procured from TARA Clinical Systems, India. We obtained creatinine and CK MB (NAC act.) assay kits from Coral Clinical Systems, India.

4.1.2. Animals

In the experiment, adult albino Wistar rats of 200±20 g were used (acquired from the Institutional animal house, IMS- BHU, Varanasi, India). All the rats were habituated for a week in a controlled temperature of 25±1°C and relative humidity of 45-55% (12/12 h light/dark cycle) with *ad libitum* supply of food (Paramount Laboratory Animal feed, Lanka, India) and water throughout the analysis. The current study was designed to curtail the number of animals used during the experiment, and all the studies

were performed as per the National Institute of Health Guidelines (publication number 85-23, revised 2013) on animal care experimentation. The experimental protocol was approved by the Central Animal Ethical Committee of Banaras Hindu University, Varanasi, India (Ref No. Dean/2021/IAEC/2557).

4.1.3. Acute oral toxicity study

The *in vivo* acute oral toxicity of BaBG was performed on healthy young adult female rats (as they are the most sensitive between the sexes) to determine the range of median lethal dose (LD_{50}) according to the OECD Guideline 423 (Acute Toxic Class Method) (OECD 2001). In the present study, 45S5 was used to compare the safety profile of BaBG. As per the experimental protocol, the animals were randomly allocated in groups with three animals in each group. Since there is no information on the toxicity profile of test substances (45S5 and BaBG), the starting dose of 300 mg/kg body weight (b.w.) was selected. If no or one animal is dead or in a moribund, then 300 mg/kg was administered in another three rats. Based on the result, higher or lower doses were tested. The detailed experimental protocol is depicted in **Figure 4.1.** 45S5 and BaBG was suspended in 0.5% carboxy methylcellulose (CMC), and the experimental protocol consists of a single-dose administration of the test substances by gavage in the overnight fasted rats. The control rats received 0.5 % CMC suspension, and all the rats were observed individually at least once during the first four hours and daily thereafter for 14 days. Various signs of toxicity like changes in the skin, fur, eyes, and mucous membranes were observed. Additionally, the rats were also monitored if any signs of tremor, convulsions, salivation, lethargy, diarrhea, sleep, and comatose conditions appeared. The individual body weight of the experimental animals in each group was also measured prior to and after administering the test substances weekly. After the 14th

day, the rats were weighed and anesthetized with 3% v/v isoflurane inhalation (Cat: R620 veterinary anesthesia machine, RWD Life Science, San Diego, USA). The animal was then killed by decapitation, and blood was collected for biochemical analysis. Various organs like the brain, heart, liver, kidney, spleen, and lungs were collected for a necropsy to observe any sign of test substance-induced pathological changes.

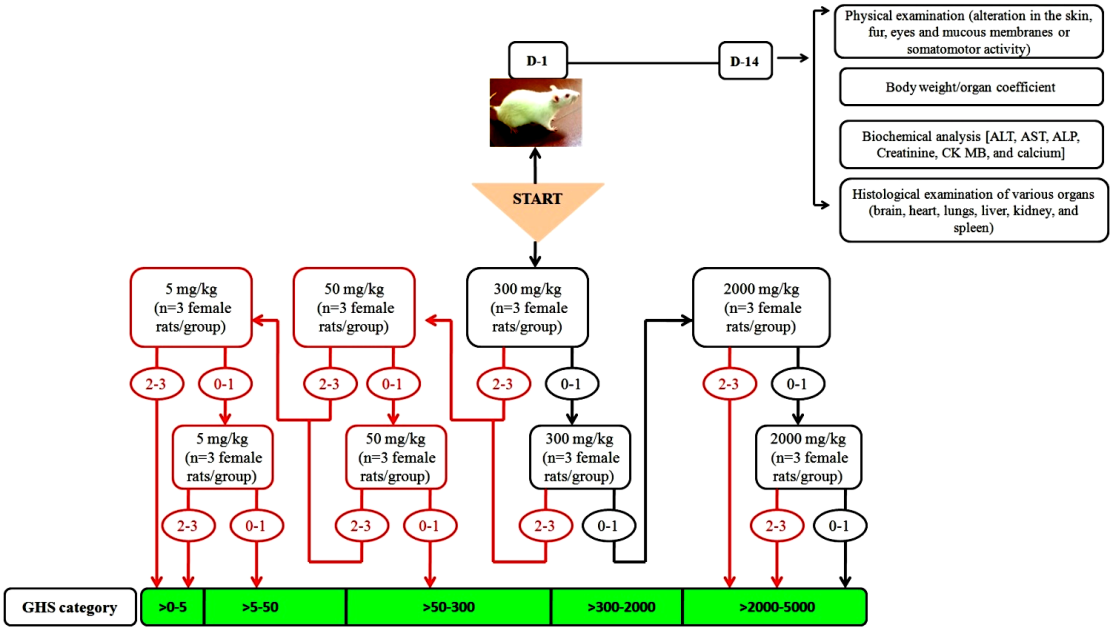

Figure 4.1: Schematic representation of the experimental protocol for single-dose acute toxicity study (OECD 423) to determine the LD_{50} cut-off (mg/kg b.w.) value. The starting dose of 300 mg/kg b.w. was selected. If 2-3 animals die, a lower test dose (i.e., 50 mg/kg) was tested and if no or one animal dies, the next higher dose (i.e., 2000 mg/kg) was tested. Black arrow indicates the test procedure followed in our study.

4.1.4. Subacute oral toxicity study

The repeated dose 28-day oral subacute toxicity study was performed in the Wistar rats according to the OECD 407 guidelines (Co-operation and Development 2008). The rats were randomly divided into groups: Control, 45S5 (50 mg/kg), 45S5 (500 mg/kg), 45S5 (1000 mg/kg), BaBG (50 mg/kg), BaBG (500 mg/kg), and BaBG (1000 mg/kg); each group containing 5 females and 5 males (n=10 rats/group). The doses were selected in such a manner that the highest dose would induce toxic effects without causing death

or severe suffering to the experimental animals and subsequently, the lowest dose would have no-observed-adverse effects (NOAEL). The control rats received 0.5% CMC suspension, while 45S5 and BaBG treatment groups were administered test substances (suspended in 0.5% CMC) daily for 28 days. All the experimental rats were observed daily for any abnormal behavior or changes in somatomotor activity. The behavioral assessment tests (like rotarod test, spontaneous locomotive activity, grip strength test, and Open-field test (OFT)) were performed on D-1, D-7, and D-28 to assess the progressive changes in motor activity and its effects on the central nervous system. Moreover, body weight and food and water intake were monitored throughout the experiment protocol. At the end of the 28th day, the experimental rats were anesthetized and sacrificed. The blood was collected for hematological analysis, and to investigate the toxic effects of BaBG on various organs (brain, heart, lungs, liver, kidney, and spleen), histopathological analysis was performed **(Figure 4.2)**.

4.1.5. Behavioral assessments

4.1.5.1. Rotarod test

The rotarod test is performed to assess the motor coordination ability of the rats (Rozas, Guerra et al. 1997). The experimental animals were trained on the rotarod (IKON Instrument, India) twice for two consecutive days at a lowest rotation speed of 5 rpm to reach stable baseline performances. On D-1, D-7, and D-28, during the test session, the speed of the rotating rod was increased to 15 rpm, and the time spent by the rats on the rod was recorded with maximum cut-off time of 300 s. The moment rats fall from the rod, the counting is stopped and reported as the retention time on rod.

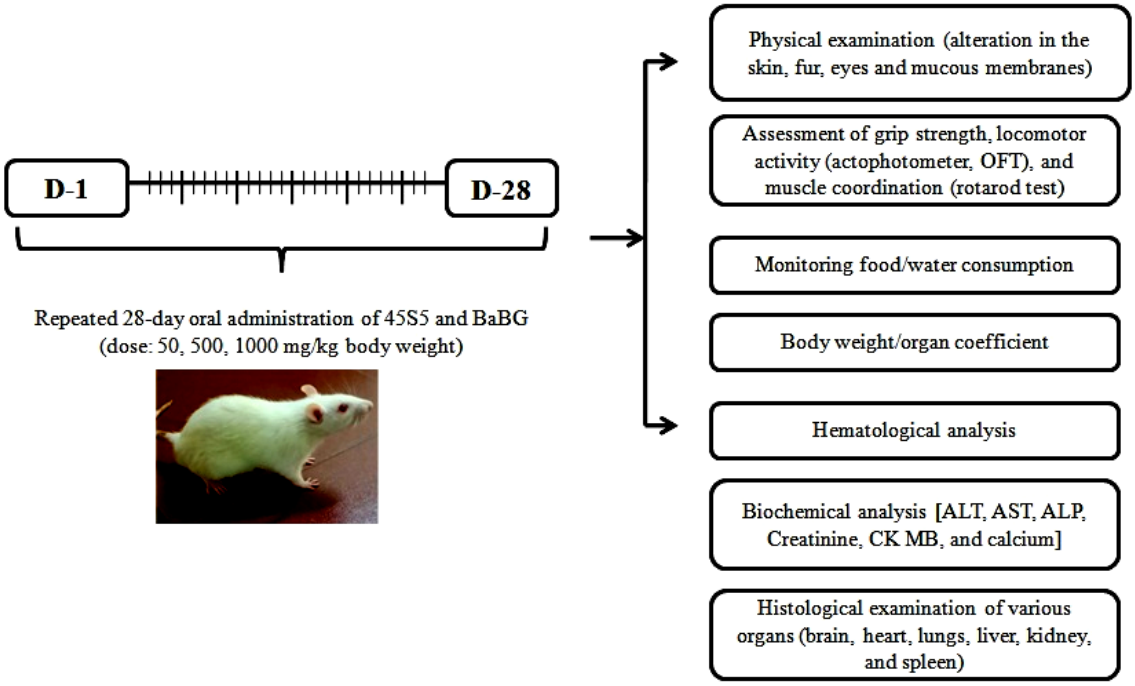

Figure 4.2: Schematic representation of the repeated 28-day oral toxicity study as per OECD 407 guidelines. In the subacute toxicity study, rats (n=10/group) were administered BaBG (dose: 50, 500, and 1000 mg/kg b.w.) and were observed daily for any sign of toxicity.

4.1.5.2. Open field test (OFT)

OFT, an important behavioral test performed to assess the locomotor activity of the experimental rats (Bronstein 1972). In this test, a square wooden box was fabricated (61x61 cm) representing an open field and is painted blank with enclosed high walls. The box is divided with white lines into 16 squares. An incandescent bulb dimly lights the apparatus suspended vertically in the central portion of the field. During the 5 min test, the animal was placed at the corner of the box facing towards the walls, and the parameters like the total number of rearing (rats stood on its hind limbs) and grooming (rats licked or scratched its face), total distance travelled, and time spent in the central region were recorded using ANY-maze^{TM} (version 3.72, USA). Prior to each experiment, the arena was cleaned with alcohol.

4.1.5.3. Grip strength test

Grip strength test is performed to determine the neuromuscular strength of the experimental animals and was performed on D-1, D-7, and D-28. The apparatus consists of a 90 cm long horizontal wire (diameter of 1mm) fixed between two vertical poles at the height of 50 cm from the flat surface. The rats were hung on the wire centrally with its forepaws and were scored as per the observations: 0-fall off; 1-hangs on the wire with both fore-paws; 2-same as 1 but also tries to climb on the wire; 3-hangs on the wire with both fore-paws and also with either of the two hind-paws; 4-hands on the wire with all four paws along with its tail wrapped around the wire; 5-escape the apparatus and falls on the flat surface (Meyer, Tilson et al. 1979, Prajapati, Garabadu et al. 2017). The cut-off time considered during this test was 90 s.

4.1.5.4. Spontaneous locomotor activity (Actophotometer)

Actophotometer is a square box (30 x 30 cm) with walls fitted with photocells and is used to measure the locomotor activity of the rats (IKON instruments, India) and was performed on D-1, D-7, and D-28. The rats were placed into the instrument, and their total activity counts were recorded for 5 min. The movement of the animal inside the box cut off the beam of light from the photocell and was recorded digitally as counts/5 min per animal (Reddy and Kulkarni 1998).

4.1.6. Organ coefficient

The organ coefficient is a vital parameter to evaluate the toxic effect of the test compounds by determining the changes in the organ's weight (Yang, Wu et al. 2019). The animals were sacrificed, and the organs were dissected and weighted properly. The organ coefficient of different organs was calculated using the following formulae:

$$\text{Organ coefficient} = \left[\frac{\text{Weight of the organ (g)}}{\text{Total body weight (g)}}\right] \text{X}100$$

4.1.7. Preclinical pathology

The hematological analysis was performed in the blood samples collected in tubes coated with anticoagulant (EDTA). For biochemical analysis, serum was collected from blood samples stored in tubes without any anticoagulant. The blood was allowed to clot at room temperature and centrifuged at 3000 rpm for 10 min; the supernatant was decanted and stored at -20°C for further analysis.

4.1.8. Hematology

To evaluate whether BaBG has any toxic effects on the blood cells, hematological blood parameters were measured using Coulter® LH750 Hematology Analyzer (Beckman Coulter Inc., CA, USA). The blood parameters like red blood cells (RBC), hemoglobin (Hb), hematocrit (HCT), mean corpuscular hemoglobin (MCH), mean cell hemoglobin concentration (MCHC), red blood cell distribution width (RDW), blood platelets (PLT), and white blood cells (WBC) were measured.

4.1.9. Biochemical analysis

The biochemical analysis was performed in the serum to access the effects of BaBG on functioning of various organs using assay kits as per the manufacturer's instructions. Alanine aminotransferase (ALT), aspartate aminotransferase (AST), and alkaline phosphatase (ALP) were measured to evaluate liver function. Similarly, the kidney and heart functions were detected by the level of creatinine (CRE) and CK-MB, respectively. Calcium (Ca^{2+}) level was also analyzed in the serum as excessive increase in its level is considered as an important pathological marker in various diseases.

4.1.10. Histological analysis

On the completion of the oral acute and subacute toxicity studies, various organs (brain, heart, lungs, liver, kidney, and spleen) were collected immediately and fixed in a 10% buffered formalin solution. The finely sliced tissues (5 µm) were stained with hematoxylin for 3 min and rinsed in running tap water. The samples were then counterstained with eosin for 1 min, dehydrated using graded series of alcohol, and mounted with dibutyl phthalate xylene (DPX). The slides prepared were observed under the microscope (Olympus DS-52, Japan) for any gross pathological aberrations (Fischer, Jacobson et al. 2008).

4.1.11. Statistical analysis

All the data were analyzed statistically by Graph Pad Prism 5.0 software (San Diego, RRID: SCR_002798). The behavioral parameters, the weight of the animals, and food consumed by them were analyzed by two-way ANOVA, while the biochemical studies, organ coefficient, and hematological parameters were assessed statistically by one-way ANOVA followed by Tukey's multiple comparison tests. $P<0.05$ was considered significant in all the analyses, and the values were presented as mean ± SD.

4.2. Results and discussion

4.2.1. Acute toxicity study

4.2.1.1. General observation and behavioral analysis

The animals were observed regularly after the oral administration of 45S5 and BaBG (300 and 2000 mg/kg b.w.), and there was no observed treatment-related mortality at any dose tested during the experimental protocol. Thus, the LD_{50} value of 45S5 and BaBG is more than 2000 mg/kg b.w. as per OECD 423, and the test compounds (45S5

and BaBG) fall under the GHS category (Globally Harmonized Classification System) 5 (non-toxic). Moreover, the animals in each group did not exhibit any treatment-related signs of toxicity like changes in the skin, fur, and mucous membrane or respiratory, circulatory, and somatosensory distress **(Table 4.1).** Additionally, there were no behavioral changes in the treated rats like salivation, convulsions, and tremors. This finding is supported by a previous report, where 45S5, when implanted into the peritoneal cavity of rats for two weeks, exhibited no toxicity like peritonitis or organ toxicity (Wilson, Pigott et al. 1981). Furthermore, in the present study, the oral administration of BaBG, as well as 45S5 at higher doses (2000 mg/kg b.w.), did not show any morphological changes in the vital organs like the liver, brain, lungs, kidneys, and spleen **(Figure 4.3).** A previous study also reported that the mesoporous bioactive glass spheres, when injected intravenously in rats, exhibited no pathological abnormalities in the internal organs (Mao, Chen et al. 2016). Thus, from these observed results, it can be affirmed that BaBG is non-toxic and can be used for various biomedical applications.

Table 4.1: General observation and behavioral analysis during the first 4 h and 24 h after single-dose administration of BaBG and 45S5 (300 and 2000 mg/kg b.w.) in rats (n=6 female rats/group).

Observation	Control		45S5(300 mg/kg)		45S5(2000mg/kg)		BaBG(300mg/kg)		BaBG(2000mg/kg)	
	4 h	24 h	4 h	24 h	4 h	24 h	4 h	24 h	4 h	24 h
Skin and fur	NC	NC	NC	NC	NC	NC	NC	NC	NC	NC
Eyes	NC	NC	NC	NC	NC	NC	NC	NC	NC	NC
Mucous membrane	NC	NC	NC	NC	NC	NC	NC	NC	NC	NC
Salivation	NC	NC	NC	NC	NC	NC	NC	NC	NC	NC
Diarrhea	NO	NO	NO	NO	NO	NO	NO	NO	NO	NO
Lethargy	NO	NO	NO	NO	NO	NO	NO	NO	NO	NO
Tremors and convulsions	NO	NO	NO	NO	NO	NO	NO	NO	NO	NO
Behavior pattern and somatosensory activity	N	N	N	N	N	N	N	N	N	N

Note: N-Normal, NO-Not observed, and NC-No change

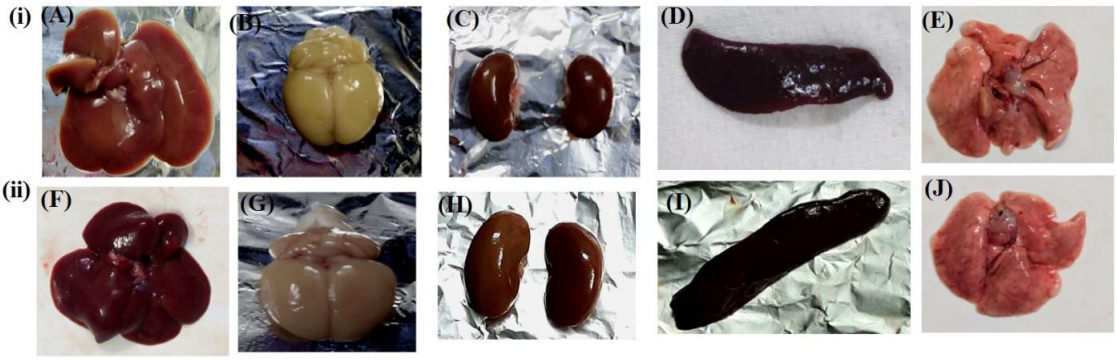

Figure 4.3: Representative macroscopic photographs showing normal morphology of (i) 45S5 [liver (A), brain (B), kidneys (C), spleen (D), and lungs (E)] and (ii) BaBG [liver (F) , brain (G), kidneys (H), spleen (I), and lungs (J)] treated rats after single-dose administration of highest dose (i.e., 2000 mg/kg b.w.) at the end of day 14.

4.2.1.2. Effect of BaBG on the body weight during the acute toxicity study

Body weight is an essential parameter to affirm the normal physiological functioning of the internal organs, and involuntary changes in it due to the administered test compounds are considered vital signs of severe pain, distress, or impending death of the experimental animals (OECD 2000, Chapman, Sewell et al. 2013). Thus, in the

present oral acute toxicity study, the body weight of the rats in each group was regularly monitored, which is depicted in **Figure 4.4.** Statistical analysis by two-way ANOVA revealed no significant differences in the body weight among the groups ([$F_{(4,75)}$ = 2.972; p >0.05]), time ([$F_{(2,75)}$ = 14.05; p > 0.05]) and their interaction ([$F_{(8,75)}$ = 0.0498; p > 0.05]). In support of our observation, previously, a study reported no differences in the body weight gain between the control and treated rodents even after the intravenous administration of mesoporous BG (Mao, Chen et al. 2016). Furthermore, Schwotzer et al. (Schwotzer, Ernst et al. 2017) also investigated the toxicity profile of barium sulfate nanoparticles. It was found that 90 days of exposure did not produce any changes in food/water consumption, with no significant differences in body weight among the groups. The above-observed result suggests that BaBG is safer and can be used for therapeutic purposes.

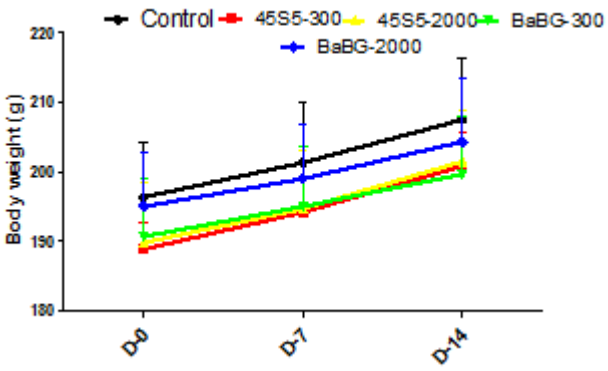

Figure 4.4: Effect of single-dose oral administration of BaBG and 45S5 on body weight of rats at various time points during the experimental protocol. All values are in mean ± SD (n=6 female rats/ group). (Two-way ANOVA followed by Bonferroni post hoc test).

4.2.1.3. Effect of BaBG on the organ coefficient during the acute toxicity study

Organ weight is an essential and sensitive parameter in experimental biology, and it often changes prior to any visible morphological changes; hence it is important to

measure it during the toxicological screening of any test compounds (Piao, Liu et al. 2013). The effect of single-dose oral administration of BaBG on the organ coefficient of vital organs (brain, heart, lungs, kidneys, liver, and spleen) during the acute toxicity study is depicted in **Figure 4.5**. Statistical analysis by one-way ANOVA revealed no significant changes in the organ coefficient of brain, heart, lungs, kidneys, liver, and spleen among the groups ([$F(_{4,29}) = 2.117$; $p>0.05$], [$F(_{4,29}) = 0.829$; $p>0.05$], [$F(_{4,29}) = 2.935$; $p>0.05$], [$F(_{4,29}) = 0.617$; $p>0.05$], [$F(_{4,29}) = 0.428$; $p>0.05$], and [$F(_{4,29}) = 2.662$; $p>0.05$] respectively). This confirms that the single-dose oral administration of BaBG had no apparent toxic effects on most of the highly perfused organs like in the 45S5 treated rats, which corroborates the biochemical estimation of various enzymes **(Figure 4.6)**. Moreover, previous studies have also similarly reported that oral administration of 45S5 in the stress-induced ulcer experimental rodents did not show evidence of any systemic toxicity due to minimal oral absorption (Ma, Gong et al. 2013). Similarly, the barium nanoparticles did not show any sign of toxicity in rats after 4-week exposure (Konduru, Keller et al. 2014) as the barium toxicity depends on their solubility (Oskarsson 2015). Previously, Majumdar et al. (Majumdar, Hira et al. 2021) reported that there is leaching out of the Ba^{2+} from the BaBG after it comes in contact with the simulated body fluid (SBF), and the free Ba^{2+} is generally deposited in the skeleton, essential for their calcification (Moore 1964, Oskarsson 2015). Therefore, it ascertains that the oral administration of BaBG does not have any toxic effects on the normal functioning of the vital organs.

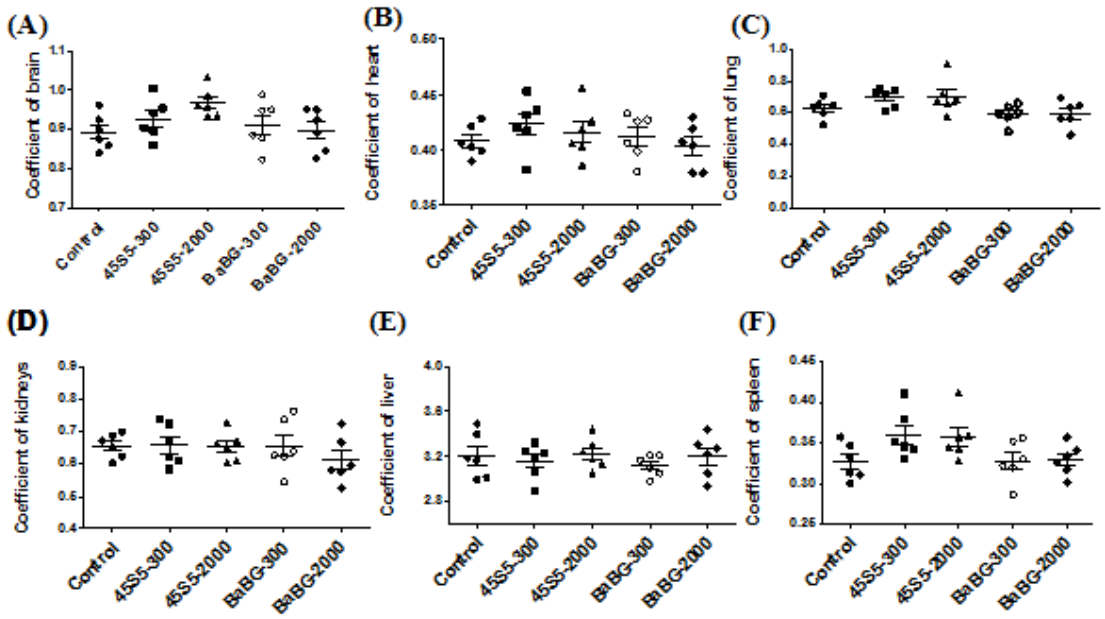

Figure 4.5: Effect of single-dose oral administration of BaBG and 45S5 on organ coefficient of the brain (A), heart (B), lung (C), kidneys (D), liver (E), and spleen (F) at the end of the experimental protocol. All values are in mean ± SD (n=6 female rats/ group). (One-way ANOVA followed by Tukey's multiple comparison post hoc test).

4.2.1.4. Effect of BaBG on various enzymes during the acute toxicity study

The assessment of the biochemical parameters (various enzymes) reflects the possible toxic effects of the test compounds on the functioning of vital organs of the body. In the present study, various enzymes were measured in the serum at the end of the experimental protocol and are shown in **Figure 4.6**. Normally, the vital organs have multifarious mechanisms to reduce their toxic load by eliminating the metabolites produced mainly through the liver and kidneys. Hence, it is essential to assess the liver and kidney functions during the acute toxicity study (**Figure 4.6A-D**) as they are mostly affected during the toxin purgation process (Liyanagamage, Jayasinghe et al. 2020). ALT, AST, and ALP are the important enzymes used clinically to screen the proper functioning of the liver (Lagarto, Bueno et al. 2011). AST is reported to be present in the mitochondria and cytosol of hepatocytes, while ALT is specifically present in the cytosol (Lagarto, Bueno et al. 2011). Thus, changes in the AST level are clinically

considered as an indication of hepatocellular necrosis. However, alteration in the serum ALT level is a specific sign of hypertrophy of hepatocytes or other liver disease conditions. Besides, ALP is another important enzyme present in the body, and an increase in its level indicates obstruction in the bile ducts (Giannini, Testa et al. 2005). In the present study, statistical analysis by one-way ANOVA revealed no significant changes in the serum level of ALT, AST, and ALP among the groups ([$F_{(4,29)}$ = 2.399; $p>0.05$], [$F_{(4,29)}$ = 0.024; $p>0.05$], and [$F_{(4,29)}$ = 2.258; $p>0.05$] respectively) (**Figure 4.6A-C**). Earlier studies have also reported that short-term oral exposure to barium salts did not produce any significant adverse health effects in rats or any microscopic hepatic lesions (Borzelleca, Condie Jr et al. 1988). Moreover, the toxicology study performed in the rodents reported that administration of barium chloride at the dose of 200 mg/kg/day did not produce any barium-related neurobiological or reproductive toxicity (Program 1994).

Kidneys are the major excretory organ that eliminates metabolic wastes from the body, and damage to it leads to azotemia, where there is the accumulation of nitrogenous wastes in the blood. Usually, creatinine is considered an essential anthropometric parameter and is used as an index of renal functions (Casal, Nolin et al. 2019). In our study, serum creatinine level was measured (shown in **Figure 4.6D**), and statistical analysis by one-way ANOVA revealed no significant changes in the serum level of creatinine among the groups ([$F_{(4,29)}$ = 2.076; $p>0.05$]. Therefore, this affirms that single-dose oral administration of 45S5 and BaBG did not affect kidney functions. Similarly, in a recent study, Hasan et al. (Hasan, Schaner et al. 2021) reported that 45S5 did not exhibit any changes in the creatinine level compared to the control rats when used to treat osteomyelitis. Further, another study also reported that bioglass, when

implanted into the bone of rabbits, did not show any changes in the creatinine level, indicating that kidney functions were not affected due to the leaching out of silicon from the glass framework (Lai, Garino et al. 2002). On the other hand, there are no reports on the oral acute toxicity profile of barium-doped BGs. Nevertheless, some studies have indicated an increase in kidney weight after 13 weeks of exposure which may be due to the long-term exposure of very high doses of barium salts (Program 1994).

The heart, a muscular organ that pumps blood to the entire body by the rhythmic contraction and relaxation of the involuntary cardiac muscle and blockage of blood flow, leads to myocardial infarction, one of the leading causes of death worldwide (Wu, Huang et al. 2019). Studies have reported that following myocardial infarction, the necrotic tissue releases enzymes like CK-MB after 4-6 h into the blood, which reaches a peak at 24-36 h and then declines rapidly (Grande, Hansen et al. 1982). Thus, estimating the serum CK-MB level is widely established clinically as a diagnostic marker for myocardial cell injury. In the present study, CK-MB level was measured in the serum and is represented in **Figure 4.6E**. Statistical analysis by one-way ANOVA revealed no significant changes in the serum level of CK-MB among the groups ([$F(_{4,29})$ = 1.511; $p > 0.05$]. This strongly indicates that single-dose oral administration of 45S5 and BaBG did not exhibit any toxic effects on the cardiac muscle, which also substantiates the heart's histoarchitecture **(Figure 4.7)**. Our finding is consistent with the previous report where a 13-week daily administration of barium salts did not exhibit any chemical-related clinical signs of cardiovascular toxicity in the male and female rats (Program 1994). Moreover, it is also reported that 45S5, formulated as elastomeric nanocomposites, are used as cardiac patches *in vivo* without any cytotoxicity (Kargozar,

Hamzehlou et al. 2017). Hence, this study suggests that like 45S5, BaBG is safer without significant toxic effects and can be used for various biomedical applications.

Further, calcium was estimated in the serum at the end of the experimental protocol (shown in **Figure 4.6F)** as it is an important element present in the body, primarily in the bone and teeth, and plays a vital role in various physiological activities like nerve conduction, muscle contraction, blood clotting, and also regulates cell death by apoptosis (Orrenius, Gogvadze et al. 2015). However, an increase in calcium in the serum is reported to play a pathogenic role in various diseases (Verma, Wills et al. 2018). In the present study, statistical analysis by one-way ANOVA revealed no significant changes in the serum level of calcium among the groups ([$F(_{4,29}) = 2.451$; $p > 0.05$]. Therefore, from the results obtained, it can be affirmed that single-dose oral administration of both 45S5 and BaBG did not exhibit any toxic effects on the vital organs.

4.2.1.5. Histological analysis of various organs of BaBG-treated rats during the acute toxicity study

Mostly following the exposure to any toxic exogenous compounds, the primary organs like the brain, heart, liver, kidney, lungs, and spleen get affected due to their metabolic reactions. Hence histopathological studies need to be performed at the end of the experimental protocol. In the present study, the histological sections of the single-dose treated tissues of the experimental rats exhibited intact architecture with no histopathological changes in any of the highly perfused organs, as depicted in **Figure 4.7**. In the brain section of control and BaBG-treated rats, there was no sign of toxicity in the neurons of the cortical region (as shown in **Figure 4.7A)** which corroborates the

organ coefficient of the brain where there were no significant changes observed compared to the control group and 45S5 treated rats (Yu, Li et al. 2013). Likewise, Lai et al. (Liang, Xiang et al. 2018) performed the subchronic oral toxicity study for the silica nanoparticles at a very high dose of 1500 mg/kg b.w. in rats and reported no chemical-induced toxicity histological changes. Further, a previous study also reported that short-term oral administration of $BaCl_2$ did not produce any significant adverse effects in the rats (Borzelleca, Condie Jr et al. 1988). Furthermore, in the liver section of the control and the treatment groups (BaBG and 45S5) at high doses (2000 mg/kg b.w.), there were normal hepatocytes with acidophilic cytoplasm and intact vesicular nucleus radiating from the central vein surrounding the portal tract. Moreover, there were no significant changes in the appearance of sinusoids in the control and the treated group, which confirmed that the test compounds (BaBG) had no toxic effects on the liver. This finding corroborates the liver enzyme level (AST, ALT, and ALP) (**Figure 4.7 A-C**), and previous studies have also reported that 45S5 administration did not produce any histological changes in the internal organs (Lai, Ducheyne et al. 1999). Similarly, Anand et al. (Anand, Lalzawmliana et al. 2019) reported that after the implantation of the mesoporous BG, the liver section displayed healthy hepatic parenchyma with limited cellular infiltration after 45 days.

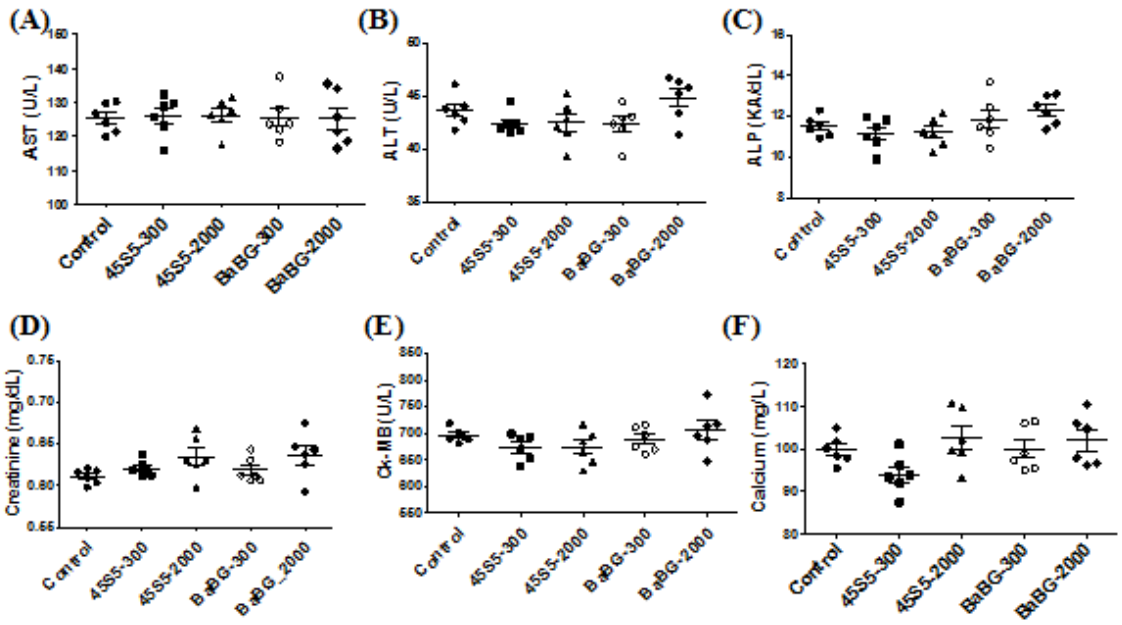

Figure 4.6: Effect of single-dose oral administration of BaBG and 45S5 on serum concentration of AST (A), ALT (B), ALP (C), creatinine (D), CK-MB (E), and calcium (F) at the end of the experimental protocol. All values are in mean ± SD (n=6 female rats/ group). (One-way ANOVA followed by Tukey's multiple comparison post hoc test)

Kidneys are the complex organs that excrete the wastes out of the body, and the hepatocytes have specialized ion channels and transporters that maintain the ionic concentration through their absorption and secretion into the urine. Hence, in the toxicity screening of BGs that leache out ions after coming in contact with the physiological fluid, it is essential to check its effect on the kidneys. At the end of the experimental protocol, the cross-section of the kidney of the control and treatment groups exhibited normal renal tubules in the present study. Moreover, it is also evident from the histological image of the renal cortical sections (shown in **Figure 4.7**) that the control and BaBG-treated groups had the typical structure of the glomeruli, bowman's capsule, and renal corpuscles like in 45S5 treated rats. Even the proximal and distal convulated tubules (PCT and DCT) showed normal architecture with no sign of toxicity which was similarly observed previously by De souza et al. (de Souza, Lopes et al.

2020) in 45S5 bioglass. Besides, fewer studies reported where the intravenous injection of mesoporous bioactive glass nanospheres did not produce any histological anomalies in the treatment groups like the test compounds in our present study, thus confirming the biological safety of BaBG (Sui, Zhong et al. 2016).

The spleen is the largest secondary lymphoid organ that contains two important structures, i.e., red pulp and white pulp. The red pulp is a blood filter that stores iron and removes foreign materials and older RBCs from the blood circulation. The white pulp is reported to contain a large number of lymphocytes that initiate immune responses in the presence of blood-borne antigens when blood flows into the spleen through the splenic artery (Cesta 2006). Thus, during the toxicity screening of any compounds, it is essential to evaluate their effect on the spleen as any compound that enters the systemic circulation after its administration reaches the spleen for elimination by phagocytosis. In the present study, the histological section of the spleen showed an indication of normal splenic tissue following the oral treatment with a single dose of 45S5 and BaBG. The cross-section exhibited a normal appearance of the lymphatic nodules of white pulp, splenic cords of red pulp, and the spleen trabecula. Previously Yang et al. (Yinhua, Jianbo et al. 1993) investigated the effect of barium chloride on the spleen and reported that daily administration of the barium salts for a month in drinking water did not produce any histological abnormalities in the structure of the spleen in the rodent model.

The heart, a muscular organ that pumps oxygenated blood to the body, and damage may lead to ischemic stroke due to reduced blood pumping to the brain. Thus it is essential to assess the effects of the administered compounds (45S5 and BaBG) on the cardiac muscle. In the present study, the photomicrograph of the heart of the control and treated

rats showed the presence of normal myocardial muscle bundles with thin fibro collagenous stroma, which substantiates the unchanged CK-MB level in the serum post-treatment with BaBG and 45S5 (**Figure 4.7E**). Further, the slice of the heart of all the groups showed single, oval, and centrally located nuclei in cardiomyocytes regularly arranged in myofibres. Similar to our observation, Fu et al. (Fu, Liu et al. 2012) examined the acute toxicity effects of silica nanorattle and reported no remarkable histological changes in the heart of the female mice after 14-day continuous administration. Correspondingly, the histological section of the lung of the control and the treated groups also exhibited normal architecture with no sign of edema, hemorrhage, and fibrosis. Moreover, there is the appearance of thinner interstitial matrix with the normal alveolar lumen and no evidence of inflammatory cells. Likewise, Loza et al. (Loza, Föhring et al. 2016) also reported that $BaSO_4$ nanoparticles produce no cytotoxic inflammatory response on the alveolar macrophages. Thus, from the above reports, it can be avowed that the single-dose oral administration of the barium-doped bioactive glass did not impart any toxic effects on the vital organs, and to our knowledge, this is the first time we are reporting the single-dose oral acute toxicity study of barium-doped BGs in rats.

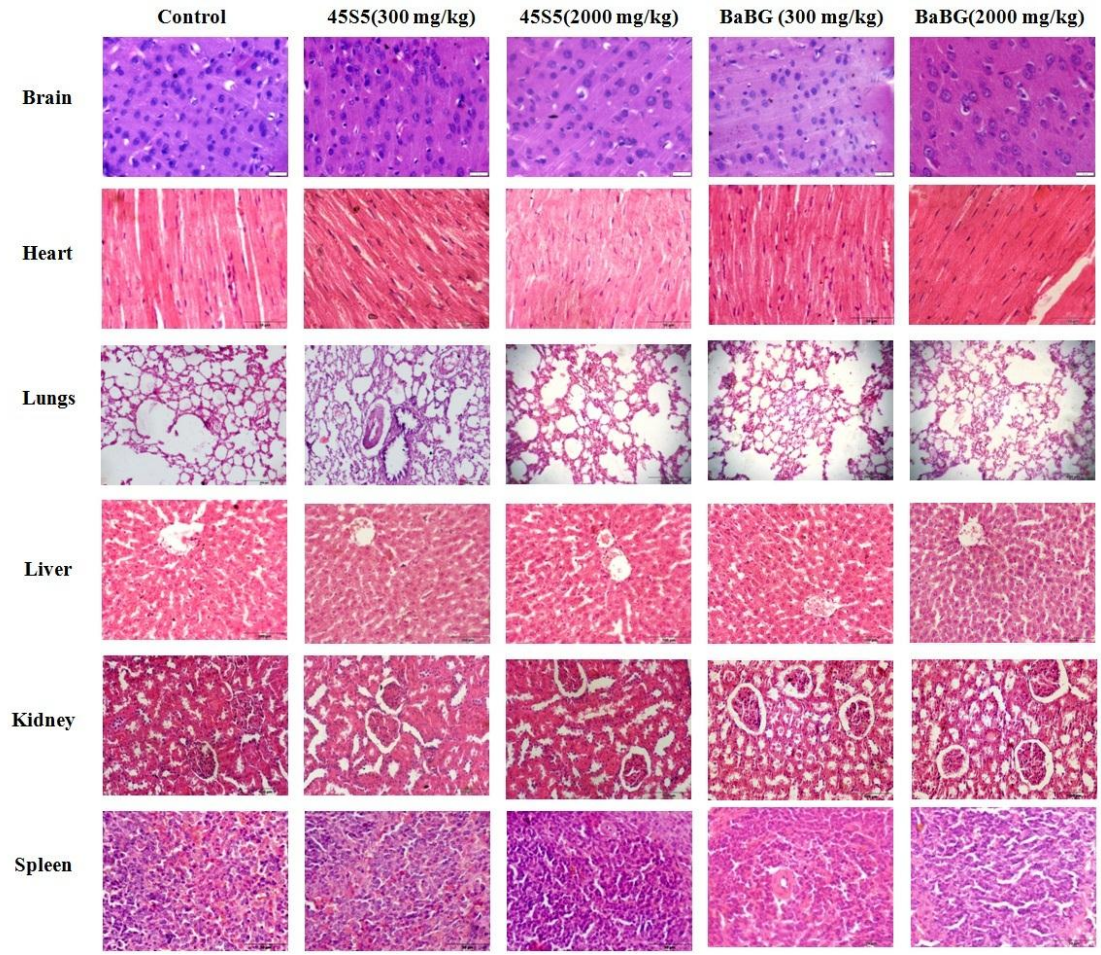

Figure 4.7: Effect of single-dose oral administration of BaBG and 45S5 (dose of 300 and 2000 mg/kg b.w.) on highly perfused organs like brain, heart, lung, liver, kidney, and spleen tissue stained with hematoxylin and eosin.

4.2.2. Sub-acute toxicity study

4.2.2.1. General observations

The animals were observed regularly following the repeated dose 28-day oral administration of 45S5 and BaBG (50, 500, and 1000 mg/kg b.w.) and the test compounds did not produce any treatment-related mortality at any dose tested during the experimental protocol. Further, no treatment-related signs of toxicity were observed, like changes in the skin, fur, and mucous membrane or any behavioral distress like salivation, convulsions, and tremors **(Table 4.2)** as previously observed (Program

1994). Moreover, the experimental rats did not exhibit any changes in the respiratory, circulatory, and somatosensory activities. Similar to our observations, a previous study reported no local or systemic toxicity in rodents following oral administration of silica nanoparticles at a dose of 1000 mg/kg b.w. (Cabellos, Gimeno-Benito et al. 2020). Besides, the toxicology study of barium chloride performed in rats reported did not produce any barium-related neurobiological toxicity (Program 1994). Thus, it can be affirmed that BaBG is safer to be used systemically for various biomedical applications like 45S5.

Table 4.2: General observation and behavioral analysis after repeated 28-day administration of 45S5 and BaBG (50, 500, and 1000 mg/kg b.w.) in rats (n=10 rats/group).

Observation	Control	45S5(50 mg/kg)	45S5 (500 mg/kg)	45S5 (1000 mg/kg)	BaBG (50 mg/kg)	BaBG (500 mg/kg)	BaBG (1000 mg/kg)
Changes in skin, fur, eyes, and mucous membrane	NC	NC	NC	NC	NC	NC	NC
Salivation	NC	NC	NC	NC	NC	NC	NC
Diarrhea	NO	NO	NO	NO	NO	NO	NO
Tonic-clonic movements	NO	NO	NO	NO	NO	NO	NO
Stereotypies (excessive grooming or repetitive circling)	NO	NO	NO	NO	NO	NO	NO
Behavior pattern and somatosensory activity	N	N	N	N	N	N	N
Sensory reactivity to auditory, visual, and proprioceptive stimuli)	N	N	N	N	N	N	N
Color and consistency of faces	N	N	N	N	N	N	N
Breathing pattern	N	N	N	N	N	N	N
Grip strength	NO	NO	NO	NO	NO	NO	NO

Note: N-Normal, NO-Not observed, and NC-No change

4.2.2.2. Effect of BaBG on the body weight and food consumption during the sub-acute toxicity study

In the sub-acute toxicity study, the effect of oral administration of 45S5 and BaBG at different doses (50, 500, and 1000 mg/kg b.w.) on body weight and food consumption is shown in **Figure 4.8.** Statistical analysis by two-way ANOVA revealed no significant changes in the body weight and food consumption among the groups ($p > 0.05$) which confirms that the test compounds did not affect the normal physiological functioning of the internal organs (Buesen, Landsiedel et al. 2014). Similarly, there was no observed significant change in the water consumption of the treated rats between all the groups recorded throughout the experimental protocol (data not shown), verifying the safety of BaBG like the 45S5.

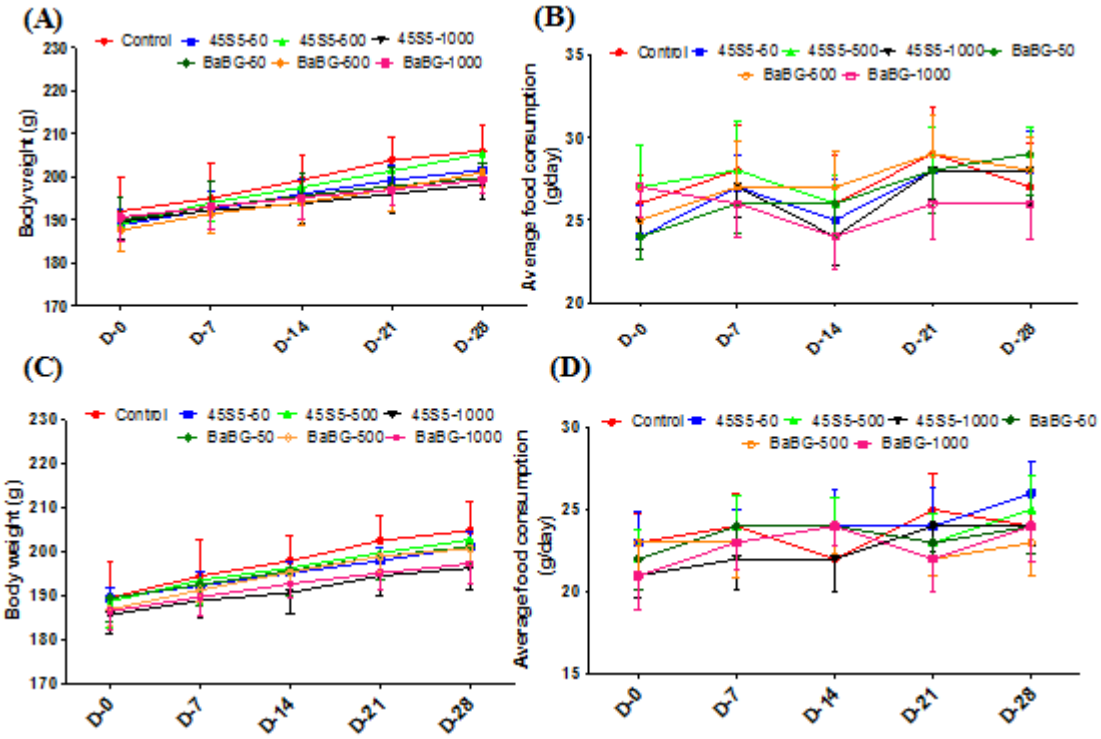

Figure 4.8: Effect of repeated-dose 28 days oral administration of BaBG and 45S5 (50, 500, and 1000 mg/kg) on body weight of male (A) and female (C) rats along with their food intake (B and D, respectively) during the experimental protocol. All values are in mean ± SD (n=5 rats/ group). (Two-way ANOVA followed by Bonferroni post -hoc test).

4.2.2.3. Effect of BaBG on hematological parameter during the sub-acute toxicity study

The hemotopoietic system is an important system of the body involved in producing the cellular blood components, and alteration in the hematological parameters indicates drug-induced toxicity in humans and animals (Buesen, Landsiedel et al. 2014). In the present study, the effects of oral administration of BaBG on the blood cells (RBC, WBC, platelets) and its associated parameters in male and female rats were evaluated and compared to the 45S5 treated rats (data not shown**)**. Statistical analysis by two-way ANOVA showed no significant differences in the blood parameters ($p > 0.05$) like RBC, Hb, HCT, MCH, MCHC, RDW, PLT, and WBC among the groups in treated rats (both male and female) when compared to the control group. Thus, it is evident that the test compounds did not interfere with hematopoiesis and leucopoiesis in the male and female experimental rats. This finding is supported by previous reports, where the oral administration of silica nanoparticles in rodents, up to a dose of 1000 mg/kg b.w. did not exhibit any dose-related adverse effects on blood cells (Yun, Kim et al. 2015). Furthermore, Majumdar et al. (Majumdar, Hira et al. 2021) reported the biocompatibility of barium-doped BG in an *in-vitro* cell-line-based study performed in a human leukemic cell line (K652). Hence, these results ascertain that BaBG does not impair erythropoiesis or have any toxic effects on the hematopoietic centers (kidney/spleen) that corroborate with the histological analysis (**Figure 4.14 & 4.15**).

4.2.2.4. Effect of BaBG on organ-coefficient during the sub-acute toxicity study

A comparative study of the effects of 45S5 and BaBG on the organ coefficient of male and female rats, 28 days post oral administration of the test substances (dose 50, 500, and 1000 mg/kg b.w.) is shown in **Table 4.3**. Statistical analysis by one-way ANOVA

showed no significant changes in the organ coefficient of the brain, heart, lungs, liver, kidneys, and spleen among the groups ($p > 0.05$) compared to the control rats. This strongly indicates that the oral administration of both 45S5 and BaBG did not disturb the normal functioning of the vital organs, hence confirming the safety profile of the BGs (45S5 and BaBG). This result also corroborates the no significant changes in the treated rat's body weight (**Figure 4.8**) and hematological parameters. Moreover, in support of our findings, previously, it has been reported that the 28-day oral exposure of $BaSO_4$ nanoparticles at a high dose of 1000 mg/kg did not exhibit any changes in the absolute organ weight of highly perfused organs of both male and female rats (Buesen, Landsiedel et al. 2014). Furthermore, Cabellos et al. (Cabellos, Gimeno-Benito et al. 2020) also reported that the short-term oral administration of mesoporous silica in mice did not significantly change body weight, hematology, and relative organ weights. Thus, we may conclude that doping of barium in the BG framework did not affect the safety profile of BG and BaBG can be considered to be safer for future therapeutic applications without any significant toxic effects.

Table 4.3: The organ coefficient of male and female rats after repeated 28 days oral administration of BaBG and 45S5 (50, 500, and 1000 mg/kg b.w.)

	Brain	Heart	Lungs	Liver	Kidneys	Spleen
(i) Male rats						
Control	0.946 ± 0.098	0.482 ± 0.0381	0.614 ± 0.056	3.371 ± 0.425	0.629 ± 0.038	0.373 ± 0.031
$45S5_{50}$	0.873 ± 0.062	0.471 ± 0.0547	0.602 ± 0.046	3.28 ± 0.334	0.582 ± 0.066	0.369 ± 0.040
$45S5_{500}$	0.834 ± 0.085	0.479 ± 0.0448	0.617 ± 0.089	3.572 ± 0.228	0.561 ± 0.041	0.379 ± 0.043
$45S5_{1000}$	0.915 ± 0.082	0.475 ± 0.0562	0.626 ± 0.084	3.723 ± 0.308	0.644 ± 0.048	0.381 ± 0.037
$BaBG_{50}$	0.979 ± 0.092	0.496 ± 0.0432	0.556 ± 0.092	3.421 ± 0.417	0.593 ± 0.075	0.346 ± 0.047
$BaBG_{500}$	0.861 ± 0.042	0.463 ± 0.0485	0.612 ± 0.063	3.521 ± 0.251	0.642 ± 0.080	0.352 ± 0.028
$BaBG_{1000}$	0.938 ± 0.079	0.476 ± 0.0703	0.632 ± 0.131	3.833 ± 0.413	0.613 ± 0.053	0.377 ± 0.036
(ii) Female rats						
Control	0.881 ± 0.011	0.463 ± 0.0235	0.581 ± 0.072	3.188 ± 0.278	0.616 ± 0.0731	0.358 ± 0.068
$45S5_{50}$	0.823 ± 0.063	0.465 ± 0.0395	0.597 ± 0.058	3.243 ± 0.388	0.611 ± 0.0636	0.344 ± 0.074
$45S5_{500}$	0.911 ± 0.098	0.438 ± 0.0162	0.604 ± 0.084	3.302 ± 0.315	0.609 ± 0.0427	0.352 ± 0.049
$45S5_{1000}$	0.904 ± 0.071	0.446 ± 0.0278	0.636 ± 0.048	3.397 ± 0.451	0.597 ± 0.0642	0.361 ± 0.052
$BaBG_{50}$	0.893 ± 0.088	0.475 ± 0.0473	0.601 ± 0.051	3.148 ± 0.294	0.612 ± 0.0209	0.353 ± 0.032
$BaBG_{500}$	0.923 ± 0.145	0.435 ± 0.0285	0.614 ± 0.044	3.177 ± 0.416	0.617 ± 0.0562	0.358 ± 0.061
$BaBG_{1000}$	0.906 ± 0.064	0.445 ± 0.0224	0.624 ± 0.068	3.355 ± 0.253	0.619 ± 0.0438	0.364 ± 0.047

All values are in mean ± SD (n=5 rats/ group). (One-way ANOVA followed by Tukey's multiple comparison post-hoc test)

4.2.2.5. Effect of BaBG on various enzymes during the sub-acute toxicity study

The biochemical analyses of various enzymes in serum are generally performed during the sub-acute toxicity study to monitor the effect of test compounds on the functioning of various organs. The liver, an essential metabolic clearance organ, acts as a biological filtration unit that sequesters most of the administered nanoparticles from the bloodstream. Thus, upon repeated administration of any compounds, their effects on liver functioning need to be assessed. In the present study, the effects of BaBG on hepatic functioning were evaluated by measuring the level of AST, ALT, and ALP in serum (represented in **Table 4.4)** and compared with the 45S5 treated rats. Statistical analysis by one-way ANOVA exhibited no significant differences in the level of AST, ALT, and ALP among the groups ($p > 0.05$) in 45S5-treated male and female rats when

compared to the control. This result substantiates the histological analysis of the liver section of 45S5 treated rats that showed intact architecture with normal hepatocytes (**Figure 4.11)**. Similar to our observation, it has been reported earlier that silica nanoparticles also did not cause any substance-induced toxicity, as evident from the unchanged level of liver enzymes in rodents (Yun, Kim et al. 2015, Cabellos, Gimeno-Benito et al. 2020). Likewise, in the case of BaBG, there were no significant differences in the level of AST, ALT, and ALP among the groups ($p > 0.05$) in male rats at all the doses tested. Thus, this confirms that BaBG did not lead to hepatotoxicity after their repeated oral administration in male rats (Program 1994). However, statistical analysis by one-way ANOVA showed a significant increase in the level of ALT among the groups ($[F(_{6,34}) = 3.436; p < 0.05]$ when compared to the female control rats. This gender-specific effect may be because the liver is a sexually dimorphic organ responsive to sex hormones (Buzzetti, Parikh et al. 2017).

Further, creatinine, a metabolic byproduct generated in the body to maintain a continuous supply of energy to the muscles, and these nitrogenous waste products are eliminated by the kidneys. Thus, measuring creatinine level is considered an advocated index to determine the efficiency of kidneys to eliminate metal ions and uremic toxins. In the present study, there were no significant differences in the serum creatinine level of BaBG-treated rats compared to control rats and 45S5-treated group ($p > 0.05$). This finding is supported by another study where the leaching of silicon from 45S5 did not exhibit any significant changes in the creatinine level (Lai, Garino et al. 2002), indicating that kidney functions were not affected in the experimental animals. Therefore, we may conclude that repeated-dose oral administration of BaBG did not affect the renal functions in male and female rats.

CK-MB, an important clinically used diagnostic marker for cardiac muscle damage, and in the present study, statistical analysis by one-way ANOVA exhibited no significant differences in its level among the groups ($p > 0.05$). This confirms that the synthesized inorganic biomaterial (BaBG) is not cardiotoxic which substantiates the normal cardiac architecture observed after repeated-dose oral administration of BaBG (**Figure 4.12**). Furthermore, calcium, an essential element present in the body, helps in various physiological functions, and administration of BaBG did not exhibit any significant changes in the serum calcium level in male and female rats like 45S5. Thus, it can be affirmed that BGs did not affect the calcium homeostasis post-oral administration of BaBG. Hence, BGs can be considered an advanced biomaterial for effective treatment purposes with no toxic effects on the highly perfused vital organs.

Table 4.4: The effect of repeated-dose 28 days oral administration of BaBG and 45S5 (50, 500, and 1000 mg/kg b.w.) on serum concentration of calcium, creatinine, CK-MB, ALP, ALT, and AST of male and female rats at the end of the experimental protocol.

Enzymes	ALP (KA/dL)	ALT (U/L)	AST (U/L)	Creatinine (md/dL)	Calcium (mg/L)	CK-MB (U/L)
(A) Male rats						
Control	12.231 ± 1.56	43.592 ± 2.453	125.893 ± 5.940	0.715 ± 0.0805	102.431 ± 6.689	696.204± 13.152
$45S5_{50}$	12.729 ± 1.799	44.220 ± 4.003	129.471 ± 4.992	0.708 ± 0.0457	105.202 ± 3.201	714.315 ± 19.237
$45S5_{500}$	12.817 ± 0.948	46.013 ± 3.177	132.760 ± 7.801	0.742 ± 0.0931	106.11 ± 5.316	722.082 ± 17.438
$45S5_{1000}$	12.173 ± 0.656	46.946 ± 1.351	135.616 ± 5.073	0.757 ± 0.069	109.887 ± 5.912	729.734 ± 20.123
$BaBG_{50}$	12.652 ± 1.648	42.289 ± 1.705	127.466 ± 4.831	0.698 ± 0.0742	103.461 ± 8.236	705.126 ± 20.231
$BaBG_{500}$	13.143 ± 0.991	45.501 ± 2.927	130.037 ± 2.316	0.718 ± 0.0624	104.115 ± 7.103	713.441 ± 14.284
$BaBG_{1000}$	13.094 ± 1.401	43.747 ± 2.461	134.188 ± 4.668	0.732 ± 0.0873	106.783 ± 9.592	718.189 ± 13.567
(B) Female rats						
Control	12.106 ± 1.248	41.127 ± 3.176	120.983 ± 3.167	0.694 ± 0.0703	105.112 ± 8.117	682.124 ± 15.462
$45S5_{50}$	12.004 ± 0.972	40.826 ± 2.851	122.015 ± 1.445	0.685 ± 0.0814	107.347 ± 7.236	684.573 ± 16.192
$45S5_{500}$	12.49 ± 1.521	44.213 ± 2.127	125.747 ± 4.448	0.702 ± 0.0469	104. 231 ± 9.297	689.403 ± 17.703
$45S5_{1000}$	11.788 ± 1.362	46.034 ± 1.186	127.105 ± 6.149	0.722 ± 0.0602	109. 678 ± 6.167	704. 865 ± 19.042
$BaBG_{50}$	12.267 ± 0.813	42.267 ± 1.935	123.028 ± 4.002	0.690 ± 0.0832	105.526 ± 7.205	691.904 ± 11.984
$BaBG_{500}$	12.089 ± 1.308	43.139 ± 4.061	126.991 ± 3.141	0.711 ± 0.0790	109.561 ± 3.648	702.706 ± 19.301
$BaBG_{1000}$	12.105 ± 0.847	47.025 ± 3.514[a,b]	127.191 ± 2.203	0.719 ± 0.0822	113.812 ± 6.875	709.911 ± 20.443

All values are in mean ± SD (n=5 rats/ group). [a]$p<0.05$ and [b]$p < 0.05$ compared to control and $45S5_{50}$ respectively. (One-way ANOVA followed by Tukey's multiple comparison post-hoc tes

4.2.2.6. Effect of BaBG on the neurobehavioral activity during sub-acute toxicity study

The central nervous system (CNS) is an integral part of the body that controls most of the bodily functions like movement, sensations, memory, speech and appetite, and slight alteration in the nervous system can profoundly affect other body activities. Usually, the phenotypic changes in motor activity are considered the first sign of neurotoxicity in animals, and there is very little information available on the neurotoxic effects of BGs. Thus, in the present study, we have also tested the effect of oral administration of BaBG on the neurobehavioral aspects in male and female rats that directly corroborates with their effects on CNS. Statistical analysis by two-way ANOVA showed no significant differences in the grip strength, locomotor activity, retention time on the rotarod, rearing, grooming, total distance travelled, and time spent in the central space of OFT ($p > 0.05$) among groups in male and female rats compared to control (**Figure 4.7**). Evaluating motor coordination or muscle strength is essential in experimental animals during toxicity testing of newly synthesized compounds. It is generally evaluated by testing the ability of the rats to retain on the revolving rod at a fixed rpm in the rotarod apparatus (Prajapati, Garabadu et al. 2017). In the present study, it was observed that BaBG did not impair the muscle coordination like 45S5 after the sub-acute exposure in both male and female rats during the rota-rod test (data not shown); hence confirming no neurotoxic effects of 45S5 and BaBG as the loss of muscle coordination is considered as an index of neurotoxicity. Similar to our observation, Tuusa et al. (Tuusa, Peltola et al. 2008) also reported that the BG fiber, did not produce any neurological damage in the rabbits when used for the calvarial bone defect,. Furthermore, the change in neuromuscular strength is as an important indicator

of neurotoxicity and was evaluated using the grip strength test. It was observed that repeated-dose 28-days oral administration of both 45S5 and BaBG did not produce any significant changes in the grip strength score of both male and female rats at all the doses tested (data not shown). Previously, studies have also reported that oral exposure to SiO_2 and $BaSO_4$ nanomaterials did not produce any substance-related adverse effects (Buesen, Landsiedel et al. 2014). Together with the rota-rod test observation, these findings confirm that BaBG did not produce any neurobehavioral deficits in the treated rats of both sexes.

Moreover, the neurological safety profile of BaBG was further evaluated by analyzing their effects on spontaneous locomotor activity using an actophotometer. Spontaneous locomotor activity is also considered an index of wakefulness or alertness of mental activity, and changes in it can be observed as motor dysfunction (Prajapati, Garabadu et al. 2017). In the present study, there was no significant change in the locomotor activity of the treated rats at all doses tested compared to the control rats and 45S5-treated rats ($p > 0.05$) (data not shown). Similarly, in the OFT, the total distance covered by the experimental rats (BaBG) indicates their voluntary locomotor activity, and statistical analysis by two-way ANOVA showed no significant changes in it among the groups compared to control and 45S5. Thus, the total distance covered by the male and female rats (track plot shown in **Figure 4.9**) corroborates the spontaneous locomotor activity observed in the actophotometer test.

Further, anxiety induced by substances can be evaluated by the increase in grooming behavior and aversion from the central area in OFT (Bronstein 1972), and in the present study, sub-acute oral administration of BaBG did not produce anxiety-like symptoms in both male and female rats. There were no significant differences in the grooming

behavior and time spent in the central square among the groups compared to the control animals and 45S5 treated rats in both male and female rats. Additionally, rearing (standing on hind limbs) in a novel environment is an important parameter that signifies learning and memory (Lever, Burton et al. 2006) were not affected by BaBG. Hence, based on the neurobehavioral studies, the neurological safety profile of BaBG as well as 45S5 can be affirmed. To the best of our knowledge, this is the first time the effect of inorganic biomaterials (45S5 and BaBG) on neurobehavioral paradigms has been studied preclinically.

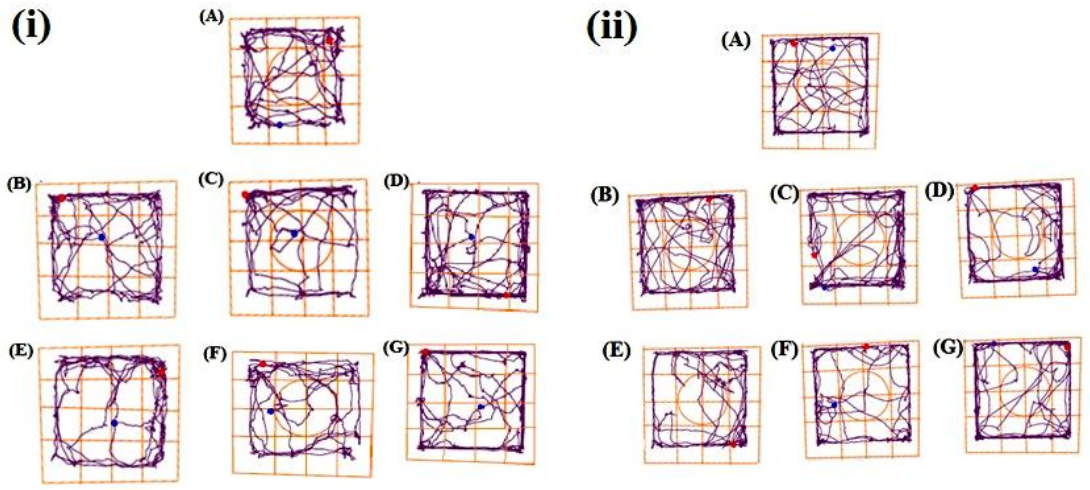

Figure 4.9: Schematic representation of the track plot of (i) male and (ii) female rats respectively divided into following groups: control (A), 45S5 (B, C, D; dose: 50, 500, and 1000 mg/kg b.w. respectively), and BaBG (E, F, G; dose: 50, 500, and 1000 mg/kg b.w. respectively) recorded during 5 min test sessions on day 28 (ANYMAZE).

4.2.3.7. Histological analysis of various organs of BaBG treated rats during the sub-acute toxicity study

Nanomaterials are widely used in biomedicine; however, most inorganic biomaterials tend to accumulate in the liver and spleen with delayed clearance. Hence, histopathological analyses were performed in vital organs like the brain, lungs, heart, spleen, and metabolic and excretory organs, such as the liver and kidneys. In the present

study, the histological section of brain tissues of repeated-dose treated experimental rats exhibited intact architecture with no histopathological changes, as depicted in **Figure 4.10**. The photomicrographs exhibited pyramidal cells with basophilic cytoplasm and a larger nucleus. Furthermore, there was the presence of granular cells having large vesicular nuclei as observed similarly in the control group. Thus, it can be affirmed that BaBG had no adverse effect on the brain which was also substantiated from the neuro-behavioral studies performed during the sub-acute toxicity study. Likewise, light microscopic examination of the lungs of the control and treated groups (BaBG and 45S5) exhibited oval-shaped alveoli with very thin epithelial walls surrounded by capillaries (as shown in **Figure 4.11**) that aid in gaseous exchange. Further, no edema or alveolar hemorrhage was observed without any sign of infiltration of the inflammatory cells in the alveolar cavities of both 45S5 and BaBG-treated groups. Besides, 28-days repeated dose oral administration of BaBG also did not impart any toxic effects on the highly perfused organs like the heart, as evident from the normal histological structure of the cardiac muscle (**Figure 4.12)** (Fu, Liu et al. 2012). Moreover, **Figure 4.12** exhibited the presence of oval nuclei without any granular or vacuolar degeneration of the myofibrils. Hence, it can be confirmed from the histopathological studies that BaBG did not impart any toxic effects on the vital organs, which acts as a supporting piece of evidence for biochemical and hematological observations.

In addition, the liver is a metabolic organ essential for the metabolism of drugs and may cause infiltration of leukocytes if the accumulated nanoparticles are not excreted effectively (Sui, Zhong et al. 2016). Thus in the present sub-acute toxicity study, the effects of BGs on the microscopic structure of the liver were analyzed. The 45S5-treated

male and female rats showed normal hepatocytes with intact nuclei arranged in the form of branched lobules embedded in connective tissue without any congestion of the central vein or dilation of the sinusoid (**Figure 4.13**). This corroborates with the serum enzyme level of hepatic markers, i.e., AST, ALT, and ALP (**Table 4.4**), and thus indicates the non-toxic nature of 45S5 on hepatocytes (de Souza, Lopes et al. 2020) as similarly observed in BaBG treated male rats (Buesen, Landsiedel et al. 2014). However, in the BaBG-treated female rats, there was very mild lymphoid infiltration in the portal areas without any sinusoid dilation or changes in the structure of hepatocytes.

Kidneys are the filtering organs that remove the wastes (toxins) from the body; hence they are susceptible to various toxicants (Krishna, Jaiswal et al. 2020). In the sub-acute toxicity study of BaBG, there were no substance-induced histological anomalies observed (**Figure 4.14**) as in the case of 45S5 treated rats (de Souza, Lopes et al. 2020). The treatment groups (45S5 and BaBG) and the control animals of both sexes exhibited normal histological architecture of the glomeruli and Bowman's capsule. Further, the PCT and DCT were intact without any sign of renal toxicity in all groups, supported by the biochemical parameter (creatinine), an important indicator of renal function. Similarly, there were no abnormal histopathological changes in the splenic tissues post-repeated dose administration of 45S5 and BaBG in male and female rats compared to the control rats **(Figure 4.18)** (Yinhua, Jianbo et al. 1993). Therefore, we can deduce that BaBG are non-toxic similar to 45S5 and do not affect the functioning of vital organs.

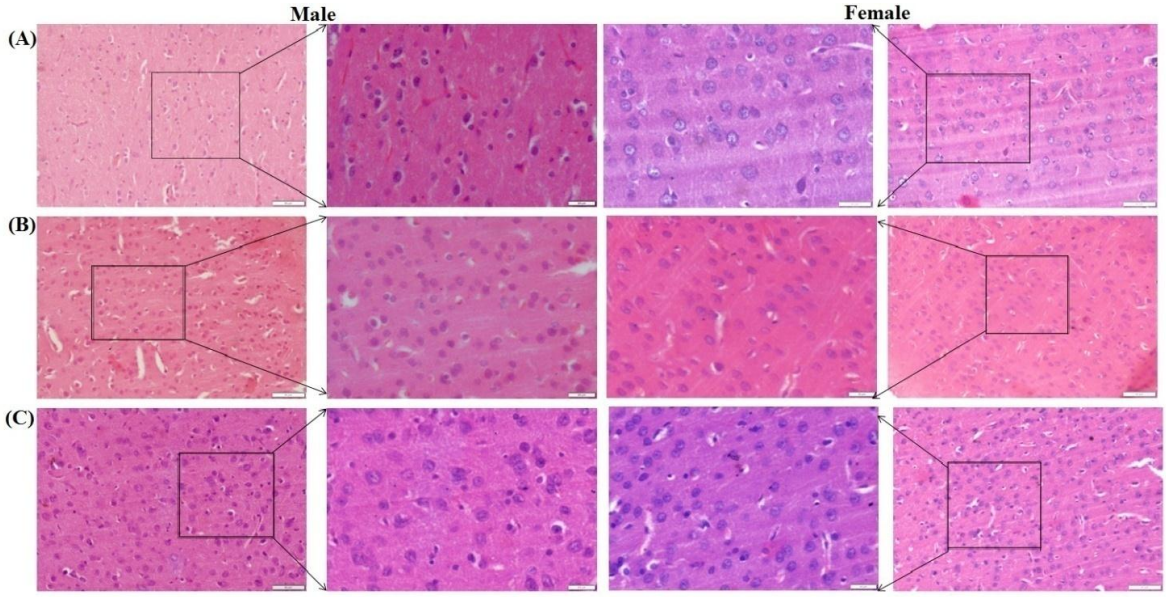

Figure 4.10: Histological analyses of the brain tissue of control (A), 45S5, and BaBG (B and C respectively; dose: 1000 mg/kg b.w.) treated male and female rats after repeated 28 days oral administation. Bar: 50 µm and 20 µm. Hematoxylin and eosin staining.

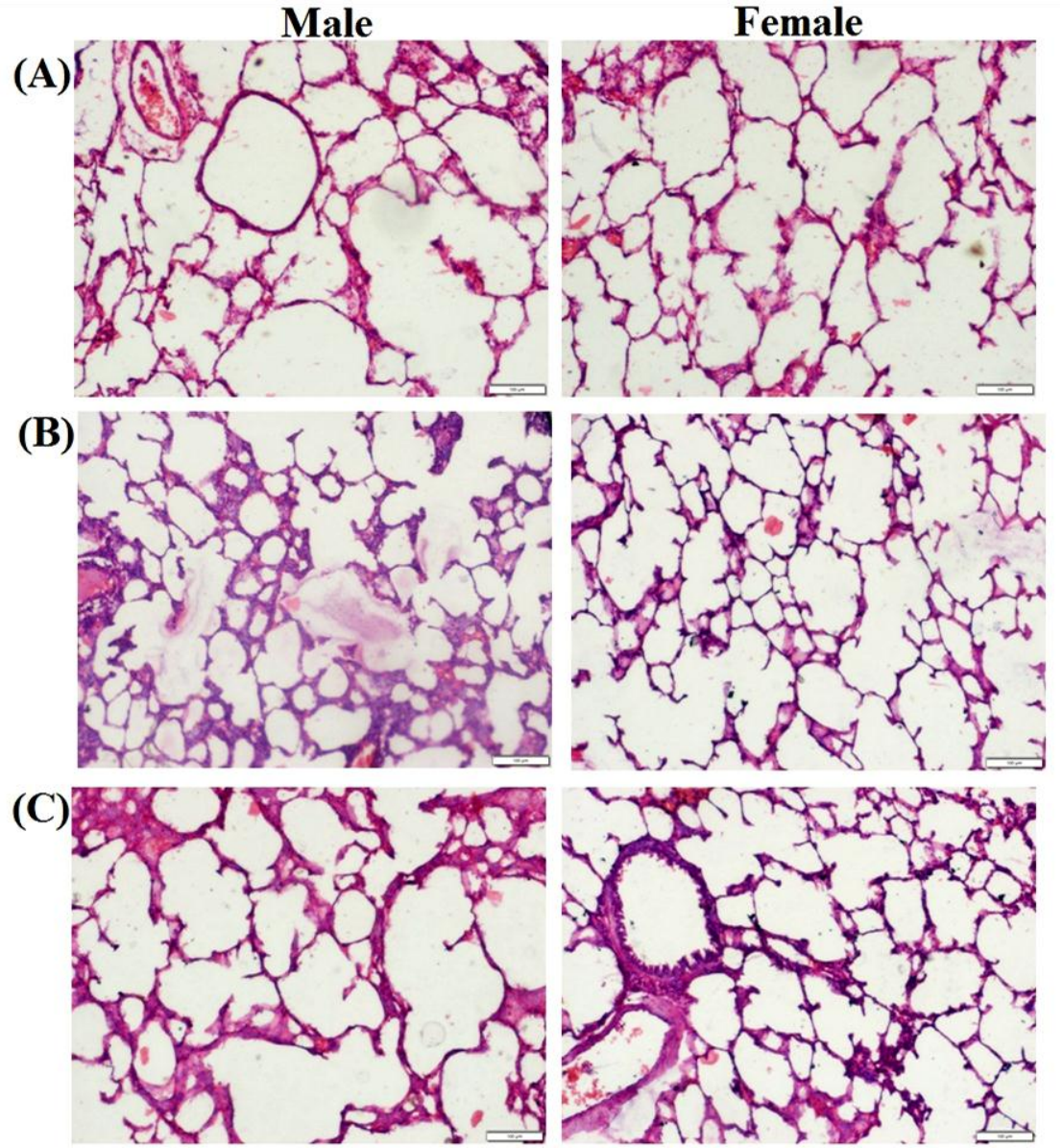

Figure 4.11: Histological analyses of the lungs of control (A), 45S5, and BaBG (B and C respectively; dose: 1000 mg/kg b.w.) treated male and female rats in subacute toxicity study. 45S5 and BaBG treated rats exhibited normal appearance of alveoli with thin epithelial walls surrounded by capillaries similar to the control rats. Edema or alveolar hemorrhage in the alveolar cavities was also not observed in the treatment groups. Bar: 100 µm. Hematoxylin and eosin staining.

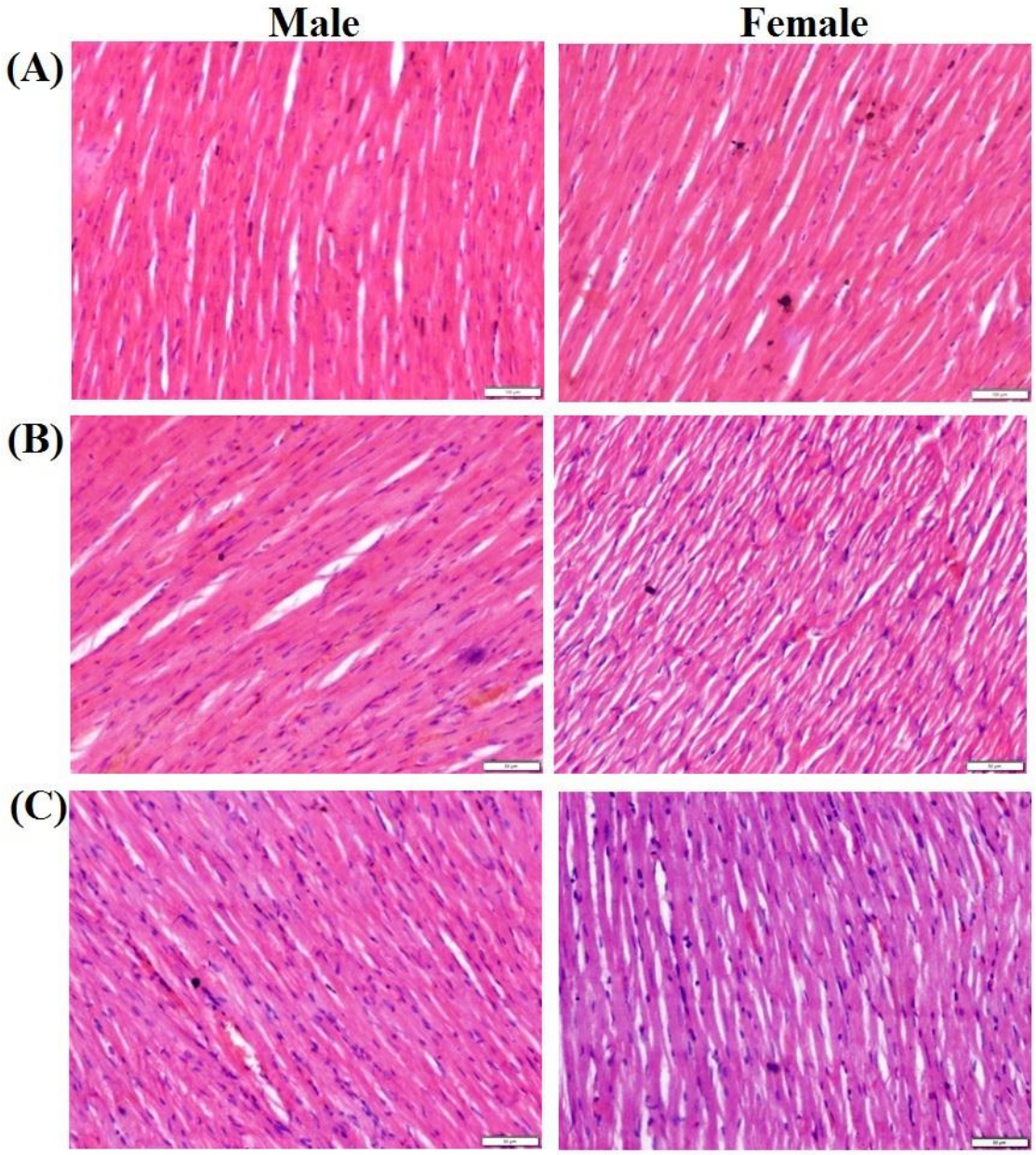

Figure 4.12: Histological analyses of the heart of control (A), 45S5, and BaBG (B and C respectively; dose: 1000 mg/kg b.w.) treated male and female rats. The heart of 45S5 and BaBG treated rats exhibited normal morphology with oval and centrally located nuclei in cardiomyocytes regularly arranged in myofibres. No vacuolar degeneration of the myofibrils was observed in 455S5 and BaBG rats. Bar: 50 µm. Hematoxylin and eosin staining.

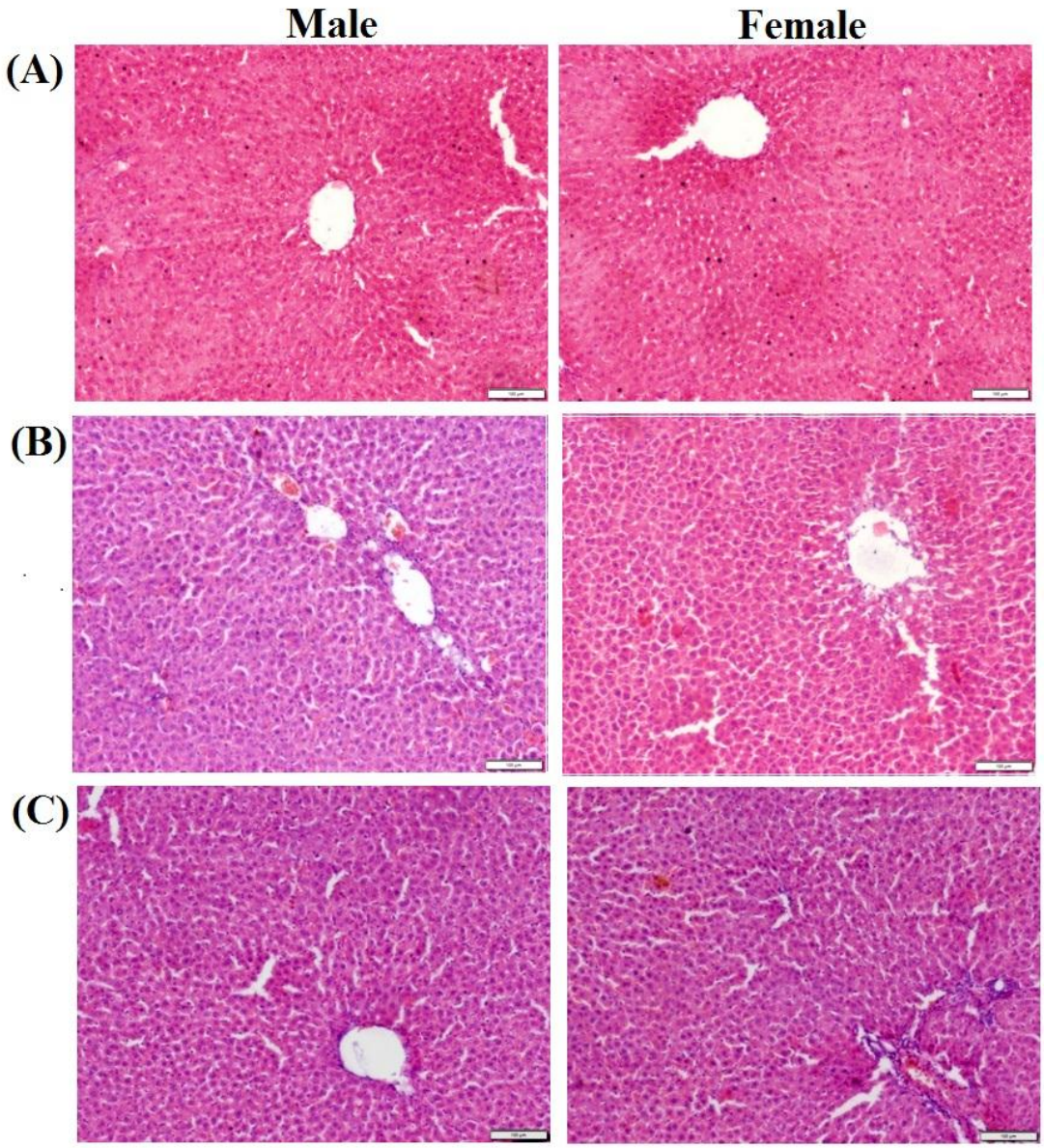

Figure 4.13: Effect of repeated-dose 28 day oral administration of BaBG and 45S5 on microstructure of liver (dose: 1000 mg/kg b.w.) in male and female rats. (A) Control and (B) 45S5 treated male and female rats exhibited normal hepatocytes with intact vesicular nucleus radiating from the central vein surrounding the portal tract. No congestion of the central vein or dilation of the sinusoid was observed. (C) The female BaBG treated rats showed mild lymphoid infiltration in the portal areas without any sinusoid dilation. Bar: 100 µm. Hematoxylin and eosin staining.

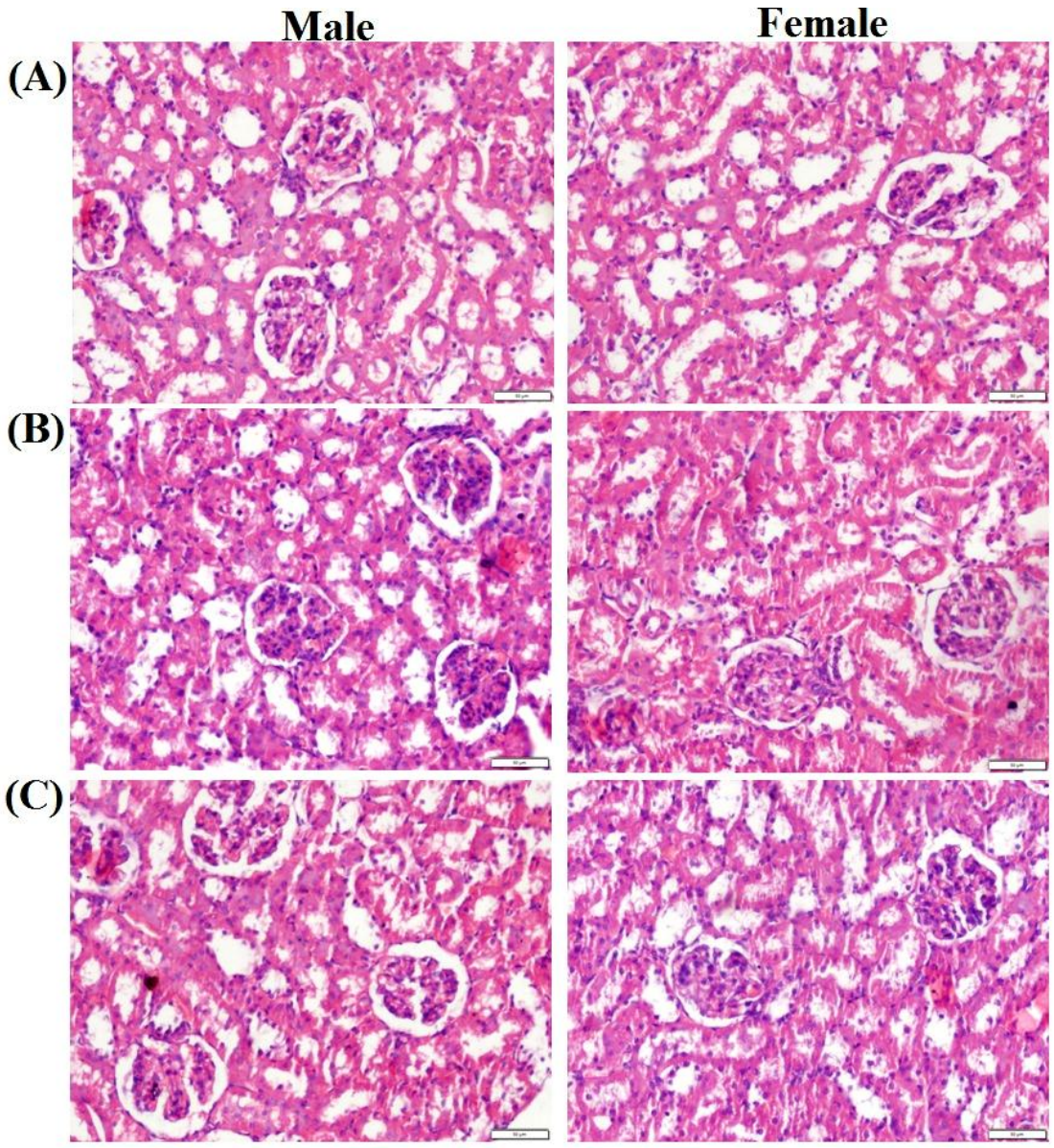

Figure 4.14: Effect of repeated-dose 28 day oral administration of BaBG and 45S5 on microstructures of kidney (dose: 1000 mg/kg b.w.) in male and female rats. The cross-section of (A) control, (B) 45S5, and (C) BaBG treated male and female rats exhibited normal architecture of glomeruli, bowman's capsule, and renal corpuscles with intact proximal and distal convulated tubules. Bar: 50 µm. Hematoxylin and eosin staining.

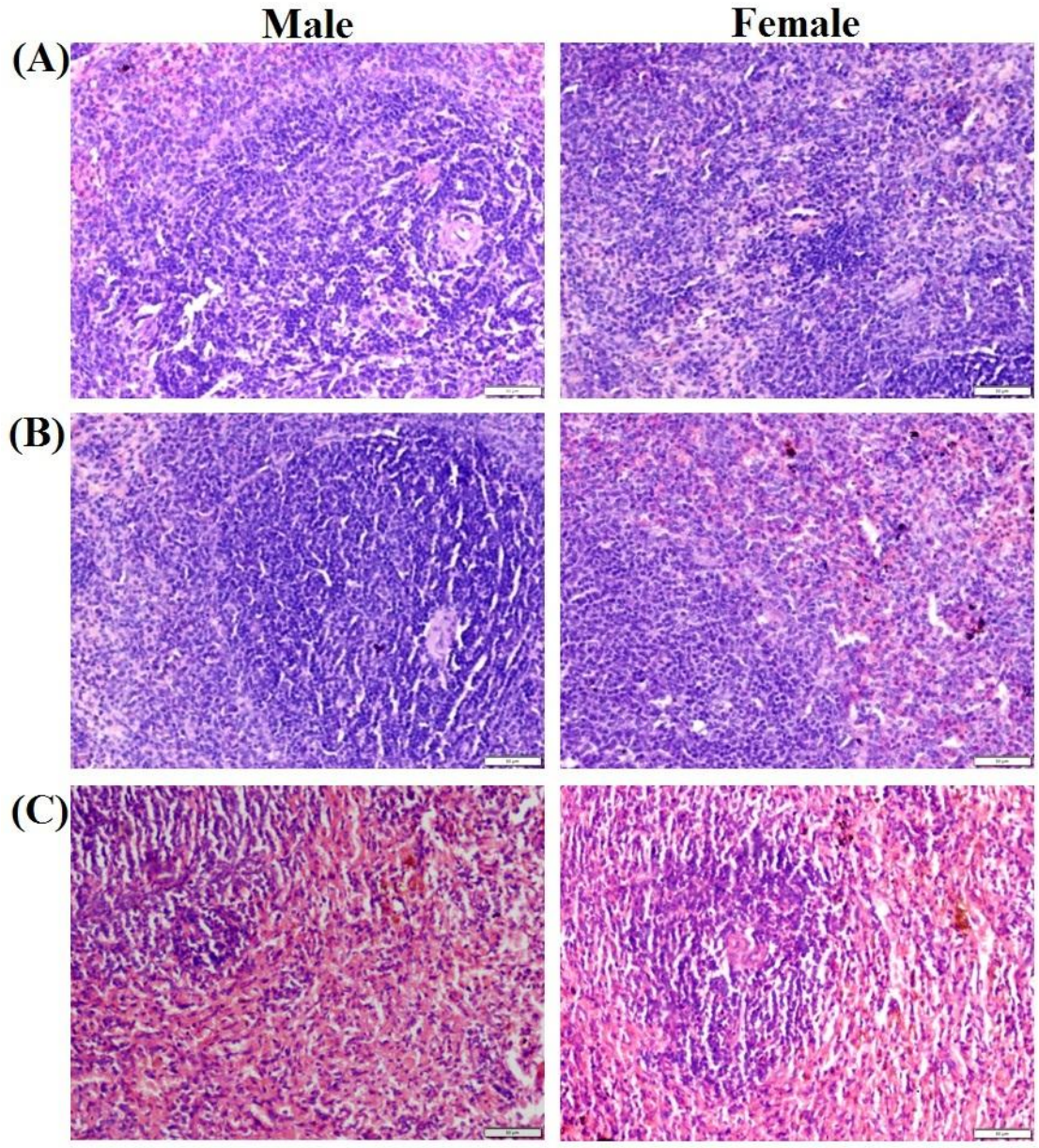

Figure 4.15: Effect of repeated-dose oral administration of BaBG and 45S5 (dose: 1000 mg/kg b.w.) on spleen of male and female rats. The cross-section of (A) control, (B) 45S5, and (C) BaBG treated male and female rats showed normal appearance of the lymphatic nodules of white pulp, splenic cords of red pulp, and the spleen trabecula. Bar: 50 µm. Hematoxylin and eosin staining.

4.3. Summary

In the current study, the acute and sub-acute toxicity of BaBG was evaluated orally in rats according to the OECD guidelines and compared to 45S5 treated rats. There was no observed mortality without any signs of toxicity during the acute toxicity study, and the LD_{50} of both the BGs was more than 2000 mg/kg b.w. Further, the organ coefficients and the biochemical parameters (AST, ALT, ALP, creatinine, and CK-MB) revealed no possible toxic effects of BaBG on the functioning of vital organs. Similarly, the safety profile of BaBG was further confirmed by the hematological parameters and histological examinations during the sub-acute toxicity study. Moreover, the neurological safety profile of BaBG was also established from the neurobehavioral studies as there were no changes in muscle coordination, spontaneous locomotion, or observed anxiety-like behavior in the treated rats as observed in the 45S5 group. Therefore, BaBG is safer and biocompatible without any significant toxic effects observed preclinically.

Chapter 5

To evaluate the temporal changes in the intracellular calcium and S100b protein levels in the pathophysiology of the CCI-induced neuropathic pain in rats

5. Introduction

Neuropathic pain (NP) is a critical and complex illness often occurring from injury to the somatosensory nervous system that eventually results in the development of multiple enduring and intricate pain syndromes (Colloca, Ludman et al. 2017). The assortment of symptoms commonly observed clinically may occur spontaneously or triggered, resulting in an increased sensitivity to pain (hyperalgesia) along with the perception of painful burning, stabbing, or electric shock-like sensations (Bannister, Sachau et al. 2020). Reportedly, the complex neuropathological mechanisms that underlie the development of NP involve sensory nociceptors and spinothalamic tract sensitization, resulting in peripheral and central sensitization (Meacham, Shepherd et al. 2017). Further, dysregulation of ion channels is reported to enhance the primary afferent neuron excitability, causing ectopic action potentials in the peripheral nervous system (PNS) (Baron 2006). All these events cause secondary neuroplastic changes in the spinal cord (SC) and brain multi-receptive neurons along with dampening the descending inhibitory pathways (Woolf and Mannion 1999). Currently, the therapeutic first-line strategies for managing chronic NP clinically include calcium channel blockers (CCBs) such as pregabalin and gabapentin (Tong, Zhengyao et al. 2021). However, its effectiveness is hindered as the pathophysiology of NP is complex involving overlaying of ion channel modulation with neuroimmune interactions (Vicario, Turnaturi et al. 2020). Besides, there is also a lack of comprehensive knowledge on the temporal changes in the ionic concentration post-injury. Therefore, there is a need to monitor the time-dependent changes in the calcium concentration $(Ca^{2+})_i$ in NP in order to identify the optimal timeframe for initiating pharmacological intervention as the time of treatment commencement is important for better efficacy.

Dysregulation of calcium homeostasis following neuronal injury is a crucial factor that contributes to the development and maintenance of NP (Siau and Bennett 2006, Cui, Wu et al. 2021). Studies have reported alteration in the voltage-gated calcium channel (VGCC) expression, leading to an elevation in the inflow of Ca^{2+}, which in turn mediates a variety of neuronal processes, including membrane excitability, neurotransmitter release, synaptic plasticity along with the release of pro-inflammatory cytokines, resulting in an exacerbation of pain sensation following sciatic nerve (SN) damage (Berridge, Lipp et al. 2000, Yaksh 2006). Similarly, the SC also exhibit enhanced $(Ca^{2+})_i$ due to upregulation in the VGCC activity in various animal models of NP (Kawamata and Omote 1996, Tilley, Cedeño et al. 2022). In addition, the activation of calcium-permeable receptors, such as TRPV1, leads to an increase in $(Ca^{2+})_i$ levels, which in turn promotes neuronal hyperexcitability (Liu, Miao et al. 2023). These mechanisms synergistically amplify synaptic transmission and increase sensitivity, resulting in persistent pain. Moreover, the elevated intracellular calcium $(Ca^{2+})_i$ also stimulate many calcium-binding proteins that activate glial cells and trigger the production of pro-inflammatory cytokines and chemokines, which further heighten the sensitivity of pain pathways (Cho and Huh 2020, Jager, Goodwin et al. 2024). Therefore, it is essential to evaluate the temporal changes in $(Ca^{2+})_i$ in the animal model of NP which would provide in-depth knowledge about the role of calcium in the development of NP phenotypes.

Sciatica pain is a clinical medical ailment caused due to compression of the SN, resulting in pain that radiates down from the hip. It is characterized by paresthesia and numbness in the afflicted limb. This clinical illness is similar to the preclinical NP induced by chronic constriction injury (CCI) animal model where loose ligatures are

tied around the common SN that constricts the nerve without altering the epineural blood flow (Bennett and Xie 1988). Compelling clinical evidence has highlighted increased levels of calcium-binding proteins i.e., S100 in the cerebrospinal fluid of patients suffering from sciatica (Brisby, Olmarker et al. 1999, Skouen, Brisby et al. 1999). In parallel, a recent study also found that S100b was elevated in individuals suffering from trigeminal neuralgia, representing all of the symptoms observed in people suffering from NP (Ito, Seki et al. 2023). Similarly, preclinically, there are reports on the enhanced expression of S100b in the SC post-spinal nerve transection with the rodents displaying behavioral hypersensitivity (Tanga, Raghavendra et al. 2006, Chen, Huang et al. 2020). Based on the above clinical and preclinical consolidated evidence, S100b is recognized as a pathophysiological marker for persistent pain caused by nervous system damage. However, there is no information on the time-dependent changes in S100b in NP. Hence, the aim of the present study was to evaluate the temporal changes in $(Ca^{2+})_i$ level as well as calcium-binding protein (S100b) in rats with CCI-induced NP. This analysis will provide valuable insights into the dynamics of disease pathophysiological progression and also will assist in identifying the optimal timing for interventions.

To validate our hypothesis, in the present study, NP was induced by CCI of SN in rats and the establishment of the symptoms of pain was confirmed by various behavioral tests. The temporal changes in the intracellular calcium $(Ca^{2+})_i$ and S100b levels in the SN and SC post-peripheral nerve injury were elucidated. Following this, the validation of the involvement of S100b in the development and progression of NP was performed for the first time using a specific S100b inhibitor i.e., pentamidine in the CCI-induced NP model. To evaluate the sensory and motor abnormalities associated with NP, we

employed a range of behavioral tests to assess the effect of pentamidine. Then the effects of pentamidine on the $(Ca^{2+})_i$ and S100b level were evaluated post-CCI injury. In addition, we assessed the impact of pentamidine on the level of pro-inflammatory cytokines. We also quantified the expression levels of the markers of astrocytes and microglial activation i.e., GFAP and Iba-1 in SN and SC post-SN injury and the effects of pentamidine on them. To investigate the axonal damage, we performed analyses involving NF-L-positive staining of SN. Moreover, we explored the alterations in the neuronal morphology in the CCI model and evaluated the effects of specific S100b inhibitor on them using Golgi-Cox staining. Additionally, we quantified myatrophy using hematoxylin and eosin staining in this model and evaluated the effects of pentamidine on it. **Figure 5.1** presents a graphical representation depicting the schematic diagram outlining the proposed hypothesis concerning the molecular mechanism underlying the pathogenesis of NP in a rat model induced by CCI of SN.

Hypothesis

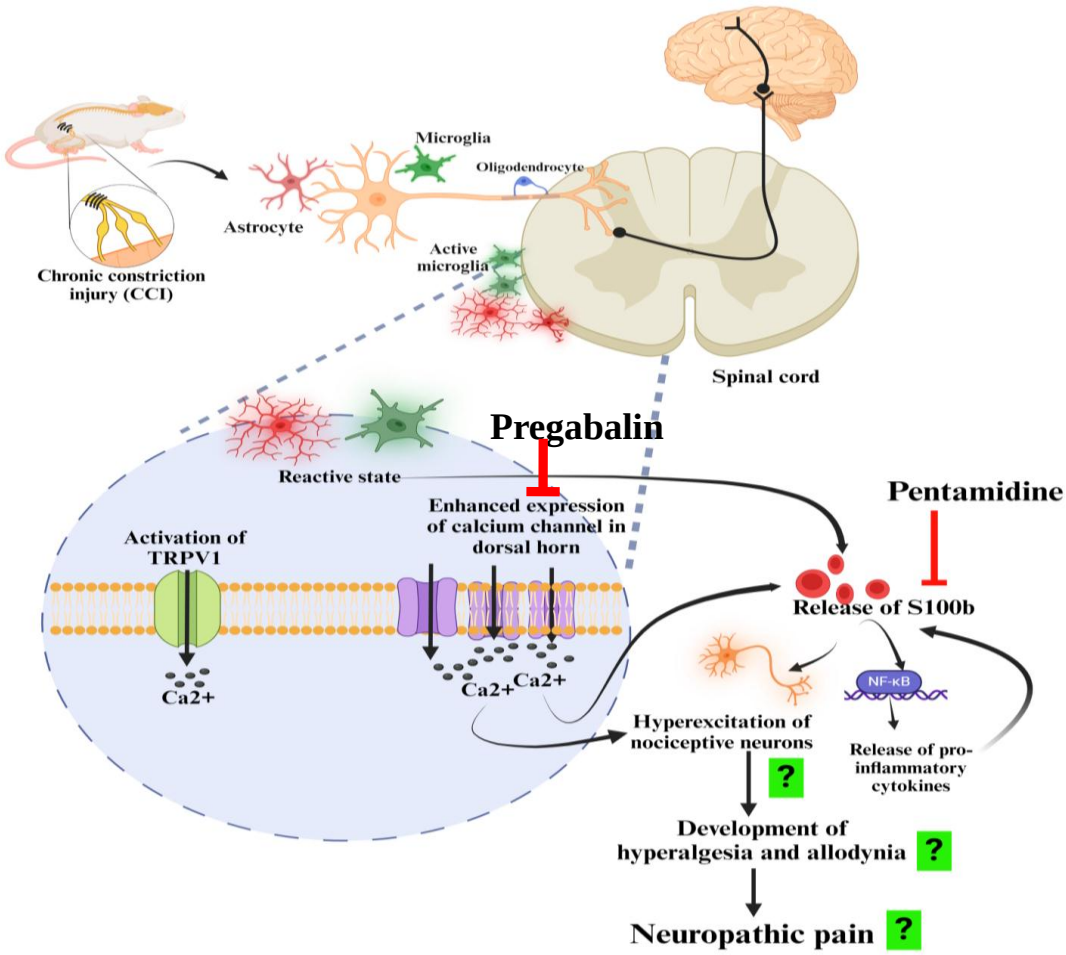

Figure 5.1. presents a graphical representation depicting the schematic diagram outlining the proposed hypothesis concerning the molecular mechanism underlying the pathogenesis of NP in a CCI-induced NP rat model. The injury to the sciatic nerve (SN) leads to the development of central sensitization due to upregulation in the expression of calcium channels ($Ca_v2.2$) in the dorsal horn of the spinal cord (SC). Besides, there are also enhanced expression of heat-sensing TRPV1 channels in the SC. Upregulation in the expression of these channels results in an increase in the influx of calcium ions leading to hyperexcitation of the nociceptive neurons and the development of NP phenotypes. In addition, the resident immune cells of CNS i.e., glial cells (astrocytes and microglia) get activated post-CCI leading to an increase in the release of calcium-binding proteins i.e., S100b. S100b gets activated in the presence of calcium ions causing the release of pro-inflammatory cytokines and progression of NP. Therefore, the temporal changes in the intracellular calcium and S100b protein level will help to identify the pharmacological window of oppourtunity. Besides, to validate the the role of S100b in the pathogenesis and progression of NP in this model, we have used a specific S100b inhibitor i.e., pentamidine to evaluate its effect on NP phenotypes.

5.1. Materials and methods

5.1.1. Materials

The molecular biology kits and reagents used in the qPCR experiment include TRI reagent & DEPC that was sourced from Sigma. The revert aid cDNA synthesis kit (Thermo Scientific), TURBO DNA-*free*^{TM} (Ambion), TURBO DNA-free™ Kit (Invitrogen), Maxima SYBR Green/ ROX qPCR master mix 2X and primers (Eurofins Genomics India), Prestained protein MW marker (Puregene) and 100bp DNA marker (MBI Fermentas), 6X DNA loading buffer (Thermo Scientific), and RNAase cocktail (Invitrogen) was used in this study. All the primer sequences used (**detailed in Table 5.1**) were sourced from Eurofins Scientific. Triton X-100, Dabco, 3-aminopropyltriethoxysilane, and formaldehyde were acquired from Sigma, USA. Tween-20 was purchased from Merck and DAPI was obtained from SRL. Fura2 AM was purchased from ChemCruz. For the study, the ELISA kits used were from Krishgen Biosystems. The primary antibodies used in the experiment are GFAP (No.: ab7260, Abcam), S100b (No. E-AB-60087; Elabscience Biotechnology Co., Ltd., USA), NF-L (No. CST-2837T; Cell Signaling Technology), and Iba1 (No. 019-19741; FUJIFILM Wako Chemicals U.S.A.). The secondary antibodies used are goat anti-rabbit IgG FITC (ab6717; Abcam) and goat anti-rabbit IgG TRITC (ab6718, Abcam).

5.1.2. Experimental animals and their ethical statement

Adult male Wistar albino rats of weight 200±20 g was used in the experiment that was obtained from the Central Animal House, IMS-BHU, Varanasi, India. Before starting the experiment, the rats were acclimatized for a week at an ambient and controlled temperature of 25±1°C with a 12-h light and dark cycle. The experimental animals had

ad libitum access to standard laboratory diet and water throughout the experiment. The rats were housed in cages (430 x 270 x 150 mm) with corn cob bedding. All the efforts were made to minimize the number of animals used during the experiment. The studies were performed in accordance with the guidelines of the Committee for the Control and Supervision of Experiments on Animals (CCSEA), Government of India and "Care and Use of Experimental Animals" (Vol.1, 2nd ed., 1993, and Vol.2, 1984) guidelines of National Institute of Health, U.S.A. The experimental protocol for the present study was approved by the Institutional Animal Ethical Committee (Ref No. IIT(BHU)/IAEC/2022/038 and IIT(BHU)/IAEC/2023/II/027).

5.1.3. Chronic constriction injury (CCI) model of Neuropathic pain

The NP was induced in the rats by CCI of the sciatic nerve (Bennett 1993). The experimental animals were anaesthetized intra-peritoneally using ketamine (80 mg/kg) and xylazine (10 mg/kg). Once the surgical level of anesthesia was attained, the rats were placed on the thermo-regulated heating mat maintained at 37°C. Then the skin of the right leg was shaved and sterilized and an incision parallel to the femur was made. The sciatic nerve was exposed by a gluteal muscle incision. Around 10 mm of the sciatic nerve proximal to the trifurcation was freed from the surrounding connective tissue and four loose ligatures (silk 4/0; Ethicon, USA) were tied with a gap of 1 mm around the nerve. The constriction of the sciatic nerve while tying the ligatures was done till a brief twitch was observed to prevent obstruction of the epineural blood flow. Then the muscle was sutured using 6/0 reabsorbable suture and the animals were kept under post-operative care. In order to limit the local infection, an iodine solution was applied prior to and after the suturing of the incision (**Figure 5.2)**.

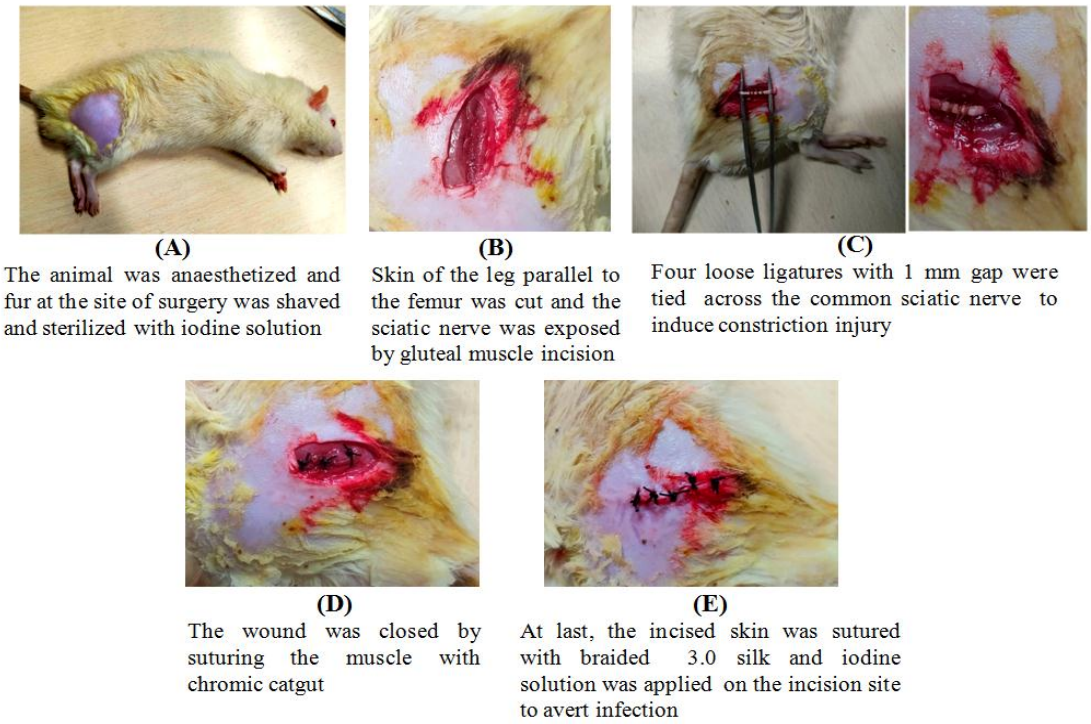

Figure 5.2: Schematic representation of the experimental protocol followed for the CCI-induced neuropathic pain model and the behavioral assessment of the symptoms developed post-surgery.

5.1.4.1. Animal experimental design for the temporal study to measure the changes in the intercellular calcium $(Ca^{2+})_i$ and S100b level

G*power analysis was conducted prior to designing the experimental protocol to determine the proper sample size, ensuring that the type I and II errors are kept under the acceptable threshold as suggested by Cohen (Cohen 1988). All the Wistar rats were weighed and were randomly divided into groups based on the time points when the rats were euthanized i.e., (i) D-0, (ii) 0.25, (iii) 0.5, (iv) 1, (v) 3, (vi) 7, (vii) 14, and (viii) 21 days post-CCI injury using the randomization technique. Each group had four animals (n= 4 rats/ group. NP was induced by CCI and behavioral assessments (hot-plate test, Randall Selitto test, acetone drop test, and BBB (Basso, Beattie, and Bresnahan) test) were performed before the surgery (D-0) and on days 3, 7, 14, and 21 post-surgery to access pain along with the motor and sensory deficits developed. On

the above-mentioned time intervals, the anaesthetized animals were sacrificed by decapitation (3% v/v isoflurane inhalation; R620 veterinary anesthesia machine, RWD life science, San Diego, USA). The SN of the ipsilateral side of the leg and SC were harvested. The dissected tissues were immediately stored at -80 °C until further research. The tissues collected were processed for biochemical analysis to measure the $(Ca^{2+})_i$ and S100b protein levels (**Figure 5.3)**.

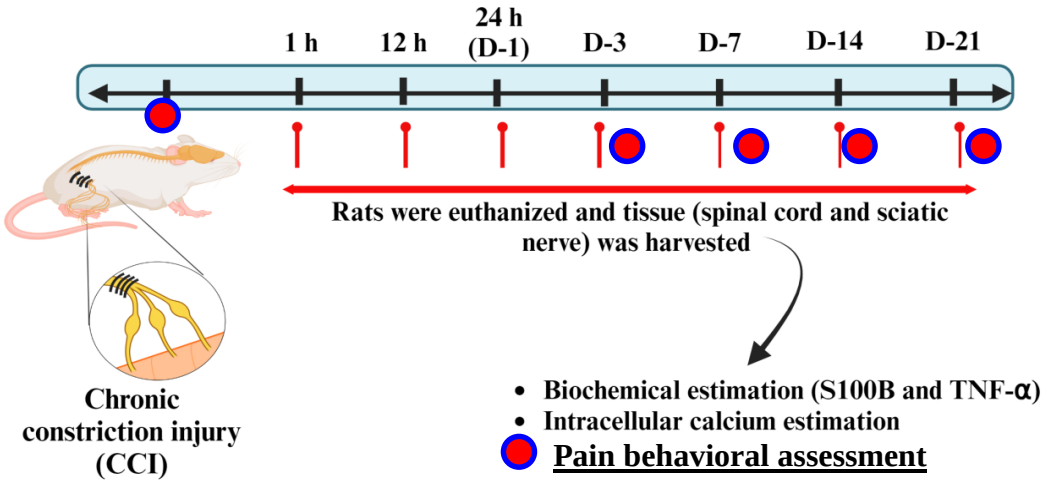

Figure 5.3: Schematic representation of the experimental protocol followed for the temporal study performed to measure the intracellular calcium and S100b level in the CCI-induced neuropathic pain model.

5.1.4.2. Animal experimental design for validation of the role of S100b in the pathogenesis/progression of NP

G*power analysis was conducted prior to designing the experimental protocol to determine the proper sample size, ensuring that the type I and II errors are kept under the acceptable threshold as suggested by Cohen (Cohen 1988). The current research consisted of 5 groups and by using A priori power analysis and ANOVA (repeated measures within-between interactions) statistical test, the minimum required sample size was determined to be 12. Consequently, we selected 12 male Wistar rats for each

group (n=12 rats/ group). All the Wistar rats were weighed and were randomly divided into five groups i.e., control, sham, CCI, CCI + pentamidine (10 mg/kg; i.p.), and CCI + pregabalin (30 mg/kg; p.o.) using the randomization technique. NP was induced by CCI and behavioral assessments like the hot-plate test, Randall Selitto test, acetone drop test, cotton swab test, Rota rod test, sciatic functional index (SFI), and BBB (Basso, Beattie, and Bresnahan) test) were performed before the surgery (D-0) and on days 7, 14, and 21 post-surgery to assess pain along with the motor and sensory deficits developed. On day 21, following the behavioral experiments, the animals were anaesthetized and sacrificed by decapitation. Then SN and SC were harvested and were immediately stored at -80 °C until further research (**Figure 5.4)**.

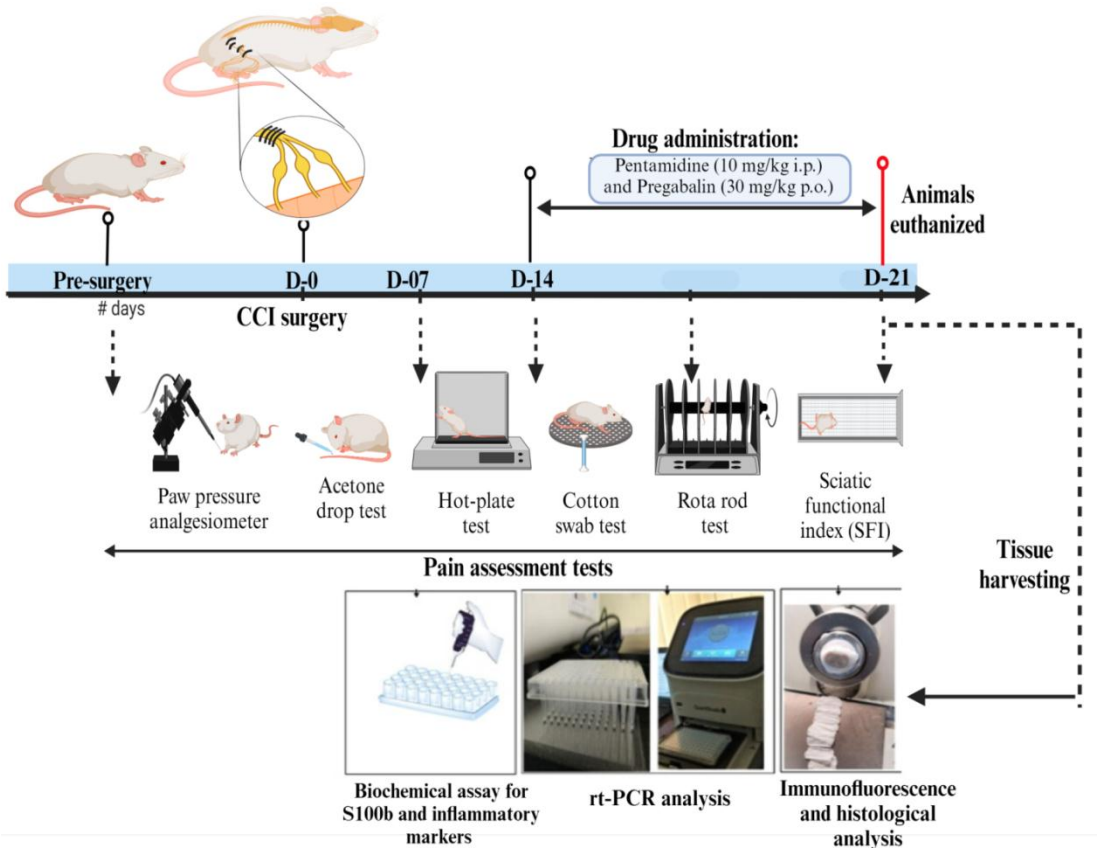

Figure 5.4: Schematic representation of the experimental protocol followed for validation of the role of S100b in the pathogenesis/progression of NP in the CCI-induced NP model in rats.

5.1.5. Behavioral analysis:

The experimental animals were acclimatized to the testing environment before the baseline behavioral testing. The development of NP phenotypes was assessed on days 7, 14, and 21 post-surgery.

5.1.5.1. Thermal hyperalgesia (hot-plate test)

The development of heat hyperalgesia in rats post-surgery was assessed using Eddy's hot plate (Orchid Scientific, India) (Khangura, Bali et al. 2017). The surface of the plate was preheated and the temperature was maintained at 52.5 ± 0.5 °C. Then animals were positioned on the heated plate and the nocifensive withdrawal reflex latency like uplifting and licking the rear paw of the injured side was recorded as the nociceptive threshold. The cut-off time of 20 sec was maintained to avoid burn injury to the animals.

5.1.5.2. Cold allodynia (acetone drop test)

The development of pain sensation due to non-noxious stimuli (cold) post-CCI surgery was evaluated by the acetone drop test. In this test, rats were first acclimatized in a chamber with a mesh floor for 20 min and then 100 µL of acetone was dropped on the dorsal surface of the hind paw of the injured leg. Cold allodynia produced in response to the evaporation of acetone is indicated by the repeated withdrawal, licking, biting, or flinching of the paw. The total duration of withdrawal of the paw in the air till it was placed back on the mess surface was recorded in seconds (Khangura, Bali et al. 2017).

5.1.5.3. Mechanical hyperalgesia (Randall Selitto test)

Hyperalgesia to the mechanical stimulation was measured in terms of the response of mechanical nociceptive threshold to the pressure applied on the paw of animals using

the digital paw pressure analgesiometer (Orchid Scientific, India) based on Randall Selitto test (Randall 1957, Ferrari, Rey et al. 2022). In this test, an increasing mechanical force is applied focally to the dorsal surface of the hind paw of the injured leg using the pressure applicator until a withdrawal nociceptive response is observed. The pressure at which the rats vocalized or displayed a painful response (flinching or withdrawal reaction of the paw or leg upon stimulation) was taken as the endpoint and recorded. The nociceptive threshold was defined as the mean of 3 subsequent readings, converted to force in grams.

5.1.5.4. Dynamic mechanical allodynia (Cotton swab test)

The dynamic mechanical allodynia developed after the CCI-induced NP were detected by the cotton swab test in rats (Field, Bramwell et al. 1999). The animals were first habituated in the plexiglass chamber with mesh flooring before the test session in order to minimize the normal movements during the test period. Then using a cotton swab, the planter part of the ipsilateral hind paw of rats was stroked gently and the latency of paw withdrawal was recorded with a cut-off time of 15 sec.

5.1.5.5. Rota rod

The rotarod test has been employed for assessing rats' motor coordination capability post-surgery (Prajapati, Garabadu et al. 2017). The animals being studied are trained for consecutive two days on the Rota rod (IKON instruments, India) at the lowest speed (i.e., 5 rpm) so that they attain stable baseline performances. Then, during the test session, the speed of the rotating rod was increased to 15 rpm. The total time spent by the animals on the rod was recorded with maximum a cut-off time of 300 sec.

5.1.5.6. Sciatic functional index (SFI):

SFI was calculated using the walking track analysis in which the animals were made to walk on a straight track (8.3 X 43 cm) that was darkened at one end (de Medinaceli, Freed et al. 1982, Komirishetty, Areti et al. 2017). The SFI value ranges from 0 to -100, with an SFI value 0 means normal while -100 denotes total impairment. After two or three trials on the track, the rats were conditioned so that they walked directly to the darkened end without exploring the track. Then a piece of white paper was placed on the walking track and the hind paws of the animals were dipped in different color solutions (the normal left paw with green and the injured right paw with red). The animal was then placed at the entrance of the track and was allowed to walk over the paper. The marks on the paper were dried and the following measurements were made:

Print length (PL): The length of one foot print of normal (NPL) and experimental side (EPL).

Total spreading (TS): The linear distance between the center of first toe print and the center of fifth toe print of normal (NTS) and experimental side (ETS).

Distance between intermediary toes (IT): The linear distance between the center of second toe print and the center of fourth toe print of normal (NIT) and experimental side (EIT).

The SFI was calculated using the following formula:

$$SFI = -38.8(EPL-NPL)/NPL + 109.5(ETS-NTS)/NTS + 13.3(EIT-NIT)/NIT – 8.8$$

5.1.5.7. BBB (Basso, Beattie, and Bresnahan) locomotor test:

BBB test is normally performed to assess the deterioration of the motor function post-CCI of the sciatic nerve in rats (Basso, Beattie et al. 1995). A score of 0 to 21 is given

according to the movement of the animal by a trained observer who was blinded to the experiment. A score of 0 was awarded when there was no spontaneous movement while a score of 21 when the rats showed normal limb movement. Normally score of 14 is given to an animal which showed complete limb coordination. In this experiment, the animals under study are placed in an open circular enclosure, observed for a period of 4 min and awarded scores accordingly.

5.1.6. Gastrocnemius muscle mass assessment:

The injury of the sciatic nerve leads to atrophy of the largest muscle supplied by it i.e., the gastrocnemius muscle which was assessed using the weight ratio of the gastrocnemius muscle 14 days after the surgery (Mohammadi, Amini et al. 2012). After the animals were euthanized, the gastrocnemius muscle was dissected from the contralateral and ipsilateral sides and weighed when still wet using an electronic balance.

5.1.7. Real Time quantitative PCR

Quantitative Real-Time PCR (qRT-PCR) was performed to assess the expression of the following genes at the mRNA level: NF-κB, $Ca_V2.2$, and TRPV1. For normalization, β-actin was used as a constitutive type control.

RNA isolation

To isolate total RNA from the SC and SN, we employed TRI reagent and followed a previously established protocol (Prajapati, Ahmed et al. 2024). Specifically, the tissues were homogenized in 1 mL of TRI reagent and centrifuged at 12,000 x g for 10 min at 4 °C. The resulting supernatant was collected, and 200 µL of chloroform was added. After vortexing for 15 s, the tubes were centrifuged again at 12,000 x g for 10 min at 4

°C, leading to the separation of three distinct phases: the phenol phase (containing nucleic acids), the protein phase (chloroform), and the colorless upper aqueous phase containing RNA. The colorless phase, containing RNA, was collected, and 0.5 mL of isopropanol was added to it. Following 5-min incubation, the tube was again centrifuged at 12,000 x g for 10 min at 4 °C. The RNA pellet formed at the bottom of the tube was then washed with 75 % ethanol, air-dried, and dissolved in 60 µL of DEPC-treated water.

DNase treatment

To eliminate any potential DNA contamination, the RNA was subjected to DNase treatment using the DNA-free Ambion. For each 20 µL of RNA extract, 2.5 µL of 10X DNase buffer, 0.5 µL of DNase enzyme, and 2 µL of DEPC-treated water were added. The mixture was then incubated for 30 min at 37 °C. Subsequently, 5 µL of DNase inhibitor was added to halt the reaction. The clear aqueous phase obtained by centrifugation at 10,000 x g at room temperature was used for RNA quantification.

cDNA synthesis

The cDNA synthesis was performed using Revert Aid's first-strand cDNA synthesis kit(Thermo Fisher Scientific, USA), utilizing RNA samples with an A260/A280 ratio ranging from 1.8 to 2.0. Initially, a reaction mixture was prepared by adding 4 µg of RNA, 1 µL of random hexamer primer, and DEPC-treated water, resulting in a total volume of 12 µL. After a brief centrifugation, the following components were added: 4 µL of 5X reaction buffer, 1 µL of RiboLock™ Ribonuclease Inhibitor (20U/µL), 2 µL of 10 mM dNTP mix, and 1 µL of reverse transcriptase, resulting in a final volume of 20 µL. The reaction mixture was incubated at 25 °C for 5 min, followed by cDNA strand

synthesis at 42 °C for 60 min. To terminate the reaction, the mixture was heated at 72 °C for 5 min. Finally, the synthesized cDNA was stored at -80 °C for future use.

Real time qPCR

The real-time qPCR was done with an ABI Prism 7500 Sequence Detection System (PE Applied Biosystems, CA, USA). The PCR reaction mixture, with a total volume of 20 μL, was comprised of 1 μL of sample cDNA (diluted 1:10), 1 μL of 10 pmol forward and reverse primers, and 10 μL of 2X SYBR Green/ROX qPCR Master Mix (Thermo Fisher Scientific, USA). The mixture was then brought to the final volume using RNase-free water. The PCR conditions involved an initial denaturation step at 95 °C for 30 s, followed by 40 cycles of amplification at 95 °C for 5 s, and 60 °C for 20 s. The amplification of each cDNA was confirmed through melting curve analysis. For data analysis, the ΔΔCT method was employed, wherein the Ct values of the target genes were normalized to the Ct values of the reference gene β-actin, relative to a control sample (Schmittgen and Livak 2008).

Table 5.1: Primer sequences used for qRTPCR

Name	Primer sequences
NF-κB	F- 5'- GCGTTTCCGTTACAAGTGCGAGG -3' R - 5'- CCCCAGGAATACTGCCTGCAGAG -3'
Cav2.2	F- 5'- AGGCCAGACATGAAGACACACA -3' R - 5'- TTGCCTTCCTTGCTTGAGTCCT -3'
TRPV1	F- 5'- GAATGACACCATCGCTCTGC -3' R - 5'- AAGAGGGTCACCAGCGTCAT -3'
β-actin	F- 5'-AGACTTCGAGCAAGAGATGGC -3' R-5'GATTCCATACCCAGGAAGGAAGG -3'

5.1.8. Assessment of S100b, TNF-α, and IL-6 protein level in sciatic nerve and spinal cord

S100b (No: KLR1360, Krishgen Biosystems), TNF-α (No: KB3145, Krishgen Biosystems), and IL-6 ELISA Kit (No: KB3068, Krishgen Biosystems) were used in this study to quantitatively assess the protein levels in SN and SC following the manufacturer's instructions. The protein concentrations were determined using the Bradford method (Bradford 1976).

5.1.9. Immunofluoresence

SN and SC were fixed in 4 % paraformaldehyde for 24 h followed by the antigen retrieval protocol was performed by boiling the tissue samples in citrate buffer (pH 5.9) for 5 min. Then tissues were transferred into 15 %, 20 %, and 20 % sucrose solutions respectively. When the SN and SC sink to the bottom of the solution, the sucrose solutions were changed. Tissues were then placed on the OCT compound in a cryomold. The OCT-embedded cryomold was gently placed into the liquid nitrogen to freeze the entire tissue in an OCT block. The blocks were stored at -80 °C. The SC sections were cut into 5µm thick coronal sections and SN longitudinally on the slides coated with 2 % APES (3-aminopropyl triethoxysilane) using cryostat microtome (Leica, USA). For immunostaining, the boundaries were made using a PAP pen on the slides which were then washed with PBS three times, 5 min each. Following this, the tissue sections were permeabilized in 0.2% Triton X-100. Then blocking was done in a solution containing 1% BSA and glycine in PBST (PBS with 0.1 % Tween 20) and incubated for 1 h. The sections were then incubated in the primary antibody at 4 °C in a humid chamber. After washing 3 times in PBS, secondary antibody (conjugated with Alexa fluorochrome) incubation was done and counterstained with 1µg/mL of 4’6-diamidino-2-phenylindole

(DAPI). The slides were mounted in DABCO, sealed and observed under a fluorescence microscope (Olympus BX53). Images captured were analyzed using the Image J program (NIH, USA) (Prajapati, Ahmed et al. 2024).

5.1.10. Golgi –Cox Staining

Golgi-Cox staining is a neurohistological technique employed to examine the cytoarchitecture of the nervous system. In this study, we have adopted the method described by (Zaqout and Kaindl 2016) with some modifications as described previously (Khanna, Chakraborty et al. 2020).

5.1.10.1 General Precautions

- Before use, all glass and plastic wares were thoroughly rinsed with fresh ddH_2O.
- Metal instruments were avoided during the impregnation step.
- All solutions were stored in a cool and dark place. Transparent glass reagent bottles were covered with aluminium foil, or small bottles were placed in a light-proof covered box.
- Careful handling of all solutions was exercised due to their toxicity. Direct skin contact or inhalation of vapours was avoided by wearing gloves and conducting experiments under a chemical hood.
- Slides coated with 3% gelatin were used in the study.

5.1.10.2. Preparation of Solutions

Sample Impregnation solution:

To prepare the 5 % w/v impregnation stock solution, potassium dichromate ($K_2Cr_2O_7$), mercuric chloride ($HgCl_2$), and potassium chromate (K_2CrO_4) were dissolved in double-distilled water (ddH_2O). The resulting solutions were stored in bottles at room

temperature in the dark without disturbance for at least 48 h. This allowed the formation of precipitates which was filtered.

Tissue protection solution:

At first, 0.1 M Phosphate buffer with a pH of 7.2 was prepared. To prepare the tissue protectant solution 300 g of Sucrose, 10 g of polyvinylpyrrolidone (PVP40; Rolex), and 300 mL of ethylene glycol ($C_2H_6O_2$) was added to 500 mL of the phosphate buffer. The volume of the cryoprotectant was then adjusted to 1000 mL using ddH_2O. The solution was then kept at 4 °C in the dark for long-term storage.

Developing solution:

The developing solution contains 50%, 70%, 95%, and 100% ethanol; Xylene (C8H10); a mixture of 3:1 parts of ammonia: double-distilled water (ddH_2O); and a solution of 5 % sodium thiosulphate ($Na_2S_2O_3.5H_2O$) in ddH_2O. All of these solutions were stored at room temperature.

5.1.10.3. Procedure for staining

Impregnation

Rats were anesthetized and transcardial perfusion was performed using 1 x PBS. SC was dissected out and kept in the impregnation solution at RT for 7-10 days. To prevent excessive impregnation of neurons, use of 4 % PFA for perfusion was avoided.

Tissue protection

Each tissue samples were carefully moved from the impregnation solution to a fresh bottle containing 10-15 mL of tissue-protectant solution. After a period of 24 h, the

tissue protectant solution was replaced with a fresh one. The SC tissues were then kept at a temperature of 4 °C in a dark environment for an additional 4-7 days.

Sectioning

Tissue sections were cut using a vibrotome (Leica) with a thickness of 150 μm onto gelatin-coated slides. To remove any excess tissue protectant solution, gentle palm pressure was applied while blotting the sections with Whatman paper. Subsequently, the slides containing the sections were air-dried for 2-3 days.

Developing step

The following process was used for development:

1. The slides were initially washed twice with distilled water for 5 min each and then transferred to a staining jar containing 50 % ethanol and left for 5 min.
2. Subsequently, the slides were placed in the ammonia solution.
3. After the ammonia treatment, the slides were washed twice with distilled water.
4. Next, the slides were immersed in sodium thiosulfate solution for 10 min, followed by washing.
5. The sections were dehydrated by immersing them in a series of ethanol gradients.
6. The slides were then cleared by placing them in xylene.
7. After clearing, the sections were mounted with DPX mounting medium.

5.1.10.4. Quantification of dendritic branching and spine density

The neurons were reconstructed at 400X magnification in a 3D manner using an Olympus BX53 microscope equipped with a motorized stage (MAC 5000 XYZ), camera, Ludl's joystick with focus control (Ludl Electronic Products, USA), and

Neurolucida software (MBF Bioscience) running on a Dell workstation. Following the completion of 3D tracing, Sholl's analysis was performed using Neuroexplorer software (MBF Bioscience) to measure the number of intersections, and dendrite lengths in each segment (Zaqout and Kaindl 2016).

5.1.11 Measurement of intracellular calcium level

SN and SC tissues were minced and digested with digestion buffer (40 unit/ml papain, 2.4 unit/ml dispase II, and 2% penicillin-streptomycin in PBS). Then the single-cell suspension of the digested tissue samples was prepared. 500µl volume of cell suspension was incubated with fura-2/acetoxymethyl ester (ChemCruz; SC-203052A) for 30 minutes at 37 °C. FURA 2/AM is rapidly metabolized in the cell by cytoplasmic esterases yielding the active dye FURA 2 which was estimated by measuring the fluorescence at 340 nm and 380 nm in the kinetic mode. For blank, a similar protocol was followed without the cell suspension (Malgaroli, Vallar et al. 1987).

5.1.12. Histological analysis of gastrocnemius muscle

The gastrocnemius muscle was fixed in a 10 % buffered formalin solution which was sliced (5 µm) using the cryostat. Then the finely sliced sections were stained with hematoxylin followed by counterstaining with eosin. Then the tissue sections were dehydrated with a graded series of alcohol and mounted with dibutyl phthalate xylene (DPX). The slides were then observed under the microscope (Olympus, Japan) for any structural abnormalities (Majumdar and Krishnamurthy 2022).

5.1.13. Statistical analysis

All data are represented as Mean ± SD and the statistical analysis was performed using the GraphPad Prism 8. The behavioral tests such as hot-plate test, acetone drop test,

Randall Selitto test, cotton swab test, Rota rod test, the BBB score, and SFI performed during the validation of S100b using pentamidine was analyzed statistically using the two-way ANOVA followed by Bonferroni post-hoc test. However, the behavioral study and changes in the intracellular calcium and S100b level performed during temporal study was analyzed by one-way ANOVA followed by Tukey multiple comparison post-hoc test. For the immunofluoresence expression of proteins and other datasets, one-way ANOVA followed by Tukey's multiple comparison post-hoc tests was followed. Differences were considered statistically significant when the P value is < 0.05 in the overall data analysis.

5.2. Results and Discussion

5.2.1. Temporal study to evaluate the development of NP phenotypes and changes in the intracellular calcium and S100b protein level

5.2.1.1. Effect of CCI on the development of NP phenotypes during the temporal study

The behavioral tests were conducted on days 3, 7, 14, and 21 after the CCI surgery to assess the development and progression of NP in rats. Previously, it has been demonstrated that CCI animal models lead to increased sensitivity to pain (hyperalgesia) and also cause the development of allodynia (Bennett, Chung et al. 2003). Similarly, in our study, statistical analysis by one-way ANOVA followed by post-hoc test revealed the development of thermal hyperalgesia, cold allodynia, and mechanical hyperalgesia ($p < 0.05$) compared to the rats on D-7 after the surgery (as shown in **Figure 5.5**). The peripheral nerve injury caused a significant reduction in the withdrawal latency when placed on the hot plate (**Figure 5.5A)** along with the elevation

in paw withdrawal duration on dropping acetone on the injured paw (**Figure 5.5B)** among the groups ([$F(4,19) = 14.45$; $p < 0.05$] and [$F(4,19) = 20.52$; $p < 0.05$] respectively). Further, on D-14, there was a substantial increase in thermal hyperalgesia and cold allodynia compared to the rats before surgery (i.e., D-0), as well as on days 3 and 7 (D-3 and D-7) and a similar trend was observed until D-21. Post-injury to the SN often leads to an increase in the sensitivity of sensory nerve fibers that detects cold sensory inputs (Xing, Chen et al. 2007). Consequently, abnormal signaling may occur in response to temperatures, accurately reflecting clinical symptoms like cold allodynia in persons with peripheral neuropathy.

Further, it was also observed that the threshold to withstand the pressure applied on the dorsal part of the paw decreased significantly during the Randall Selitto test (**Figure 5.5C)** among the groups ([$F(4,19) = 15.54$; $p < 0.05$]). Over time, mechanical hyperalgesia gradually increased, reaching maxima on D-14 following which, a plateau was observed. The development of mechanical hyperalgesia in the CCI model can be explained due to the complex and overlaying interplay between the peripheral and central nervous systems mostly due to neuroplastic alterations in the SN and SC (Calvo, Dawes et al. 2012) that increases the ectopic discharges and excitability of nociceptive nerve fibres; hence, exacerbating the non-noxious sensory input (Chen, Tan et al. 2019). In extension, we also observed that post-CCI, there was development of motor in-coordination as evident from the statistically lower BBB score (**Figure 5.5D**) among the groups ([$F(4,19) = 107.5$; $p < 0.05$]). Similar to our observation, Bagriyanik et al. (Bagriyanik, Ersoy et al. 2014) reported that injury to the SN after CCI surgery produced significant changes in the neuromuscular coordination in rodents which is similar to the motor disability observed clinically (Goswami, Aleem et al. 2021).

Therefore, it can be affirmed that CCI of SN caused sensory and motor deficits in rats which started from D-7 and was maximum on D-14 following which the symptoms stabilized in this NP model.

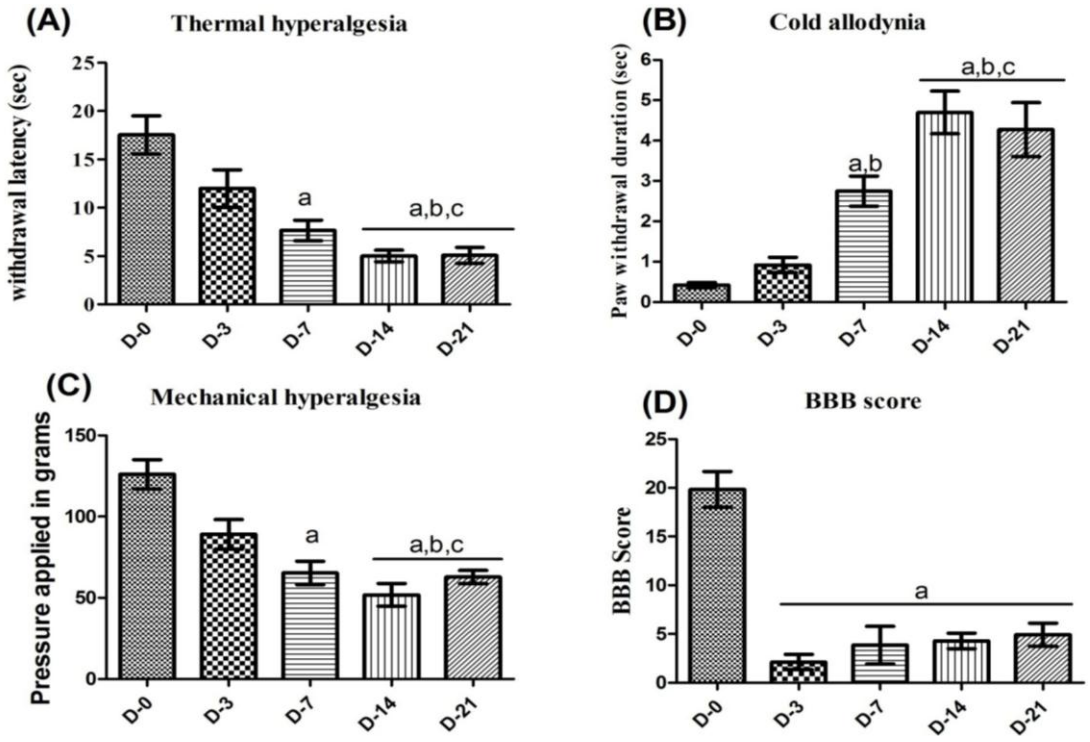

Figure 5.5: Sensory and motor deficit due to chronic constriction injury in rats. The effect of CCI on the development of (A) thermal hyperalgesia, (B) cold allodynia, (C) mechanical hyperalgesia, and (D) changes in the BBB score. All values are in mean ± SD (n=4 rats/ group). $^{a}p<0.05$, $^{b}p<0.05$, and $^{c}p<0.05$ compared to D-0, D-3, and D-7 respectively. (One-way ANOVA followed by Tukey multiple comparison post-hoc test)

5.2.1.2. Temporal changes in the intracellular calcium, S100b, and pro-inflammatory cytokine (TNF-α) level post-CCI of sciatic nerve

The development and maintenance of NP are significantly influenced by an increase in the intracellular calcium $(Ca^{2+})_i$ level as an increase in the influx of calcium causes neuronal hyperexcitability of the primary afferent neurons in the SN and SC (Hogan, McCallum et al. 2000) that perpetuates NP phenotypes. Thus, our investigation aimed to determine the changes in the $(Ca^{2+})_i$ level in order to identify the pharmacological

window of opportunity so that we can know the probable time window to start the treatment (**Figure 5.6**). In the CCI paradigm of NP, statistical analysis by one-way ANOVA followed by post hoc test revealed that there was a significant increase in the $(Ca^{2+})_i$ level in SN acutely 1 h after the surgery compared to the rats before surgery ((D-0); ([F(7,31) = 81.76; p <0.05])) (as represented in **Figure 5.6A)**. The $(Ca^{2+})_i$ level increased gradually and the maximum concentration was observed on D-14 following which it stabilized. However, in the SC, a significant increase in the $(Ca^{2+})_i$ level was observed on D-1 among the groups (([F(7,31) = 35.23; p <0.05]) as shown in **Figure 5.6D**. The $(Ca^{2+})_i$ level had further increased as observed in the SN with the maximum concentration on D-14. This corroborates with the pain behavioral assessment test performed where the sensory and motor deficits reached their peak on D-14, after which the symptoms in this NP model stabilized (**Figure 5.5**). The increase in the $(Ca_2^{+})_i$ has been reported to facilitate further increase in the influx of calcium through various ion channels leading to neuroplastic changes in the primary afferent fibres and glial cell-induced neuroinflammation that exacerbates pain (Kawamata and Omote 1996).

Similarly, injury to the PNS often leads to glial cell activation that is linked with the increase in calcium-binding protein i.e., S100b which plays a significant role in neuroinflammation and sensitization of the pain pathways. Therefore, the temporal changes in the S100b and pro-inflammatory cytokine (TNF-α) were evaluated in SN and SC. Statistical analysis by one-way ANOVA revealed significant changes in the S100b and TNF-α among the groups (([F(7,31) = 63.90; p <0.05] and ([F(7,31) = 109.4; p <0.05]) respectively) in SN. Post-hoc analysis indicates that the CCI rats demonstrated a significant increase in S100b and TNF-α from 12 h compared to the naïve rats (i.e., D-0) and the maximum concentration was observed on D-14 (**Figure**

5.6B and C). Likewise, in the SC, one-way ANOVA followed by post-hoc analysis data showed significant differences in S100b and TNF-α levels among the groups (([F(7,31) = 112.1; $p < 0.05$] and ([F(7,31) = 90.55; $p < 0.05$]) respectively) compared to the rats without SN injury (**Figure 5.6 E and F**). The observed elevated S100b level in SN may be associated with altered Schwann cell proliferation and Wallerian degeneration post-injury, thereby impacting the nerve regeneration process. While in SC, the excessive increase in S100b level compared to the control group can be linked with activated glial cells that lead to a heightened state of neuroinflammation and neuronal damage, contributing to persistent painful phenotypes. In the present study, we, for the first time report that there are time-dependent changes in the $(Ca^{2+})_i$ and S100b in the CCI model of NP in rats.

Additionally, the correlation between $(Ca^{2+})_i$, S100b and TNF-α level on D-21 post-CCI was performed and is illustrated in **Figure 5.7a**. S100b was significantly and positively correlated with $(Ca^{2+})_i$, and TNF-α ($p<0.05$). This implicates the involvement of $(Ca^{2+})_i$ and S100b in the regulation of inflammation in the CCI model in a time-dependent manner. Further, a significant positive correlation of S100b with NP phenotypes was observed (**Figure 5.7b**). Therefore, it is probable that S100b is involved in the progression of NP. Besides, S100b also regulates the neuroinflammation as TNF-α increases in a time-dependent manner.

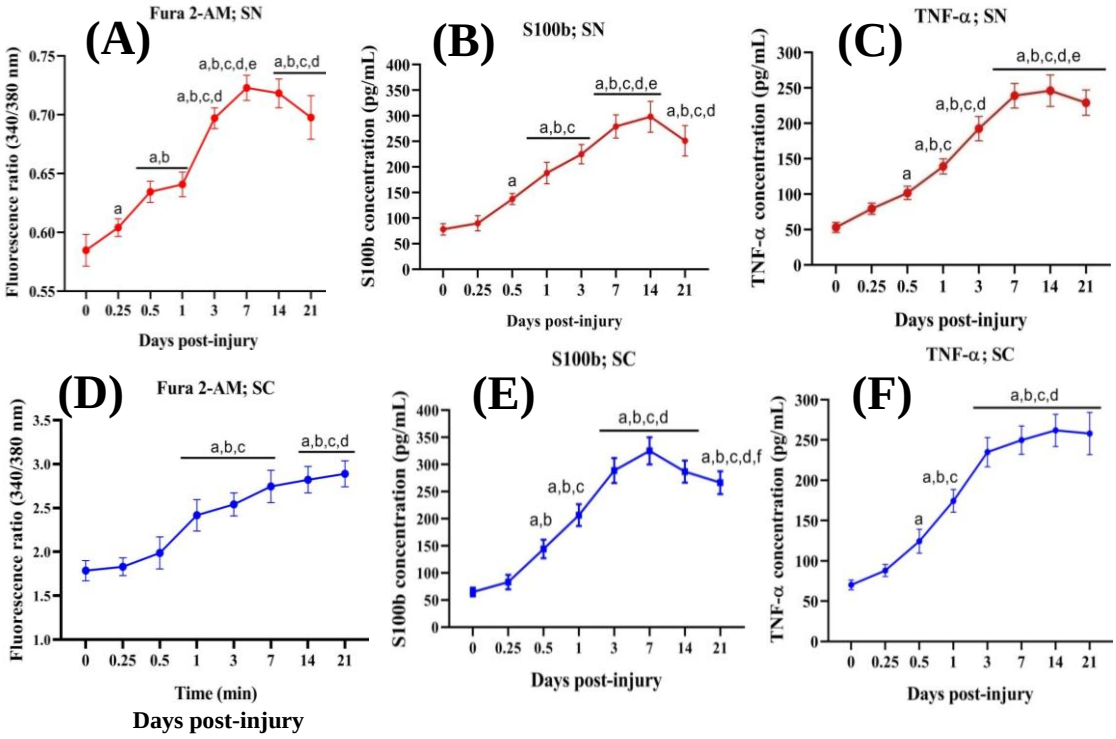

Figure 5.6: Temporal changes in the intracellular calcium, S100b and TNF-α level in SN and SC post-CCI injury. All values are in mean ± SD (n=4 rats/ group). $^{a}p<0.05$, $^{b}p<0.05$, $^{c}p<0.05$, $^{d}p<0.05$, $^{e}p<0.05$, and $^{f}p<0.05$ compared to 0, 0.25, 0.5, 1, 3, and 7 days post-injury. (One-way ANOVA followed by Tukey's multiple comparison post-hoc test)

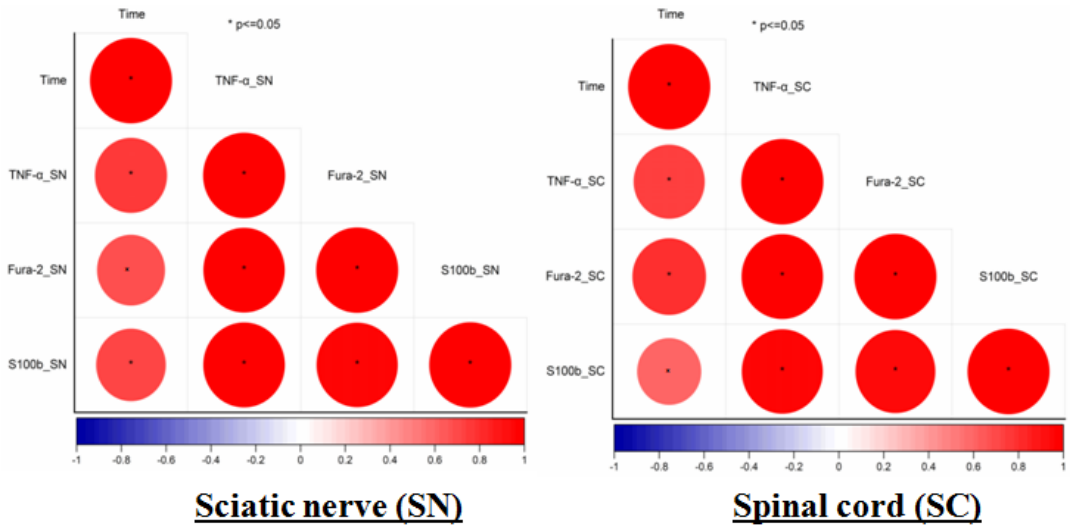

Figure 5.7a: A correlation between intracellular calcium level, S100b, and TNF-α level on D-21 post-CCI of peripheral nerve.

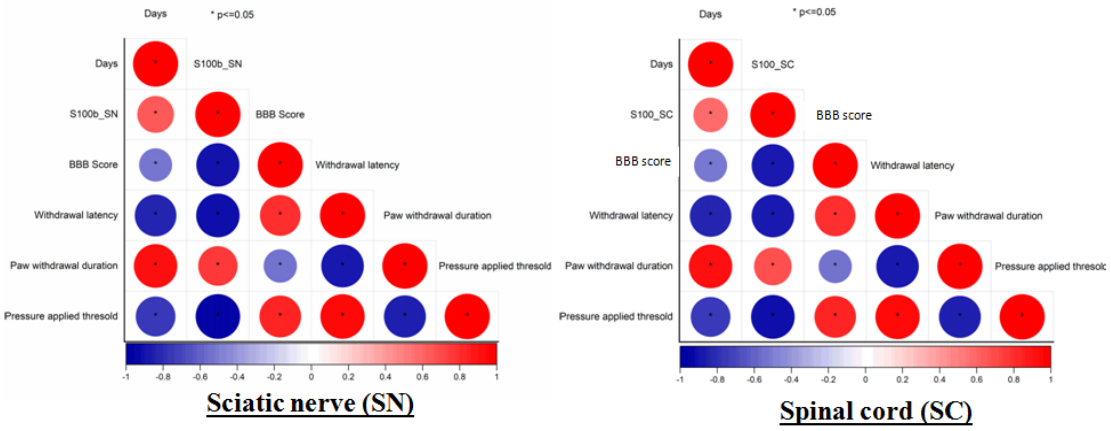

Figure 5.7b: A correlation between S100b level and NP phenotypes on D-21 post-CCI of peripheral nerve.

5.2.2. Validation of the role of S100b in the pathogenesis/progression of NP in rat CCI model

5.2.2.1. Effect of pentamidine on the CCI-induced sensory and motor deficits

CCI animal model induces the development of hyperalgesia and allodynia in response to various non-noxious stimuli. In the present study, statistical analysis by two-way ANOVA revealed the development of thermal hyperalgesia and cold allodynia among the groups ([F (4, 220) = 298.0; $p < 0.05$] and [F (4, 220) = 456.9; $p < 0.05$] respectively), time periods ([F (3, 220) = 205.4; $p < 0.05$] and [F (3, 220) = 363.4; $p < 0.05$] respectively), and the interaction between group and time ([F (12, 220) = 40.05; $p < 0.05$] and [F (12, 220) = 68.17; $p < 0.05$] respectively). Post-hoc test represented that there was a significant decrease in paw withdrawal latency when placed on the hot-plate with a simultaneous increase in paw withdrawal duration when acetone was sprayed on the paw of the injured leg following CCI compared to control from D-7 onwards till D-21 (**Figure 5.8A and B**). This finding is supported by a previous study, where CCI caused thermal and cold hypersensitivity in rodents similar to the clinically observed symptoms (Hamidi, Ramezani et al. 2012). Further, for the first time we

observed that the treatment with a specific S100b inhibitor i.e., pentamidine attenuated thermal hyperalgesia and cold allodynia similarly to pregabalin as observed on D-21. However, there were significant differences between the effects of pregabalin and pentamidine observed on these NP phenotypes. Notably, no significant differences in thermal hyperalgesia and cold allodynia were observed between the control and sham. Hence, the above results suggest that S100b is involved in the development and progression of NP symptoms in this model as a specific S100b inhibitor reversed these NP phenotypes.

Furthermore, chronic pain is clinically characterized by hypersensitivity induced by mechanical stimuli (Bannister, Sachau et al. 2020). Thus, in the present study, we have evaluated whether pentamidine can mitigate mechanical hyperalgesia and dynamic mechanical allodynia in the CCI model using Randall Selitto and cotton swab test (**Figure 5.8 C and D**). In the Randall Selitto and cotton swab paradigm, the pressure applied on the ipsilateral side and paw withdrawal latency was decreased after CCI ([$F(4, 220) = 256.8$; $p < 0.05$] and [$F(4, 220) = 366.4$; $p < 0.05$] respectively), with time ([$F(3, 220) = 240.6$; $p < 0.05$] and [$F(3, 220) = 251.9$; $p < 0.05$] respectively). Further, there was a significant interaction between groups and time ([$F(12, 220) = 34.55$; $p < 0.05$] and [$F(12, 220) = 45.26$; $p < 0.05$] respectively) in this paradigm. Post-hoc analysis revealed that there was a significant decrease in mechanical hyperalgesia and dynamic mechanical allodynia following CCI compared to the naïve rats from D-7 onwards till D-21. However, pentamidine reversed these CCI-induced NP phenotypes as observed on D-21 evident from a significant increase in the threshold to withstand the pressure applied compared to the untreated group. Similarly, Aδ fibre-mediated dynamic allodynia was also attenuated by pentamidine compared to the CCI rats. This

confirms that S100b plays a vital role progression of heterogeneous NP symptoms in this paradigm. Notably, there were no observed changes in the NP phenotypes in between the contralateral paws of rats after nerve injury and before CCI of SN and also following the drug treatment.

Moreover, we found motor deficits following the CCI and statistical analysis using repeated measures of two-way ANOVA revealed a significant differences in the rotarod retention time among the different groups [$F(4, 220) = 166.6$, $p < 0.05$] as well as over time [$F(3, 220) = 129.7$, $p < 0.05$]. Additionally, an interaction between group and time was also observed [$F(12, 220) = 24.75$, $p < 0.05$] as shown in **Figure 5.8E.** Similar to our observation, Bagriyaniket al. (Bagriyanik, Ersoy et al. 2014) reported that injury to the SN after CCI surgery produced significant changes in the neuromuscular coordination in rodents which is similar to the motor disability observed clinically (Goswami, Aleem et al. 2021). Post-hoc analysis showed CCI rats exhibited significant decrease in the retention time on the rotating rod compared to control animals from D-7 and was maintained till D-21 which was reserved by pentamidine treatment. In this context, a recent study reported that pentamidine improved motor impairment in a chronic experimental autoimmune encephalomyelitis model (Barros, Barateiro et al. 2022).

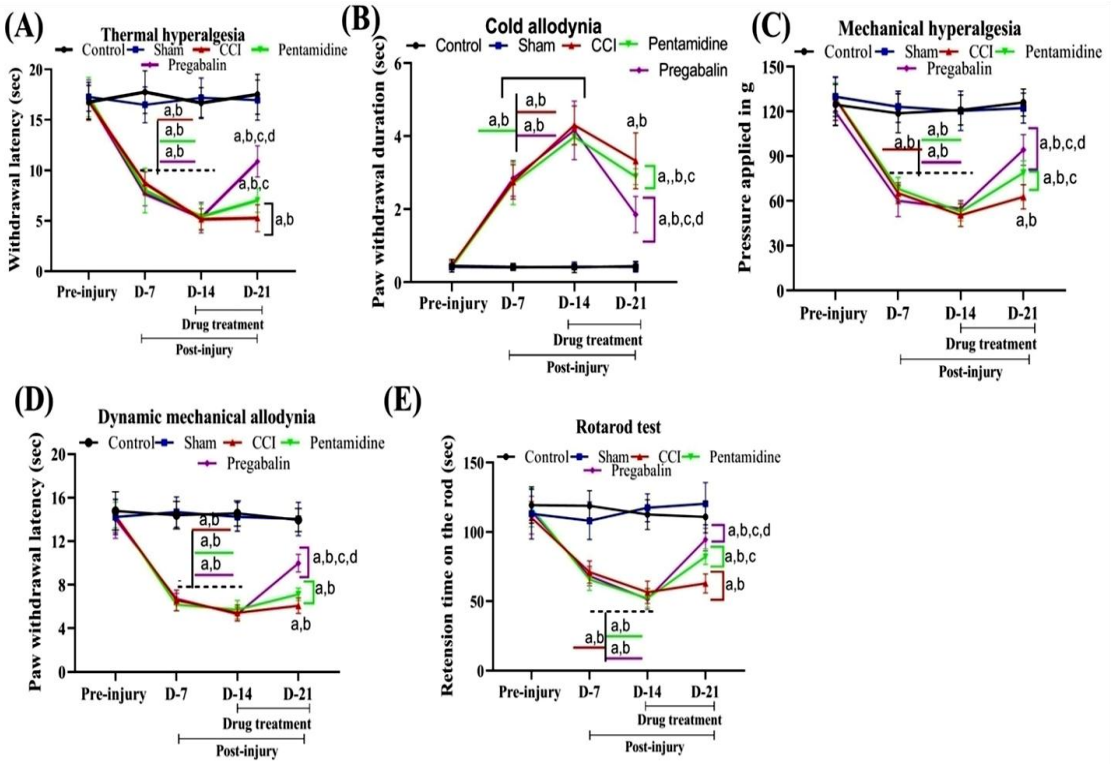

Figure 5.8: Sensory and motor deficit due to chronic constriction injury in rats. Effect of pentamidine on (A) thermal hyperalgesia, (B) cold allodynia, (C) mechanical hyperalgesia, (D) dynamic mechanical allodynia, and (E) retention time on the rota-rod. All values are in mean ± SD (n=12 rats/ group). $^{a}p<0.05$, $^{b}p<0.05$, $^{c}p<0.05$, and $^{d}p<0.05$ compared to control, sham, CCI, and pentamidine respectively. (Two-way ANOVA followed by Bonferroni post-hoc test)

5.2.2.2. Effect of pentamidine on the CCI-induced motor coordination

The impairment in motor coordination post-injury to the peripheral nerve along with the evaluation of the functional condition of the injured SN was performed using the BBB score and SFI (**Figure 5.9**). Post-CCI, we observed that the injured hind paw was awkwardly positioned when walking, and the toes were somewhat ventroflexed and the rodents walked with an obvious limp as shown in **Figure 5.9i**. The hind paw was everted and the animal stood and walked with the full medial border of its hind paw contacting the ground. However, post-treatment, there was an improvement in the gait with less limping observed. **Figure 5.9iiB** below illustrates the effect of pentamidine on BBB Score and SFI in CCI rats. Statistical analysis by repeated measure two-way

ANOVA revealed significant differences in BBB Score and SFI among the group ([F (4,220)= 2413; P<0.05] and [F (4,220)= 1478; P<0.05] respectively), time [F (3, 220)=1840; P<0.05] and [F (3,220)= 997.4; P<0.05], respectively) and a significant interaction between groups and time ([F (12,220)=334.0]; P<0.05] and [F (12,220)= 181.6; P<0.05] respectively). The control and sham groups did not exhibit significant differences according to the post hoc analysis. The SFI of the CCI rats on day 14 was found to be -77.67 ± 10.01 compared to 5.98 ± 1.03 before surgery. Previously, studies have also reported that ligation of the SN produced a reduction in the total spreading of the paw with an increase in print length and hence decreased SFI, denoting functional deficits of the nerve and development of walking impairment due to pain (Wang, Chen et al. 2021). Therefore, it can be affirmed that CCI caused sensory and motor deficits in rats along with the development of NP phenotypes. However, treatment with pentamidine restored the motor function as the SFI improved to -61.85 ± 8.11 after seven days of treatment. Hence, together with the improvement in the BBB score, these findings confirm that the specific inhibitor of S100b not only mitigated the core symptoms of NP but also improved motor performances in the CCI model.

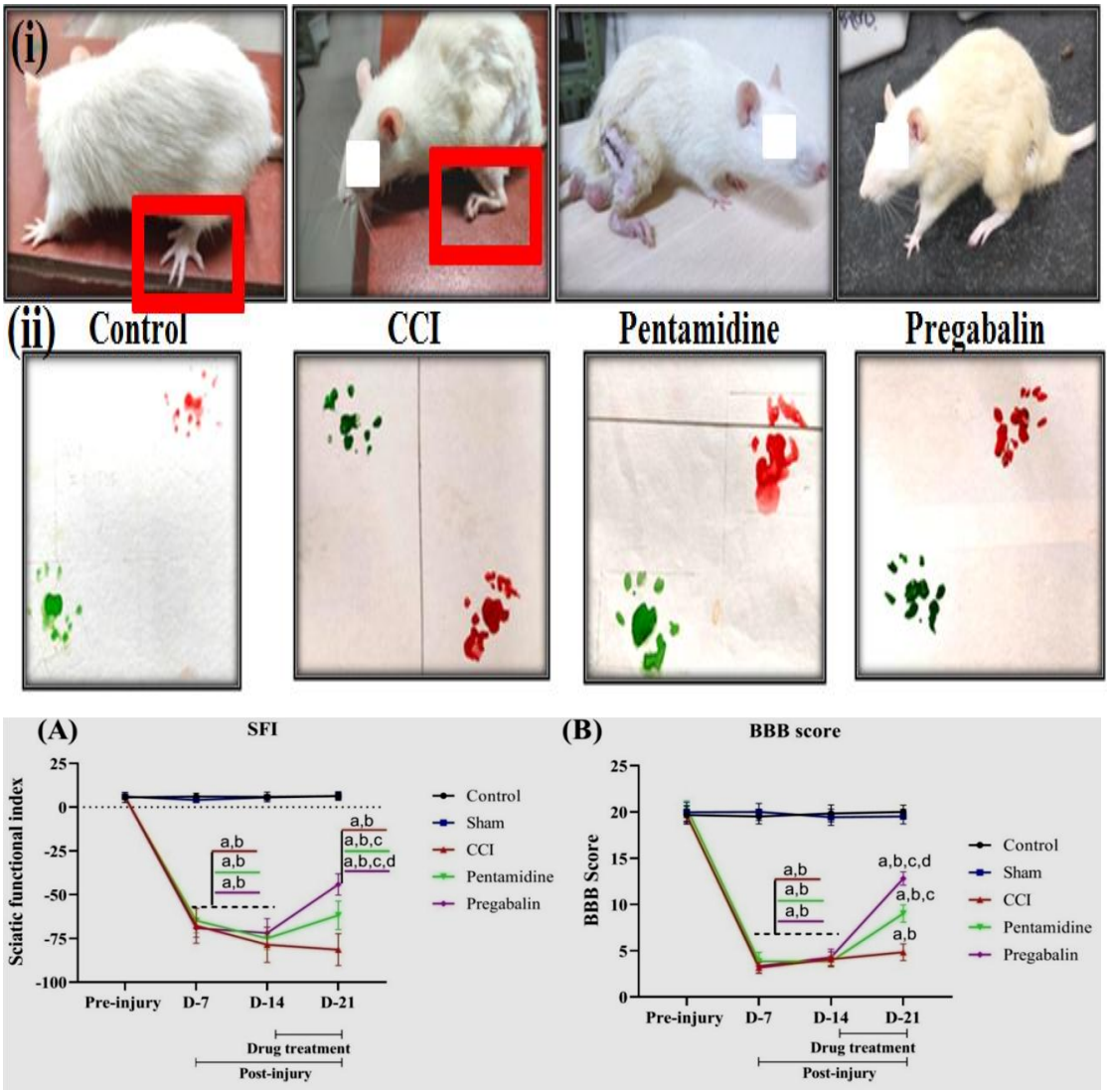

Figure 5.9: Representative images of the (i) paw of the ipsilateral side and (ii) footprints of control, CCI, pentamidine and pregabalin treated rats. (ii) Effect of pentamidine on SFI and BBB score. All values are in mean ± SD (n=12 rats/ group). $^{a}p<0.05$, $^{b}p<0.05$, $^{c}p<0.05$, and $^{d}p<0.05$ compared to control, sham, CCI, and pentamidine respectively. (Two-way ANOVA followed by Bonferroni post-hoc test)

5.2.2.3. Effect of pentamidine on the intracellular calcium $(Ca^{2+})_i$ and S100b level in SN and SC

Increased $(Ca^{2+})_i$ levels play a crucial role in the development of NP as it increases neuronal excitability, stimulates the release of neurotransmitters, triggers pro-nociceptive pathways along with the activation of downstream cascades that facilitate further release of calcium and exacerbates painful phenotypes (Cui, Wu et al. 2021).

Further, a series of studies reported that post-tissue injury, the calcium-binding protein (S100b) is actively released from the activated glial cells creating a pro-inflammatory environment that contributes to the pathophysiology of any disease (Michetti, Di Sante et al. 2021, Michetti, Clementi et al. 2023). Similarly, in our study, we have observed that there was a time-dependent increase in the $(Ca^{2+})_i$ and S100b levels in both SN and SC post-injury to the SN (as shown in **Figure 5.6**). As a result, our study sought to determine if the administration of a specific S100b inhibitor will result in the reduction of $(Ca^{2+})_i$ level post-CCI of SN. To analyze the effects of pentamidine on $(Ca^{2+})_i$ level and to identify the significant differences among the groups, statistical analysis by one-way ANOVA was employed ($[F(4,19) = 20.97; p<0.05]$ and $[F(4,19) = 24.41; p<0.05]$ respectively). Post-hoc analysis revealed a significant increase in $(Ca^{2+})_i$ level in both SN and SC following CCI compared to control and sham rats. Pregabalin, a CCB and the first-line treatment for NP significantly mitigated the increased $(Ca^{2+})_i$ level as observed on D-21. Interestingly, unlike pregabalin, treatment with pentamidine did not significantly alter the elevated $(Ca^{2+})_i$ level post-injury (**Figure 5.10iA and B**).

Furthermore, in our study, one-way ANOVA revealed a difference in S100b level post-treatment with pentamidine in SN $[F(4,19)= 156.7; p<0.05]$ and SC $[F(4,19)= 280.2; p<0.05]$ among the groups. Tukey's post-hoc test showed a significant increase in S100b level in both SN and SC following CCI compared to the control group. Notably, there were no significant differences in the S100b level between the control and sham rats. Nevertheless, following 7 days of treatment with pentamidine, we observed a significantly decreased S100b level in both SN and SC by 2.2-fold. However, the group that received pregabalin exhibited no significant differences compared to the disease group (**Figure 5.10iiA and B**). Additionally, the correlation between S100b and NP

phenotypes after the pentamidine treatment (10 mg/kg b.w.) revealed that they are positively correlated ($p<0.05$) (**Figure 5.11**). Therefore, our investigation suggests that pentamidine attenuated the core symptoms of NP phenotypes in the CCI model by regulating the S100b.

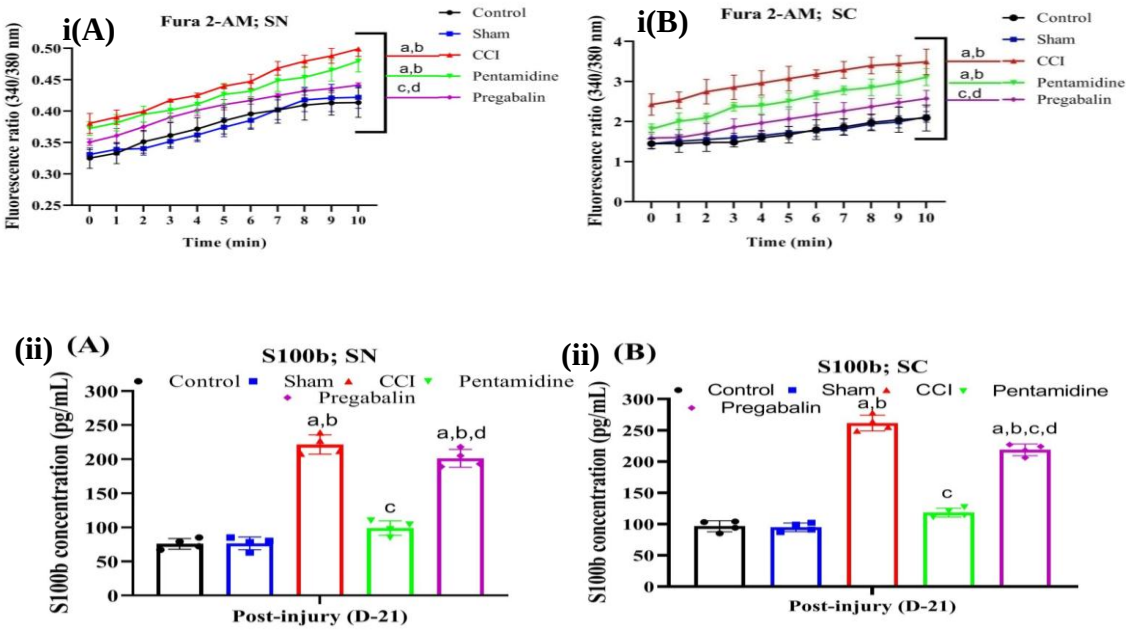

Figure 5.10: Effect of pentamidine on (i) intracellular calcium and (ii) S100b level in SN and SC. All values are in mean ± SD (n=4 rats/ group). [a]$p<0.05$, [b]$p<0.05$, [c]$p<0.05$, and [d]$p<0.05$ compared to control, sham, CCI, and pentamidine respectively. (Two-way ANOVA followed by Bonferroni post-hoc test for Fura 2-AM assay) (One-way ANOVA followed by Tukey's multiple comparison post-hoc tests for S100b level)

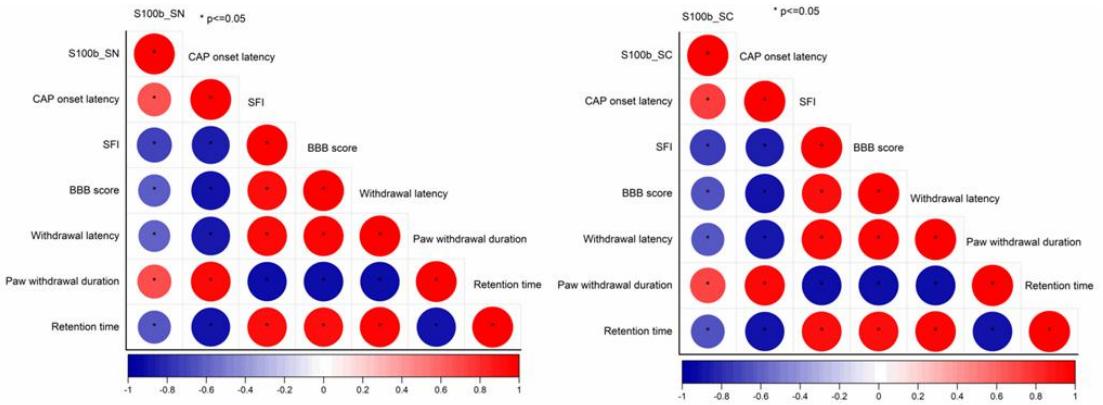

Figure 5.11: A correlation between S100b and NP phenotypes after the pentamidine treatment (10 mg/kg b.w.)

5.2.2.4. Effect of pentamidine on the $Ca_V2.2$ and TRPV1 mRNA expression in SN and SC

In the present study, we have analyzed the $Ca_V2.2$ and TRPV1 mRNA expression in the SN and SC as there were enhanced levels of $(Ca^{2+})_i$ observed post-CCI (illustrated in **Figure 5.10**). Statistical analysis revealed that there was a significant increase in the fold change mRNA expression of $Ca_V2.2$ among the groups in both SN and SC ([$F(4,19) = 57.57$, $p<0.05$] and $F(4,19) = 187.3$, $p<0.05$] respectively). The post-hoc test showed an increase in $Ca_V2.2$ expression following injury to the peripheral nerve compared to the control and sham groups. The over-expression of $Ca_V2.2$ has also been observed previously in rats with CCI-induced NP (Luo, Calcutt et al. 2002, Bucci, Mochida et al. 2011, Cai, Quan et al. 2022) leading to a persistent influx of calcium in the primary afferent terminals (Alles, Garcia et al. 2018). This reportedly activates downstream cascade pathways of synaptic vesicle fusion with the antidromic release of neurotransmitters, contributing to the positive feedback mechanism of peripheral sensitization (Cai, Quan et al. 2022). Besides, elevated intracellular calcium level also results in long-term potentiation of nociceptive transmission to spinal and supraspinal regions causing central amplification of pain (Sun, Tong et al. 2022). Elevated $(Ca^{2+})_i$ level is also involved in glial cell activation especially astrocytes that contributes to the release of gliotransmitters that modulate neuronal activity and pain perception (Cho and Huh 2020). Treatment with a CCB i.e., pregabalin caused a significant decrease in the $Ca_V2.2$ expression compared to untreated NP rats (**Figure 5.12 (A and B)**) along with the reversal of abnormal rise in $(Ca^{2+})_i$ post-injury to the peripheral nerve. However, a specific S100b inhibitor (pentamidine) reduced the CCI-induced increase in the $Ca_V2.2$ mRNA expression in the SN and SC but was not as effective as pregabalin. Therefore,

the analgesic effects of pentamidine observed in the CCI-induced NP model are more associated with S100b regulation as corroborated by the reversal of the NP phenotypes observed after pentamidine treatment (**Figure 5.8**).

Furthermore, in our study, one-way ANOVA revealed a difference in the mRNA expression of TRPV1 (Transient receptor potential vanilloid 1) post-treatment with pentamidine among the groups in the SN ($F(4,19) = 231.3$, $p<0.05$]) and SC ($F(4,19) = 105.6$, $p<0.05$]). Tukey's post-hoc test showed a significant increase in TRPV1 expression in both SN and SC following CCI compared to the control group. TRPV1 is a calcium-permeable ion channel that is predominantly expressed in the sensory neurons and is primarily involved in sensing temperature > 43 °C (Malek, Pajak et al. 2015). During NP conditions, TPRV1 are reportedly upregulated in the C and A-fibers after peripheral nerve injury leading to the development of thermal hyperalgesia (Huang, Lu et al. 2020). This is coherent with our study where CCI of SN led to the development of thermal hyperalgesia in rats (**Figure 5.8**). Besides, there are previous studies providing links between TRPV1 upregulation, glial cell activation and development of hypersensitivity to thermal stimuli in various NP animal models (Chen, Willcockson et al. 2009). TRP channels have also been identified in regulating the calcium ion homeostasis (Lee, Jo et al. 2021) and aberrant changes in the expression of TRPV1 following the peripheral nerve injury may lead to excessive release of calcium-mediated neurotransmitters causing sensitization of path pathways and exaggerate the pain sensation. However, treatment with pregabalin and pentamidine produced a significant decrease in the TRPV1 mRNA expression in SN and SC compared to the CCI group (**Figure 5.12(C and D**)). Therefore, inhibiting S100b using pentamidine mitigated thermal hypersensitivity by alleviating the TRPV1 expression in SN and SC.

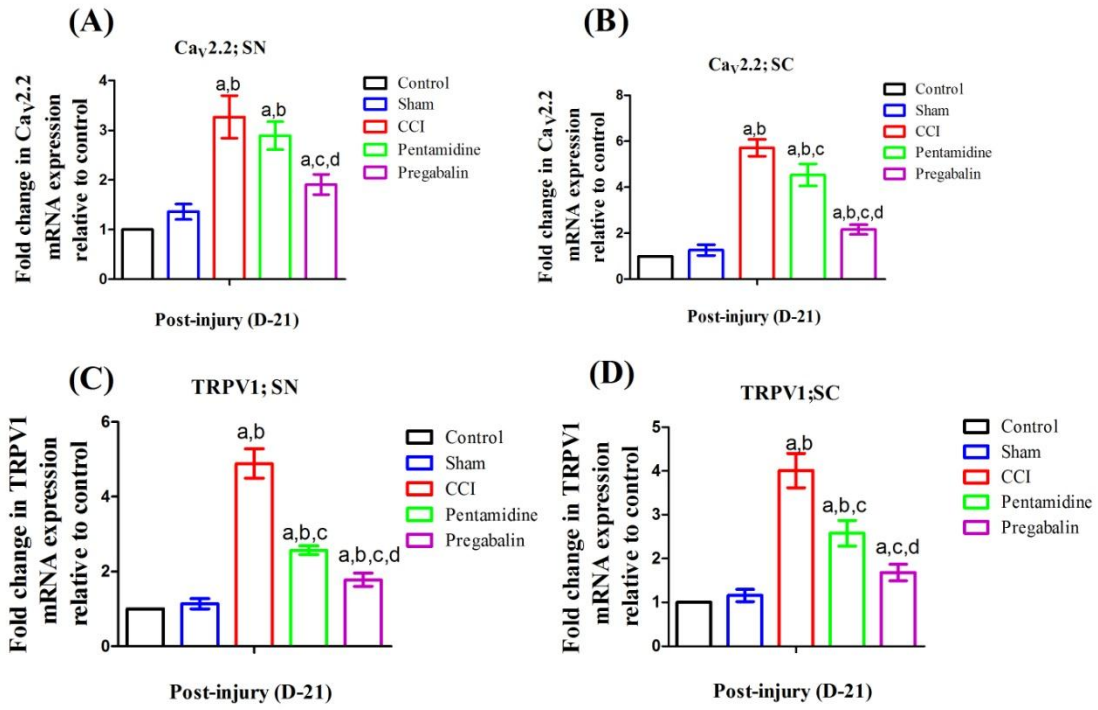

Figure 5.12: Effect of pentamidine on $Ca_V2.2$ and TRPV1 mRNA expression in the SN (A and C respectively) and SC (B and D respectively). All values are in mean ± SD (n=4 rats/ group). $^{a}p<0.05$, $^{b}p<0.05$, $^{c}p<0.05$, and $^{d}p<0.05$ compared to control, sham, CCI, and pentamidine respectively. (One-way ANOVA followed by Tukey's multiple comparison post-hoc test)

5.2.2.5. Effect of pentamidine on the expression of S100b in SN and SC

To further validate the effects of pentamidine on the S100b post-CCI in the SN and SC, we performed an immunofluorescence assay to observe the localization of S100b as illustrated in **Figures 5.13 and 5.14**. Our findings showed that there was increased fluorescence intensity in the CCI group. One-way ANOVA followed by post hoc test revealed a significant difference in fluorescence intensity of S100b expression among the groups in SN ([$F(4,14) = 16.84$; $p<0.05$]) and SC ([$F(4,14) = 22.48$; $p<0.05$]) compared to the control and sham group. Treatment with pentamidine and pregabalin significantly attenuated the CCI-induced increase in the fluorescence intensity of S100b. However, the effect produced by pentamidine was more prominent compared

to pregabalin. These observations are consistent with the clinical reports which showed an exaggerated response of S100b in traumatic brain injury (Lécuyer, Mercier et al. 2021). Further, S100 family proteins are reported to get activated upon binding with calcium and in the CCI model of NP, we observed elevated $(Ca^{2+})_i$ level in SN and SC. The activated S100 proteins tend to modulate glial cell activation, triggering inflammatory responses due to the release of pro-inflammatory cytokines and chemokines via NF- κB or calcium-dependent pathway, contributing to the chronic nature of NP (Michetti, Di Sante et al. 2021). Coherently, pharmacological blockade of S100b with pentamidine treatment in CCI rats mitigated NP phenotypes and also improved neuroinflammation as shown in **Figure 5.18**.

5.2.2.6. Effect of pentamidine on the CCI-induced microglial activation in SN and SC

The CCI-induced increase in the microglia activation was confirmed by immunofluorescence assay as depicted in **Figure 5.15**. The fluorescence intensity of Iba-1 (ionized calcium-binding adapter molecule 1) was used as a measure of microglial activation and DAPI was used for counterstaining the nucleus. Statistically, one-way ANOVA revealed that there was a significant difference in fluorescence intensity of Iba-1 expression in SC sections among the group ([$F(4,14) = 14.70$; $p<0.05$]**)**. The post hoc test demonstrated that Iba-1 intensity had significantly elevated in the CCI group compared to naïve rats that were almost abrogated by the pentamidine treatment ($p < 0.05$) on D-21. However, pregabalin-treated animals did not show any effect on CCI-induced increase in Iba-1. Notably, there were no significant differences between the control and sham group. Hence, our findings confirm that there was activation of microglia following CCI as suggested earlier (Nishihara, Tanaka et al. 2020). Besides,

previous studies have also reported that abnormal increase in S100b induces persistent microglial activation that is associated with the maintenance of hyperalgesia and allodynia (Hains and Waxman 2006) and also contributes to the complex pathophysiology of NP (Adami, Sorci et al. 2001). The injury-induced abnormal rise in S100b is reported to be detrimental to the neurons as well as the glial cells and via neuron-glial interactions; they amplify the release of pro-inflammatory cytokines contributing to the sensitization of the ascending pain pathways (Michetti, D'Ambrosi et al. 2019).

5.2.2.7. Effect of pentamidine on the CCI-induced astrocytes activation in SN and SC

The initiation of peripheral injury-induced NP is documented to be highly influenced by the neuroimmune alterations that activate resident immune cells of the nervous system (Hains and Waxman 2006). Therefore, the CCI-induced increase in the astrocyte activation in SN and SC was confirmed by immunofluoresence assay as depicted in **Figure 5.16 and 5.17** respectively. Statistically, one-way ANOVA revealed that there was a significant difference in fluorescence intensity of GFAP expression in SN and SC sections among the group ([$F(4,14) = 25.17$; $p<0.05$] and [$F(4,14) = 26.95$; $p<0.05$] respectively**)**. The post hoc test demonstrated that GFAP intensity had significantly elevated in the SN and SC of the CCI group compared to naïve rats. Treatment with pentamidine alleviated these alterations significantly ($p < 0.05$) on D-21 of the experimental protocol. However, pregabalin-treated animals did not show any significant effect on the CCI-induced increase in GFAP. Besides, in the SC, the GFAP-positive astrocytes of the naïve group exhibited round nuclei with a slender process while in the CCI group, they were swollen with hypertrophic appearance throughout

the section as shown in **Figure 5.17** which indicates the activated phenotype of astrocytes. So overall, our findings demonstrate that the glial cells are activated in this model of NP which was mitigated by a specific S100b inhibitor. Similar to our observation, research has demonstrated that inhibition of GFAP expression decreased NP phenotypes implying a possible and positive cause-and-effect connection between the astrocyte activation and chronic pain (Ji, Berta et al. 2013). Additionally, astrocytes are strongly associated with the preservation of the blood-brain barrier's integrity. Studies have shown that aberrant activation of the astrocytes may lead to a disruption in the selective permeability of the blood-brain barrier (Michinaga and Koyama 2019). Hence, our results clearly confirm that even though there is an injury caused to the peripheral nervous system in the CCI model of NP but neuroinflammation is also observed in the central nervous system i.e., SC.

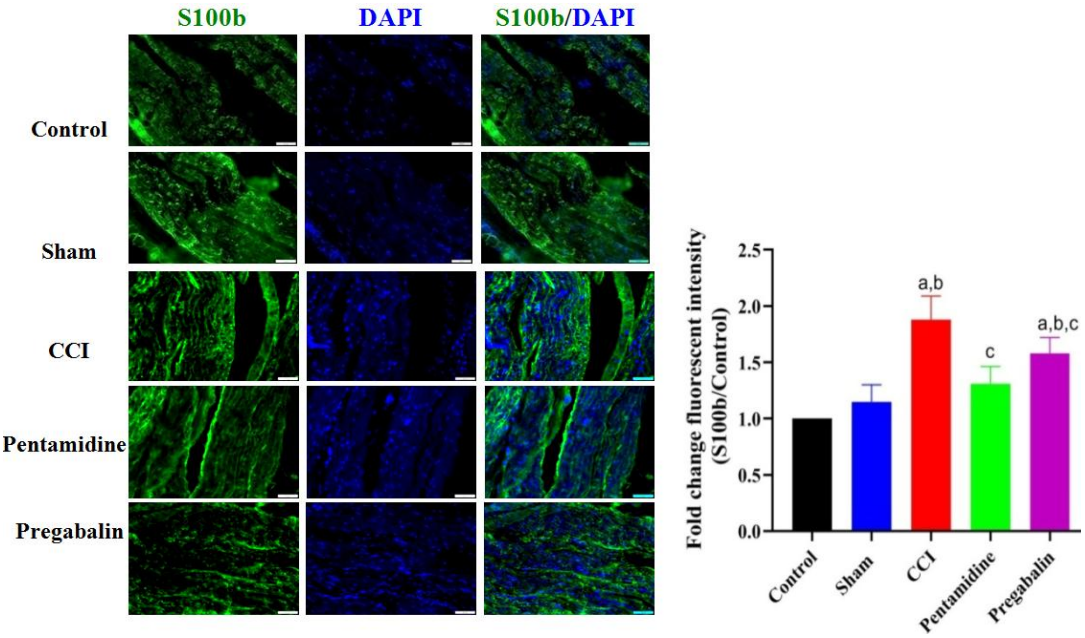

Figure 5.13: Effect of pentamidine on S100b expression in the SN. Scale bar was set at 50 µM with 20X magnification. All values are in mean ± SD (n=3 rats/ group). $^{a}p<0.05$, $^{b}p<0.05$, $^{c}p<0.05$, and $^{d}p<0.05$ compared to control, sham, CCI, and pentamidine respectively. (One-way ANOVA followed by Tukey's multiple comparison post-hoc test)

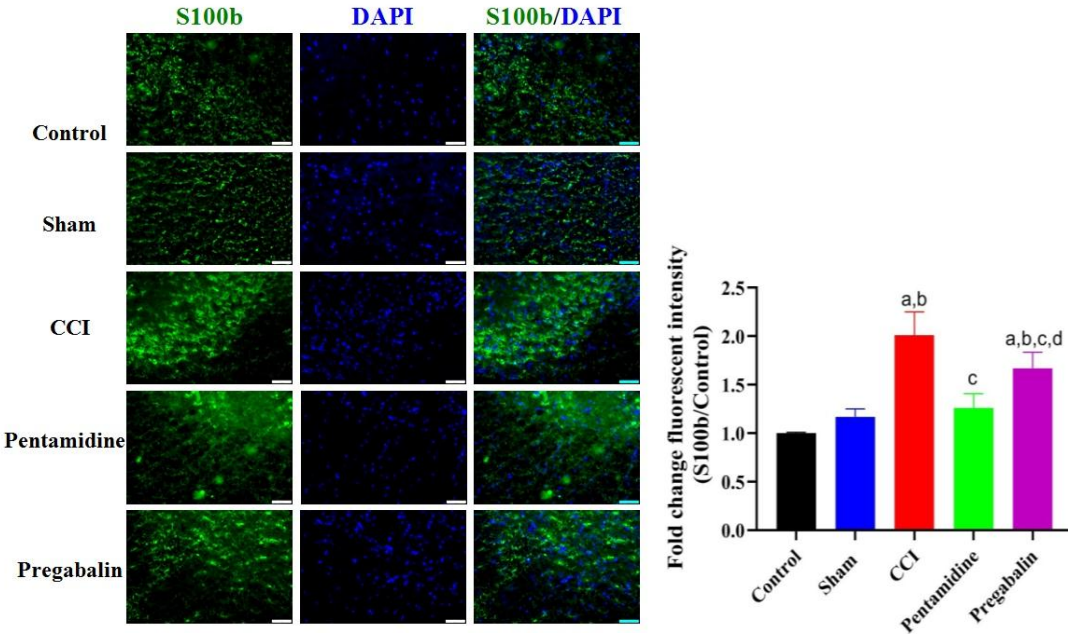

Figure 5.14: Effect of pentamidine on S100b expression in the SC. Scale bar was set at 50 µM with 20X magnification. All values are in mean ± SD (n=3 rats/ group). $^{a}p<0.05$, $^{b}p<0.05$, $^{c}p<0.05$, and $^{d}p<0.05$ compared to control, sham, CCI, and pentamidine respectively. (One-way ANOVA followed by Tukey's multiple comparison post-hoc test)

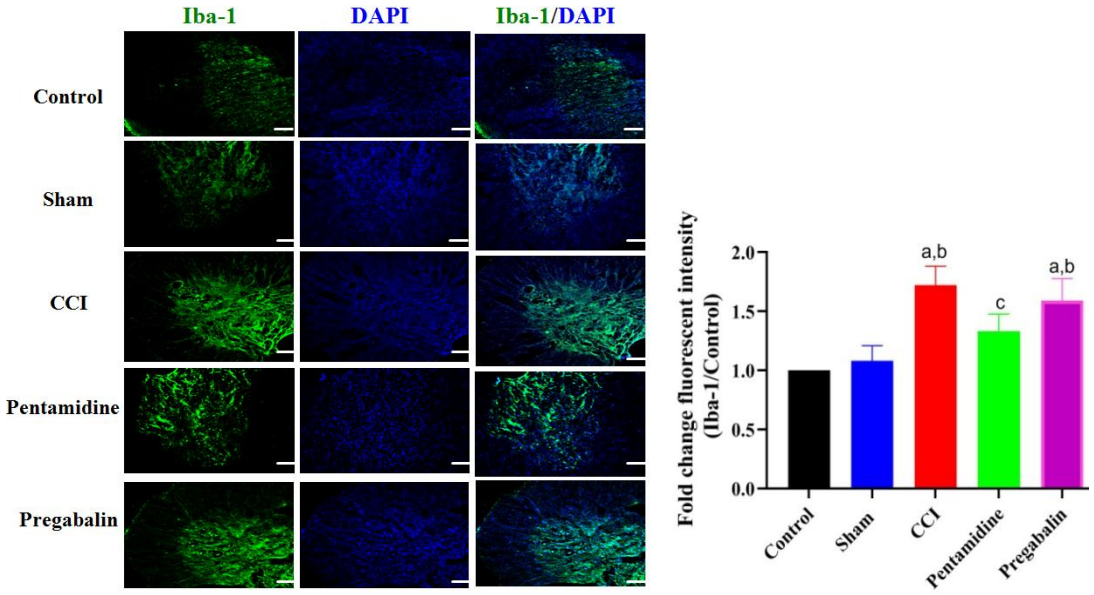

Figure 5.15: Effect of pentamidine on Iba-1 expression in the SC. Scale bar was set at 50 µM with 20X magnification. All values are in mean ± SD (n=3 rats/ group). $^{a}p<0.05$, $^{b}p<0.05$, and $^{c}p<0.05$ compared to control, sham, and CCI respectively. (One-way ANOVA followed by Tukey's multiple comparison post-hoc test)

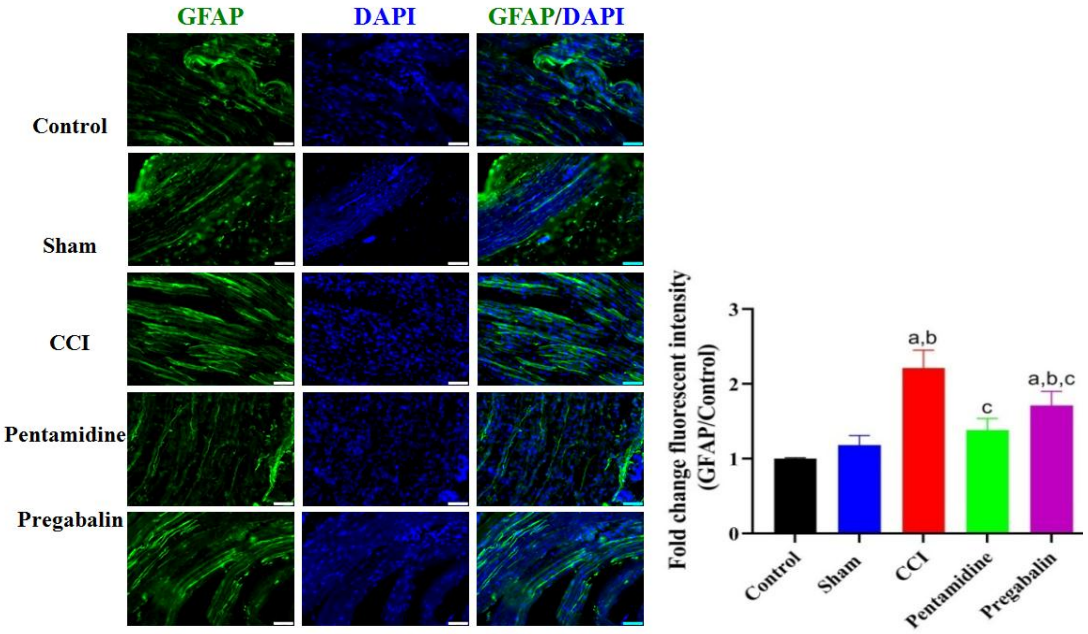

Figure 5.16: Effect of pentamidine on GFAP expression in the SN. Scale bar was set at 50 µM with 20X magnification. All values are in mean ± SD (n=3 rats/ group). $^{a}p<0.05$, $^{b}p<0.05$, and $^{c}p<0.05$ compared to control, sham, and CCI respectively. (One-way ANOVA followed by Tukey's multiple comparison post-hoc test)

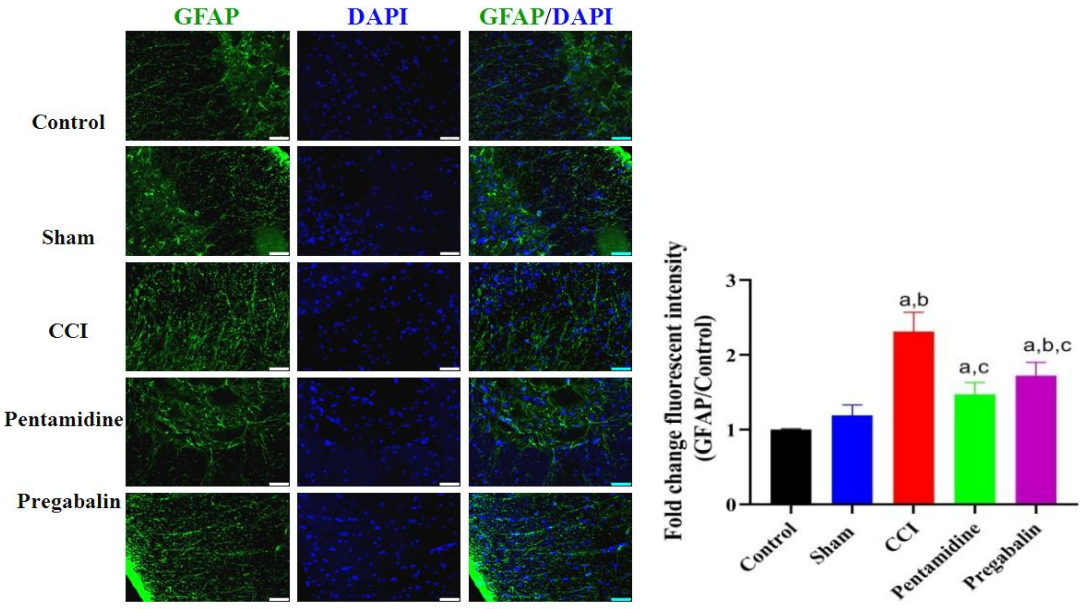

Figure 5.17: Effect of pentamidine on GFAP expression in the SC. Scale bar was set at 50 µM with 20X magnification. All values are in mean ± SD (n=3 rats/ group). $^{a}p<0.05$, $^{b}p<0.05$, and $^{c}p<0.05$ compared to control, sham, and CCI respectively. (One-way ANOVA followed by Tukey's multiple comparison post-hoc test)

5.2.2.8. Effect of pentamidine on the CCI-induced neuroinflammation

The CCI-induced increase in the pro-inflammatory cytokines was measured in the SN and SC of the rats expressing NP phenotypes as represented in **Figure 5.18**. The objective was to investigate the downstream pro-inflammatory cytokines that are produced after the activation of S100b and whether specific S100b inhibitors can alleviate NP via mitigation of neuroinflammation. In our study, the mRNA gene expression of NF-κB was performed and significant differences were observed among different groups. One-way ANOVA revealed significant variations in NF-κB gene expression in SN and SC ([F (4, 19) = 49.49; $p < 0.05$] and [F (4, 19) = 39.48; $p < 0.05$] respectively) (**Figure 5.18i and ii**). The post hoc test demonstrated that NF-κB mRNA expression had significantly elevated in the SN and SC of the CCI group compared to naïve and sham rats. Specifically, there was a 2.48 and 2.06-fold increase in NF-κB expression in SN and SC of CCI rats respectively. However, the treatment with pentamidine alleviated the increase in NF-κB significantly ($p < 0.05$), a key regulator of inflammatory responses on D-21.

Further, statistically, one-way ANOVA also revealed that there was a significant difference in TNF-α level in the SN and SC among the group ([$F(4,19) = 154.8$; $p<0.05$] and [$F(4,19) = 136.2$; $p<0.05$] respectively**)** as depicted in **Figure 5.18ii A and C**. Similarly, we observed significant differences in pro-inflammatory cytokine i.e., IL-6 among the various groups in SN and SC ([$F(4,19) = 37.91$; $p<0.05$] and [$F(4,19) = 52.68$; $p<0.05$] respectively**)** as shown in **Figure 5.18ii B and D**. The post hoc test demonstrated that TNF-α and IL-6 levels was significantly elevated in CCI group compared to naïve that was reversed following pentamidine treatment ($p < 0.05$). Likewise, in support of our observation, previous reports have demonstrated S100b-

mediated NF-κB pathway activation that led to downstream pro-inflammatory cascade activation (Barros, Barateiro et al. 2022).

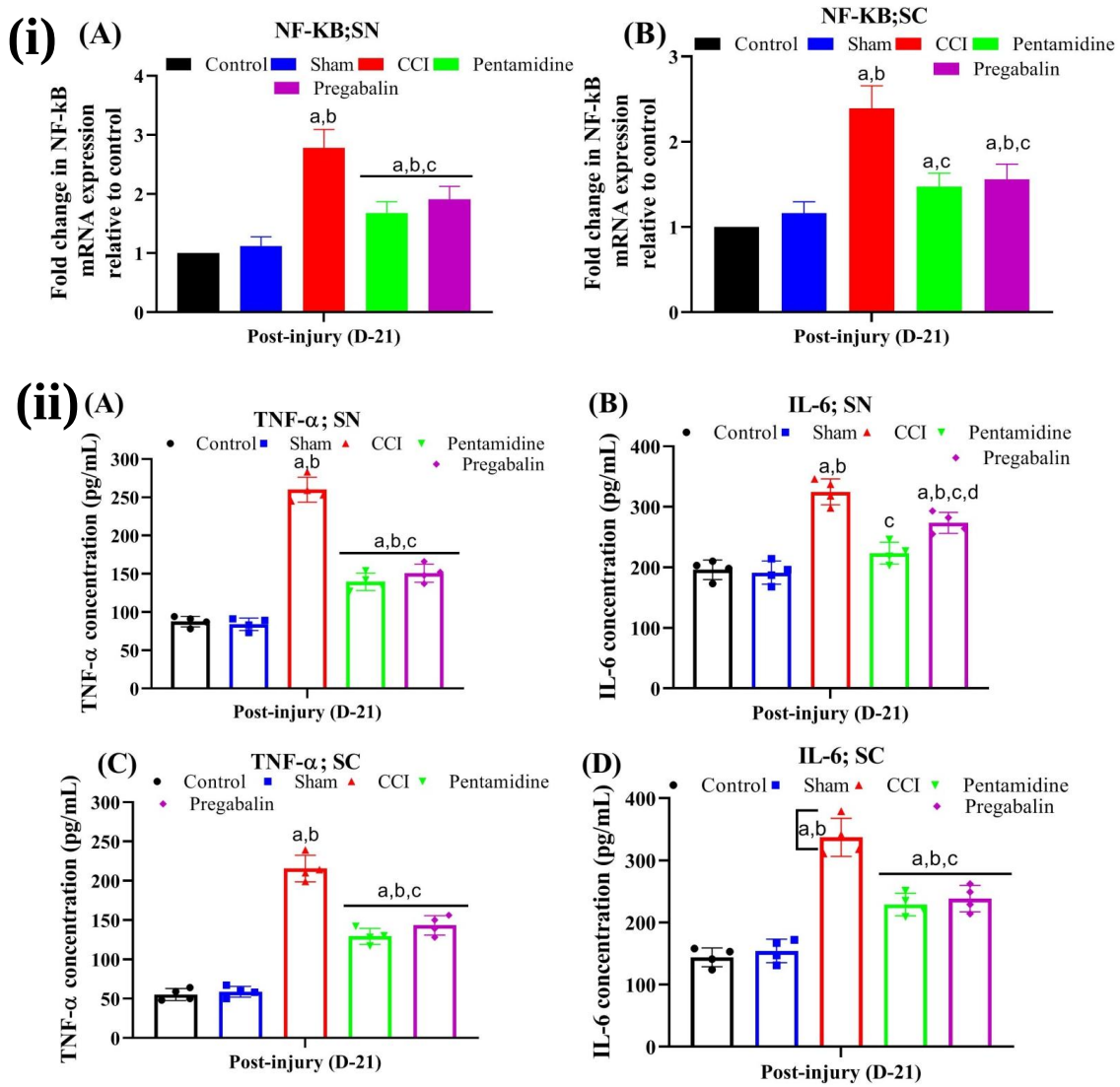

Figure 5.18: Effect of pentamidine on (i) NF- κB mRNA expression and (ii) TNF-α and IL-6 levels in the SN and SC. All values are in mean ± SD (n=4 rats/ group). $^{a}p<0.05$, $^{b}p<0.05$, $^{c}p<0.05$, and $^{d}p<0.05$ compared to control, sham, CCI, and pentamidine respectively. (One-way ANOVA followed by Tukey's multiple comparison post-hoc test)

5.2.2.9. Effect of pentamidine on the neuronal morphology post-CCI injury

We analyzed the neuronal morphology in the SC sections post-CCI injury as shown in **Figure 5.19**. In the CCI rats, there was disintegration and retraction of the dendrites of

neurons present in the SC. The dendrites were broken into small fragments and there was also a reduction in the number of branching across the soma following injury to the peripheral nerve. However, treatment with pentamidine as well as pregabalin led to dendrite arborization. Further, we traced individual neurons that were subjected to Sholl analysis as represented in **Figure 5.20i**. The results showed that the intersections of dendrites with concentric circles at each radius were dramatically decreased in the injured rats. Statistical analysis using the one-way ANOVA approach demonstrated significant differences in the total length of the dendrites [$F(4, 19) = 12.29$, $p < 0.05$, **Figure 5.20iiC**] among different experimental groups. Post-hoc analysis revealed that following treatment with pentamidine significantly increased the total length of the dendrites compared to the CCI group which had decreased significantly post-injury to the nerve. Furthermore, the dendritic arbors in the treatment group were longer and had more intersections at each radius compared with those in the CCI group, as determined by Sholl analysis (**Figure 5.20iiA and B**). These results indicate that spinal neuronal dendrite arborization degenerated dramatically after CCI, but the degeneration was alleviated upon specific inhibition of S100b. Similarly to our observations, it has been reported that when synaptic rewiring occurs, the remaining neurons try to rewire to make newer synaptic neural connections in order to repair and compensate for the loss of function (Tan, Stamboulian et al. 2008). The extent of functional recovery post-injury depends on the efficiency of neural circuit reconnection such as reactivating and reorganizing the intraspinal neuronal connections.

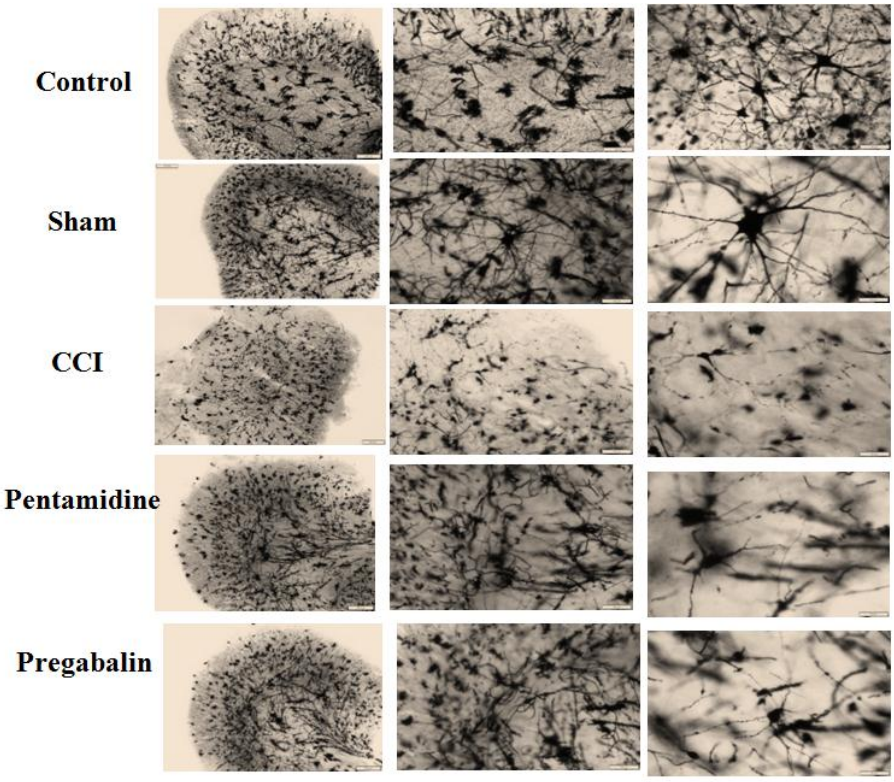

Figure 5.19: Representative images of Golgi-cox impregnated spinal cord slice of control, sham, CCI, pentamidine, and pregabalin treated rats. Scale bar was set at 200, 100, and 50 μM with 4, 10, 20X magnification.

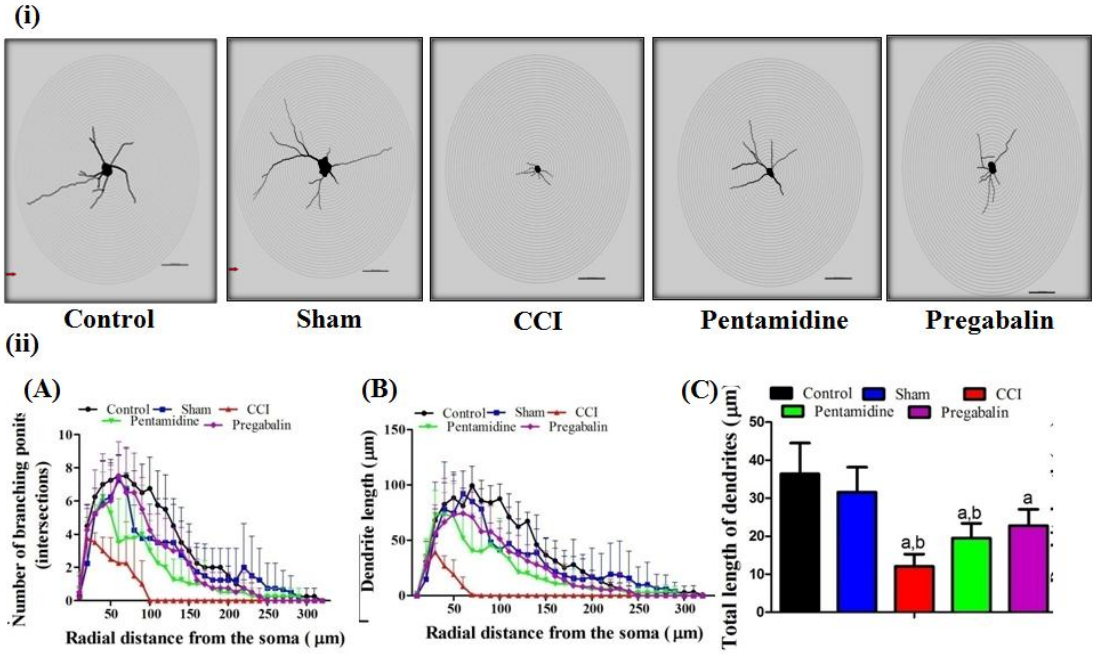

Figure 5.20: (i) Representative image of the camera lucida drawing of neuron of SC which is superimposed over concentric circles using Sholl analysis. (ii) Effect of pentamidine on (A) number of branching points across the soma, (B) dendrite length at radial distance from the soma and (C) the total length of dendrites. All values are in

mean ± SD (n=4 / group). [a]$p<0.05$ and [b]$p<0.05$ compared to control and sham respectively. (One-way ANOVA followed by Tukey's multiple comparison post-hoc test)

5.2.2.10. Effect of pentamidine on the CCI-induced changes in NF-L expression in the SN

Neurofilament (NF) proteins are the crucial components of the cytoskeleton in the neurons of nervous systems and they serve as the structural framework for axons (Huehnchen, Schinke et al. 2022). In the context of NP, the negative symptoms are often reported to be correlated with the deterioration of bigger myelinated axons, whereas positive and pain symptoms are typically connected to the impairment of smaller unmyelinated fibers (Scripture, Figg et al. 2006). Therefore, in the present study, we evaluated the effect of CCI on NF-L and observed that there was a significant decrease in the fluorescent intensity of NF-L in the rats after the injury. One-way ANOVA followed by a post-hoc test demonstrated significant changes among the group [$F(4,14) = 35.34$; $p<0.05$]. In the control group, the alignment of NF-L is observed but in the CCI rats, NF-L is found to be fragmented and scrambled as illustrated in **Figure 5.21**. Treatment with pentamidine rats exhibited elevated NF-L expression in the SN compared to the CCI group, indicative of axonal regrowth. However, the pregabalin treatment was found to be not as effective as a specific S100b inhibitor. Our data agree with previous preclinical work where axonal damage elevated S100b levels that contributed to a pro-inflammatory environment and decreased the NF level in the axon (Kuhle, Gaiottino et al. 2015, Adamczyk, Morawiec et al. 2023). Therefore, these results ascertain that modulating S100b has the axonal repairing potential and thus the functional repair was observed during the pain behavioral assessment tests (**Figure 5.9**).

5.2.2.11. Effect of pentamidine on the gastrocnemius muscle post-CCI injury

Post-CCI injury, there was a significant reduction in the weight of gastrocnemius muscle of the ipsilateral side of CCI rats (i.e., 0.462 ± 0.064187 g) compared to the control rats i.e., 1.48 ± 0.070214 suggesting muscle atrophy (**Figure 5.22**). One-way ANOVA revealed significant variations in the muscle weight among groups ([F (4, 24) = 280.5; $p < 0.05$] (**Figure 5.22C**). Tukey's post hoc test demonstrated that following the constriction injury to SN, the weight of gastrocnemius muscle had reduced significantly in the CCI group compared to naïve and sham rats which was reversed following pentamidine treatment ($p < 0.05$). The gastrocnemius muscle is the largest muscle which is innervated by the branches of the SN and helps in the flexion of the knee, aiding in body movement. However, denervated muscles lose signal transmission from the nervous system and are unable to maintain the contraction function. Thus, injury to the SN is reported to cause immobilization or reduced use of the affected limb (Choe, Kim et al. 2011). Prolonged disuse or restricted movement of the affected limb subsequently causes muscle atrophy as reported preclinically (Choe, Kim et al. 2011) and this is consistent in patients suffering from NP (Bhindi, Angliss et al. 2022). Further, there are reports of reduced muscular protein synthesis and an increase in protein breakdown, causing myatrophy and reduced gastrocnemius muscle weight (Wang, Chen et al. 2021) as observed in our study **Figure 5.22A**. Moreover, the histological analyses of the gastrocnemius muscle of control rats revealed homogeneous morphology with the densely packed polygonal-shaped skeletal muscle fibres along with the peripheral oval nuclei. On the other hand, the CCI group exhibited fragmentation of the sarcoplasm with mononuclear cell infiltration (**Figure 5.22B)**. There was also a widening of endomysium observed in the injured rats. However,

treatment with pentamidine significantly increased the gastrocnemius muscle fiber cross-section area to 49.6 ± 3.51 from 37.8 ± 3.89 % as observed in CCI rats. In light of these findings, it can be inferred that motor impairments are closely linked to the CCI model of NP and specific S100b inhibitor reversed all core symptoms of NP along with the observed motor incoordination.

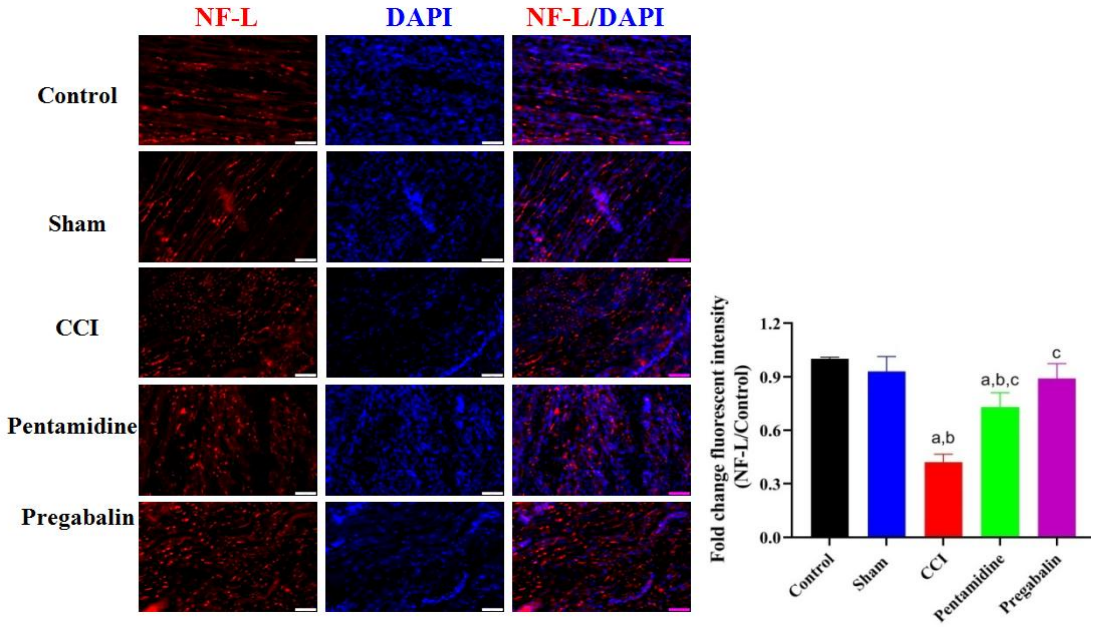

Figure 5.21: Effect of pentamidine on NF-L expression in the SN. Scale bar was set at 50 µM with 20X magnification. All values are in mean ± SD (n=3 rats/ group). $^{a}p<0.05$, $^{b}p<0.05$, and $^{c}p<0.05$ compared to control, sham, and CCI respectively. (One-way ANOVA followed by Tukey's post-hoc test)

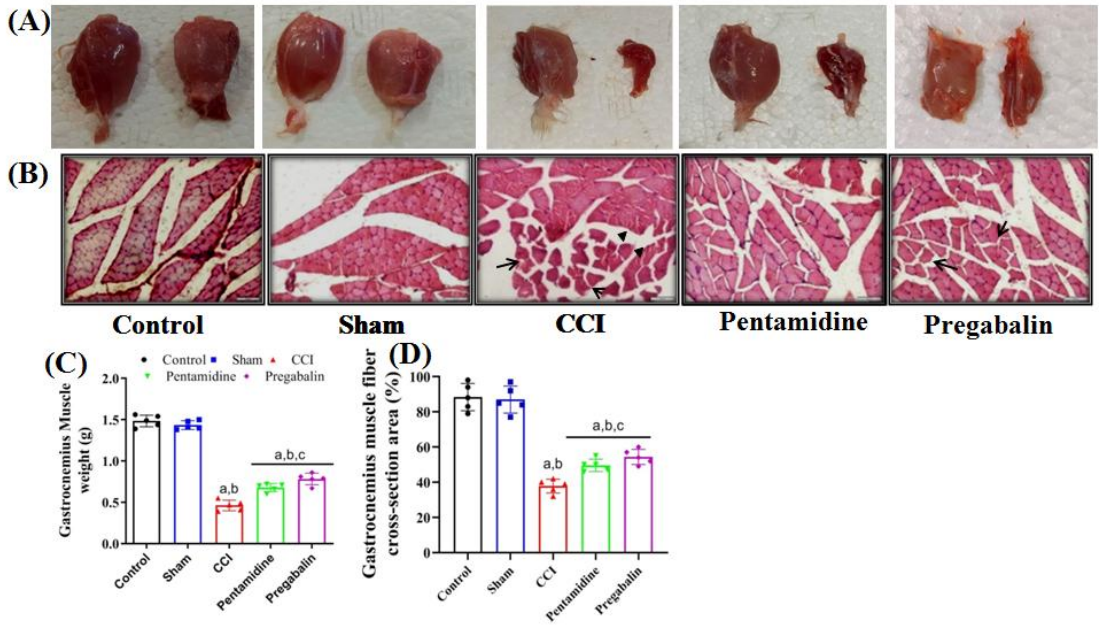

Figure 5.22: (A) Representative images of the gastrocnemius muscle of the contralateral and ipsilateral side of the leg. (B) Representative image of the histological analyses of gastrocnemius muscle stained with hematoxylin and eosin at the end of 21st day post-surgery. (C and D) The effect of pentamidine on gastrocnemius muscle weight and cross-section area of muscle fibers. All values are in mean ± SD (n=5 rats/ group). $^{a}p<0.05$, $^{b}p<0.05$, $^{c}p<0.05$, and $^{d}p<0.05$ compared to control, sham, CCI, and pentamidine respectively. (One-way ANOVA followed by Tukey's multiple comparison post-hoc test)

5.3. Conclusion

In the current study, our findings establish the temporal dynamics and significant details about the involvement of intracellular calcium and S100b protein levels in the progression and sustenance of CCI-induced NP in rats. Following CCI, there was a notable time-dependent increase in the intracellular calcium and S100b protein level in both the SN and SC acutely 1 h post-injury. However, treatment with a specific S100b inhibitor i.e., pentamidine significantly reversed the NP phenotypes induced by CCI, suggesting that S100b plays a pivotal role in the pathophysiology of NP. Pentamidine treatment also demonstrated efficacy in alleviating motor deficits associated with the CCI model. Notably, the study also demonstrated hyperactivation of astrocytes and microglia induced by S100b which was reduced following the pentamidine

administration. Therefore, by inhibiting glial cell activation, pentamidine disrupted the feed-forward loop of inflammation and pain, contributing to the reversal of NP phenotypes. Moreover, pentamidine treatment significantly lowered the S100b-induced increase in pro-inflammatory markers, specifically TNF-α and IL-6, in SC and SN post-injury. However, unlike pregabalin, pentamidine was unable to reverse the elevated intracellular calcium levels in the SN and SC post-injury. In conclusion, these findings provide compelling evidence supporting the role of S100b in the pathogenesis of NP and highlight the therapeutic potential of S100b inhibition.

Summary

- There is temporal increase in the intracellular calcium and S100b level in SN and SC post-CCI.
- Treatment with specific S100b inhibitor i.e., pentamidine significantly reversed the NP phenotypes.
- The motor deficits due to CCI were also alleviated following pentamidine treatment.
- Pentamidine lowered the S100b-induced increase in pro-inflammatory markers (TNF-α and IL-6) in SC and SN post-injury to the peripheral nerve.
- Pentamidine also reduced the S100b-induced hyperactivation of astrocytes and microglia.
- Unlike pregabalin, pentamidine was unable to reverse the elevated intracellular calcium level in the SN and SC post injury to the peripheral nervous system.

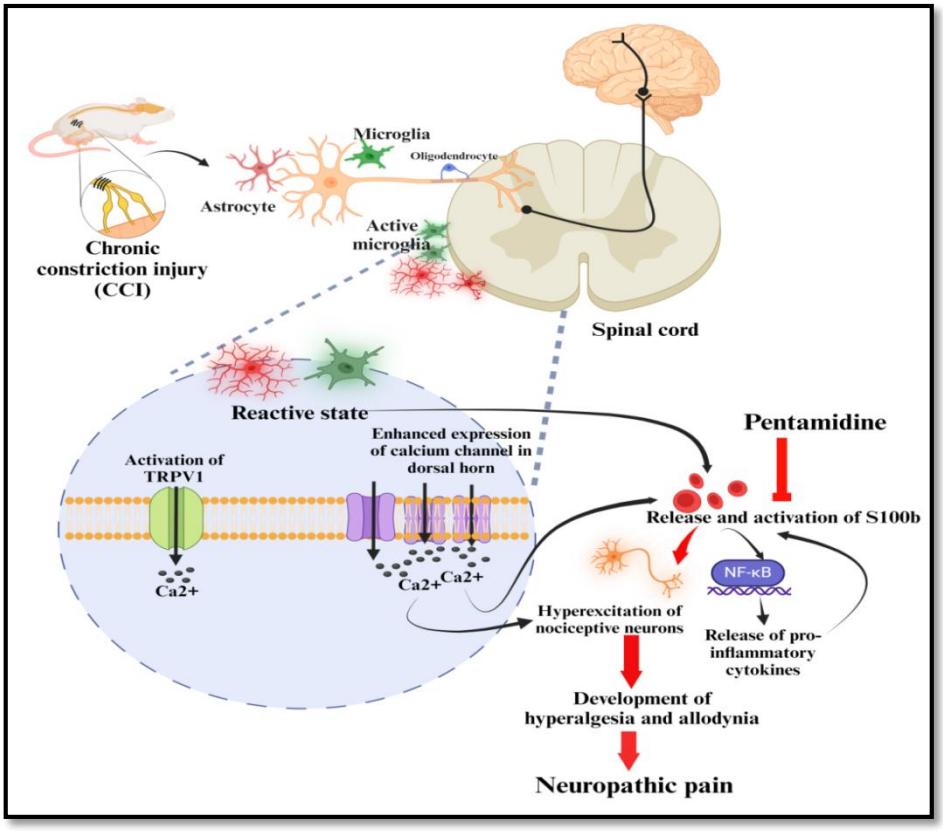

Figure 5.23 showcases the specific objective's outcome in exploring the molecular mechanism behind neuropathic pain (NP) in a CCI-induced rat NP model. It suggests that the development and progression of NP is associated temporal increase in the intracellular calcium and calcium-binding protein i.e., S100b. Treatment with pentamidine, a specific S100B inhibitor, significantly reversed the neuropathic pain phenotypes induced by CCI. Besides, CCI of peripheral nerve caused hyperactivation of astrocytes and microglia that was induced by S100B and pentamidine attenuated these observed changes. Treatment with pentamidine also lowered the S100B-induced increase in pro-inflammatory markers, specifically TNF-α and IL-6, in both the SC and SN post-injury. Therefore, these findings highlight that S100b is involved in progression and development of NP phenotypes in the CCI-induced NP model and could be the essential factor for an analgesic drug for better management of NP.

Chapter 6

Pharmacological evaluation of BaBG in the treatment of Neuropathic pain

6. Introduction

Damage to the peripheral nervous system (PNS) can result in the development of atypical painful conditions collectively known as neuropathic pain (NP) (Colloca, Ludman et al. 2017). It involves an overlay of multiple pathophysiological alterations in the PNS and CNS, resulting in peripheral and central sensitization (Meacham, Shepherd et al. 2017). NP is a multifaceted and complicated phenomenon that encompasses numerous pain syndromes with different etiology, but they often have common symptoms such as heightened sensitivity to pain triggered by non-painful stimuli, with sudden and unpredictable pain episodes and abnormal sensations (Colloca, Ludman et al. 2017, Bannister, Sachau et al. 2020). Further, studies have demonstrated that neuropathy causes alterations in the expression of ion channels in the affected nerves, resulting in neuroplastic changes in the spinal and supraspinal tracts (Baron 2006). These changes play a significant role in the development and persistence of NP. It entails an aberrant increase in the intracellular calcium level [$(Ca^{2+})_i$], which further contributes to the pathogenesis of the disease (Siau and Bennett 2006, Cui, Wu et al. 2021). Currently, the primary pharmacological approaches for clinically managing chronic NP involve the use of calcium channel blockers (CCBs) such as pregabalin and gabapentin (Tong, Zhengyao et al. 2021). The efficacy of gabapentinoids (GBP) has been demonstrated clinically and in several preclinical NP models (Verma, Singh et al. 2014, Derry, Bell et al. 2019, Forouzanfar, Tanha et al. 2023). Previous studies have shown that GBP binds to the auxiliary unit of calcium channels and effectively reduces the central release of excitatory neurotransmitters, causing hyperexcitability of the nociceptors leading to hyperalgesia and allodynia (Patel and Dickenson 2016). All the CCBs that are currently used are organic compounds and the primary and common

adverse effects identified in GBP that result in its discontinuation in clinical usage are associated with the increased likelihood of atrial fibrillation along with somnolence and dizziness (Park, Hunter et al. 2023). Therefore, it is imperative to develop novel therapeutic approaches targeting calcium channels to effectively treat NP.

Barium is a rare trace element present in the human body (22 mg in a 70 kg adult) (Schroeder, Tipton et al. 1972), mainly in the bones and also in muscle, skin, connective tissue, and the lungs and elicits various physiological functions (Satoh, Kubota et al. 1987, Majumdar, Gupta et al. 2021, Majumdar, Hira et al. 2021). According to reports, barium is found in exoplanets, indicating that all living organisms have developed with barium in their bodies (Silva, Demangeon et al. 2022). In addition, barium is found in rocks, soil, and water (Myrvang, Gjengedal et al. 2016), meaning that every living organism is inevitably exposed to barium. Thus, our body has mechanisms to utilize as well as eliminate it, unlike the organic compounds that are foreign to the body. Previously, fewer reports indicated that the presence of Ba^{2+} in the extracellular fluid resulted in prolonged action potential plateaus observed in the growth cone of regenerating axon of lamprey (Macvicar's and Llinas 1985). Barium is also reported to generate a barium spike in the growth cone of the regenerating axon (Macvicar's and Llinas 1985). Besides, the calcium channels exhibit greater selectivity for Ba^{2+} ions compared to Ca^{2+} ions (Hagiwara and Byerly 1981). In light of the aforementioned facts, we have selected inorganic barium-doped bioactive glass (BaBG) in our current investigation. BaBG is safe and devoid of organ toxicity (Majumdar and Krishnamurthy 2022) as mentioned in **Chapter 4**. BaBG also possesses regenerative potential, as observed in the scratch assay which is an *in-vitro* transection model of neurotrauma (Majumdar, Hira et al. 2021). Additionally, our previous studies have established the

anti-inflammatory properties of BaBG, which have been extensively discussed in detail in **Chapter 2** and NP development is closely linked with neuroinflammation (Ellis and Bennett 2013, Teixeira-Santos, Albino-Teixeira et al. 2020). Further, in our previous preliminary work, the BaBG scaffold (Indian patent No.: 484408) has exhibited the ability to regenerate the deafferented nerve in the complete transection model of NP. Therefore, BaBG has the potential to be used for the treatment of NP which would probably act on the calcium channels and CCBs are widely used for the management of NP.

Further, in **Chapter 5**, we have observed that there was a time-dependent increase in the intracellular calcium and S100b levels in the CCI-induced NP model. Besides, S100b induces the aberrant release of pro-inflammatory cytokines that are involved in the development and progression of NP phenotypes (Tanga, Raghavendra et al. 2006, Stefani, Leite et al. 2019). In addition, prior research has shown that the presence of Ba^{2+} inhibits the release of S100b from primary astrocyte cultures (Vizuete, Hansen et al. 2019). Consequently, we believe that barium leached from the BaBG has the potential to mitigate the S100-induced neuroinflammation, a crucial factor involved in the persistence of NP.

To validate our hypothesis, in the present study, NP was induced by chronic constriction injury (CCI) of sciatic nerve (SN) in rats and the effect of BaBG on the development of the sensory hypersensitivity and characteristic motor impairment observed in NP were evaluated for the first time by various behavioral tests. Then the calcium-regulating mechanism of BaBG was elucidated in the *ex vivo* electrophysiology set-up. Additionally, the effects of BaBG on the $(Ca^{2+})_i$ and S100b level were evaluated post-CCI injury. Following this, we measured the severity of neuroinflammation developed

in this model and assessed the impact of BaBG on the level of pro-inflammatory cytokines. We also quantified the expression levels of the markers of glial cell activation i.e., GFAP in SN and spinal cord (SC) post-SN injury and the effects of BaBG on them. Further, to investigate the effect of BaBG axonal damage, we performed analyses involving NF-L-positive staining of SN. Moreover, we investigated the effect of BaBG on alterations in the neuronal morphology in the CCI model using Golgi-Cox staining. Additionally, we quantified myatrophy using hematoxylin and eosin staining in this model and evaluated the effects of BaBG on it. **Figure 6.1** illustrates the graphical representation depicting the schematic diagram outlining the proposed hypothesis concerning the molecular mechanism underlying the pathogenesis of NP in a rat model induced by CCI of SN and the effect of BaBG on them.

Hypothesis

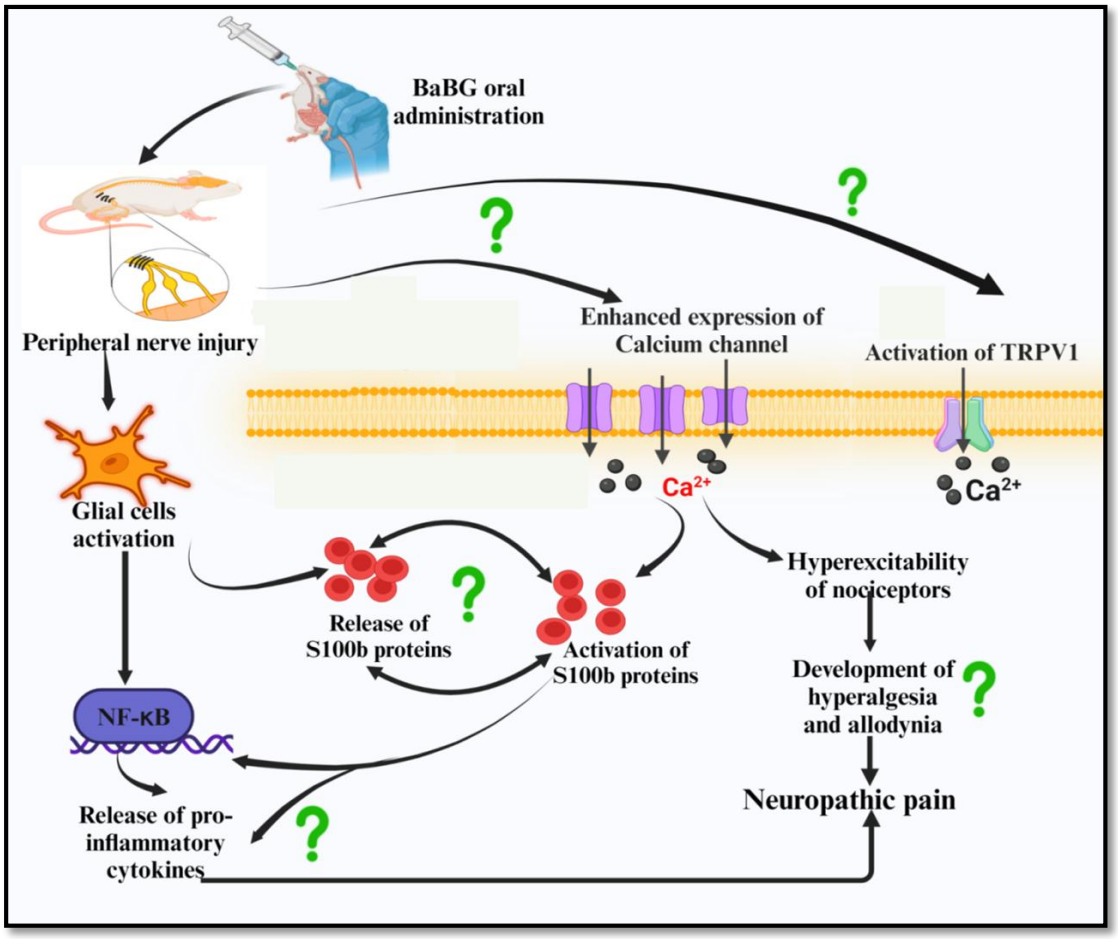

Figure 6.1 presents a graphical representation depicting the schematic diagram outlining the proposed hypothesis concerning the molecular mechanism underlying the pathogenesis of NP in a CCI-induced NP rat model. The injury to the sciatic nerve (SN) leads to central sensitization due to upregulation in the expression of calcium channels ($Ca_v2.2$) in the dorsal horn of the spinal cord (SC). Besides, there are also enhanced expression of heat-sensing TRPV1 channels in the SC. Enhanced expression of these channels increases the influx of calcium ions leading to hyper excitation of the nociceptive neurons and the development of NP phenotypes. In addition, the glial cells get activated post-CCI leading to an increase in the release of calcium-binding proteins i.e., S100b that further triggers the release of pro-inflammatory cytokines and contributes to the progression of NP. Barium-doped bioactive glass (BaBG) leaches barium ions from its framework after coming in contact with the physiological fluid. BaBG, due to its calcium-modulating effects may alleviate sensory and motor deficits observed in the CCI-induced NP in rats. It may also prevent the activation of calcium-binding protein i.e., S100b, reduce neuroinflammation, and concurrently cause axonal repair and remodeling; hence may have disease-modifying effects.

6.1. Materials and methods

6.1.1. Materials

The molecular biology kits and reagents used in the qPCR experiment include TRI reagent & DEPC that was sourced from Sigma. The revert aid cDNA synthesis kit (Thermo Scientific), TURBO DNA-freeTM (Ambion), TURBO DNA-free™ Kit (Invitrogen), Maxima SYBR Green/ ROX qPCR master mix 2X and primers (Eurofins Genomics India), Prestained protein MW marker (Puregene) and 100bp DNA marker (MBI Fermentas), 6X DNA loading buffer (Thermo Scientific), and RNAase cocktail (Invitrogen) was used in this study. All the primer sequences used (**detailed in Table 6.1**) were sourced from Eurofins Scientific. Triton X-100, Dabco, 3-aminopropyltriethoxysilane, and formaldehyde were acquired from Sigma, USA. Tween-20 was purchased from Merck and DAPI was obtained from SRL. Fura2 AM was purchased from ChemCruz. For the study, the ELISA kits used were from Krishgen Biosystems. The primary antibodies used in the experiment are GFAP (No.: ab7260, Abcam), S100b (No. E-AB-60087; Elabscience Biotechnology Co., Ltd., USA), NF-L (No. CST-2837T; Cell Signaling Technology), and Iba1 (No. 019-19741; FUJIFILM Wako Chemicals U.S.A.). The secondary antibodies used are goat anti-rabbit IgG FITC (ab6717; Abcam) and goat anti-rabbit IgG TRITC (ab6718, Abcam). The Luxol fast blue stain (CAS No. 1328-51-4) was obtained from Himedia, India.

6.1.2. Experimental animals and their ethical statement

The experiment used adult male Wistar albino rats weighing 200 ± 20 g, which were procured from the Central Animal House, IMS-BHU, Varanasi, India. Before commencing the experiment, the rats had one week of acclimatization at a consistent temperature of 25±1°C, with a 12-hour cycle of light and darkness. The experimental

animals were provided with *ad libitum* supply to a regular laboratory feed and water during the entire course of the trial. The rats were kept in cages measuring 430 x 270 x 150 mm and filled with corn cob bedding. Every possible attempt was made to decrease the quantity of animals utilized throughout the experiment. The experiments were conducted following the guidelines of the Committee for the Control and Supervision of Experiments on Animals (CCSEA), Government of India and "Care and Use of Experimental Animals" (Vol.1, 2nd ed., 1993, and Vol.2, 1984) guidelines of National Institute of Health, U.S.A. The experimental protocol for the present study evaluating the pharmacological effects of BaBG for the treatment of NP was approved by the Institutional Animal Ethical Committee (IIT(BHU)/IAEC/2022/037). Similarly, for performing the *ex vivo* electrophysiological assessment of calcium channel blocking effects of BaBG was approved by the Institutional Animal Ethical Committee (IIT(BHU)/IAEC/2023/029).

6.1.3. *Ex vivo* electrophysiological assessment of calcium channel blocking effects of BaBG

6.1.3.1. Preparation of physiological fluid (PF)

To prepare the PF, 112 mM NaCl, 2mM KCl, 2 mM NaH_2PO_4, and 1 mM $CaCl_2$ were used. All the salts were weighed and dissolved in distilled water and the pH was adjusted to 7.4. The solution was then stored at room temperature before usage. Before using the PF for the experiment, BaBG and 45S5 were weighed (1.5 mg/mL) and incubated in it for 3 days at room temperature. Then the PF was filtered and the supernatant was utilized in the *ex vivo* electrophysiological study.

6.1.3.2. *Ex vivo* electrophysiological assessment

All the Wistar rats were weighed and randomly allocated to seven experimental groups namely: (A) In the PF, (B) In the PF containing Pregabalin, (C) In the PF containing

BaBG, (D) In the PF containing $BaCl_2$, (E) In the PF containing 45S5, (F) In the PF containing reduced calcium ions and BaBG, and (G) In the PF containing BaBG and Pregabalin. Each group had four animals (n=4 rats/ group). The rats were anesthetized using thiopental sodium (50 mg/kg, *i.p.*) and euthanized. The sciatic nerve (SN) was isolated and care was taken not to touch the nerve with any metal forceps as metals touching the tissue may conduct electrical charges and alter the physiological activity of it. The isolated nerve was then stabilized in physiological fluid (PF) at 37 °C for 30 min. Then SN was placed on the nerve chamber (iWorx NCB-401) and stimulated at 1V. The compound nerve action potential (CAP) was generated was recorded using aniWorx214-two channel data recorder connected to the laboratory desktop PC running LabScribe (version 4.014000) (Medler 2022) as illustrated in **Figure 6.2**. Immediately after recoding, the SN was transferred back to the fresh PF to prevent drying out and to recover from the treatment effect.

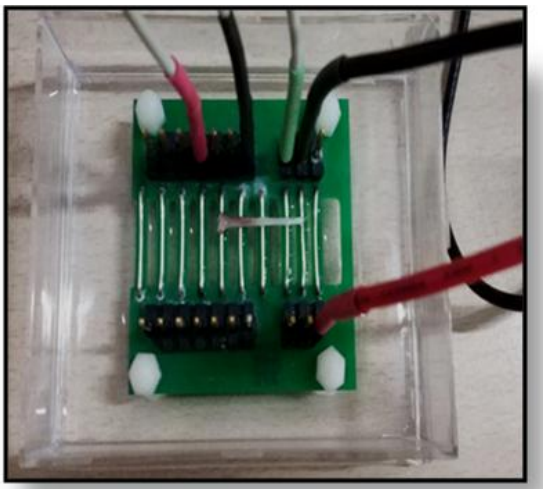

Figure 6.2. Schematic representation of the Plexiglas nerve bath chamber nerve apparatus with the ground, stimulating, and recording electrode used in the experiment. The isolated sciatic nerve (SN) is placed over the platform of the nerve chamber in the presence of physiological fluid containing the test compounds is stimulated and the compound nerve action potential (CAP) generated is recorded.

6.1.4. Chronic constriction injury (CCI) model of Neuropathic pain

The NP was induced in the rats by CCI of the sciatic nerve (Bennett 1993) as mentioned in **Chapter 5**. The experimental animals were anaesthetized intra-peritoneally using ketamine (80 mg/kg) and xylazine (10 mg/kg). Once under anesthesia, the rats were put on a 37 °C thermo-regulated heating surface. An incision parallel to the femur was made after shaving and sterilizing the right leg skin. The sciatic nerve was exposed by a gluteal muscle incision. Around 10 mm of the sciatic nerve proximal to the trifurcation was freed from the surrounding connective tissue and four loose ligatures (silk 4/0; Ethicon, USA) were tied with a gap of 1 mm around the nerve. The constriction of the sciatic nerve while tying the ligatures was done till a brief twitch was observed to prevent obstruction of the epineural blood flow. After suturing the muscle with 6/0 reabsorbable suture, the animals were kept under observation. Iodine solution was applied before and after incision suturing to reduce local infection.

6.1.5. Experimental design for pharmacological evaluation of BaBG for the treatment of NP

Before establishing the experimental protocol, a G*power analysis was performed to identify the appropriate sample size. This analysis aimed to ensure that the type I and II errors are maintained below the acceptable level, as proposed by Cohen (Cohen 1988). All the Wistar rats were weighed and a randomized allocation was employed to assign animals to the seven experimental groups: Control, CCI, CCI + BaBG (1 mg/kg *p.o*), CCI + BaBG (5 mg/kg *p.o*), CCI + BaBG (10 mg/kg *p.o*), CCI + 45S5 (10 mg/kg *p.o*), and CCI + Pregabalin (30 mg/kg *p.o*). Each group had twelve animals (n=12 rats/ group). The experiment was performed for a period of 28 days. NP was induced by CCI

of SN and the behavioral assessments (hot-plate test, Randall Selitto test, acetone drop test, cotton swab test, rota rod test, sciatic functional index (SFI), and BBB (Basso, Beattie, and Bresnahan) test) were performed before the surgery (D-0) and on day 7, 14, 21, and 28 post-surgery to access NP phenotypes developed. Dosing was started from D-14 after the NP phenotypes were stabilized following CCI and continued up to D-28 (**Figure 6.3**). Following this, the anaesthetized animals were sacrificed by decapitation (3% v/v isoflurane inhalation; R620 veterinary anesthesia machine, RWD life science, San Diego, USA). The SN of the ipsilateral side of the leg and SC were harvested. The dissected tissues were immediately stored at -80 °C until further research. The tissues collected were processed for neurochemical and molecular analysis.

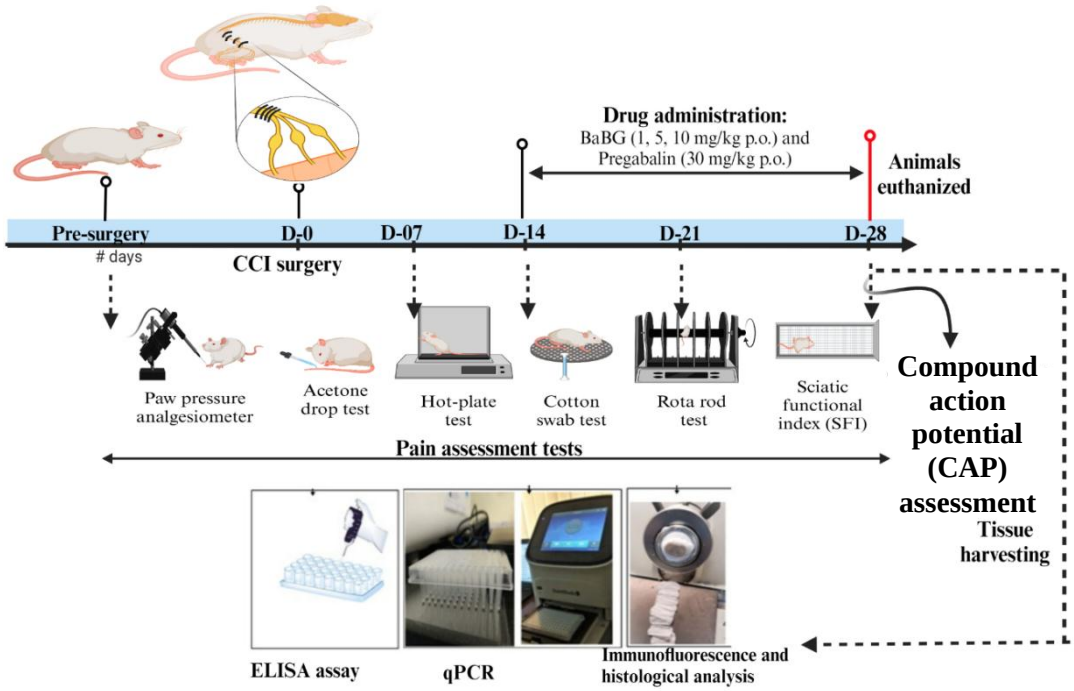

Figure 6.3: Schematic representation of the experimental protocol followed for the pharmacological evaluation of BaBG for the treatment of NP in rat CCI model.

6.1.6. Behavioral analysis:

The experimental animals were acclimatized to the testing environment before the baseline behavioral testing. The development of NP phenotypes was assessed before CCI surgery and on days 7, 14, 21, and 28 post-surgery.

6.1.6.1. Thermal hyperalgesia (hot-plate test)

The assessment of heat hyperalgesia in rats after surgery was conducted using Eddy's hot plate (Orchid Scientific, India) (Khangura, Bali et al. 2017). The plate's surface was warmed and the temperature was consistently maintained at 52.5 ± 0.5 °C. Next, the animals were placed on the hot plate and the time it took for them to exhibit the nocifensive withdrawal reaction, such as elevating and licking the rear paw of the injured side was recorded as nociceptive threshold. In order to prevent burn injuries to the animals, a cut-off period of 20 seconds was upheld.

6.1.6.2. Cold allodynia (acetone drop test)

The acetone drop test was used to assess the emergence of pain sensation in response to non-noxious stimuli (cool) following CCI surgery. During this experiment, the rats were initially adapted to a room with a mesh floor for 20 minutes. Subsequently, a volume of 100 µL of acetone was applied to the upper surface of the hind paw of the wounded leg. The frequent withdrawal, licking, biting, or flinching of the paw indicates the presence of cold allodynia, which is caused by the evaporation of acetone. The entire time of the withdrawal of the paw in the air, until it was placed back on the surface of the mess, was measured in seconds (Khangura, Bali et al. 2017).

6.1.6.3. Mechanical hyperalgesia (Randall Selitto test)

The Randall Selitto test-based digital paw pressure analgesiometer (Orchid Scientific, India) evaluated hyperalgesia to mechanical stimulation by measuring the mechanical nociceptive threshold to animal paw pressure. This test applies an increasing mechanical force focally to the dorsal surface of the impaired leg's hind paw using the pressure applicator until a withdrawal nociceptive response is detected. Pressure at which rats vocalized or displayed painful responses (flinching or withdrawal of paw or leg following stimulation) was recorded as the endpoint. The mean of three values interpreted to force in grams was the nociceptive threshold (Randall 1957, Ferrari, Rey et al. 2022).

6.1.6.4. Dynamic mechanical allodynia (Cotton swab test)

The cotton swab test in rats identified the development of dynamic mechanical allodynia after the induction of neuropathic pain by CCI (Field, Bramwell et al. 1999). Prior to the test session, the animals were acclimated to the Plexiglas chamber with mesh flooring to reduce their usual movements throughout the test duration. Next, a cotton swab was used to gently touch the planter portion of the ipsilateral hind paw of rats. The time it took for the paw to withdraw was measured, with a maximum time limit of 15 seconds.

6.1.6.5. Rota rod

The rotarod test is used to evaluate the motor coordination skills of rats after surgery (Prajapati, Garabadu et al. 2017). The animals under investigation are subjected to a two-day training period on the Rota rod (IKON instruments, India) at a minimum speed of 5 rpm. This is done to ensure that they achieve a consistent baseline performance.

Subsequently, in the testing phase, the rotational speed of the rod was elevated to 15 revolutions per minute. The animals' entire duration on the rod was recorded, with a maximum time limit of 300 seconds.

6.1.6.6. Sciatic functional index (SFI):

The SFI (sciatic functional index) was determined using the walking track analysis method, where the animals were required to travel on a straight track of 8.3 X 43 cm darkened at one end (de Medinaceli, Freed et al. 1982, Komirishetty, Areti et al. 2017). The SFI value is a scale that spans from 0 to -100. A number of 0 indicates normal functioning, while a value of -100 indicates complete impairment. Following two or three attempts on the track, the rats were trained to go directly to the dimly lit end without engaging in any exploration of the route. Subsequently, a sheet of white paper was positioned on the pathway, and the rear paws of the rats were immersed in distinct color solutions, with the uninjured left paw in green and the wounded right paw in red. Subsequently, the animal was positioned at the beginning of the track and given permission to traverse the paper. The ink on the paper had dried, and subsequent measurements were taken:

Print length (PL): The length of one foot print of normal (NPL) and experimental side (EPL).

Total spreading (TS): The linear distance between the center of first toe print and the center of fifth toe print of normal (NTS) and experimental side (ETS).

Distance between intermediary toes (IT): The linear distance between the center of second toe print and the center of fourth toe print of normal (NIT) and experimental side (EIT).

The SFI was calculated using the following formula:

$$SFI = -38.8(EPL-NPL)/NPL + 109.5(ETS-NTS)/NTS + 13.3(EIT-NIT)/NIT – 8.8$$

6.1.6.7. BBB (Basso, Beattie, and Bresnahan) locomotor test:

The BBB test is typically used to evaluate the decline in motor function following CCI of the SN in rats (Basso, Beattie et al. 1995). A trained observer, who was unaware of the experiment, assigns a score ranging from 0 to 21 based on the animal's movement. A score of 0 was assigned in the absence of any voluntary movement, whereas a score of 21 was given when the rats exhibited typical limb movement. Typically, a score of 14 is assigned to an animal that demonstrates full limb coordination. In this experiment, the animals being studied are placed in an open circular cage and monitored for 4 minutes and awarded scores accordingly.

6.1.7. Electrophysiological measurement of action potential

The rats were anesthetized and their core temperature was maintained at 37 °C using a homeothermic blanket device (Harvard, UK). Then the fur covering the hind limbs was shaved when the animals were already under analgesia. To ensure that no pathogens were introduced during the process, the shaved surface of the ipsilateral limb was cleaned with 70 % ethanol. Further, to ensure optimal conductivity and minimize transfer resistance while placing the electrodes, the contact gel was applied. The motor nerve conduction velocity (MNCV) was assessed by applying a single stimulus to the SN (proximal to the sciatic notch) and the tibial nerve (distal to the ankle) using bipolar needle electrodes with a diameter of 26 1/2 gauge and an intensity of 3 volts (Saini, HS et al. 2007). In the study, the Power Lab 8sp system (AD Instruments, Australia) was utilized to measure the Motor Nerve Conduction Velocity (MNCV). The CMAP (compound motor action potential) generated was recorded and its amplitude which is

a measure of the magnitude between the highest positive and lowest negative points of the CMAP signal, expressed in millivolts (mV) was calculated. Latencies were measured in each case from the initial onset of the CMAP. Further, MNCV was calculated using the formula:

$$\text{MNCV} = \frac{\text{Distance between sciatic and tibial nerve stimulation point}}{\text{Sciatic M wave latency} - \text{Tibial M wave latency}}$$

After completion of measurement, the rats were transferred to a separate cage until it has regained sufficient consciousness.

6.1.8. Electromyogram (EMG) recordings

During the CMAP recording, the EMG from the gastrocnemius muscle was measured in response to cold stimuli while the animal was regaining consciousness in order to measure changes in nocifensive reflexes. This was done by dropping acetone on the upper surface of the hind paw of the wounded leg (Monassi, Bandler et al. 2003). The raw EMG signals were then subjected to fast Fourier transformation (FFT; Chart v 4 software, AD Instrument), using 10 s epochs.

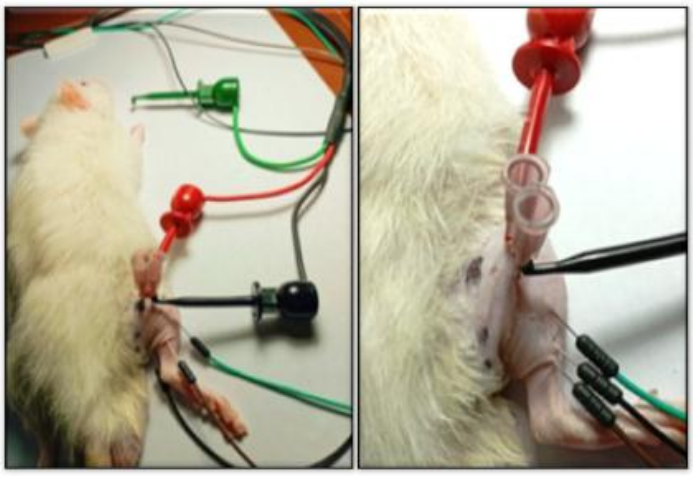

Figure 6.4: Representative images of the EMG recording from the gastrocnemius muscle in response to the cold-stimulus-evoked allodynia in the experimental rats.

6.1.9. Gastrocnemius muscle mass assessment:

The injury of the sciatic nerve leads to atrophy of the largest muscle supplied by it i.e., the gastrocnemius muscle which was assessed using the weight ratio of the gastrocnemius muscle 14 days after the surgery (Mohammadi, Amini et al. 2012). After the animals were euthanized, the gastrocnemius muscle was dissected from the contralateral and ipsilateral sides and weighed when wet using an electronic balance.

6.1.10. Real Time quantitative PCR

Quantitative Real-Time PCR (qRT-PCR) was performed as per the protocol mentioned in section 5.1.7 to assess the expression of the following genes at the mRNA level: NF-κB, $Ca_V2.2$, TRPV1 GFAP, and S100b. For normalization, β-actin was used as a constitutive type control.

Table 6.1: Primer sequences used for qRTPCR

Name	Primer sequences
NF-κB	F- 5'- GCGTTTCCGTTACAAGTGCGAGG -3' R - 5'- CCCCAGGAATACTGCCTGCAGAG -3'
$Ca_V2.2$	F- 5'- AGGCCAGACATGAAGACACACA -3' R - 5'- TTGCCTTCCTTGCTTGAGTCCT -3'
TRPV1	F- 5'- GAATGACACCATCGCTCTGC -3' R - 5'- AAGAGGGTCACCAGCGTCAT -3'
GFAP	F- 5'- AAGAAAACCGCATCACCATTCC -3' R - 5'- CCTTAATGACCTCGCCATCCC -3'
S100b	F- 5'- GAGAGAGGGTGACAAGCACAA -3' R - 5'- GGCCATAAACTCCTGGAAGTC -3'
β-actin	F- 5'-AGACTTCGAGCAAGAGATGGC -3' R-5'GATTCCATACCCAGGAAGGAAGG -3'

6.1.11. Assessment of S100b, TNF-α, IL-6, and IL-10 protein level in sciatic nerve and spinal cord

S100b (No: KLR1360, Krishgen Biosystems), TNF-α (No: KB3145, Krishgen Biosystems), IL-6 ELISA Kit (No: KB3068, Krishgen Biosystems), and IL-10 (No: E-EL-R0016, Elabscience, USA) were used in this study to quantitatively assess the protein levels in SN and SC following the manufacturer's instructions. The protein concentrations were determined using the Bradford method (Bradford 1976).

6.1.12. Immunofluoresence analysis

The expression of GFAP, S100b, and NF-L in the SN and SC were performed according to the protocol mention in section 5.1.9. (Prajapati, Ahmed et al. 2024).

6.1.13. Golgi –Cox Staining

Golgi-Cox staining is a neurohistological technique employed to examine the cytoarchitecture of the nervous system. In this study, we followed the protocol mention in section 5.1.10.

6.1.14. Measurement of intracellular calcium level

The intracellular calcium level was measured in the SN and SC following the protocol mentioned in section 5.1.11 (Malgaroli, Vallar et al. 1987).

6.1.15. Histological analysis of gastrocnemius muscle

The gastrocnemius muscle was fixed in a 10% buffered formalin solution which was sliced (5 µm) using the cryostat. Then the finely sliced sections were stained with hematoxylin followed by counterstaining with eosin. Then the tissue sections were dehydrated with a graded series of alcohol and mounted with dibutyl phthalate xylene

(DPX). The slides were then observed under the microscope (Olympus, Japan) for any structural abnormalities (Majumdar and Krishnamurthy 2022).

6.1.16. Histological analysis of sciatic nerve (SN) using luxol fast blue staining

The luxol fast blue stain is used to stain the myelinated axons and Nissil substance to identify the damage caused to the neuronal structure post-CCI of SN. The SN was fixed in a 10 % buffered formalin solution and sliced (5 µm) using cryostat. Then the tissue slices were hydrated in distilled water followed by incubation in the luxol fast blue stain solution for 2 h at 60 °C as per the manufacturer's instructions (ab150675; Abcam). The slides were rinsed thoroughly in distilled water and dipped in lithium carbonate solution for 20 sec. Subsequently, the tissue sections were treated with alcohol to remove the excess stain followed by rinsing it using water. The slides were then incubated in cresol echt violet for 3 min and rinsed quickly. Then the tissue sections were dehydrated with a graded series of alcohol and mounted with dibutyl phthalate xylene (DPX).The slides were then observed under the microscope (Olympus, Japan) for any structural abnormalities (Nazeri, Derakhshan et al. 2022).

6.1.17. *In silico* docking of S100b proteins with metal ions (Ca^{2+} and Ba^{2+})

6.1.17.1. Preparation of Ligand and Protein

The MIB2 website, namely the Metal Ion-Binding site prediction and docking server, contains information regarding the presence of calcium and barium metal ions (Lu, Chen et al. 2022). The website may be accessed via http://combio.life.nctu.edu.tw/MIB2/.The rat S100b protein was acquired from the RCSB Protein Data Bank (https://www.rcsb.org/search) with PDB ID: 1XYD. The ligands and proteins were prepared using Chimera version 1.15, which can be downloaded from https://www.cgl.ucsf.edu/chimera/download.html.

6.1.17.2. Analysis and Visualization

Chimera version 1.15 is utilized for the examination and graphical representation of docking outcomes. Visualization is employed to elucidate the interaction between ligands and receptor protein residues, which manifests as the interaction of amino acids and the bond distance between ligands and receptor protein residues.

6.1.18. Statistical analysis

The data has been represented as Mean ± SD and the statistical analysis was conducted using GraphPad Prism 8. The CAP recorded during the *ex vivo* electrophysiological study was analyzed using one-way ANOVA followed by a Tukey multiple. The behavioral tests, including the hot-plate test, acetone drop test, Randall Selitto test, cotton swab test, rota rod test, BBB score, and SFI, were statistically assessed using a two-way ANOVA followed by a Bonferroni post-hoc test. The changes in intracellular calcium and pro-inflammatory cytokines levels after the BaBG treatment were examined using one-way ANOVA followed by Tukey multiple comparison post-hoc tests. Statistical significance was determined when the P value was less than 0.05 in the in entire data analysis.

6.2. Results and Discussion

6.2.1. Effect of calcium channel blocking (CCB) properties of BaBG in the *ex vivo* setup

NP following nerve damage is characterized by the upregulation in the voltage-gated calcium channel (VGCC) leading to maladaptive changes in the pain axis (Luo, Chaplan et al. 2001),resulting in elevated intracellular calcium ion concentration $(Ca^{2+})_i$. This is a key factor in the progression of NP as it enhances the excitability of neurons

due to the abnormal release of neurotransmitters that trigger pain-inducing downstream cascades; hence, facilitating additional calcium release, thereby worsening the painful symptoms (Cui, Wu et al. 2021). As a result, CCBs are used clinically for the management of NP symptoms (Alles, Cain et al. 2020). Similarly, in our investigation, we examined the CCB potential of BaBG using an *ex vivo* isolated SN setup. This setup was stimulated to generate CAP, as shown in **Figure 6.5**. Upon stimulation of the SN stabilized in PF, we observed the production of a CAP (**Figure 6.5A**). PF includes all the necessary ions (Na^+, Ca^{2+}, and K^+) that are involved in the various stages of action potential generation and transmission. Nevertheless, when the SN was submerged in the CCB solution, specifically pregabalin, there was an instantaneous and notable block in CAP generation (**Figure 6.5B**). This indicates that calcium is crucial for the onset and propagation of action potential. Further, **Figure 6.5C** illustrates the effect of BaBG on the CAP of the isolated SN. It is evident that when the SN is stimulated, a CAP is generated. However, the repolarization phase of the CAP was prolonged, indicating that BaBG impeded the transmission of CAP. We sought to determine if the observed effects of BaBG as observed in **Figure 6.5C** are attributable to the barium or other ions that have been released from the BaBG framework into the PF. Therefore, we have conducted stimulation on the SN that has been stabilized using barium salt, specifically $BaCl_2$. **Figure 6.5D** demonstrates that the presence of $BaCl_2$ resulted in the total absence of CAP formation. Hence, the observed effects in case of BaBG as represented in **Figure 6.5C** can be attributed to the combination of ions released from the BaBG network into the PF, which aids in the production of CAP but decelerate its rate of transmission and in case of NP, hypersensitivity of nociceptors is observed (Cahill, Holdridge et al. 2022). Further, research has indicated that complete blocking of

calcium channels as observed in case of organic CCBs has a greater number of negative consequences compared to partial blockers as organic CCBs exhibits physical interaction with the calcium channel and blocks the calcium-conducting pathway located in the central cavity of the channel (Tang, Gamal El-Din et al. 2016). This strong physical interaction with the calcium channel produces adverse effects like increased risk of atrial fibrillation (Moore, Straube et al. 2009, Park, Hunter et al. 2023) as seen in case of gabapentinoids. However, the inorganic compounds are most likely to have physiological interactions that modulate the potential difference across the neuronal membrane and impart its action.

Furthermore, we stimulated the SN after immersing it in a 45S5 solution that includes all ions present in BaBG, except for barium, as depicted in **Figure 6.5D**. It was noted that the generation and propagation of CAP were similar to that observed in the PF (**Figure 6.5A**), with the exception for a detected overshoot in the CAP. The rise in the amplitude of the CAP can be attributed to the release of Ca^{2+} from 45S5, resulting in an overall elevation in the extracellular fluid (ECM) concentration of Ca^{2+}. Previous reports have indicated that an excessive amount of Ca^{2+} in the ECM triggers an increase in the amplitude of the CAP, resulting in a "calcium spike" (Walsh Jr and Singer 1980).

Moreover, the CAP was measured in the presence of PF containing lower levels of calcium ions and BaBG, as shown in **Figure 6.5E**. We noticed an immediate depolarization phase caused by the presence of Na^{+} in PF and the dissolution fluid of BaBG. This was followed by an overshoot in CAP, known as the "barium spike" and then a prolonged repolarization phase. Supporting our observation, it has been reported that Ba^{2+} can substitute for Ca^{2+} (Walsh Jr and Singer 1980). Additionally, at the last phase of depolarization when the calcium channel opens, Ba^{2+} enters because it has

greater permeability for voltage-dependent calcium channels compared to Ca^{2+} (Hagiwara and Byerly 1981, Satoh, Kubota et al. 1987). Consequently, the action potential experiences a decreased rate of repolarization, potentially caused by its impact on the Ca^{2+}-activated K^{+} current (Vassort 1975). A prior study also demonstrated that the presence of Ba^{2+} in the extracellular fluid resulted in an extended action potential plateau observed in the growth cone of a regenerated axon in lamprey along with the concentration-dependent elongation in the spike (Macvicar's and Llinas 1985). Moreover, when BaBG in the PF was used alongside the CCB (pregabalin), the generation of CAP failed (**Figure 6.5G**). This confirms that the observed effects of BaBG in the *ex vivo* electrophysiological assessment are mediated through the calcium channel. Further, under NP conditions, there are reports of a reduction in the threshold required to elicit an action potential, resulting in hypersensitivity (Djouhri, Fang et al. 2012). Since, we observed that BaBG has the capacity to extend the repolarization phase of the produced CAP, thereby causing a delay in the propagation of the action potential. Hence, it has the potential to be used as a therapeutic strategy for NP treatment.

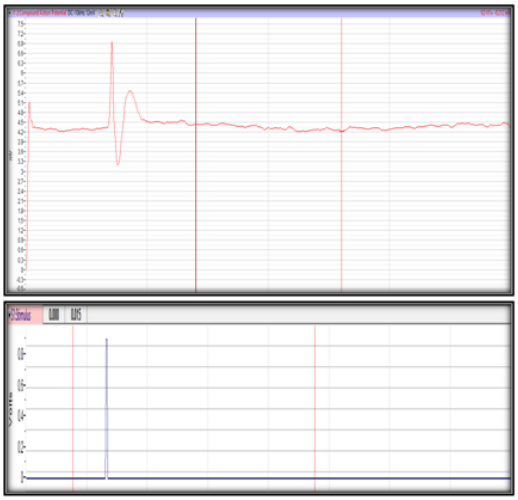

(A) In the PF

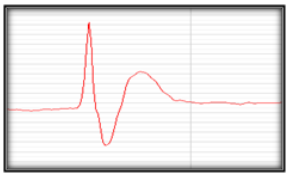

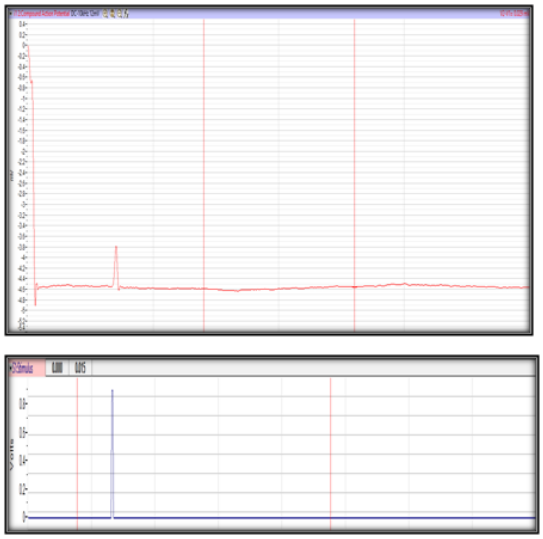

(B) In the PF containing Pregabalin

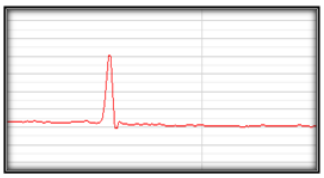

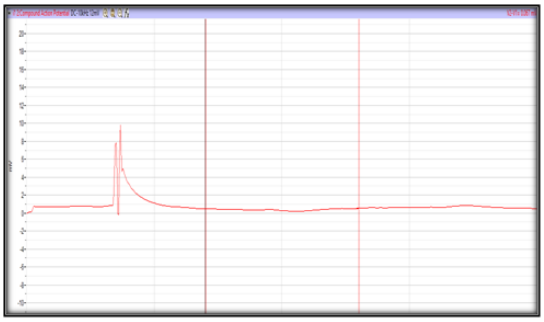

(C) In the PF containing BaBG

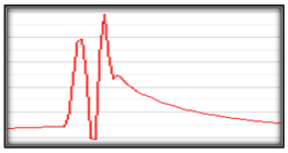

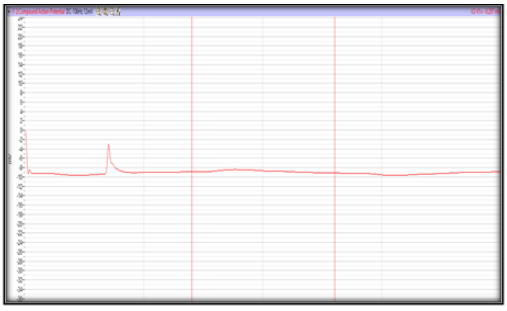

(D) In the PF containing $BaCl_2$

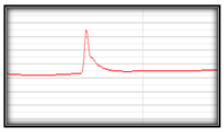

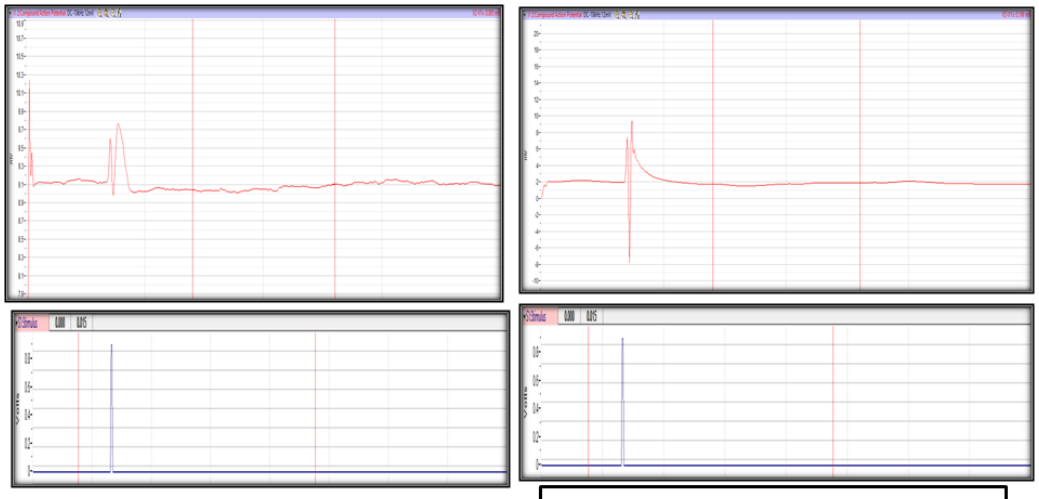

(E) In the PF containing 45S5

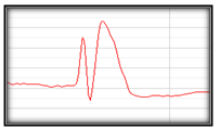

(F) In the PF containing reduced calcium ions and BaBG

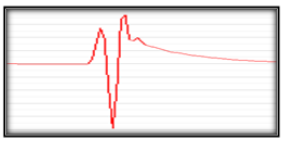

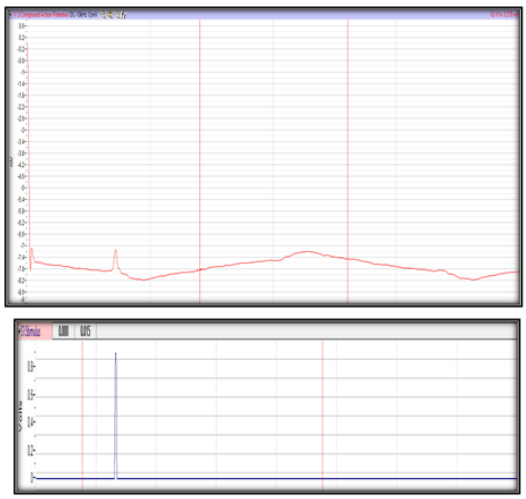

(G) In the PF containing BaBG and Pregabalin

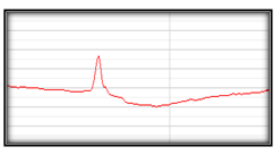

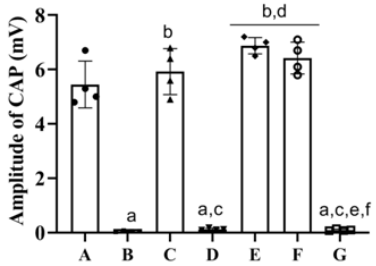

A	In the PF
B	In the PF containing Pregabalin
C	In the PF containing BaBG
D	In the PF containing $BaCl_2$
E	In the PF containing 45S5
F	In the PF containing reduced calcium ions and BaBG
G	In the PF containing BaBG and Pregabalin

Figure 6.5: Effect of BaBG on the generation of CAP. All values are mean ± SD (n=4). $^{a}P<0.05$, $^{b}P<0.05$, $^{c}P<0.05$, $^{d}P<0.05$, $^{e}P<0.05$, and $^{f}P<0.05$ compared to groups i.e., in the PF, in the PF containing Pregabalin, in the PF containing BaBG, in the PF containing $BaCl_2$, in the PF containing 45S5, in the PF containing reduced calcium ions and BaBG, and in the PF containing BaBG and Pregabalin respectively. (One-way ANOVA followed by Tukey's post hoc test).

6.2.2. Effect of BaBG on mechanical /thermal hyperalgesia and allodynia

The heightened hypersensitivity to non-noxious thermal and mechanical stimuli is an instructive trait observed clinically and preclinically in NP conditions (Jensen and Finnerup 2014, Edhi, Heijmans et al. 2020). Consequently, we used Randall Selitto and Eddy's hot-plate test in order to assess the efficacy of BaBG in reducing the severity of mechanical and thermal hyperalgesia respectively. In this study, after the CCI surgery, we observed the development of mechanical and thermal hyperalgesia as evident from a decrease in the threshold of withstand pressure (TWP) applied on the dorsal part of the paw and the paw withdrawal latency (PWL) in nerve-injured rats in response to thermal stimuli that started from day 7 and was maximum on day 14 (**Figure 6.6A and B**). The TWP and PWL of the ipsilateral side of CCI decreased to 61.48 ± 9.06 g and 5.16 ± 1.56 sec respectively compared to baseline 128.47 ± 14.38 g and 16.83 ± 1.26 sec respectively, suggesting the development of sensory hypersensitivity at the end of experimental protocol. Several research groups have also reported that CCI of SN can cause prolonged allodynia and hyperalgesia, as well as spontaneous pain behaviors (Edhi, Heijmans et al. 2020). Notably, there were no significant changes in the PWL and TWP of the contralateral paw compared to pre-CCI. Statistical analysis by two-way ANOVA exhibited differences in the ipsilateral paw mechanical withdrawal threshold and PWL after the treatment with BaBG among the groups ([$F(6, 385) = 203.5$; $p < 0.05$] and [$F(6, 385) = 205.8$; $p < 0.05$] respectively), time periods ([$F(4, 385) = 520.4$; $p < 0.05$] and [$F(4, 385) = 466.4$; $p < 0.05$] respectively) and the interaction between group and time ([$F(24, 385) = 25.42$; $p < 0.05$] and [$F(24, 385) = 25.20$; $p < 0.05$] respectively). Post hoc analysis revealed that all the doses (1, 5, and 10 mg/kg) of BaBG significantly improved the CCI-induced decrease in PWL and TWP. However, the

effect of BaBG at the doses of 5 and 10 mg/kg was more significant compared to BaBG 1 mg/kg and the onset of action was observed on day 21 and it continued till day 28 in a dose-dependent manner. Further, 45S5 (10 mg/kg) did not have significant effects in improving PWL and TWP compared to BaBG as shown in **Figure 6.6**. The ability of BaBG to mitigate the hyperalgesia to mechanical and thermal stimulus developed post-injury to the peripheral nerve may be due to its calcium channel blocking potential as observed in **Figure 6.5**. In support of our observation, previously, studies have confirmed that excessive upregulation of accessory units of VGCC contributes to the development of NP phenotypes after peripheral axonal injury due to excessive influx of Ca^{2+} that increases the excitability of primary afferent neurons (Luo, Chaplan et al. 2001).

Moreover, BaBG also attenuated the dynamic mechanical and cold allodynia in a dose-dependent manner during the acetone spray and cotton swab test respectively as shown in **Figure 6.6(C and D)**. Statistical analysis using repeated measures of two-way ANOVA revealed significant differences in paw withdrawal duration (PWD) and paw withdrawal latency in cotton swab test among the different groups ([$F(6, 385) = 200.7$, $p < 0.05$] and [$F(6, 385) = 264.0$, $p < 0.05$] respectively), as well as over time ([$F(4, 385) = 512.9$, $p < 0.05$] and [$F(4, 385) = 608.0$, $p < 0.05$] respectively). Additionally, an interaction between group and time was observed ([$F(24, 385) = 23.02$, $p < 0.05$] and [$F(24, 385) = 22.67$, $p < 0.05$] respectively). The contralateral paw did not exhibit significant differences according to post hoc analysis (data not shown). Post hoc analysis represented that all the doses of BaBG ameliorated CCI-induced increase in cold and dynamic mechanical allodynia on D-28 of experimental protocol. On the other hand, 45S5 (10 mg/kg) attenuated cold and dynamic mechanical allodynia; however,

the effects seen were not as significant as BaBG. Taken together, our results suggest that BaBG reversed all the core sensory phenotypes of NP in a dose-dependent manner.

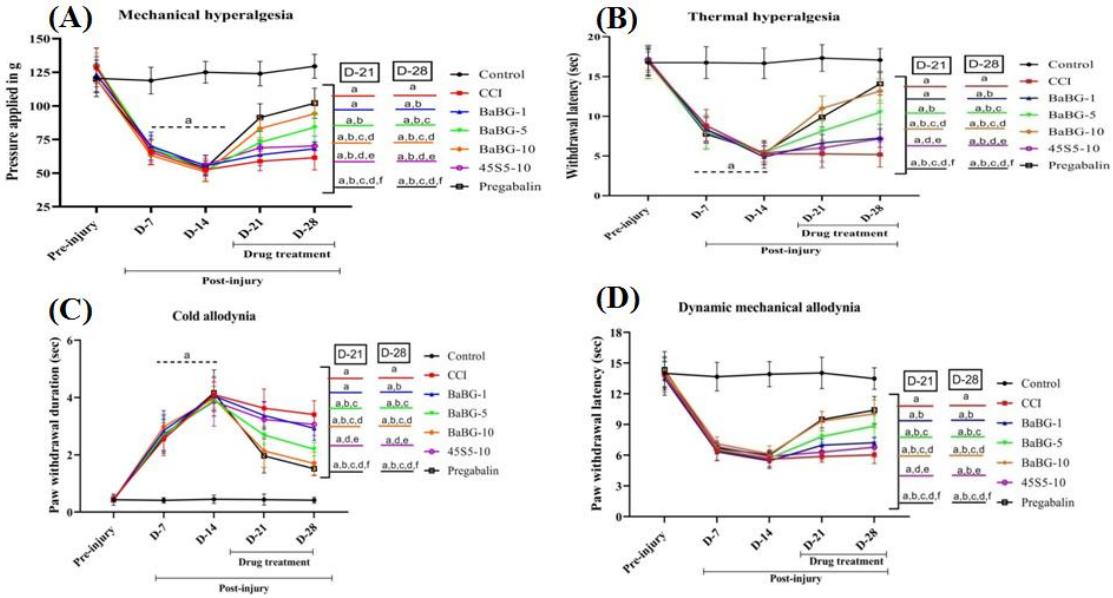

Figure 6.6: Effect of BaBG on (A) mechanical hyperalgesia, (B) thermal hyperalgesia, (C) cold allodynia, and (D) dynamic mechanical allodynia. All values are in mean ± SD (n=12 rats/ group). $^{a}p<0.05$, $^{b}p<0.05$, $^{c}p<0.05$, $^{d}p<0.05$, $^{e}p<0.05$, and $^{f}p<0.05$ compared to control, CCI, BaBG-1, BaBG-5, BaBG-10, and 45S5-10 respectively (Two-way ANOVA followed by Bonferroni post-hoc test)

6.2.3. Effect of BaBG on the CCI-induced alterations in motor functions

The SN innervates various muscles in the lower limb that are essential for plantar flexion of the foot at the ankle joint and flexion of the leg at the knee joint. Therefore, injury to SN in the CCI model of NP leads to the development of motor incoordination and gait abnormalities (Ahmad, Subhan et al. 2021). The gait and weight bearing of rodents can be examined as an alternative measure of nociception and are commonly regarded as indicators of non-evoked or stimulus-independent 'pain'. Gait analysis in freely ambulating rodents is employed to investigate alterations in limb motion and sensorimotor impairment. In order to assess the extent of functional recovery after the BaBG treatment, we conducted a walking track test and the SFI was calculated on a

weekly basis. In the walking track analysis paradigm, the SFI decreased with CCI injury [$F(6,385) = 902.1$; $p<0.05$]. These changes were observed with respect to time [$F(4,385) = 2009$; $p<0.05$] (**Figure 6.7A**). Further, there was a significant interaction between groups and time [$F(24,385) = 83.65$; $p<0.05$] in this paradigm. Post hoc analysis represented that, all the doses of BaBG (1, 5, and 10 mg/kg) ameliorated CCI-induced decrease in SFI(-75.58 ± 6.33) on D-28. Further, the effect of BaBG on SFI at the dose of 5 and 10 mg/kg (-48.48 ± 8.13 and -25.91 ± 4.09 respectively) was more significant compared to the lowest dose of BaBG i.e., 1 mg/kg (-59.36 ± 4.23). Further, 45S5 (10 mg/kg) also improved the CCI-induced motor deficits but was not as potent as BaBG of the same dose and its effects were comparable to the lowest dose of BaBG. Moreover, the impairment in the motor coordination post-injury to the peripheral nerve was confirmed by the BBB score of the CCI group which had reduced to 4.91 ± 0.99 on day-28 compared to baseline 19.66 ± 0.65. However, BaBG (10 mg/kg) significantly improved the BBB score to 17.01 ± 0.72 after two weeks of treatment compared to the nerve-injured rats.

Furthermore, the effect of BaBG on neuromuscular coordination was also assessed using the rotarod tests. Statistical analysis using repeated measures of two-way ANOVA revealed significant differences in rotarod retention time (RRT) observed among the different groups [$F (6, 385) = 117.4$, $p < 0.05$], over time [$F(4, 385) = 335.0$, $p < 0.05$] and interaction between group and time [$F (24, 385) = 18.65$, $p < 0.05$] as shown in **Figure 6.7C**. The CCI group exhibited a decline in RRT starting from D-7 compared to the control group, indicating the presence of motor deficits similar to the observed limping gait in patients (Drăghici, Văcăraş et al. 2023). We observed that RRT for the CCI rats has reduced significantly to 65.05 ± 8.14 seconds at the end of the experimental

protocol compared to baseline 112.16 ± 11.75 seconds. However, administration of BaBG (1, 5, 10 mg/kg) significantly restored motor function, resulting in an increase in RRT compared to the CCI group as observed on day 28 (i.e. after 14 days of treatment) of the study protocol. These effects continued to increase progressively up to D-28. On day 28, no significant differences were observed between the higher dose-treated group and the pregabalin-treated group in terms of RRT. The highest dose of BaBG improved RRT to 103.11 ± 8.87 sec while the RRT in the moderate dose i.e., 5 mg/kg was increased to 87.93 ± 9.94. On the contrary, treatment with 45S5 (10 mg/kg) did not show any significant improvement in the motor deficits compared to CCI rats. Hence, it can be concluded that BaBG improved CCI-induced motor deficits in a dose-dependent manner.

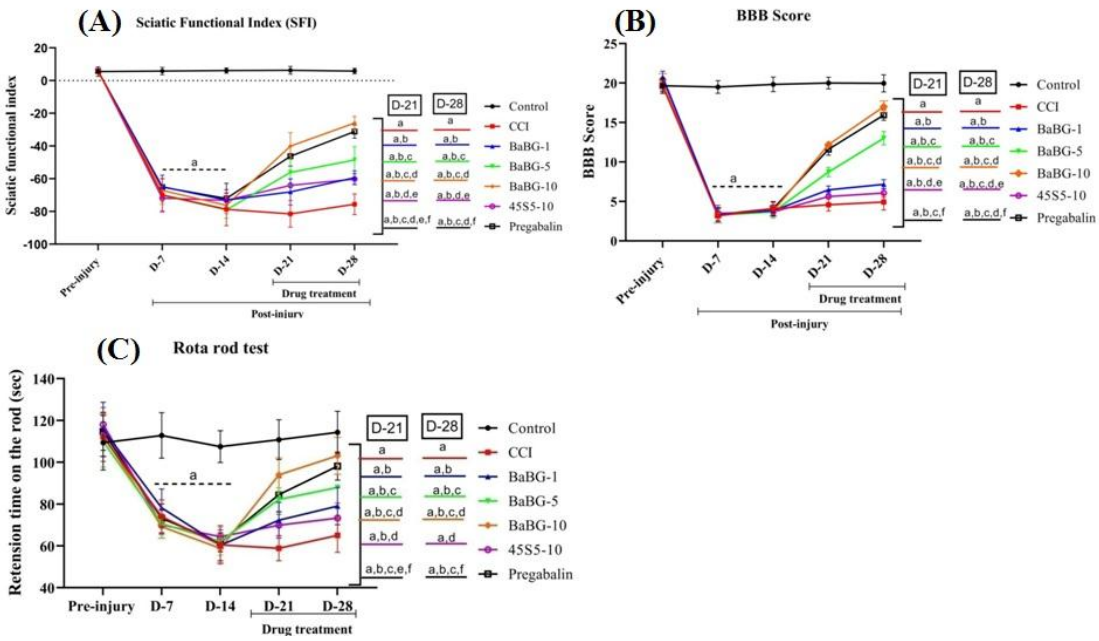

Figure 6.7: Effect of BaBG on (A) SFI, (B) BBB score, and (C) time spent on rota rod. All values are in mean ± SD (n=12 rats/ group). $^{a}p<0.05$, $^{b}p<0.05$, $^{c}p<0.05$, $^{d}p<0.05$, $^{e}p<0.05$, and $^{f}p<0.05$ compared to control, CCI, BaBG-1, BaBG-5, BaBG-10, and 45S5-10 respectively (Two-way ANOVA followed by Bonferroni post-hoc test)

6.2.4. Effect of BaBG on the mRNA expression of TRPV1 and Ca_V 2.2 along with the intracellular calcium level $(Ca^{2+})_i$ in the SN and SC post-CCI

To analyze the effects of BaBG on the $Ca_V2.2$ expression in the SN and SC and to identify the significant differences among the groups, statistical analysis by one-way ANOVA was employed ([$F(6,27) = 64.77$; $p<0.05$] and ([$F(6,27) = 132.4$; $p<0.05$] respectively). Post-hoc analysis revealed a significant increase in the mRNA expression of $Ca_V2.2$ in both SN and SC following CCI compared to control rats (**Figure 6.8 iC and D**). The over-expression of VGCC, specifically Ca_V 2.2, in nociceptors, has also been reported previously that leads to an influx of cations, which causes depolarization of the corresponding neuronal ending. The depolarization triggers the formation of an action potential that carries the nociceptive signal from A-δ and C nerve fibers into the central nervous system (CNS) (Saegusa, Matsuda et al. 2002, Antunes, Campos et al. 2023). Further, the upregulated Ca_V 2.2 post-injury has been directly linked to the development of behavioral hypersensitivity and synaptic plasticity during the NP conditions (Luo, Calcutt et al. 2002). In addition, tactile allodynia, which is commonly observed in patients with NP and animal models of NP, has been associated with an increase in the auxiliary unit of VGCC (Luo, Calcutt et al. 2002). However, BaBG treatment exhibited a substantial decrease in the expression of $Ca_V2.2$ in SN and SC in a dose-dependent manner. It was observed that there was an attenuation of 47.90 and 39.63 % in the $Ca_V2.2$ expression in SN and SC respectively post-BaBG treatment at the highest dose compared to the CCI group. On the contrary, 45S5 at a dose of 10 mg/kg could not reverse the CCI-induced enhanced expression of $Ca_V2.2$ in SN and SC. Therefore, our findings suggest that the addition of barium to the 45S5 framework

imparts these observed molecular effects in the CCI-induced NP model leading to attenuation of the sensory hypersensitivity.

Voltage-dependent calcium channels have a multifaceted role in nociception, as they allow Ca^{2+} to enter the cell. These ions contribute to membrane depolarization and also act as a second messenger, triggering a wide range of cellular processes including the release of neurotransmitters such as glutamate, substance P, and calcitonin gene-related peptides and increasing the chronicity of pain (Smith, Cabot et al. 2002, Takasusuki and Yaksh 2011). In our study, one-way ANOVA revealed a difference in $(Ca^{2+})_i$ level post-treatment with BaBG in SN [$F(6,27)= 14.14$; $p<0.05$] and SC [$F(6,27)= 61.79$; $p<0.05$] among the groups. Tukey's post-hoc test showed a significant increase in $(Ca^{2+})_i$ level in both SN and SC following CCI compared to the control group. However, this elevation was mitigated by BaBG after 14 days of treatment in a dose-dependent manner. Dose-dependent effects of BaBG on the calcium channel suggest its specific calcium-modulating pharmacological action with minimum off-target interactions. Besides, the changes observed in $(Ca^{2+})_i$ level in the BaBG-treated group can be due to the calcium channel modulating effects observed in **Figure 6.5**. Interestingly, unlike BaBG, treatment with 45S5 did not significantly alter the elevated $(Ca^{2+})_i$ level in SN and SC post-injury to the peripheral nerve compared to CCI rats ($P > 0.05$) (as shown in **Figure 6.8ii A and B**).

Thermal sensitivity is a frequently observed symptom in both clinical and preclinical reports following nerve damage (Chen, Willcockson et al. 2009, Huang, Lu et al. 2020). The transient receptor potential channel (TRPV1) is known to be linked to the development of increased sensitivity to heat (thermal hyperalgesia) (Huang, Lu et al. 2020). Therefore, we have examined the effect of BaBG on the expression of TRPV1

in the SN and SC following CCI injury (**Figure 6.8iA and B**). One-way ANOVA represented significant alteration in TRPV1 mRNA expression in the SC and SC among the groups ([F(6,27) = 84.08; p<0.05] and ([F(6,27) = 108.1; p<0.05] respectively on D-28. Post-hoc analysis demonstrated a substantial increase in the TRPV1 expression in both SN and SC compared to the control group. Treatment with various doses (1, 5, and 10 mg/kg) of BaBG effectively mitigated the expression of TRPV1 compared to CCI rats. In addition, the effect of BaBG at the dose of 5 and 10 mg/kg was more pronounced compared to the lowest dose of BaBG i.e., 1 mg/kg. Nevertheless, when given at a dose of 10 mg/kg, the administration of 45S5 exhibited mild pharmacological activity in the CCI model in alleviating heat sensitivity that was comparable to the lowest dose of BaBG (1 mg/kg). The results of our study demonstrate that the inclusion of barium enhances the effectiveness of 45S5 in reversing NP phenotypes. This is achieved by regulating calcium ions through calcium channels and altering the expression of TRPV1, which is responsible for aberrant temperature perceptions in NP.

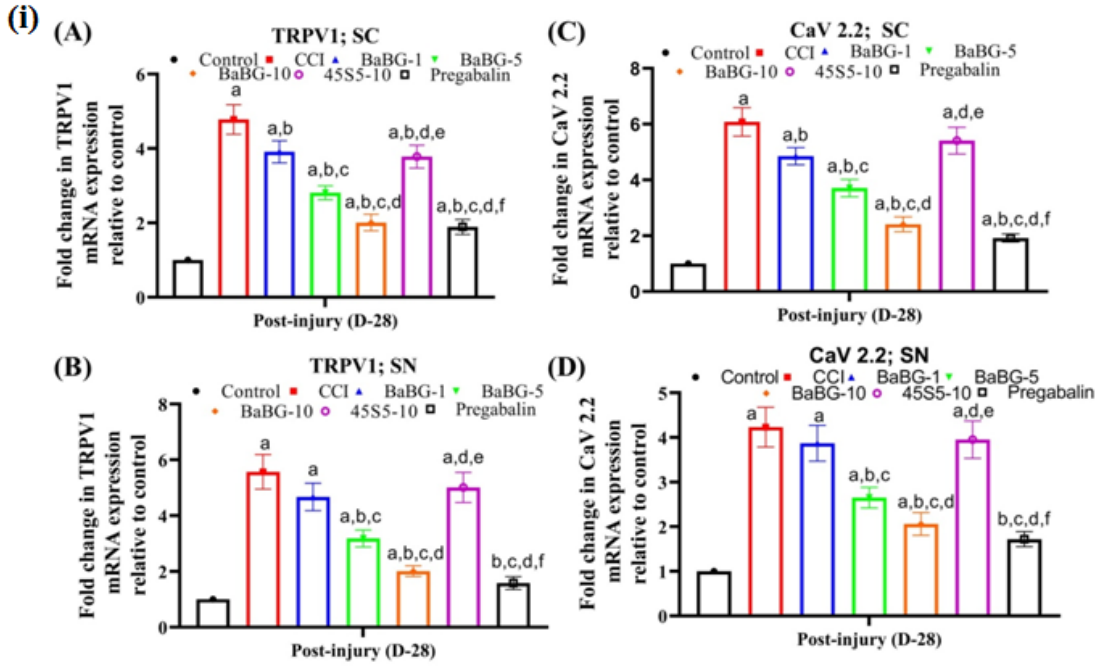

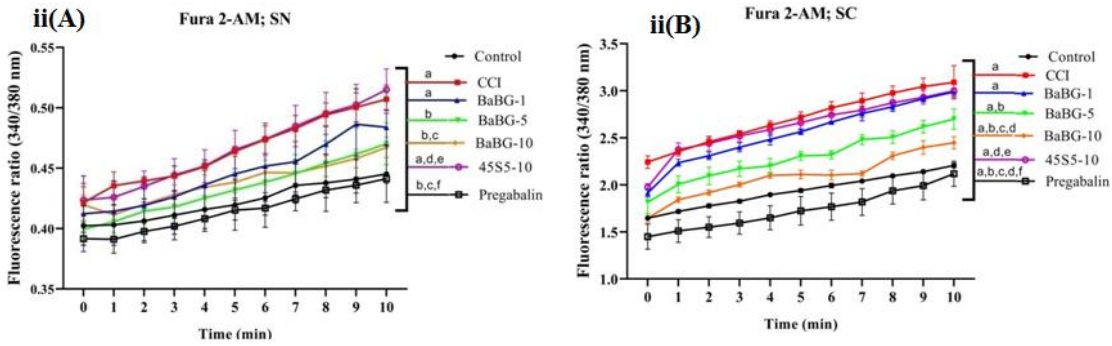

Figure 6.8: Effect of BaBG on the (i) mRNA expression of TRPV1 and Cav2.2, and on (ii) the intracellular calcium level in the SN and SC. (ii). All values are in mean ± SD (n=4 / group). $^{a}p<0.05$, $^{b}p<0.05$, $^{c}p<0.05$, $^{d}p<0.05$, $^{e}p<0.05$, and $^{f}p<0.05$ compared to control, CCI, BaBG-1, BaBG-5, BaBG-10, and 45S5-10 respectively. (One-way ANOVA followed by Tukey's multiple comparison post-hoc test)

6.2.5. Effect of BaBG on the expression of S100b in SN and SC

Chapter 5 has demonstrated a direct relationship between the S100b level and the onset and progression of NP phenotypes. Additionally, the specific S100b inhibitor, pentamidine, has been found to alleviate sensory and motor impairments in the CCI model of NP. Therefore, we have evaluated the effects of BaBG on the expression of calcium-binding protein i.e., S100b in the SN and SC. One-way ANOVA revealed a significant difference in the fluorescence intensity of S100b expression among the groups in SN ([$F(6,20) = 30.16$; $p<0.05$]) and SC ([$F(6,20) = 11.78$; $p<0.05$]) compared to the control group as shown in **Figure 6.9 and 6.10** respectively. Post-hoc test showed a significant increase in the S100b protein expression following CCI injury in the SN and SC compared to the control rats. A similar trend was observed in the mRNA expression of S100b in the SN and SC post-injury to the peripheral nerve as shown in **Figure 6.13 (iB and iiB)**. These observations are consistent with the clinical reports which showed an exaggerated response of S100b in traumatic injury (Lécuyer, Mercier et al. 2021). Similarly, previous studies found enhanced expression of S100b in chronic pain models in rodents (Celikbilek, Akyol et al. 2014). Interestingly, treatment with

different doses of BaBG significantly alleviated the CCI-induced increased S100b expression in a dose-dependent manner. In support of our observation, previous studies have demonstrated that the presence of Ba^{2+} prevented the secretion of S100b from the primary astrocyte culture (Vizuete, Hansen et al. 2019). However, 45S5 (10 mg/kg) did not produce a significant effect on the increased S100b level following CCI. Elevated levels of S100b reflect the activation of glial cells, which in turn stimulates inflammatory responses, hence contributing to the chronic nature of NP (Michetti, Di Sante et al. 2021). Nevertheless, our earlier investigation showed that the release of barium from BaBG exhibits anti-inflammatory properties in the LPS-induced neuroinflammation in the C6 cell line (Majumdar, Hira et al. 2021). Hence, the anti-inflammatory properties of BaBG may hinder the feedback process that triggers the continued release of S100b from the activated glial cells. In addition, after CCI injury, we saw a gradual rise in the intracellular calcium concentration $(Ca^{2+})i$, which subsequently led to an increase in the release and activation of the calcium-binding protein (S100b) as described in **Chapter 6.5**. Further, based on the observations in **Figures 6.5 and 6.8**, it can be inferred that BaBG has the ability to modulate calcium levels. Consequently, the decline in intracellular calcium concentration $(Ca^{2+})_i$ may have led to a reduction in the expression of S100b after BaBG treatment. However, pregabalin (30 mg/kg) did not have significant effects on the elevated S100b level following CCI injury compared to BaBG, thus highlighting the effectiveness of BaBG in the injury-induced glial cell activation that is involved in the pathophysiological process in chronic pain.

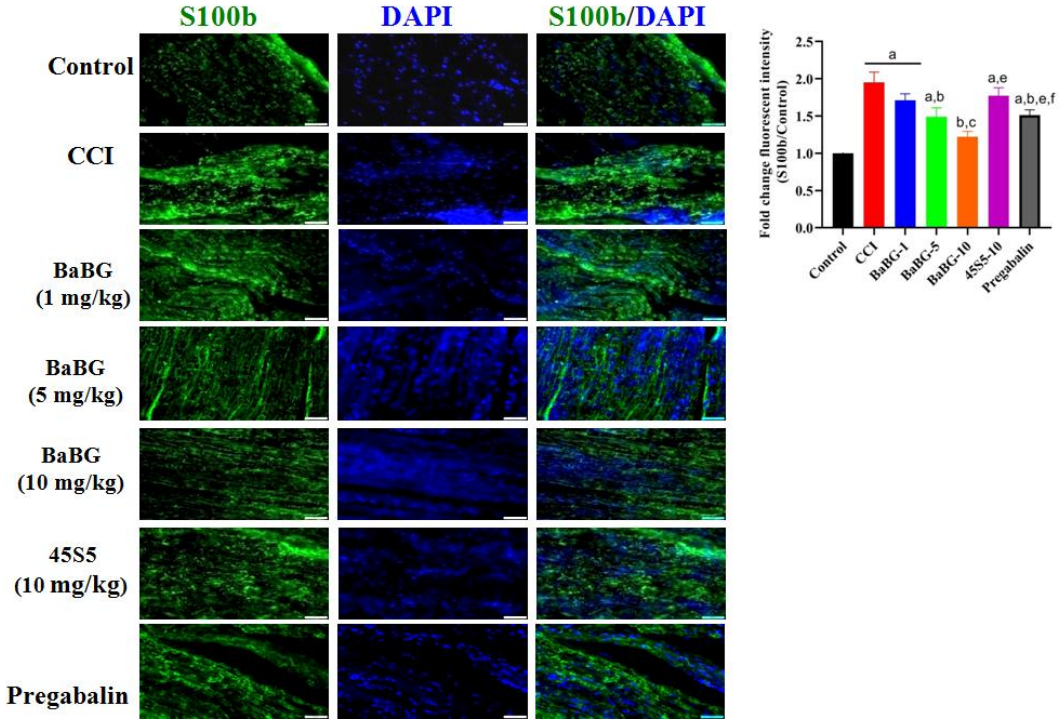

Figure 6.9: Effect of BaBG on S100b expression in the SN. Scale bar was set at 50 µM with 20X magnification. All values are in mean ± SD (n=3 rats/ group). [a]p<0.05, [b]p<0.05, [c]p<0.05, [d]p<0.05, [e]p<0.05, and [f]p<0.05 compared to control, CCI, BaBG-1, BaBG-5, BaBG-10, and 45S5-10 respectively. (One-way ANOVA followed by Tukey's multiple comparison post-hoc test)

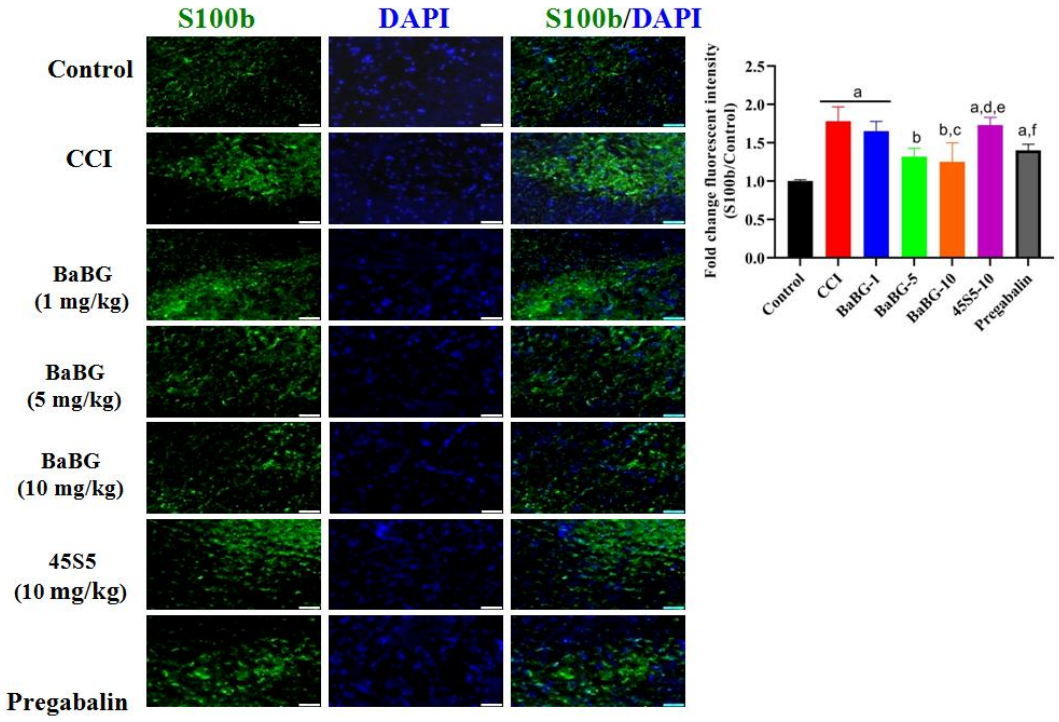

Figure 6.10: Effect of BaBG on S100b expression in the SC. Scale bar was set at 50 µM with 20X magnification. All values are in mean ± SD (n=3 rats/ group). [a]p<0.05, [b]p<0.05, [c]p<0.05, [d]p<0.05, [e]p<0.05, and [f]p<0.05 compared to control, CCI, BaBG-1, BaBG-5, BaBG-10, and

45S5-10 respectively. (One-way ANOVA followed by Tukey's multiple comparison post-hoc test)

6.2.6. Effect of BaBG on the CCI-induced astrocytes activation in SN and SC

In the present study, we have measured the GFAP expression in the SN and SC as an indicator of the astrocytes activation post-CCI of SN using an immunofluoresence assay. Statistical analysis using one-way ANOVA showed a significant difference in the fluorescence intensity of S100b expression among the groups in SN ($F(6,20) = 22.37$; $p<0.05$) and SC ($F(6,20) = 10.91$; $p<0.05$) compared to the control group, as depicted in **Figure 6.11 and 6.12**, respectively. The post-hoc test revealed a statistically significant rise in the expression of the GFAP protein after CCI injury in the SN and SC when compared to the control rats. A comparable pattern was noted in the mRNA levels of GFAP in the injured SN and SC following peripheral nerve damage, as depicted in **Figure 6.13 (iA and iiA)**. These data align with the preclinical reports in rodent models of chronic pain that show an amplified response of GFAP in cases of severe spinal nerve injury (Romero-Sandoval, Chai et al. 2008). The aberrant glial cell activation contributes to hypersensitivity and aids in the maintenance of hyperalgesia and allodynia in NP (Romero-Sandoval, Chai et al. 2008). In addition, prolonged activation of astroglia following neuronal injury is reported to be associated with the maintenance of a prolonged state of chronic neuroinflammation, contributing to the persistence of NP (Fan, Zhang et al. 2023). Treatment with BaBG alleviated these alterations significantly ($p < 0.05$) on D-28 of the experimental protocol in a dose-dependent manner. The effect of BaBG at the dosage of 5 and 10 mg/kg was more prominent in comparison to the lowest dosage of BaBG, which is 1 mg/kg. However, when administered at a dosage of 10 mg/kg, 45S5 showed slight pharmacological effects in

the CCI model by reducing the GFAP expression, which was similar to the lowest dosage of BaBG (1 mg/kg). Further, the highest dose of BaBG (10 mg/kg) was found to mitigate the CCI-induced increase in GFAP expression which was comparable to the pregabalin treated group ($p > 0.05$).

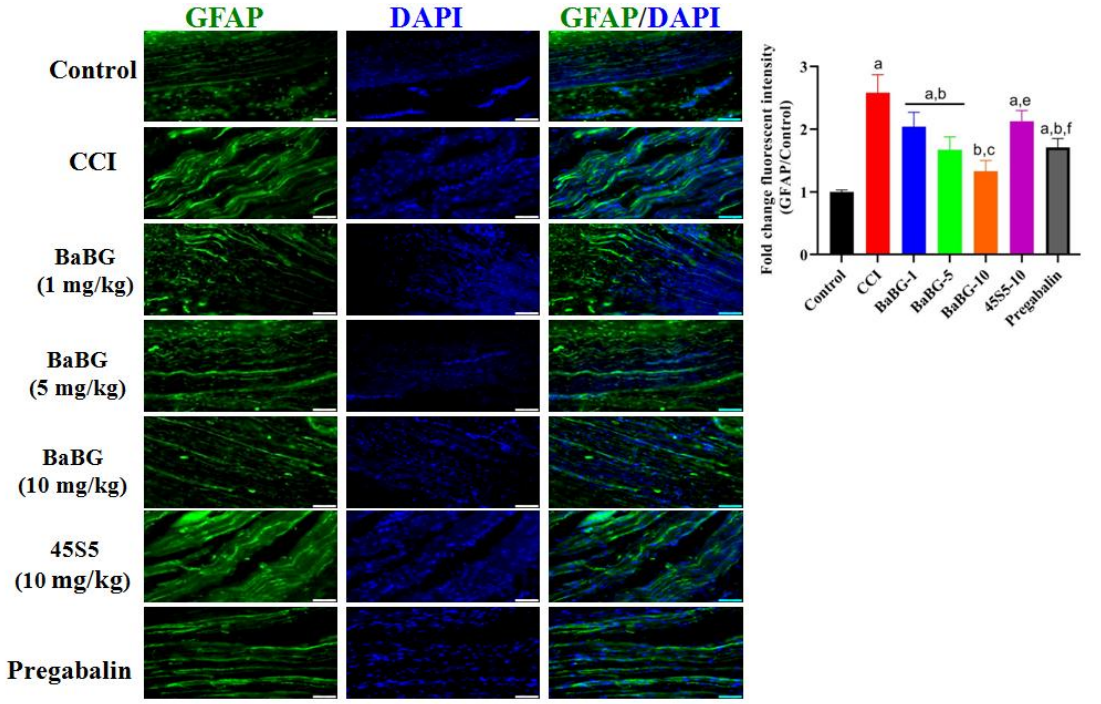

Figure 6.11: Effect of BaBG on GFAP expression in the SN. Scale bar was set at 50 µM with 20X magnification. All values are in mean ± SD (n=3 rats/ group). [a]p<0.05, [b]p<0.05, [c]p<0.05, [d]p<0.05, [e]p<0.05, and [f]p<0.05 compared to control, CCI, BaBG-1, BaBG-5, BaBG-10, and45S5-10 respectively. (One-way ANOVA followed by Tukey's multiple comparison post-hoc test)

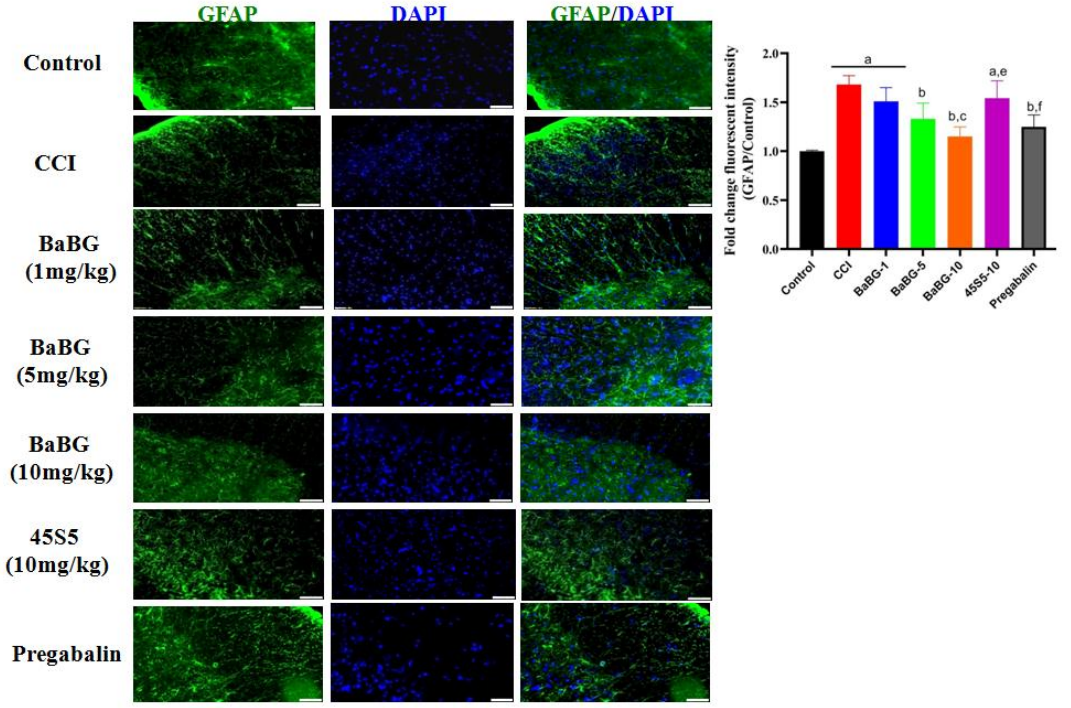

Figure 6.12: Effect of BaBG on GFAP expression in the SC. Scale bar was set at 50 μM with 20X magnification. All values are in mean ± SD (n=3 rats/ group). [a]p<0.05, [b]p<0.05, [c]p<0.05, [d]p<0.05, [e]p<0.05, and [f]p<0.05 compared to control, CCI, BaBG-1, BaBG-5, BaBG-10, and 45S5-10 respectively. (One-way ANOVA followed by Tukey's multiple comparison post-hoc test)

6.2.7. Effect of BaBG on the CCI-induced neuroinflammation

To investigate the effect of BaBG (1, 5, and 10 mg/kg) on CCI-induced neuroinflammation, we analyzed the levels of pro-inflammatory cytokines and investigated the underlying mechanisms. In the present study, one-way ANOVA showed that there were significant differences in pro-inflammatory cytokine i.e., TNF-α level in the SN and SC among the group ([F(6,27) = 77.85 p<0.05] and [F(6,27) = 57.60; p<0.05] respectively**)** as depicted in **Figure 6.14(B and E)**. Following the CCI, there were also notable variations in IL-6 levels among different groups in the SN and SC, as indicated by the statistical analysis ([F(6,27) = 19.19; p<0.05] and [F(6,27) = 20.35; p<0.05] respectively**),** illustrated in **Figure 6.14(A and D)**. Post hoc analysis revealed that there was a significant increase in the pro-inflammatory cytokines level

(TNF-α and IL-6) compared to the control rats. In the CCI group, the levels of TNF-α were elevated by 3.86-fold and 2.93-fold in the SN and SC, respectively compared to the control rats. Similarly, the levels of IL-6 in the disease group had increased by a factor of 1.84 and 2.12 in the SN and SC, respectively. Treatment with BaBG5 and 10 mg/kg significantly alleviated the CCI-induced alteration in TNF-α and IL-6. BaBG at the highest dose reduced the TNF-α 2.56-fold and 2.14-fold in SN and SC respectively compared to CCI rats. Likewise, IL-6 level was attenuated in the SN and SC by 1.62-fold and 1.74-fold respectively by the treatment with 10 mg/kg of BaBG. Nevertheless, the lowest dose of BaBG proved to be ineffective in this regard. The CCB used in the study i.e., Pregabalin (30 mg/kg) also elicited a reduction in the CCI-induced neuroinflammation but was not as effective as BaBG (10 mg/kg). Further, 45S5 (10 mg/kg) did not show any changes in the pro-inflammatory cytokine levels compared to the CCI group.

Moreover, the anti-inflammatory effect elicited by BaBG in the CCI model was clearly demonstrated by the significant increase in IL-10 levels in the SC and SN as shown in **Figure 6.14(C and F)**. Through the utilization of a one-way ANOVA analysis, notable changes were observed between various groups in terms of IL-10 protein level in the SN [$F(6, 27) = 35.65$; $p < 0.05$] and SC [$F(6, 27) = 39.93$; $p < 0.05$]. In rats following CCI, there was a substantial reduction in the levels of IL-10 protein in SN and SC by 1.95-fold and 1.99-fold respectively compared to the control group. However, BaBG exhibited a dose-dependent significant increase in the IL-10 level compared to CCI rats. These observations are consistent with our previous study where BaBG exhibited anti-inflammatory effects in the *in vitro* LPS-induced neuroinflammation model (Majumdar, Hira et al. 2021) as demonstrated in **Chapter 2**.

As we saw in **Chapter 5**, there was an aberrant rise in the intracellular calcium level in the SN and SC after the CCI, which augmented the levels of the calcium-binding protein, or S100b. In addition, there was neuroinflammation caused by injury, as indicated by the increased levels of pro-inflammatory cytokines (**Figure 6.14**). Further, in our study, there were significant differences in the mRNA gene expression of NF-κB among different groups as shown in **Figure 6.13(iC and iiC)**. One-way ANOVA revealed significant variations in NF-κB gene expression in SN and SC ([F (6, 27) = 17.09; $p < 0.05$] and [F (6, 27) = 27.20; $p < 0.05$] respectively). The post hoc test revealed that NF-κB mRNA expression had significantly elevated in the SN and SC of the CCI group compared to naïve rats. More precisely, there was a 3.18 and 3.27-fold rise in NF-κB expression in SN and SC respectively of CCI rats. Following an injury, there is glial activation that triggers the aberrant release of calcium-binding proteins (S100b) that interact with a range of cell surface receptors, including RAGE and toll-like receptors, by attaching to calcium ions and exposing its hydrophobic binding site (Singh and Ali 2022, Goswami, Anuradha et al. 2023). These events initiate a pro-inflammatory cascade through downstream signaling, which activates numerous transcription factors, including NF-κB (Yesudhas, Gosu et al. 2014). However, the treatment with BaBG effectively alleviated the notable increase in NF-κB ($p < 0.05$), a key regulator of inflammatory responses on D-28. In contrast, 45S5 (10 mg/kg) did not exhibit a significant effect on CCI-induced increase in NF-κB expression in SN and SC. This implies that the anti-inflammatory effects observed are due to the doping of barium into the 45S5 framework.

In addition, we conducted molecular docking experiments of the S100b protein with Ca^{2+} and Ba^{2+} ions using MIB2, as depicted in **Figure 6.15**. The calcium and barium

metal ions are depicted as bright yellow circles positioned within the bonded amino acid residues, as seen in **Figure 6.15 i and ii**, respectively. The 3D prediction model indicates that both Ca^{2+} and Ba^{2+} ions bind to the same active region on the EF-hand of the S100b protein in rats. Nevertheless, the affinity of Ba^{2+} for binding was determined to be greater than that of Ca^{2+}, as depicted in **Figure 15iii**. In addition, prior research has shown that the presence of Ba^{2+} inhibits the release of S100b from primary astrocyte cultures (Vizuete, Hansen et al. 2019). Consequently, the barium released from the BaBG tends to reduce the release of S100b from the activated glial cells following CCI, thereby mitigating the activation of pro-inflammatory pathways.

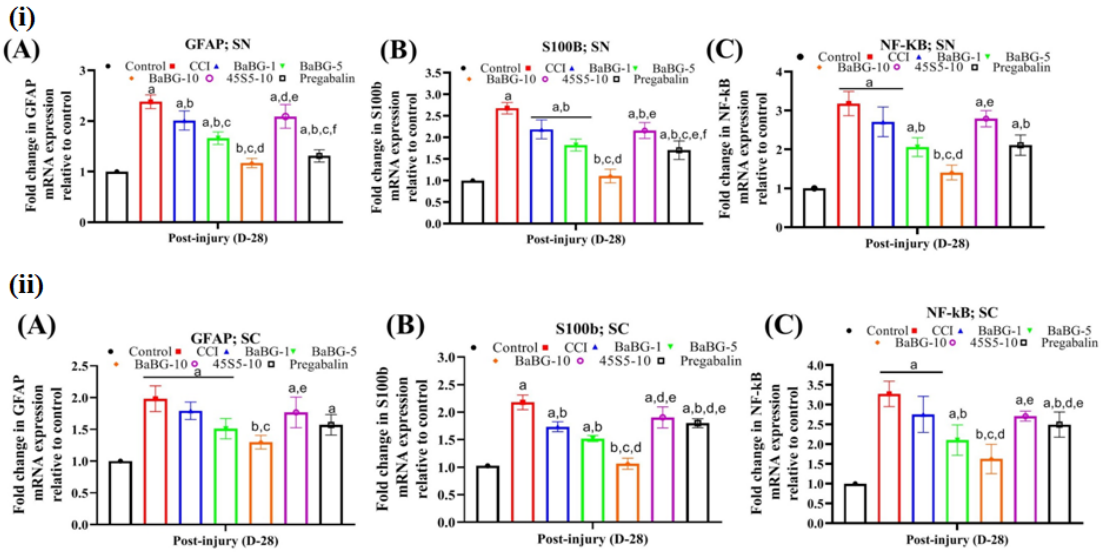

Figure 6.13: Effect of BaBG in the mRNA expression of GFAP, S100b, and NF-kB expression in the SN (i) and SC (ii). All values are in mean ± SD (n=4 / group). $^{a}p<0.05$, $^{b}p<0.05$, $^{c}p<0.05$, $^{d}p<0.05$, $^{e}p<0.05$, and $^{f}p<0.05$ compared to control, CCI, BaBG-1, BaBG-5, BaBG-10, and 45S5-10 respectively. (One-way ANOVA followed by Tukey's multiple comparison post-hoc test)

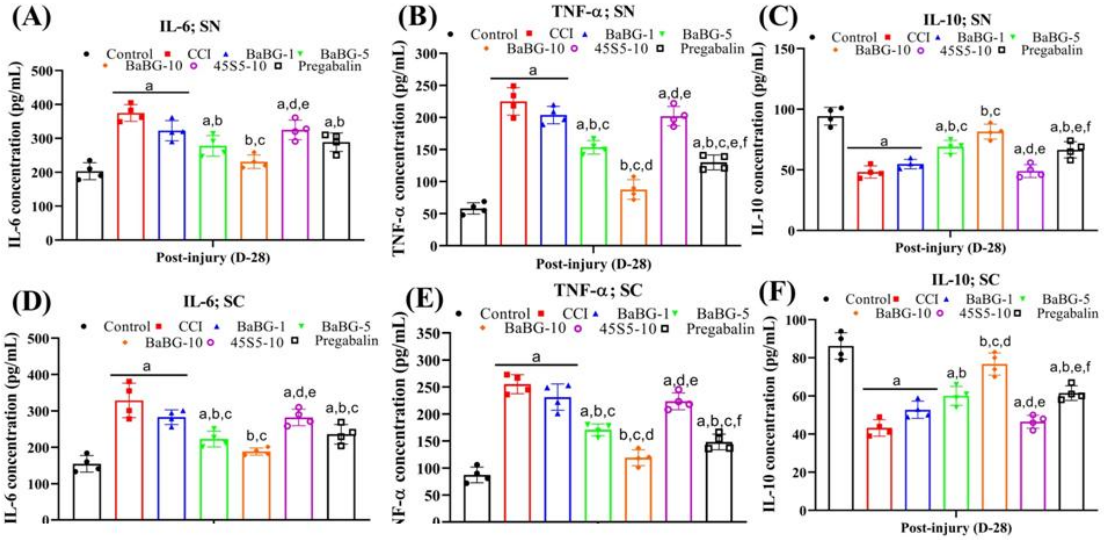

Figure 6.14: Effect of BaBG on TNF- α, IL-6, and IL-10 levels in the SN and SC. All values are in mean ± SD (n=4 / group). [a]p<0.05, [b]p<0.05, [c]p<0.05, [d]p<0.05, [e]p<0.05, and [f]p<0.05 compared to control, CCI, BaBG-1, BaBG-5, BaBG-10, and 45S5-10 respectively. (One-way ANOVA followed by Tukey's multiple comparison post-hoc test)

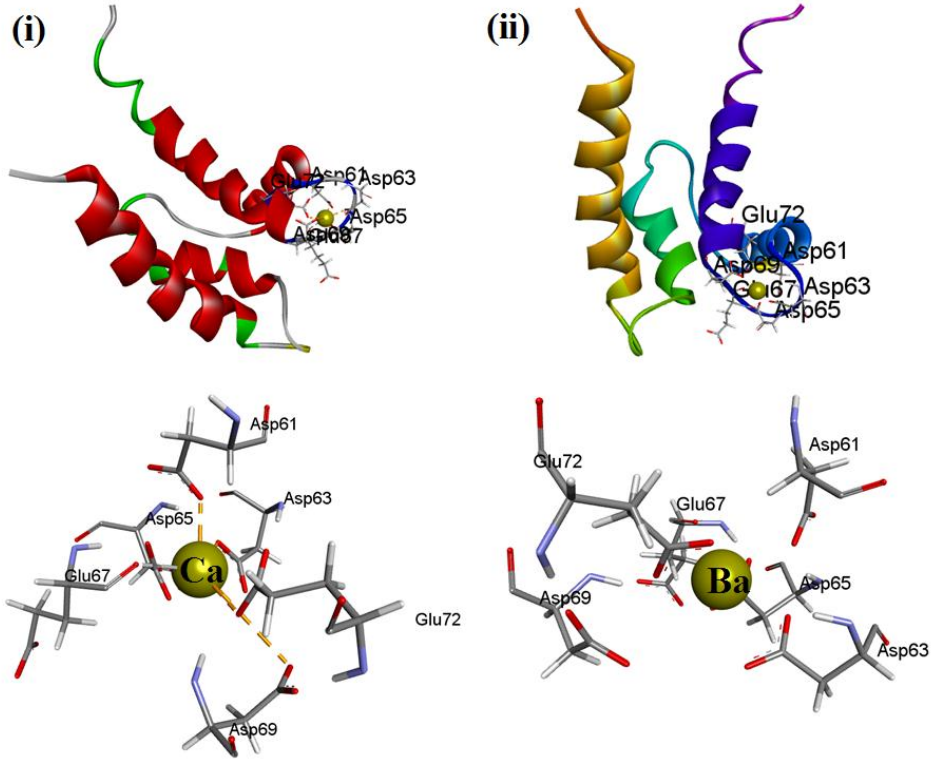

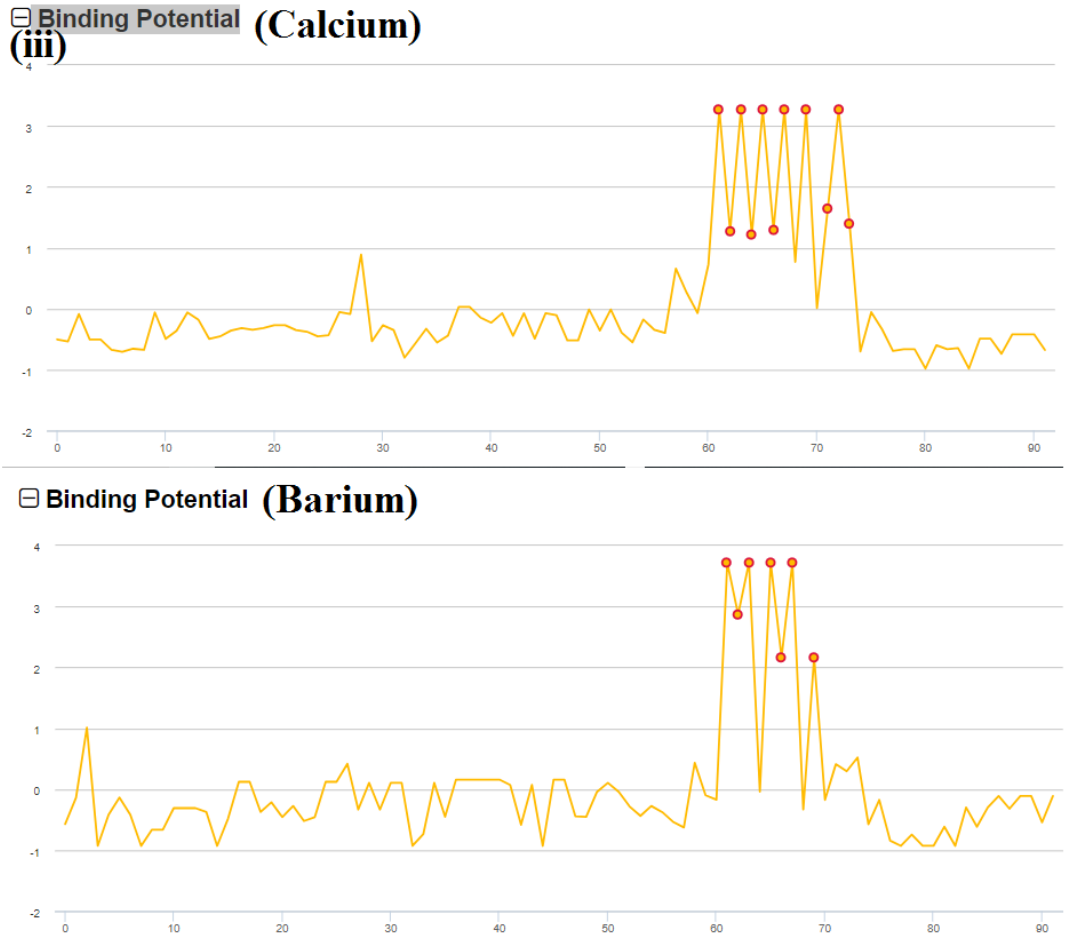

Figure 6.15: Molecular docking showing interaction of calcium (Ca^{2+}) and barium (Ba^{2+}) against S100b protein. 3D docking diagram of S100b bound to (i) Ca^{2+} and (ii) Ba^{2+}along with their (iii) binding potential.

6.2.8. Effect of BaBG on the neuronal morphology post-CCI injury

We examined the structure of neurons in the sections of the spinal cord after CCI injury, as depicted in **Figure 6.16**. The dendrites of neurons in the SC of CCI rats exhibited disintegration and retraction. After the peripheral nerve injury, the dendrites were fragmented and there was a decrease in the number of branches around the soma. However, treatment with BaBG as well as pregabalin led to dendrite arborization. In addition, we conducted a Sholl analysis on individual neurons, as shown in **Figure 6.17i**. The results showed that the intersections of dendrites with concentric circles at each radius were dramatically decreased in the injured rats. Statistical analysis using

the one-way ANOVA demonstrated significant differences in the total length of the dendrites [$F(4, 19) = 7.64$, $p < 0.05$, **Figure 6.17iiC**] among different experimental groups. Post-hoc analysis revealed that following treatment with BaBG (10 mg/kg) significantly increased the total length of the dendrites compared to the CCI group which had decreased significantly post-injury to the nerve. Furthermore, the dendritic arbors in the treatment group were longer and had more intersections at each radius compared with those in the CCI group, as determined by Sholl analysis (**Figure 6.17iiA and B**). The total length of the dendrites in the BaBG-treated group was 23.34 ± 6.58 µm significantly higher in comparison to the CCI group (9.89 ± 4.26 µm). Similarly, in the 45S5 and pregabalin-treated group, the total length of dendrites was found to be 19.91 ± 3.47 and 11.96 ± 6.39 µm respectively. The above results indicate that spinal neuronal dendrite arborization degenerated dramatically after CCI, but the degeneration was alleviated upon BaBG treatment. Similarly to our observations, it has been reported that when synaptic rewiring occurs, the remaining neurons try to rewire to make newer synaptic neural connections in order to repair and compensate for the loss of function (Tan, Stamboulian et al. 2008). The extent of functional recovery post-injury depends on the efficiency of neural circuit reconnection such as reactivating and reorganizing the intraspinal neuronal connections. Therefore, BaBG has the potential to rewire and reconnect which is essential for functional recovery.

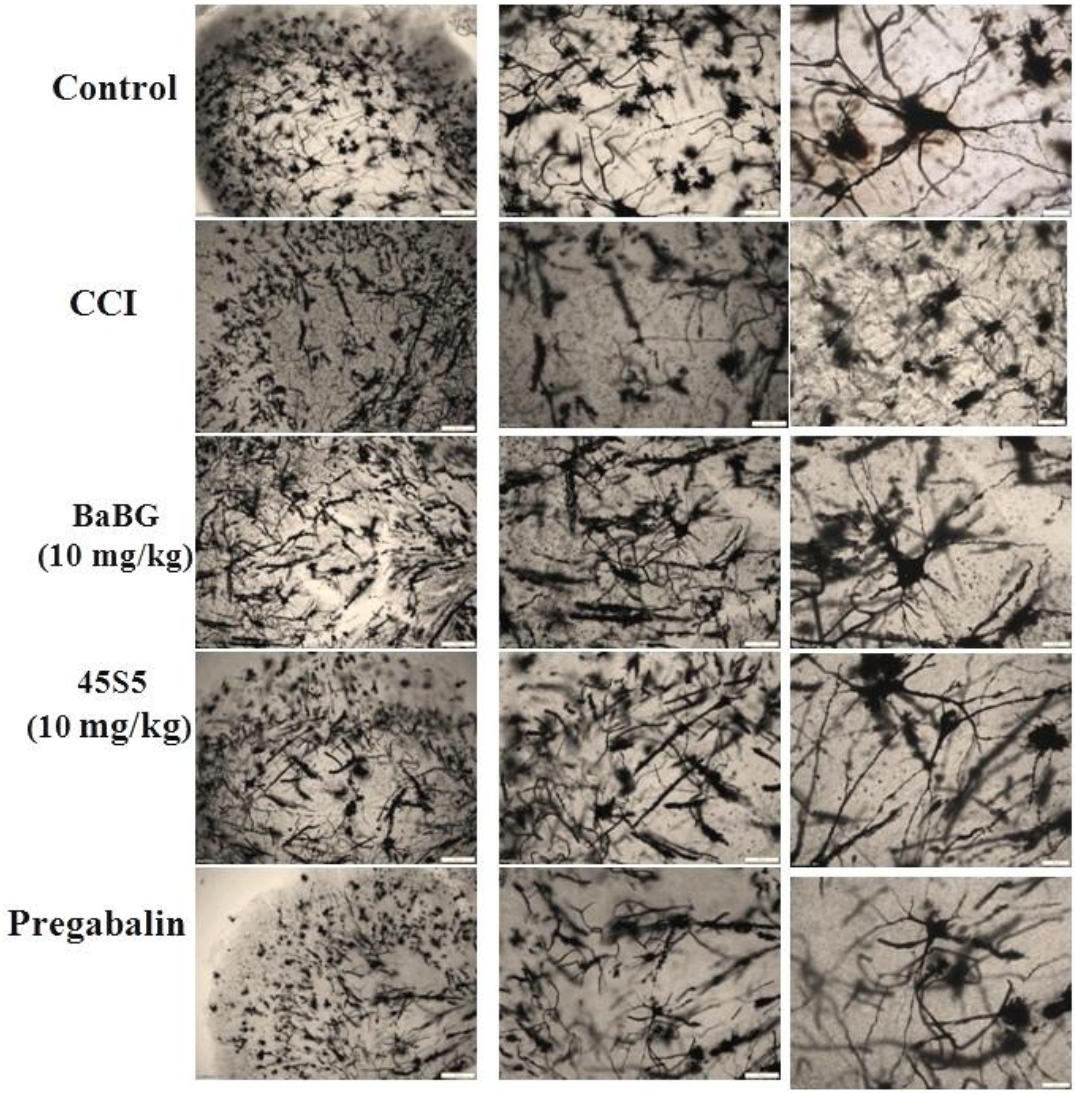

Figure 6.16: Representative images of Golgi-Cox impregnated SC slice of control, CCI, BaBG-10, 45S5-10 and pregabalin treated rats. Scale bar was set at 200, 100, and 50 μM with 4, 10, and 20X magnification.

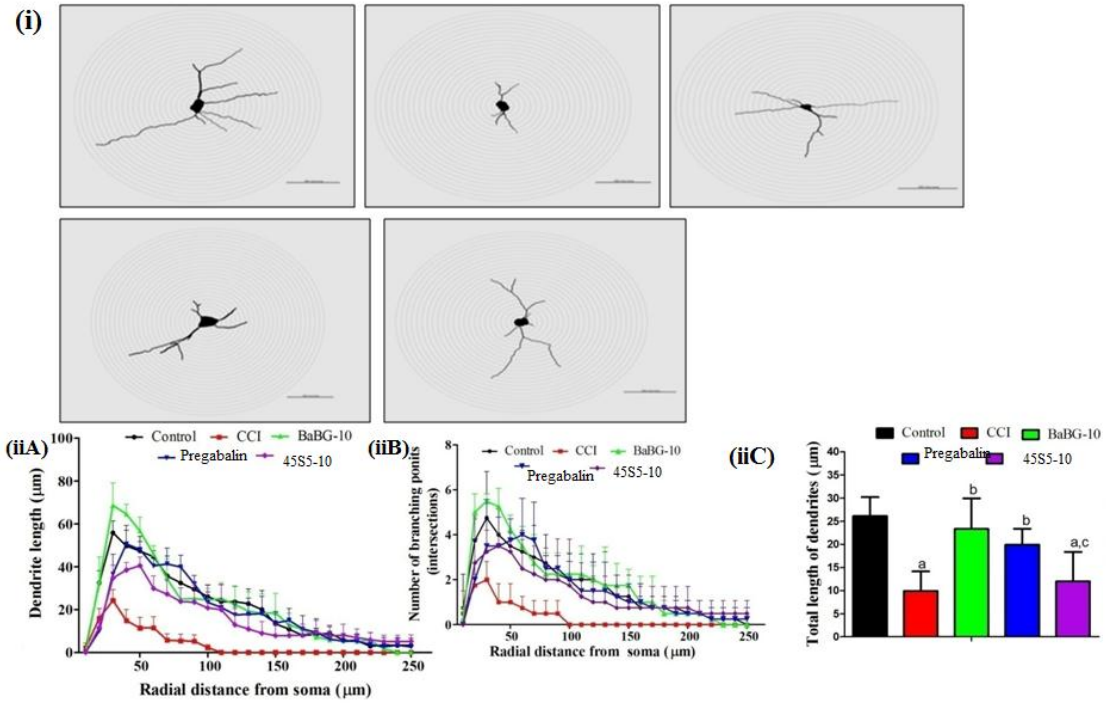

Figure 6.17: (i) Representative image of the camera Lucida drawing of neuron of SC which is superimposed over concentric circles using Sholl analysis. (ii) Effect of BaBG on (A), number of branching points (B) dendrite length across the soma, and (C) total length of dendrites. All values are in mean ± SD (n=4 / group). $^{a}p<0.05$, $^{b}p<0.05$, and $^{c}p<0.05$ compared to control, CCI, and BaBG-10 respectively. (One-way ANOVA followed by Tukey's post-hoc test)

6.2.9. Effect of BaBG on the CCI-induced axonal degeneration

Neurofilament light chain (NF-L) is a neuronal cytoplasmic protein particularly prominent in the large myelinated axons (Gaetani, Blennow et al. 2019). During the NP conditions, following the injury, there are reports of axonal degeneration leading to the fragmentation of NF-L, resulting in an increase in its concentration in the extracellular space and bloodstream(Widyadharma and Tedyanto 2022, Mortensen, Steffensen et al. 2023). Consequently, we have evaluated the effects of BaBG on the CCI-induced changes in NF-L expression in the SN as represented in **Figure 6.18**. One-way ANOVA followed by the post-hoc test indicated significant changes in the NF-L expression among the group [$F(6,20) = 28.19$; $p<0.05$]. Post-hoc test revealed a significant decrease in the fold change fluorescent intensity of NF-L in the SN of the CCI group

compared to the control rats. The control group exhibited alignment in NF-L, however after the CCI; NF-L was shown to be fragmented and scrambled, indicating axonal degeneration, as depicted in **Figure 6.18**. Following injury, the axon undergoes degeneration, resulting in the loss of myelin proteins that surround the axon in layers (**Figure 6.19**). This loss of myelin proteins leads to a decrease in the conduction velocity of the action potential, as seen in **Figure 6.21**. However, following the treatment with BaBG, the rats had increased NF-L expression in the SN in comparison to the CCI group, suggesting axonal repair. In contrast, the administration of pregabalin at a dosage of 30 mg/kg was found to be less efficacious in reversing the CCI-induced axonal damage than the barium-doped biomaterial (BaBG). Additionally, we also noted that there was no significant difference in the NF-L expression between the 45S5 (10 mg/kg) treated group and the CCI group. Thus, these findings confirm that BaBG possesses the axonal repair ability, leading to observable functional restoration during the pain behavioral assessment tests.

Further, the morphometric assessment by Luxol Fast Blue (LFB) tissue staining enabled the characterization of the effect of BaBG in terms of alterations in myelin sheath thickness caused by CCI of SN. The histological examination of the specimens revealed a normal SN appearance in the control group with a regular distribution of myelin that is stacked as long and neat columns surrounded by the basement membrane (**Figure 6.19**, control). However, as anticipated, the CCI group had an irregular distribution of nerve fibers that were thinly myelinated (**Figure 6.19**, CCI – black arrows) with a high degree of myelin vacuolation, suggesting axonal atrophy (**Figure 6.19**, CCI –red star). In contrast, animals treated with BaBG exhibited a significant and dose-dependent restoration of myelin in their nerves. This was evident from the increased number of

nerve fibers that were enveloped by a greater amount of myelin, in comparison to the CCI group.

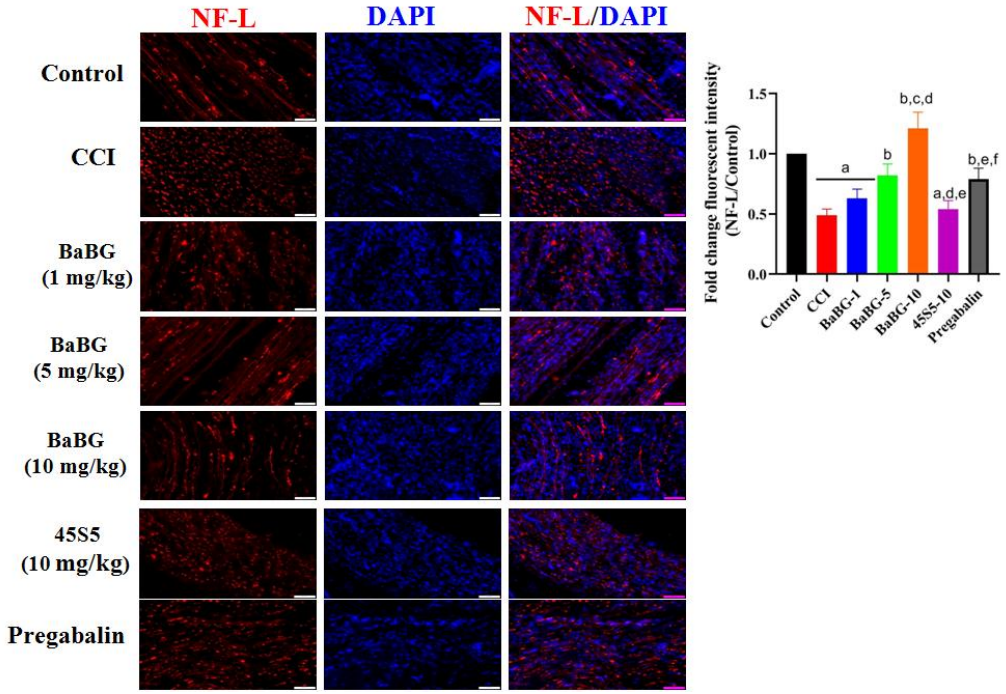

Figure 6.18: Effect of BaBG on NF-L expression in the SN. Scale bar was set at 50 µM with 20X magnification. All values are in mean ± SD (n=3 rats/ group). $^{a}p<0.05$, $^{b}p<0.05$, $^{c}p<0.05$, $^{d}p<0.05$, $^{e}p<0.05$, and $^{f}p<0.05$ compared to control, CCI, BaBG-1, BaBG-5, BaBG-10, and 45S5-10 respectively. (One-way ANOVA followed by Tukey's multiple comparison post-hoc test)

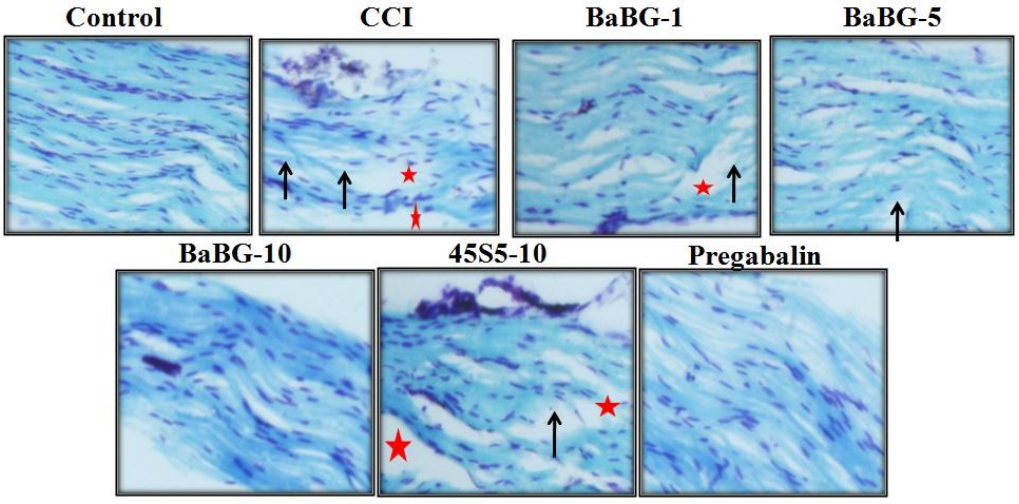

Figure 6.19: Representative image of the histological analyses of SN stained with luxol fast blue at the end of 28th day post-surgery. The arrangement of nerve fibre is disrupted (shown in black arrow) with high degree of myelin vacuolation (red star) in the disease group.

6.2.10. Effect of BaBG on the electrophysiological response upon stimulating the sciatic nerve

Previously, we have observed that following CCI of the SN, there is axonal degeneration causing loss of myelin layer from the SN as reported in **Figures 6.18** and **6.19**. In line with our observation, studies have corroborated these changes in the CCI model of NP that lead to alterations in the electrophysiological response and peripheral nerve functions (Chan, Tsai et al. 2022). Therefore, we have examined the effect of BaBG on the amplitude and latency of the onset of CAP along with its conduction velocity following CCI injury (**Figure 6.20**). One-way ANOVA represented significant alteration in the amplitude, latency of CAP, and MNCV among the groups ([$F(6,34) = 64.69$; $p<0.05$], [$F(6,34) = 396.4$; $p<0.05$],and ([$F(6,34) = 48.01$; $p<0.05$] respectively on D-28 of the experimental protocol. Post-hoc analysis demonstrated that the CCI of the SN caused a significant reduction in the amplitude of CAP and MNCV (2.0 ± 0.71 mV and 19.0 ± 2.91 m/s respectively) compared to the control group i.e., 13.4 ± 2.41 mV and 45.2 ± 4.43 respectively (**Figure 6.20A and C**). Similarly, there was a substantial increase in the latency of onset of CAP (2.92 ± 0.108 ms) in the nerve-injured group than the control rats (1.61 ± 0.078 ms) (**Figure 6.20B**). The reduction in conduction velocity can be ascribed to the loss of the myelin layer resulting from axonal atrophy, which aligns with the findings of investigations conducted on rats (Foudah, Alqarni et al. 2022). Although the MNCV has decreased, the presence of mechanical and cold allodynia indicates a surge in peripheral nerve sensitivity. The hypersensitivity found in this paradigm can be attributable to the heightened expression of VGCC and TRPV1, leading to an increase in intracellular calcium levels as shown in **Figure 6.8**. This rise in calcium levels is essential for maintaining action potential (Helmchen, Borst

et al. 1997, Liu, Xiong et al. 2020). However, treatment with various doses (1, 5, and 10 mg/kg) of BaBG effectively mitigated the CCI-induced changes in the electrophysiological parameters in rats. In addition, the effect of BaBG at the dose of 10 mg/kg (amplitude = 11 ± 1.41 mV, latency = 1.67 ± 0.05 ms, and MNCV = 40.02 ± 3.57 m/s) was more pronounced compared to the moderate and lowest dose of BaBG i.e., 5 and 1 mg/kg. Nevertheless, when given at a dose of 10 mg/kg, the administration of 45S5 was found to be ineffective in the CCI model in alleviating the amplitude and conductive velocity of CAP generated upon stimulating the nerve (amplitude = 1.2 ± 0.44 mV, latency = 2.89 ± 0.073 ms, and MNCV = 19.61 ± 2.71 m/s). Further, the CCB i.e., pregabalin (amplitude = 11.6 ± 1.67 mV, latency = 1.74 ± 0.033 ms, and MNCV = 35.28 ± 3.42 m/s) was found to be comparable to the highest dose of BaBG.

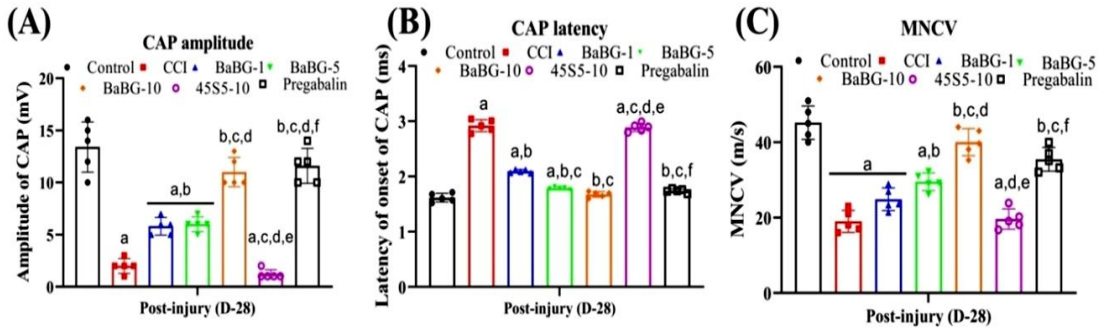

Figure 6.20: Effect of BaBG on (A) amplitude, (B) latency of CAP, and (C) MNCV. All values are in mean ± SD (n=5 rats/ group). [a]p<0.05, [b]p<0.05, [c]p<0.05, [d]p<0.05, [e]p<0.05, and [f]p<0.05 compared to control, CCI, BaBG-1, BaBG-5, BaBG-10, and 45S5-10 respectively. (One-way ANOVA followed by Tukey's multiple comparison post-hoc test)

6.2.11. Effect of BaBG on the muscle functioning in response to the cold-stimulus-evoked allodynia

The alterations in nocifensive reflexes in response to the cold stimuli have been recorded from the gastrocnemius muscle using EMG recordings, as depicted in **Figure 6.21**. The withdrawal response is noticed when a noxious stimulus, such as a cold

sensation from acetone dropped on an injured paw, is present. This reflex is due to the function of the gastrocnemius muscle to lower limb flexion. We observed that the control rats had a longer delay in the flexor EMG response compared to the CCI group, and the magnitude of the EMG was less when acetone was dropped on the rats' paws. However, the flexor EMG response of the CCI group exhibited a lower threshold and prolonged afterdischarges, as depicted in **Figure 6.21**; CCI. This observation is consistent with previous findings in the CCI model of NP (Bennett and Xie 1988); suggesting an exaggerated sensitivity to cold stimuli that are not normally painful and the occurrence of cold allodynia. Nevertheless, following the administration of BaBG, there was a decrease in the magnitude of EMG and after discharges in response to acetone stimulation, suggesting alleviation of CCI-induced sensory hypersensitivity. The EMG recording from the 45S5-treated group exhibited a reduction in the magnitude of discharges post-acetone stimulation without much difference in after discharges observed during flexion of the gastrocnemius muscle. Therefore, we can conclude that BaBG alleviated CCI-induced cold allodynia that corroborates the pain behavioral assessment tests as shown in **Figure 6.6**.

6.2.12. Effect of BaBG on the gastrocnemius muscle post-CCI injury

The gastrocnemius muscle, innervated by branches of the sciatic nerve, is the major muscle responsible for knee flexion and assisting in overall body movement. Denervated muscles have a loss of signal transmission from the nervous system, resulting in an inability to sustain contraction. As a result, damage to the SN is known to result in immobility or decreased function of the injured limb clinically and preclinically leading to muscle atrophy (Choe, Kim et al. 2011, Bhindi, Angliss et al. 2022). Further, there are reports of reduced muscular protein synthesis and an increase in protein breakdown, causing myatrophy and reduced thegastrocnemius muscle weight (Wang, Chen et al. 2021) as observed in our study in **Figure 6.22**. Following a CCI

injury, there was a notable decrease in the weight of the gastrocnemius muscle of the ipsilateral side of CCI rats (i.e., 0.488±0.1178g) compared to the control rats i.e., 1.49 ± 0.109, indicating muscle atrophy (**Figure 6.22**). One-way ANOVA demonstrated significant changes in the muscle weight among groups ([$F(6, 41) = 61.77$; $p < 0.05$] (**Figure 6.22**). The Tukey's post hoc test revealed that following the injury to the peripheral nerve, the weight of gastrocnemius muscle had reduced significantly in the CCI group compared to naïve rats which was reversed following BaBG treatment in a dose-dependent manner ($p < 0.05$). Pregabalin (30 mg/kg) treatment also reversed the CCI-induced muscle weight decrease but was significantly less potent compared to the highest dose of BaBG. Similarly, 45S5 (10 mg/kg) did not show any changes in the gastrocnemius muscle weight compared to the CCI rats.

Similarly, thehistological analyses of the H & E stained gastrocnemius muscle post-CCI revealed muscle atrophy. The control rats exhibited homogeneous morphology with densely packed acidophilic polygonal-shaped skeletal muscle fibres and the peripheral nuclei are ovalin shape as shown in **Figure 6.22**.While in the CCI group, there was fragmentation of the sarcoplasm (shown in black arrow) with the mononuclear cell infiltration (**Figure 6.22)**. We also observed a widening of the endomysium in the injured rats (shown in black stars) and some of them exhibited vacuolations (red arrow) However, treatment with BaBG significantly increased the gastrocnemius muscle fiber cross-section area. The fiber cross-section area of the highest dose of BaBG (10mg/kg) treated ratswas increased to 70.16 ± 4.16% from 38.83 ± 4.30 % as observed in CCI rats. In the pregabalin (30 mg/kg) and 45S5 (10 mg/kg) treated rats, the gastrocnemius muscle fiber cross-section area was found to be 54.33 ± 3.82 and 47.66 ± 3.92 % respectively which was significantly lesser than BaBG (10 mg/kg). In light of these findings, it can be inferred that motor impairments are closely linked to the CCI model of NP and BaBG treatment reversed all core symptoms of NP along with the observed motor impairment.

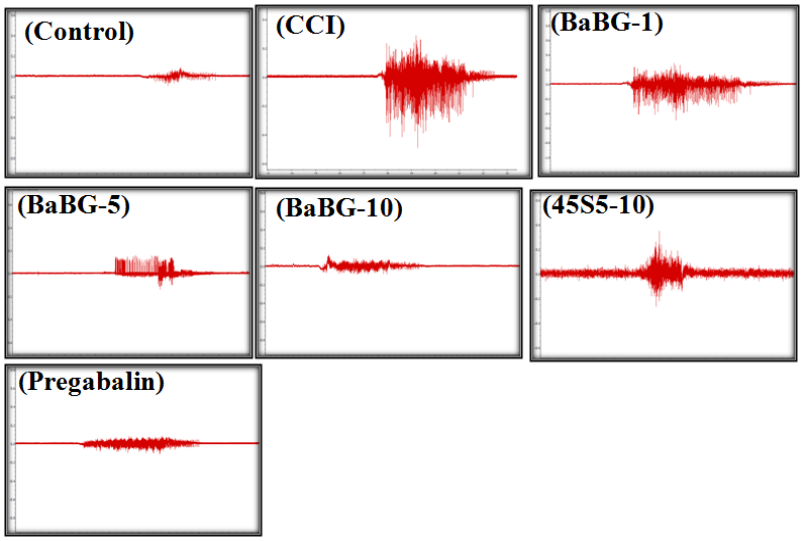

Figure 6.21: Representative images of the EMG recording in response to the cold-stimulus-evoked allodynia in control, CCI, BaBG-1, BaBG-5, BaBG-10, 45S5-10, and pregabalin treated rats.

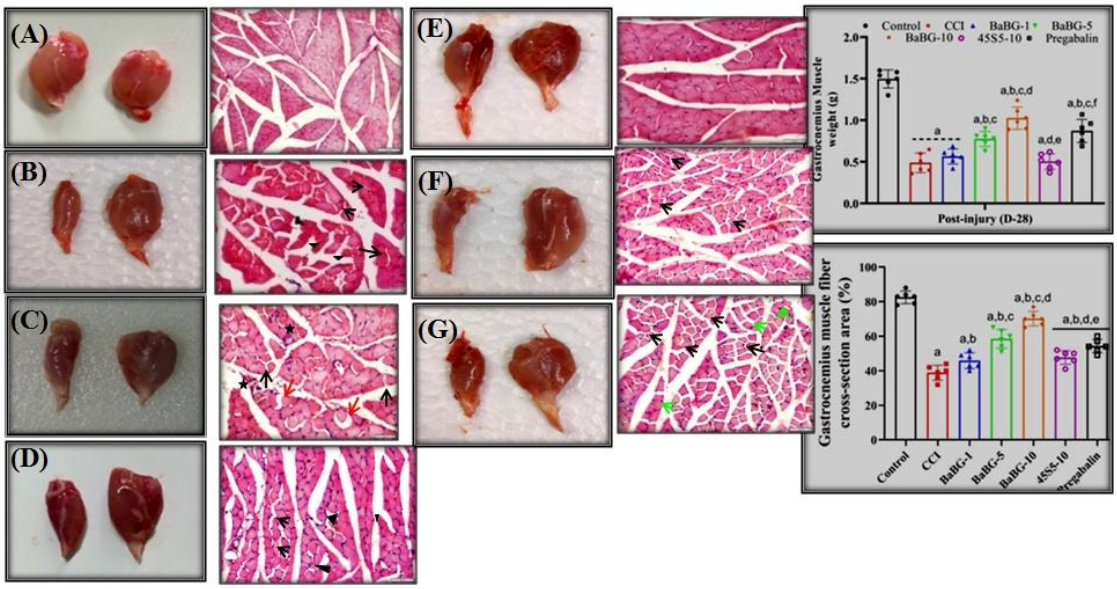

Figure 6.22: Representative images of the gastrocnemius muscle of the contralateral and ipsilateral side of the leg along with the histological analyses of gastrocnemius muscle stained with hematoxylin and eosin at the end of experimental protocol. Effect of BaBG on gastrocnemius muscle weight and cross-section area of muscle fiber. All values are in mean ± SD (n=5 rats/ group). $^{a}p<0.05$, $^{b}p<0.05$, $^{c}p<0.05$, $^{d}p<0.05$, $^{e}p<0.05$, and $^{f}p<0.05$ compared to control, CCI, BaBG-1, BaBG-5, BaBG-10, and 45S5-10 respectively. (One-way ANOVA followed by Tukey's multiple comparison post-hoc test)

6.3. Conclusion

The current findings establish that BaBG exhibits a significant effect in mitigating the CCI-induced sensory hypersensitivity and the characteristic motor impairments observed in NP. Calcium ions play a crucial role in neuronal signaling and excitability, and dysregulation of calcium homeostasis has been implicated in NP. In the *ex vivo* electrophysiological setup, BaBG prolonged the repolarization phase of action potential in the SN. Consequently, BaBG decreased the propagation of action potential and under NP circumstances; there is heightened sensitivity of nociceptors observed. Further, BaBG reversed all NP symptoms in a dose-dependent manner in the CCI model in rats. It also hindered the activation of S100b and decreased inflammation post-CCI of peripheral nerve. Treatment with BaBG caused axonal repair and remodeling of the dendrites. Similar to pregabalin, BaBG attenuated the elevated intracellular calcium levels in the SN and SC post-injury in rats. Notably, these effects exhibit a dose-dependent relationship, with 10 mg/kg proving to be the most effective dose compared to 1 and 5 mg/kg. In conclusion, these findings provide compelling evidence supporting the calcium-regulating potential of BaBG, thus potentially impeding calcium-associated NP pathogenesis.

Summary

- ❖ BaBG has the calcium regulating potential.
- ❖ BaBG reduced the intracellular calcium level in the sciatic nerve and spinal cord post-CCI injury in a dose-dependent manner.
- ❖ It ameliorated the CCI-induced sensory hypersensitivity (hyperalgesia and allodynia).
- ❖ The motor deficits caused due to the CCI were alleviated by BaBG in a dose-dependent manner.

- ❖ BaBG also lowered the S100b expression and pro-inflammatory marker level in the sciatic nerve and spinal cord post-peripheral nerve injury.
- ❖ Treatment with BaBG improved the compound action potential conduction velocity and amplitude which was comparable to the pregabalin treated group.
- ❖ BaBG treatment caused axonal repair and remyelination in dose-dependent manner.
- ❖ BaBG caused dendritic arborization, a mechanism contributing to neuronal connectivity and communications that helps in functional recovery.

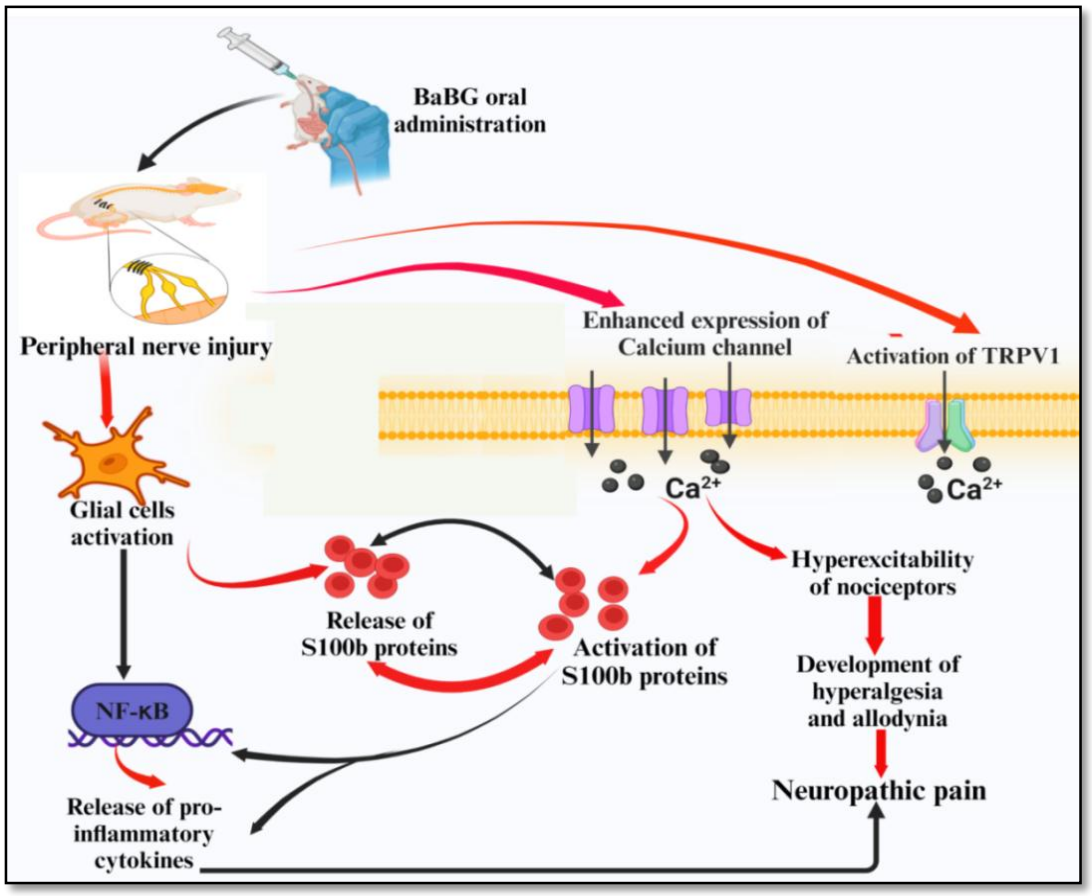

Figure 6.23 Showcases the specific objective's outcome in exploring the molecular mechanism behind the effect of BaBG in attenuating neuropathic pain (NP) in a CCI-induced NP rat model. It suggests that the development and progression of NP is associated with the enhanced calcium channel and TRPV1 expression that caused increase in the intracellular calcium and calcium-binding protein i.e., S100b level. These events led to glial cell activation that releases cytokine storm, thus exaggerating

NP sensation. BaBG exhibited novel calcium regulating mechanism as it prolonged the repolarization phase of action potential. The Treatment with BaBG significantly reversed the NP phenotypes induced by CCI. Besides, CCI of peripheral nerve caused glial cell hyperactivation that was attenuated by BaBG. BaBG also lowered the S100B-induced increase in pro-inflammatory markers, specifically TNF-α and IL-6, in both the SC and SN post-injury.

Chapter 7

Summary & Scope for Further Work

7. Summary and Conclusion

Since the dysregulation of calcium homeostasis following neuronal injury is a crucial factor that contributes to the development and maintenance of neuropathic pain (NP), we have developed a novel inorganic barium-doped bioactive glass (BaBG) that has calcium-regulating properties. The inorganic bioactive glass was amorphous and showed a higher tendency to form hydroxyapatite which affirms its bioactivity. The *in vitro* release profile for Si, Ca and Ba from the BaBG framework in the simulated physiological milieu exhibited controlled release of the dopants which are within the permissible physiological limits. The maximum concentration was observed at 24 h for Ca, Si, and Ba. BaBG exhibited biocompatibility and cytocompatibility, and it enhanced the migration of horizontal cells in the scratch assay, thereby emphasizing its regenerative capacity. In addition, BaBG demonstrated notable anti-inflammatory properties in the *in vitro* LPS model of neuroinflammation. Therefore, BaBG has regenerative and anti-inflammatory potential for treating traumatic injuries.

Further, we examined the pharmacokinetics, biodistribution, and excretion of dopants leached from BaBG in a pre-clinical study following single-dose oral administration to comprehend the fate of the dopants released is crucial for optimizing the dose regimens. The *in vivo* oral pharmacokinetics investigation demonstrated dose-dependent plasma release of network modifiers, with the maximum concentration of Ca, Si, and Ba observed at 24 h (T_{max}). The biodistribution study revealed that Ca, Ba, and Si were primarily accumulated in the excretory organs of the body and feces are the primary route for elimination. Furthermore, we have noted that barium, which was released from BaBG, was found in both the peripheral organs and the central nervous system, specifically the brain. Hence, the therapeutic ions released from BaBG possess the

capability to exert their effects on the central nervous system. Moreover, the safety profile of BaBG was affirmed through an acute and sub-acute oral toxicity study performed in rats in accordance with the OECD guidelines and its LD_{50} was more than 2000 mg/kg b.w. Further, the organ coefficients and the biochemical parameters did not indicate any potential adverse effects on the functioning of vital organs. The neurological safety profile of BaBG was also established as there were no changes in muscle coordination, spontaneous locomotion, or observed anxiety-like behavior in the rats treated with a dose as high as 1000 mg/kg b.w. during the sub-acute toxicity study. Thus, BaBG exhibits greater safety and biocompatibility in preclinical studies and can be used as a therapeutic strategy.

The important finding of our study was establishing the temporal dynamics and significant details about the involvement of intracellular calcium and calcium-binding protein i.e., S100b level in the progression of NP in the chronic constriction injury (CCI) model. There was a notable time-dependent increase in the intracellular calcium and S100b protein levels in both the sciatic nerve and spinal cord acutely 1 h post-injury. However, pentamidine, an S100b inhibitor, mitigated CCI-induced NP sensory and motor impairments, proving that S100b is essential to NP pathogenesis. Pentamidine also reduced astrocyte and microglia hyperactivation in this NP model. By inhibiting glial cell activation, pentamidine reversed NP by breaking the inflammation-pain feed-forward loop. In addition, pentamidine significantly reduced S100b-induced inflammation by reducing CCI-induced TNF-α and IL-6 levels in the sciatic nerve and spinal cord. In conclusion, these data provided substantial evidence supporting the role of S100b in the pathophysiology of NP and emphasized the therapeutic potential of S100b inhibition.

Further, we thoroughly investigated BaBG's pharmacological effects and found that it mitigated CCI-induced sensory hypersensitivity and motor deficits. In the *ex vivo* electrophysiological setup, BaBG resulted in an elongation of the repolarization phase of the action potential. Therefore, BaBG delays action potential propagation and therefore can be used during NP as an increased nociceptors' sensitivity is reported. In the CCI paradigm in rats, BaBG dose-dependently attenuated all NP symptoms. It also hindered the activation of S100b and decreased inflammation post-CCI. BaBG repaired and remodeled dendrites, hence exhibiting disease-modifying properties. Similar to pregabalin, BaBG dose-dependently attenuated the elevated intracellular calcium levels in the SN and SC post-injury in rats. Therefore, BaBG has a disease-modifying and calcium-regulating potential, thus potentially impeding calcium-associated NP pathogenesis. Remarkably, our research stands as the first to demonstrate the pharmacological potential of inorganic materials in the NP treatment.

BaBG attenuates NP phenotypes via calcium-regulatory mechanisms

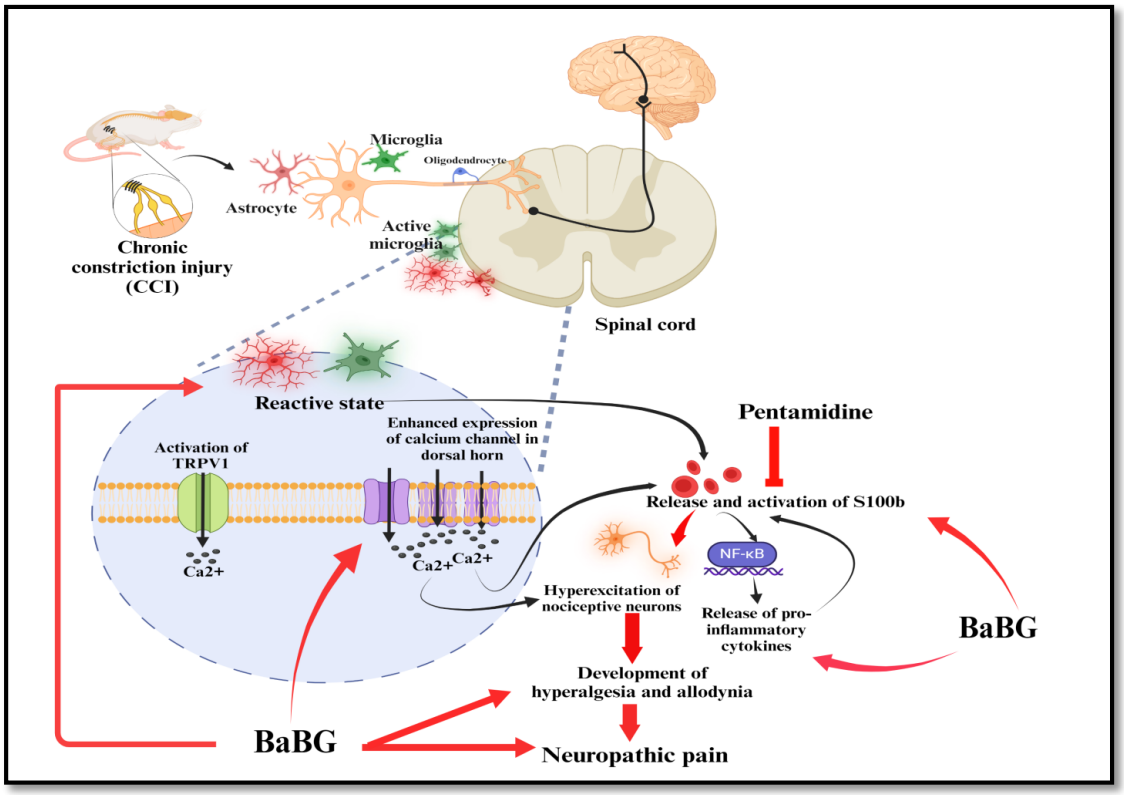

Figure 7.1. Summary and conclusion of the study: red arrow denotes decrease.

The injury to the sciatic nerve results in central sensitization through an increase in the expression of calcium channels (Cav2.2) in the dorsal horn of the spinal cord. In addition, there is an increased expression of heat-sensing TRPV1 channels in the spinal cord. Increased expression of these channels leads to an increase in the influx of calcium ions, causing hyper excitation of the nociceptive neurons and the development of NP phenotypes. In addition, the resident immune cells of CNS i.e., glial cells (astrocytes and microglia) get activated post-CCI leading to an increase in the release of calcium-binding proteins i.e., S100b. S100b gets activated in the presence of calcium ions causing the release of pro-inflammatory cytokines and progression of NP. However, treatment with a specific S100b inhibitor i.e., pentamidine significantly reversed NP phenotypes and lowered S100b-induced downstream inflammatory cascade like NF-

κB. Further, BaBG also ameliorated the CCI-induced sensory hypersensitivity (hyperalgesia and allodynia) and motor deficits. Moreover, it reduced intracellular calcium levels and calcium-binding protein (S100b) in the sciatic nerve and spinal cord post-CCI. BaBG also mitigated the CCI-induced glial cell activation and subsequent release of pro-inflammatory cytokines.

7.1. Important outcomes

- BaBG has regenerative and anti-inflammatory potential.
- There was dose-dependent plasma release of dopants (Ca, Si, and Ba) from BaBG following oral administration which is within the permissible physiological limits.
- Barium released from BaBG was found in both the peripheral organs and the central nervous system, specifically the brain. Hence, the therapeutic ions released from BaBG possess the capability to exert their effects on the central nervous system.
- There was a time-dependent increase in the intracellular calcium and S100b protein levels in both the sciatic nerve and spinal cord acutely 1 h post-injury of the sciatic nerve.
- S100b was found to be involved in the NP pathogenesis in the chronic constriction injury (CCI) model of neuropathic pain.
- BaBG resulted in an elongation of the repolarization phase of the action potential thus delaying the action potential propagation.
- BaBG has a disease-modifying and calcium-regulating potential.
- BaBG dose-dependently attenuated all NP phenotypes.

7.2 Scope for Further Work

Our research has yielded significant insights into the effect of BaBG on calcium currents through *ex vivo* electrophysiological investigations. However, investigating the molecular processes by which BaBG influences calcium currents could yield a precise understanding of its effects on various calcium channel subtypes. The safety profile of BaBG was validated preclinically in the acute and subacute oral toxicity study, and the *in vivo* pharmacokinetic parameters indicated that the concentration of therapeutic dopants released after post-oral administration remained within the physiological limits. Consequently, BaBG is safer and possesses the potential for clinical application, necessitating a clinical trial. Moreover, the optimal pharmaceutical administration form of BaBG will be oral suspensions, owing to enhanced patient compliance. Consequently, addressing these aspects could substantially improve our comprehension of BaBG's effect on calcium channel modulation and its potential role in the treatment of neuropathic pain.

Bibliography

Adamczyk, B., et al. (2023). "The Comparison of the Selected Parameters of Brain Injury and Interleukins in the CSF in Patients Diagnosed De Novo with RRMS Compared to the Control Group." Diagnostics **13**(22): 3436.

Adami, C., et al. (2001). "S100B expression in and effects on microglia." Glia **33**(2): 131-142.

Ahmad, N., et al. (2021). "A novel gabapentin analogue assuages neuropathic pain response in chronic sciatic nerve constriction model in rats." Behavioural Brain Research **405**: 113190.

Ajita, J., et al. (2015). "Effect of size of bioactive glass nanoparticles on mesenchymal stem cell proliferation for dental and orthopedic applications." Materials Science and Engineering: C **53**: 142-149.

Akula, P. and L. PK (2018). "Effect of pH on weakly acidic and basic model drugs and determination of their ex vivo transdermal permeation routes." Brazilian Journal of Pharmaceutical Sciences **54**.

Ali, A., et al. (2018). "Studies on effect of CuO addition on mechanical properties and in vitro cytocompatibility in 1393 bioactive glass scaffold." Materials Science and Engineering: C **93**: 341-355.

Alles, S. R., et al. (2020). "Pregabalin as a pain therapeutic: beyond calcium channels." Frontiers in cellular neuroscience **14**: 83.

Alles, S. R., et al. (2018). "Peripheral nerve injury increases contribution of L-type calcium channels to synaptic transmission in spinal lamina II: Role of α2δ–1 subunits." Molecular pain **14**: 1744806918765806.

Alles, S. R. and P. A. Smith (2021). "Peripheral voltage-gated cation channels in neuropathic pain and their potential as therapeutic targets." Frontiers in Pain Research **2**: 750583.

Altier, C. and G. W. Zamponi (2004). "Targeting Ca2+ channels to treat pain: T-type versus N-type." Trends in pharmacological sciences **25**(9): 465-470.

Anand, A., et al. (2019). "Preparation and in vivo biocompatibility studies of different mesoporous bioactive glasses." Journal of the mechanical behavior of biomedical materials **89**: 89-98.

Andorko, J. I. and C. M. Jewell (2017). "Designing biomaterials with immunomodulatory properties for tissue engineering and regenerative medicine." Bioengineering & translational medicine **2**(2): 139-155.

Antunes, F. T. T., et al. (2023). "Current drug development overview: targeting voltage-gated calcium channels for the treatment of pain." Int J Mol Sci **24**(11): 9223.

Apkarian, A. V., et al. (2005). "Human brain mechanisms of pain perception and regulation in health and disease." European journal of pain **9**(4): 463-484.

Arepalli, S. K., et al. (2016). "Enhanced bioactivity, biocompatibility and mechanical behavior of strontium substituted bioactive glasses." Materials Science and Engineering: C **69**: 108-116.

Arepalli, S. K., et al. (2015). "Influence of barium substitution on bioactivity, thermal and physico-mechanical properties of bioactive glass." Materials Science and Engineering: C **49**: 549-559.

Arkudas, A., et al. (2013). "Evaluation of angiogenesis of bioactive glass in the arteriovenous loop model." Tissue Engineering Part C: Methods **19**(6): 479-486.

ASTM, F. (2000). "756-00. Standard practice for assessment of hemolytic properties of materials." Philadelphia: American Society for Testing and Materials.

Aurilio, C., et al. (2008). "Ionic channels and neuropathic pain: phisiopatology and applications." Journal of Cellular Physiology **215**(1): 8-14.

Austin, C., et al. (2013). "Barium distributions in teeth reveal early-life dietary transitions in primates." Nature **498**(7453): 216-219.

Bagriyanik, H., et al. (2014). "The effects of resveratrol on chronic constriction injury of sciatic nerve in rats." Neuroscience Letters **561**: 123-127.

Baino, F. (2019). Functionally graded bioactive glass-derived scaffolds mimicking bone tissue. Biomedical, Therapeutic and Clinical Applications of Bioactive Glasses, Elsevier**:** 443-466.

Baino, F., et al. (2018). "Bioactive sol- gel glasses: processing, properties, and applications." International Journal of Applied Ceramic Technology **15**(4): 841-860.

Baino, F., et al. (2018). "Bioactive glasses: where are we and where are we going?" Journal of functional biomaterials **9**(1): 25.

Balasubramanian, P., et al. (2017). "Angiogenic potential of boron-containing bioactive glasses: in vitro study." Journal of Materials Science **52**(15): 8785-8792.

Ball, J. P., et al. (2014). "Biocompatible evaluation of barium titanate foamed ceramic structures for orthopedic applications." Journal of Biomedical Materials Research Part A **102**(7): 2089-2095.

Bannister, K., et al. (2020). "Neuropathic pain: mechanism-based therapeutics." Annual Review of Pharmacology and Toxicology **60**: 257-274.

Barabadi, Z., et al. (2016). "Fabrication of hydrogel based nanocomposite scaffold containing bioactive glass nanoparticles for myocardial tissue engineering." Materials Science and Engineering: C **69**: 1137-1146.

Barateiro, A., et al. (2016). "S100B as a potential biomarker and therapeutic target in multiple sclerosis." Molecular neurobiology **53**: 3976-3991.

Baron, R. (2006). "Mechanisms of disease: neuropathic pain—a clinical perspective." Nature clinical practice Neurology **2**(2): 95-106.

Baron, R., et al. (2010). "Neuropathic pain: diagnosis, pathophysiological mechanisms, and treatment." The Lancet Neurology **9**(8): 807-819.

Baron, R., et al. (2017). "Peripheral neuropathic pain: a mechanism-related organizing principle based on sensory profiles." Pain **158**(2): 261.

Barros, C., et al. (2022). "S100B inhibition protects from chronic experimental autoimmune encephalomyelitis." Brain Communications **4**(3): fcac076.

Baskić, D., et al. (2006). "Analysis of cycloheximide- induced apoptosis in human leukocytes: Fluorescence microscopy using annexin V/propidium iodide versus acridin orange/ethidium bromide." Cell Biology International **30**(11): 924-932.

Basso, D. M., et al. (1995). "A sensitive and reliable locomotor rating scale for open field testing in rats." Journal of neurotrauma **12**(1): 1-21.

Beherei, H. H., et al. (2009). "Fabrication and characterization of bioactive glass (45S5)/titania biocomposites." Ceramics International **35**(5): 1991-1997.

Bennett, G. J. (1993). "An animal model of neuropathic pain: a review." Muscle & Nerve: Official Journal of the American Association of Electrodiagnostic Medicine **16**(10): 1040-1048.

Bennett, G. J., et al. (2003). "Models of neuropathic pain in the rat." Current protocols in neuroscience **22**(1): 9.14. 11-19.14. 16.

Bennett, G. J. and Y.-K. Xie (1988). "A peripheral mononeuropathy in rat that produces disorders of pain sensation like those seen in man." Pain **33**(1): 87-107.

Bernardeschi, D., et al. (2015). "Cutaneous and labyrinthine tolerance of bioactive glass S53P4 in mastoid and epitympanic obliteration surgery: prospective clinical study." BioMed research international **2015**.

Berridge, M. J., et al. (2000). "The versatility and universality of calcium signalling." Nature reviews Molecular cell biology **1**(1): 11-21.

Bhandari, S., et al. (2021). "The scavenger function of liver sinusoidal endothelial cells in health and disease." Frontiers in Physiology **12**: 757469.

Bhattarai, B., et al. (2007). "Chronic pain and cost: an epidemiological study in the communities of Sunsari district of Nepal." Nepal Med Coll J **9**(1): 6-11.

Bhindi, N., et al. (2022). "Targeted Muscle Reinnervation of the Gastrocnemius for Preventing Neuropathic Pain." J Clin Med Surgery **2**(2): 1051.

Blaine, J., et al. (2015). "Renal control of calcium, phosphate, and magnesium homeostasis." Clinical journal of the American Society of Nephrology: CJASN **10**(7): 1257.

Bligh, P. and D. Taylor (1963). "Comparative studies of the metabolism of strontium and barium in the rat." Biochemical Journal **87**(3): 612.

Boehler, R. M., et al. (2011). "Tissue engineering tools for modulation of the immune response." Biotechniques **51**(4): 239-254.

Borzelleca, J., et al. (1988). "Short-term toxicity (one-and ten-day gavage) of barium chloride in male and female rats." Journal of the American College of Toxicology **7**(5): 675-685.

Bouali-Benazzouz, R., et al. (2021). "Neuropathic pain modeling: Focus on synaptic and ion channel mechanisms." Progress in Neurobiology **201**: 102030.

Bourinet, E., et al. (2016). "T-type calcium channels in neuropathic pain." Pain **157**: S15-S22.

Bradford, M. M. J. A. b. (1976). "A rapid and sensitive method for the quantitation of microgram quantities of protein utilizing the principle of protein-dye binding." **72**(1-2): 248-254.

Brisby, H., et al. (1999). "Markers of nerve tissue injury in the cerebrospinal fluid in patients with lumbar disc herniation and sciatica." Spine **24**(8): 742-746.

Bronstein, P. M. (1972). "Open-field behavior of the rat as a function of age: Cross-sectional and longitudinal investigations." Journal of Comparative and Physiological Psychology **80**(2): 335.

Brückner, R., et al. (2016). "Controlling the ion release from mixed alkali bioactive glasses by varying modifier ionic radii and molar volume." Journal of Materials Chemistry B **4**(18): 3121-3134.

Bucci, G., et al. (2011). "Inhibition of synaptic transmission and G protein modulation by synthetic CaV2. 2 Ca2+ channel peptides." The Journal of physiology **589**(13): 3085-3101.

Buesen, R., et al. (2014). "Effects of SiO 2, ZrO 2, and BaSO 4 nanomaterials with or without surface functionalization upon 28-day oral exposure to rats." Archives of Toxicology **88**(10): 1881-1906.

Buonocore, M., et al. (2016). "Dynamic Mechanical Allodynia—One Clinical Sign, Several Mechanisms: Five Illustrative Cases." Pain Practice **16**(3): E48-E55.

Buzzetti, E., et al. (2017). "Gender differences in liver disease and the drug-dose gender gap." Pharmacological Research **120**: 97-108.

Cabellos, J., et al. (2020). "Short-term oral administration of non-porous and mesoporous silica did not induce local or systemic toxicity in mice." Nanotoxicology **14**(10): 1324-1341.

Cahill, C. M., et al. (2022). "Delta opioid receptor activation modulates affective pain and modality- specific pain hypersensitivity associated with chronic neuropathic pain." Journal of Neuroscience Research **100**(1): 129-148.

Cai, Z., et al. (2022). "High-voltage long-duration pulsed radiofrequency attenuates neuropathic pain in CCI rats by inhibiting Cav2. 2 in spinal dorsal horn and dorsal root ganglion." Brain Research **1785**: 147892.

Calvo, M., et al. (2012). "The role of the immune system in the generation of neuropathic pain." The Lancet Neurology **11**(7): 629-642.

Casal, M. A., et al. (2019). "Estimation of kidney function in oncology: implications for anticancer drug selection and dosing." Clinical Journal of the American Society of Nephrology **14**(4): 587-595.

Cavalli, E., et al. (2019). "The neuropathic pain: An overview of the current treatment and future therapeutic approaches." International journal of immunopathology and pharmacology **33**: 2058738419838383.

Celikbilek, A., et al. (2014). "S100B as a glial cell marker in diabetic peripheral neuropathy." Neuroscience Letters **558**: 53-57.

Cesta, M. F. (2006). "Normal structure, function, and histology of the spleen." Toxicologic Pathology **34**(5): 455-465.

Chan, K.-Y., et al. (2022). "Ameliorative potential of hot compress on sciatic nerve pain in chronic constriction injury-induced rat model." Frontiers in Synaptic Neuroscience **14**: 859278.

Chapman, K., et al. (2013). "A global pharmaceutical company initiative: An evidence-based approach to define the upper limit of body weight loss in short term toxicity studies." Regulatory Toxicology and Pharmacology **67**(1): 27-38.

Chen, Q.-Y., et al. (2019). "Mechanism of persistent hyperalgesia in neuropathic pain caused by chronic constriction injury." Neural Regeneration Research **14**(6): 1091.

Chen, Q., et al. (2010). "Elastomeric nanocomposites as cell delivery vehicles and cardiac support devices." Soft Matter **6**(19): 4715-4726.

Chen, S.-H., et al. (2020). "Controllable forces for reproducible chronic constriction injury mimicking compressive neuropathy in rat sciatic nerve." Journal of Neuroscience Methods **335**: 108615.

Chen, Y., et al. (2009). "Influence of the vanilloid receptor TRPV1 on the activation of spinal cord glia in mouse models of pain." Experimental Neurology **220**(2): 383-390.

Chen, Z., et al. (2018). "A rapid hemostatic sponge based on large, mesoporous silica nanoparticles and N-alkylated chitosan." Nanoscale **10**(43): 20234-20245.

Chen, Z., et al. (2014). "Osteogenic differentiation of bone marrow MSCs by β-tricalcium phosphate stimulating macrophages via BMP2 signalling pathway." Biomaterials **35**(5): 1507-1518.

CHENG, H. p., et al. (2006). Calcium signaling in physiology and pathophysiology, Wiley Online Library. **27:** 767-772.

Cho, J. and Y. Huh (2020). "Astrocytic calcium dynamics along the pain pathway." Frontiers in cellular neuroscience **14**: 594216.

Choe, M.-A., et al. (2011). "Hindlimb muscle atrophy occurs from peripheral nerve damage in a rat neuropathic pain model." Biological research for nursing **13**(1): 44-54.

Clark, A. K., et al. (2007). "Role of spinal microglia in rat models of peripheral nerve injury and inflammation." European journal of pain **11**(2): 223-230.

Co-operation, O. f. E. and Development (2008). Test No. 407: repeated dose 28-day oral toxicity study in rodents, OECD Publishing.

Cohen, J. (1988). "Statistical Power Analysis for the Behavioral Sciences Hillsdale New Jersey L Erlbaum."

Cohen, S. P. and J. Mao (2014). "Neuropathic pain: mechanisms and their clinical implications." BMJ **348**.

Cohen, S. P., et al. (2021). "Chronic pain: an update on burden, best practices, and new advances." The Lancet **397**(10289): 2082-2097.

Colloca, L., et al. (2017). "Neuropathic pain." Nature reviews Disease primers **3**(1): 1-19.

Crofford, L. J. (2013). "Use of NSAIDs in treating patients with arthritis." Arthritis Res Ther **15**: 1-10.

Croia, C., et al. (2019). "One year in review 2019: pathogenesis of rheumatoid arthritis." Clin Exp Rheumatol **37**(3): 347-357.

Cui, W., et al. (2021). "The calcium channel α2δ1 subunit: Interactional targets in primary sensory neurons and role in neuropathic pain." Frontiers in cellular neuroscience **15**: 699731.

D'Mello, R. and A. H. Dickenson (2008). "Spinal cord mechanisms of pain." British Journal of Anaesthesia **101**(1): 8-16.

da Rocha, A. P., et al. (2020). "Tramadol for management of fibromyalgia pain and symptoms: Systematic review." International Journal of Clinical Practice **74**(3): e13455.

da Silva, A., et al. (2022). "Micro-and nanocarriers for pain alleviation." Advanced drug delivery reviews **187**: 114359.

Dahlhamer, J. (2018). "Prevalence of chronic pain and high-impact chronic pain among adults—United States, 2016." MMWR. Morbidity and Mortality Weekly Report **67**.

Dai, C., et al. (2009). "Degradable, antibacterial silver exchanged mesoporous silica spheres for hemorrhage control." Biomaterials **30**(29): 5364-5375.

Day, R. M. (2005). "Bioactive glass stimulates the secretion of angiogenic growth factors and angiogenesis in vitro." Tissue engineering **11**(5-6): 768-777.

Day, R. M., et al. (2004). "Assessment of polyglycolic acid mesh and bioactive glass for soft-tissue engineering scaffolds." Biomaterials **25**(27): 5857-5866.

de Medinaceli, L., et al. (1982). "An index of the functional condition of rat sciatic nerve based on measurements made from walking tracks." Experimental neurology **77**(3): 634-643.

De Oliveira, A. A. R., et al. (2013). "Synthesis, characterization and cytocompatibility of spherical bioactive glass nanoparticles for potential hard tissue engineering applications." Biomedical Materials **8**(2): 025011.

de Souza Balbinot, G., et al. (2020). "Synthesis of sol–gel derived calcium silicate particles and development of a bioactive endodontic cement." Dental Materials **36**(1): 135-144.

de Souza, L. P., et al. (2020). "Evaluation of effectiveness of 45S5 bioglass doped with niobium for repairing critical- sized bone defect in in vitro and in vivo models." Journal of Biomedical Materials Research Part A **108**(3): 446-457.

Decker, T. and M.-L. Lohmann-Matthes (1988). "A quick and simple method for the quantitation of lactate dehydrogenase release in measurements of cellular cytotoxicity and tumor necrosis factor (TNF) activity." Journal of Immunological Methods **115**(1): 61-69.

Deliormanlı, A. M. (2016). "Electrospun cerium and gallium-containing silicate based 13-93 bioactive glass fibers for biomedical applications." Ceramics International **42**(1): 897-906.

Della Pepa, G. and M. L. Brandi (2016). "Microelements for bone boost: the last but not the least." Clinical Cases in Mineral and Bone Metabolism **13**(3): 181.

Derry, S., et al. (2019). "Pregabalin for neuropathic pain in adults." Cochrane Database of Systematic Reviews(1).

Di Sante, G., et al. (2020). "The S100B inhibitor pentamidine ameliorates clinical score and neuropathology of relapsing—remitting multiple sclerosis mouse model." Cells **9**(3): 748.

Djouhri, L., et al. (2012). "Partial nerve injury induces electrophysiological changes in conducting (uninjured) nociceptive and nonnociceptive DRG neurons: Possible relationships to aspects of peripheral neuropathic pain and paresthesias." PAIN® **153**(9): 1824-1836.

Dong, X., et al. (2017). "Bioglass promotes wound healing through modulating the paracrine effects between macrophages and repairing cells." Journal of Materials Chemistry B **5**(26): 5240-5250.

Dowell, D. (2022). "CDC clinical practice guideline for prescribing opioids for pain—United States, 2022." MMWR. Recommendations and reports **71**.

Drăghici, N. C., et al. (2023). "Diagnostic approach to lower limb entrapment neuropathies: A narrative literature review." Diagnostics **13**(21): 3385.

Du, Z., et al. (2019). "Silica nanoparticles induce cardiomyocyte apoptosis via the mitochondrial pathway in rats following intratracheal instillation." International Journal of Molecular Medicine **43**(3): 1229-1240.

Dumala, N., et al. (2019). "Repeated oral dose toxicity study of nickel oxide nanoparticles in Wistar rats: a histological and biochemical perspective." Journal of Applied Toxicology **39**(7): 1012-1029.

Dureja, G. P., et al. (2014). "Prevalence of chronic pain, impact on daily life, and treatment practices in India." Pain Practice **14**(2): E51-E62.

Dworkin, R. H., et al. (2007). "Pharmacologic management of neuropathic pain: evidence-based recommendations." Pain **132**(3): 237-251.

Dziadek, M., et al. (2018). "A simple way of modulating in vitro angiogenic response using Cu and Co-doped bioactive glasses." Materials Letters **215**: 87-90.

Earl, J. S., et al. (2011). "Physical and chemical characterization of dentin surface following treatment with NovaMin technology." The Journal of clinical dentistry **22**(3): 62-67.

Edhi, M. M., et al. (2020). "Time-dynamic pulse modulation of spinal cord stimulation reduces mechanical hypersensitivity and spontaneous pain in rats." Scientific reports **10**(1): 20358.

El-Gohary, M. I., et al. (2013). "Influence of composition on the in-vitro bioactivity of bioglass prepared by a quick alkali-mediated sol–gel method." Nature and Science **11**(3): 26-33.

Ellis, A. and D. Bennett (2013). "Neuroinflammation and the generation of neuropathic pain." British Journal of Anaesthesia **111**(1): 26-37.

Fan, X., et al. (2023). "GFAP palmitoylcation mediated by ZDHHC23 in spinal astrocytes contributes to the development of neuropathic pain." Regional Anesthesia and Pain Medicine.

Fayaz, A., et al. (2016). "Prevalence of chronic pain in the UK: a systematic review and meta-analysis of population studies." BMJ Open **6**(6): e010364.

Ferrari, L. F., et al. (2022). "Characterization of the Dahl salt-sensitive rat as a rodent model of inherited, widespread, persistent pain." Scientific reports **12**(1): 19348.

Field, M. J., et al. (1999). "Detection of static and dynamic components of mechanical allodynia in rat models of neuropathic pain: are they signalled by distinct primary sensory neurones?" Pain **83**(2): 303-311.

Fischer, A. H., et al. (2008). "Paraffin embedding tissue samples for sectioning." CSH protocols **2008**: pdb. prot4989-pdb. prot4989.

Fornasari, D. (2012). "Pain mechanisms in patients with chronic pain." Clinical drug investigation **32**: 45-52.

Forouzanfar, F., et al. (2023). "Synergistic effect of ellagic acid and gabapentin in a rat model of neuropathic pain." Metabolic Brain Disease **38**(4): 1421-1432.

Foudah, A. I., et al. (2022). "Analgesic action of catechin on chronic constriction injury–induced neuropathic pain in Sprague–Dawley rats." Frontiers in Pharmacology **13**: 895079.

Fredholm, Y. C., et al. (2010). "Strontium containing bioactive glasses: glass structure and physical properties." Journal of non-crystalline solids **356**(44-49): 2546-2551.

Fu, C., et al. (2013). "The absorption, distribution, excretion and toxicity of mesoporous silica nanoparticles in mice following different exposure routes." Biomaterials **34**(10): 2565-2575.

Fu, C., et al. (2012). "Acute toxicity and oxidative damage induced by silica nanorattle in vivo." Chinese Science Bulletin **57**(20): 2525-2532.

Gaetani, L., et al. (2019). "Neurofilament light chain as a biomarker in neurological disorders." Journal of Neurology, Neurosurgery and Psychiatry **90**(8): 870-881.

Giannini, E. G., et al. (2005). "Liver enzyme alteration: a guide for clinicians." CMAJ **172**(3): 367-379.

Gierthmühlen, J. and R. Baron (2016). Neuropathic pain. Seminars in Neurology, Thieme Medical Publishers.

Gilron, I. and S. J. Flatters (2006). "Gabapentin and pregabalin for the treatment of neuropathic pain: A review of laboratory and clinical evidence." Pain Research and Management **11**: 16A-29A.

Gloor, Y., et al. (2019). "Old problem, new solutions: biomarker discovery for acetaminophen liver toxicity." Expert opinion on drug metabolism & toxicology **15**(8): 659-669.

Gorustovich, A. A., et al. (2010). "Effect of bioactive glasses on angiogenesis: a review of in vitro and in vivo evidences." Tissue Engineering Part B: Reviews **16**(2): 199-207.

Goswami, D., et al. (2023). "Pharmacological and pathological relevance of S100 proteins in neurological disorders." CNS & Neurological Disorders-Drug Targets (Formerly Current Drug Targets-CNS & Neurological Disorders) **22**(10): 1403-1416.

Goswami, N., et al. (2021). "Clinical relevance of chronic neuropathic pain phenotypes in mice: A comprehensive behavioral analysis." Behavioural Brain Research **400**: 113055.

Grada, A., et al. (2017). "Research techniques made simple: analysis of collective cell migration using the wound healing assay." Journal of Investigative Dermatology **137**(2): e11-e16.

Grande, P., et al. (1982). "Estimation of acute myocardial infarct size in man by serum CK-MB measurements." Circulation **65**(4): 756-764.

Grinsell, D. and C. Keating (2014). "Peripheral nerve reconstruction after injury: a review of clinical and experimental therapies." BioMed research international **2014**.

Gruden, M. A., et al. (2011). "Immunoprotection against toxic biomarkers is retained during Parkinson's disease progression." Journal of neuroimmunology **233**(1-2): 221-227.

Gryshchuk, V. and N. Galagan (2016). "Silica nanoparticles effects on blood coagulation proteins and platelets." Biochemistry research international **2016**.

Gupta, S., et al. (2021). "Bioactive glass: A multifunctional delivery system." Journal of Controlled Release **335**: 481-497.

Guy, S., et al. (2014). "Anticonvulsant medication use for the management of pain following spinal cord injury: systematic review and effectiveness analysis." Spinal Cord **52**(2): 89-96.

Hagiwara, S. and L. Byerly (1981). "Calcium channel." Annual Review of Neuroscience **4**(1): 69-125.

Hains, B. C. and S. G. Waxman (2006). "Activated microglia contribute to the maintenance of chronic pain after spinal cord injury." Journal of Neuroscience **26**(16): 4308-4317.

Hamidi, G. A., et al. (2012). "Ethosuximide reduces allodynia and hyperalgesia and potentiates morphine effects in the chronic constriction injury model of neuropathic pain." European Journal of Pharmacology **674**(2-3): 260-264.

Haro Durand, L. A., et al. (2017). "In vitro human umbilical vein endothelial cells response to ionic dissolution products from lithium-containing 45S5 bioactive glass." Materials **10**(7): 740.

Hasan, R., et al. (2021). "A Bioglass-Based Antibiotic (Vancomycin) Releasing Bone Void Filling Putty to Treat Osteomyelitis and Aid Bone Healing." Int J Mol Sci **22**(14): 7736.

He, X., et al. (2019). "Wound Dressings Based on Rubidium-Doped Bioactive Glass Nanospheres Promote Diabetic Wound Healing." Journal of biomedical nanotechnology **15**(10): 2059-2071.

Heckbert, S. R., et al. (1998). "Outcome after hemorrhagic shock in trauma patients." Journal of Trauma and Acute Care Surgery **45**(3): 545-549.

Heizmann, C. W. (2022). "S100 Proteins." Encyclopedia of Molecular Pharmacology: 1381-1386.

Helmchen, F., et al. (1997). "Calcium dynamics associated with a single action potential in a CNS presynaptic terminal." Biophysical Journal **72**(3): 1458-1471.

Hench, L. L. (2006). "The story of Bioglass®." Journal of Materials Science: Materials in Medicine **17**(11): 967-978.

Hench, L. L. (2013). "Chronology of bioactive glass development and clinical applications."

Hench, L. L., et al. (1971). "Bonding mechanisms at the interface of ceramic prosthetic materials." Journal of Biomedical Materials Research **5**(6): 117-141.

Hira, S. K., et al. (2014). "Targeted delivery of doxorubicin-loaded poly (ε-caprolactone)-b-poly (N-vinylpyrrolidone) micelles enhances antitumor effect in lymphoma." PLoS ONE **9**(4): e94309.

Hogan, Q., et al. (2000). "Painful neuropathy decreases membrane calcium current in mammalian primary afferent neurons." Journal of the Peripheral Nervous System **5**(4): 245-245.

Hong, S., et al. (2004). "Early painful diabetic neuropathy is associated with differential changes in tetrodotoxin-sensitive and-resistant sodium channels in dorsal root ganglion neurons in the rat." Journal of Biological Chemistry **279**(28): 29341-29350.

Hoppanova, L. and L. Lacinova (2022). "Voltage-dependent CaV3. 2 and CaV2. 2 channels in nociceptive pathways." Pflügers Archiv-European Journal of Physiology **474**(4): 421-434.

Hoppe, A., et al. (2011). "A review of the biological response to ionic dissolution products from bioactive glasses and glass-ceramics." Biomaterials **32**(11): 2757-2774.

http://etissuesolutions.com/ (2017). "MIRRAGEN®." from http://etissuesolutions.com/.

Hu, G., et al. (2012). "Antibacterial hemostatic dressings with nanoporous bioglass containing silver." Int J Nanomedicine **7**: 2613.

Huang, Y. K., et al. (2020). "Cytokine activin C ameliorates chronic neuropathic pain in peripheral nerve injury rodents by modulating the TRPV1 channel." British Journal of Pharmacology **177**(24): 5642-5657.

Hudson, L. J., et al. (2001). "VR1 protein expression increases in undamaged DRG neurons after partial nerve injury." European Journal of Neuroscience **13**(11): 2105-2114.

Huehnchen, P., et al. (2022). "Neurofilament proteins as a potential biomarker in chemotherapy-induced polyneuropathy." JCI insight **7**(6).

Ito, E., et al. (2023). "Increased cerebrospinal fluid S100B protein levels in patients with trigeminal neuralgia and hemifacial spasm." Acta Neurochirurgica **165**(4): 959-965.

Iuvone, T., et al. (2007). "Cannabinoid CB 1 receptor stimulation affords neuroprotection in MPTP-induced neurotoxicity by attenuating S100B up-regulation in vitro." Journal of molecular medicine **85**: 1379-1392.

Jager, S. E., et al. (2024). "In vivo calcium imaging shows that satellite glial cells have increased activity in painful states." Brain Communications **6**(2): fcae013.

Jagodic, M. M., et al. (2008). "Upregulation of the T-type calcium current in small rat sensory neurons after chronic constrictive injury of the sciatic nerve." Journal of Neurophysiology **99**(6): 3151-3156.

Jensen, T. S. and N. B. Finnerup (2014). "Allodynia and hyperalgesia in neuropathic pain: clinical manifestations and mechanisms." The Lancet Neurology **13**(9): 924-935.

Jergová, S. and D. Čížková (2007). "Microglial activation in different models of peripheral nerve injury of the rat." Journal of molecular histology **38**: 245-251.

Jha, M. K., et al. (2012). "Glia as a link between neuroinflammation and neuropathic pain." Immune network **12**(2): 41.

Ji, R.-R., et al. (2013). "Glia and pain: is chronic pain a gliopathy?" PAIN® **154**: S10-S28.

Jones, J. R. (2015). "Reprint of: Review of bioactive glass: From Hench to hybrids." Acta biomaterialia **23**: S53-S82.

Jones, J. R., et al. (2016). "Bioglass and bioactive glasses and their impact on healthcare." International Journal of Applied Glass Science **7**(4): 423-434.

Julius, D. (2013). "TRP channels and pain." Annual Review of Cell and Developmental Biology **29**(1): 355-384.

Kamerman, P. R., et al. (2015). "World Health Organization (WHO) essential medicines lists: where are the drugs to treat neuropathic pain?" Pain **156**(5): 793.

Kansal, I., et al. (2011). "Structure, surface reactivity and physico-chemical degradation of fluoride containing phospho-silicate glasses." J Mater Chem **21**(22): 8074-8084.

Kargozar, S., et al. (2017). "Potential of bioactive glasses for cardiac and pulmonary tissue engineering." Materials **10**(12): 1429.

Kargozar, S., et al. (2016). "Synthesis, physico-chemical and biological characterization of strontium and cobalt substituted bioactive glasses for bone tissue engineering." Journal of non-crystalline solids **449**: 133-140.

Kawamata, M. and K. Omote (1996). "Involvement of increased excitatory amino acids and intracellular Ca2+ concentration in the spinal dorsal horn in an animal model of neuropathic pain." Pain **68**(1): 85-96.

Keskin- Erdogan, Z., et al. (2021). "Utilization of GelMA with phosphate glass fibers for glial cell alignment." Journal of Biomedical Materials Research Part A **109**(11): 2212-2224.

Khan, J., et al. (2018). "Effect of Pregabalin and Diclofenac on tactile allodynia, mechanical hyperalgesia and pro inflammatory cytokine levels (IL-6, IL-1β) induced by chronic constriction injury of the infraorbital nerve in rats." Cytokine **104**: 124-129.

Khangura, R. K., et al. (2017). "Neuropathic pain attenuating effects of perampanel in an experimental model of chronic constriction injury in rats." Biomedicine and Pharmacotherapy **94**: 557-563.

Khanna, A., et al. (2020). "SIRT1 activation by resveratrol reverses atrophy of apical dendrites of hippocampal CA1 pyramidal neurons and neurobehavioral impairments in moderate grade hepatic encephalopathy rats." Journal of Chemical Neuroanatomy **106**: 101797.

Kim, K. J., et al. (2022). "Cardiovascular risks associated with calcium supplementation in patients with osteoporosis: a nationwide cohort study." European Heart Journal-Cardiovascular Pharmacotherapy **8**(6): 568-577.

Kim, Y. P., et al. (2012). "Phosphate glass fibres promote neurite outgrowth and early regeneration in a peripheral nerve injury model." Journal of tissue engineering and regenerative medicine **9**(3): 236-246.

Kivi, A., et al. (2000). "Effects of barium on stimulus- induced rises of [K+] o in human epileptic non- sclerotic and sclerotic hippocampal area CA1." European Journal of Neuroscience **12**(6): 2039-2048.

Kligman, D. and D. C. Hilt (1988). "The S100 protein family." Trends in biochemical sciences **13**(11): 437-443.

Kneser, U., et al. (2006). "Tissue engineering of bone: the reconstructive surgeon's point of view." Journal of cellular and molecular medicine **10**(1): 7-19.

Kokubo, T. and H. Takadama (2006). "How useful is SBF in predicting in vivo bone bioactivity?" Biomaterials **27**(15): 2907-2915.

Komirishetty, P., et al. (2017). "Combination strategy of PARP inhibitor with antioxidant prevent bioenergetic deficits and inflammatory changes in CCI-induced neuropathy." Neuropharmacology **113**: 137-147.

Konduru, N., et al. (2014). "Biokinetics and effects of barium sulfate nanoparticles." Particle and fibre toxicology **11**(1): 1-15.

Kovrlija, I., et al. (2021). "Incorporation of barium ions into biomaterials: dangerous liaison or potential revolution?" Materials **14**(19): 5772.

Kravchenko, J., et al. (2014). "A review of the health impacts of barium from natural and anthropogenic exposure." Environmental geochemistry and health **36**: 797-814.

Krishna, S., et al. (2020). "Barium poisoning with analytical aspects and its management." International Journal of Advanced Research in Medicinal Chemistry **2**(1): 20-27.

Kuhle, J., et al. (2015). "Serum neurofilament light chain is a biomarker of human spinal cord injury severity and outcome." Journal of Neurology, Neurosurgery and Psychiatry **86**(3): 273-279.

Kumaria, A. (2017). "In vitro models as a platform to investigate traumatic brain injury." Alternatives to Laboratory Animals **45**(4): 201-211.

Lagarto, A., et al. (2011). "Acute and subchronic oral toxicities of Calendula officinalis extract in Wistar rats." Experimental and Toxicologic Pathology **63**(4): 387-391.

Lai, J., et al. (2003). "The role of voltage-gated sodium channels in neuropathic pain." Current Opinion in Neurobiology **13**(3): 291-297.

Lai, W., et al. (1999). "Removal pathway of bioactive glass resorption products from the body." MRS Online Proceedings Library Archive **599**.

Lai, W., et al. (2002). "Silicon excretion from bioactive glass implanted in rabbit bone." Biomaterials **23**(1): 213-217.

Lanas, A. and F. K. Chan (2017). "Peptic ulcer disease." The Lancet **390**(10094): 613-624.

Lapa, A., et al. (2020). "Phosphate glass fibres with therapeutic ions release capability–a review." Advances in Applied Ceramics **119**(1): 1-14.

Leclerc, E., et al. (2009). "Binding of S100 proteins to RAGE: an update." Biochimica et Biophysica Acta (BBA)-Molecular Cell Research **1793**(6): 993-1007.

Lécuyer, J. B., et al. (2021). "S100B protein level for the detection of clinically significant intracranial haemorrhage in patients with mild traumatic brain injury: a subanalysis of a prospective cohort study." Emergency Medicine Journal **38**(4): 285-289.

Lee, J.-A., et al. (2014). "Tissue distribution and excretion kinetics of orally administered silica nanoparticles in rats." Int J Nanomedicine **9**(sup2): 251-260.

Lee, K., et al. (2021). "Functional importance of transient receptor potential (TRP) channels in neurological disorders." Frontiers in cell and developmental biology **9**: 611773.

Leenakul, W., et al. (2013). "Structural and magnetic properties of SiO2–CaO–Na2O–P2O5 containing BaO–Fe2O3 glass–ceramics." Journal of Magnetism and Magnetic Materials **325**: 102-106.

Lever, C., et al. (2006). "Rearing on hind legs, environmental novelty, and the hippocampal formation." Reviews in the Neurosciences **17**(1-2): 111-134.

Li, R., et al. (1991). "An investigation of bioactive glass powders by sol- gel processing." Journal of Applied Biomaterials **2**(4): 231-239.

Li, Z. and J. Guan (2011). "Hydrogels for cardiac tissue engineering." Polymers **3**(2): 740-761.

Liang, C. L., et al. (2018). "Subchronic oral toxicity of silica nanoparticles and silica microparticles in rats." Biomedical and Environmental Sciences **31**(3): 197-207.

Liu, C., et al. (2023). "Research progress and challenges of TRPV1 channel modulators as a prospective therapy for diabetic neuropathic pain." European journal of medicinal chemistry **245**: 114893.

Liu, M.-X., et al. (2020). "IL-6 contributes to Nav1. 3 up-regulation in trigeminal nerve following chronic constriction injury." Neurological Research **42**(6): 504-514.

Liu, T., et al. (2020). "Altered calcium handling produces reentry-promoting action potential alternans in atrial fibrillation–remodeled hearts." JCI insight **5**(8).

Liyanagamage, D. S. N. K., et al. (2020). "Acute and Subchronic Toxicity Profile of a Polyherbal Drug Used in Sri Lankan Traditional Medicine." Evidence-Based Complementary and Alternative Medicine **2020**.

Loeser, J. D. and R.-D. Treede (2008). "The Kyoto protocol of IASP basic pain terminology." PAIN® **137**(3): 473-477.

Lonergan, G. J., et al. (2003). "From the archives of the AFIP: Child abuse: radiologic-pathologic correlation." Radiographics **23**(4): 811-845.

Long, T., et al. (2015). "Fabrication of three- dimensional porous scaffold based on collagen fiber and bioglass for bone tissue engineering." Journal of Biomedical Materials Research Part B: Applied Biomaterials **103**(7): 1455-1464.

Lorenzo, J. (2000). "Interactions between immune and bone cells: new insights with many remaining questions." The Journal of clinical investigation **106**(6): 749-752.

Loza, K., et al. (2016). "Barium sulfate micro-and nanoparticles as bioinert reference material in particle toxicology." Nanotoxicology **10**(10): 1492-1502.

Lu, C.-H., et al. (2022). "MIB2: metal ion-binding site prediction and modeling server." Bioinformatics **38**(18): 4428-4429.

Luo, Z., et al. (2002). "Injury type-specific calcium channel α2δ-1 subunit up-regulation in rat neuropathic pain models correlates with antiallodynic effects of gabapentin." Journal of Pharmacology and Experimental Therapeutics **303**(3): 1199-1205.

Luo, Z. D., et al. (2001). "Upregulation of dorsal root ganglion α2δ calcium channel subunit and its correlation with allodynia in spinal nerve-injured rats." Journal of Neuroscience **21**(6): 1868-1875.

Ma, A.-n., et al. (2013). "Local protective effects of oral 45S5 bioactive glass on gastric ulcers in experimental animals." Journal of Materials Science: Materials in Medicine **24**(3): 803-809.

Macon, A. L., et al. (2015). "A unified in vitro evaluation for apatite-forming ability of bioactive glasses and their variants." Journal of Materials Science: Materials in Medicine **26**: 1-10.

Macon, A. L. B., et al. (2015). "A unified in vitro evaluation for apatite-forming ability of bioactive glasses and their variants of bioactive glasses and their variants." J. Mater. Sci. Mater. Med **26**: 115.

Macvicar's, B. and R. Llinas (1985). "Barium action potentials in regenerating axons of the lamprey spinal cord." Journal of Neuroscience Research **13**(1- 2): 323-335.

Macvicar's, B. A. and R. R. Llinas (1985). "Barium action potentials in regenerating axons of the lamprey spinal cord." Journal of Neuroscience Research **13**(1- 2): 323-335.

Madanat, R., et al. (2009). "Radio-opaque bioactive glass markers for radiostereometric analysis." Acta Biomater **5**(9): 3497-3505.

Majumdar, S., et al. (2021). "Multifarious applications of bioactive glasses in soft tissue engineering." Biomaterials science **9**(24): 8111-8147.

Majumdar, S., et al. (2022). "Bioactive glass: soft tissue reparative and regenerative applications." Bioactive Glasses and Glass- Ceramics: Fundamentals and Applications: 479-517.

Majumdar, S., et al. (2021). "Synthesis and characterization of barium-doped bioactive glass with potential anti-inflammatory activity." Ceramics International **47**(5): 7143-7158.

Majumdar, S. and S. Krishnamurthy (2022). "In vivo toxicological evaluation of barium-doped bioactive glass in rats." Ceramics International **48**(22): 33288-33305.

Malek, N., et al. (2015). "The importance of TRPV1-sensitisation factors for the development of neuropathic pain." Molecular and Cellular Neuroscience **65**: 1-10.

Malgaroli, A., et al. (1987). "Dopamine inhibits cytosolic Ca2+ increases in rat lactotroph cells. Evidence of a dual mechanism of action." Journal of Biological Chemistry **262**(29): 13920-13927.

Mao, C., et al. (2016). "Acute toxicity and in vivo biodistribution of monodispersed mesoporous bioactive glass spheres in intravenously exposed mice." Materials Science and Engineering: C **58**: 682-691.

Mao, C., et al. (2014). "Enhanced healing of full-thickness diabetic wounds using bioactive glass and Yunnan baiyao ointments." Journal of Wuhan University of Technology-Mater. Sci. Ed. **29**(5): 1063-1070.

Marenholz, I., et al. (2004). "S100 proteins in mouse and man: from evolution to function and pathology (including an update of the nomenclature)." Biochemical and biophysical research communications **322**(4): 1111-1122.

Mariani, E., et al. (2019). "Biomaterials: foreign bodies or tuners for the immune response?" Int J Mol Sci **20**(3): 636.

Markman, J. D. and R. H. Dworkin (2006). "Ion channel targets and treatment efficacy in neuropathic pain." The Journal of Pain **7**(1): S38-S47.

Matikainen, N., et al. (2021). "Physiology of calcium homeostasis: an overview." Endocrinology and Metabolism Clinics **50**(4): 575-590.

McGinnis, A. and R.-R. Ji (2023). "The similar and distinct roles of satellite glial cells and spinal astrocytes in neuropathic pain." Cells **12**(6): 965.

Meacham, K., et al. (2017). "Neuropathic pain: central vs. peripheral mechanisms." Current pain and headache reports **21**: 1-11.

Medler, S. (2022). "Effects of local anesthetics on compound action potentials generated from the frog sciatic nerve." Advances in Physiology Education **46**(4): 658-666.

Meyer, O. A., et al. (1979). "A method for the routine assessment of fore-and hindlimb grip strength of rats and mice." Neurobehavioral Toxicology **1**(3): 233-236.

Meyer, R. A., et al. (2005). "Neural mechanisms of hyperalgesia after tissue injury." Johns Hopkins APL technical digest **26**(1): 56-66.

Michetti, F., et al. (2023). "The S100B protein: a multifaceted pathogenic factor more than a Biomarker." Int J Mol Sci **24**(11): 9605.

Michetti, F., et al. (2019). "The S100B story: from biomarker to active factor in neural injury." Journal of Neurochemistry **148**(2): 168-187.

Michetti, F., et al. (2021). "Growing role of S100B protein as a putative therapeutic target for neurological-and nonneurological-disorders." Neuroscience and Biobehavioral Reviews **127**: 446-458.

Michinaga, S. and Y. Koyama (2019). "Dual roles of astrocyte-derived factors in regulation of blood-brain barrier function after brain damage." Int J Mol Sci **20**(3): 571.

Mika, J., et al. (2013). "Importance of glial activation in neuropathic pain." European Journal of Pharmacology **716**(1-3): 106-119.

Mills, S. E., et al. (2019). "Chronic pain: a review of its epidemiology and associated factors in population-based studies." British Journal of Anaesthesia **123**(2): e273-e283.

Moffett, D., et al. (2007). "Toxicological profile for barium and barium compounds."

Mohammadi, R., et al. (2012). "Homeopathic treatment for peripheral nerve regeneration: an experimental study in a rat sciatic nerve transection model." Homeopathy **101**(3): 141-146.

Monassi, C. R., et al. (2003). "A subpopulation of rats show social and sleep–waking changes typical of chronic neuropathic pain following peripheral nerve injury." European Journal of Neuroscience **17**(9): 1907-1920.

Monchau, F., et al. (2013). "Calcite as a bone substitute. Comparison with hydroxyapatite and tricalcium phosphate with regard to the osteoblastic activity." Materials Science and Engineering: C **33**(1): 490-498.

Moore, B. W. (1965). "A soluble protein characteristic of the nervous system." Biochemical and biophysical research communications **19**(6): 739-744.

Moore Jr, W. (1964). "Comparative metabolism of barium-133 and calcium-45 by embryonic bone grown in vitro." Radiation Research **21**(3): 376-382.

Moore, R. A., et al. (2009). "Pregabalin for acute and chronic pain in adults." Cochrane Database of Systematic Reviews(3).

Moore, W. (1964). "Comparative metabolism of barium-133 and calcium-45 by embryonic bone grown in vitro." Radiation Research **21**(3): 376-382.

Moosvi, S. R. and R. M. Day (2009). "Bioactive glass modulation of intestinal epithelial cell restitution." Acta biomaterialia **5**(1): 76-83.

Mortensen, C., et al. (2023). "Neurofilament light chain as a biomarker of axonal damage in sensory neurons and paclitaxel-induced peripheral neuropathy in patients with ovarian cancer." Pain **164**(7): 1502-1511.

Mozafari, M., et al. (2019). "Calcium carbonate: Adored and ignored in bioactivity assessment." Acta Biomater **91**: 35-47.

Muramatsu, Y., et al. (2003). "Expression of S- 100 protein is related to neuronal damage in MPTP- treated mice." Glia **42**(3): 307-313.

Muresanu, D. F., et al. (2021). Psychopharmacotherapy of pain. NeuroPsychopharmacotherapy, Springer**:** 1-32.

Myrvang, M. B., et al. (2016). "Geochemistry of barium in soils supplied with carbonatite rock powder and barium uptake to plants." Applied geochemistry **75**: 1-8.

Nadeau, S. E., et al. (2021). "Opioids and chronic pain: an analytic review of the clinical evidence." Frontiers in Pain Research **2**: 721357.

Naseri, S., et al. (2017). "Bioactive glasses in wound healing: hope or hype?" Journal of Materials Chemistry B **5**(31): 6167-6174.

Nazeri, N., et al. (2022). "Improvement of sciatic nerve regeneration by multichannel nanofibrous membrane-embedded electro-conductive conduits functionalized with laminin." Journal of Materials Science: Materials in Medicine **33**(6): 50.

Netto, C. B., et al. (2006). "Serum S100B protein is increased in fasting rats." Archives of medical research **37**(5): 683-686.

Nicholas, M., et al. (2019). "The IASP classification of chronic pain for ICD-11: chronic primary pain." Pain **160**(1): 28-37.

Nishihara, T., et al. (2020). "Chronic constriction injury of the sciatic nerve in rats causes different activation modes of microglia between the anterior and posterior horns of the spinal cord." Neurochemistry International **134**: 104672.

Niu, H.-l., et al. (2021). "Inhibition of Nav1. 7 channel by a novel blocker QLS-81 for alleviation of neuropathic pain." Acta Pharmacologica Sinica **42**(8): 1235-1247.

Nowycky, M. C., et al. (1985). "Three types of neuronal calcium channel with different calcium agonist sensitivity." Nature **316**(6027): 440-443.

OECD (2000). "Guidance Document on the Recognition, Assessment, and Use of Clinical Signs as Humane Endpoints for Experimental Animals Used in Safety Evaluation." Organisation for Economic Co-operation and Development.

OECD, O. (2001). "Guideline for the Testing of Chemicals. Acute Oral Toxicity e Acute Toxic Class Method: Test No-423." Organization for Economic Cooperation and Development.

Orrenius, S., et al. (2015). "Calcium and mitochondria in the regulation of cell death." Biochemical and Biophysical Research Communications **460**(1): 72-81.

Oskarsson, A. (2015). Barium. Handbook on the Toxicology of Metals, Elsevier**:** 625-634.

Paglia, M. D. G., et al. (2021). "Use of corticoids and non-steroidal anti-inflammatories in the treatment of rheumatoid arthritis: Systematic review and network meta-analysis." PLoS ONE **16**(4): e0248866.

Paliwal, P., et al. (2018). "Pharmacological application of barium containing bioactive glass in gastro-duodenal ulcers." Materials Science and Engineering: C **92**: 424-434.

Paliwal, P., et al. (2018). "Pharmacological application of barium containing bioactive glass in gastro-duodenal ulcers." Materials Science and Engineering: C **92**: 424-434.

Panahifar, A., et al. (2019). "Biodistribution of strontium and barium in the developing and mature skeleton of rats." Journal of Bone and Mineral Metabolism **37**: 385-398.

Park, H. J. and D. E. Moon (2010). "Pharmacologic management of chronic pain." The Korean journal of pain **23**(2): 99-108.

Park, S. H., et al. (2023). "Atrial fibrillation induced by gabapentin: a case report." J Med Case Rep **17**(1): 236.

Patel, K. K., et al. (2019). "Antibiofilm potential of silver sulfadiazine-loaded nanoparticle formulations: a study on the effect of DNase-I on microbial biofilm and wound healing activity." Molecular pharmaceutics **16**(9): 3916-3925.

Patel, R. and A. H. Dickenson (2016). "Mechanisms of the gabapentinoids and α2δ- 1 calcium channel subunit in neuropathic pain." Pharmacology research & perspectives **4**(2): e00205.

Patel, S. and R. Docampo (2010). "Acidic calcium stores open for business: expanding the potential for intracellular Ca2+ signaling." Trends in Cell Biology **20**(5): 277-286.

Pazarçeviren, A. E., et al. (2018). "Investigation of bismuth doped bioglass/graphene oxide nanocomposites for bone tissue engineering." Ceramics International **44**(4): 3791-3799.

Peirs, C. and R. P. Seal (2016). "Neural circuits for pain: recent advances and current views." Science **354**(6312): 578-584.

Pereira, M. M. and L. L. Hench (1996). "Mechanisms of hydroxyapatite formation on porous gel-silica substrates." Journal of Sol-Gel Science and Technology **7**(1-2): 59-68.

Perez, R. A., et al. (2017). "Silica-based multifunctional nanodelivery systems toward regenerative medicine." Materials Horizons **4**(5): 772-799.

Petzold, A., et al. (2002). "Markers for different glial cell responses in multiple sclerosis: clinical and pathological correlations." Brain **125**(7): 1462-1473.

Piao, Y., et al. (2013). "Change trends of organ weight background data in Sprague Dawley rats at different ages." Journal of toxicologic pathology **26**(1): 29-34.

Pirayesh, H. and J. A. Nychka (2013). "Sol–gel synthesis of bioactive glass- ceramic 45S5 and its in vitro dissolution and mineralization behavior." Journal of the American Ceramic Society **96**(5): 1643-1650.

Pires, E. G., et al. (2018). "Silver- doped 58S bioactive glass as an anti- Leishmania agent." International Journal of Applied Glass Science **9**(1): 52-61.

Pocock, J. M. and H. Kettenmann (2007). "Neurotransmitter receptors on microglia." Trends in Neurosciences **30**(10): 527-535.

Pourshahrestani, S., et al. (2017). "Potency and cytotoxicity of a novel gallium-containing mesoporous bioactive glass/chitosan composite scaffold as hemostatic agents." ACS applied materials & interfaces **9**(37): 31381-31392.

Prajapati, S. K., et al. (2024). "Suvorexant improves mitochondrial dynamics with the regulation of orexinergic and mTOR activation in rats exhibiting PTSD-like symptoms." Journal of Affective Disorders **350**: 24-38.

Prajapati, S. K., et al. (2017). "Coenzyme Q10 prevents mitochondrial dysfunction and facilitates pharmacological activity of atorvastatin in 6-OHDA induced dopaminergic toxicity in rats." Neurotoxicity research **31**(4): 478-492.

Prajapati, S. K., et al. (2017). "Coenzyme Q10 prevents mitochondrial dysfunction and facilitates pharmacological activity of atorvastatin in 6-OHDA induced dopaminergic toxicity in rats." Neurotoxicity research **31**: 478-492.

Prajapati, S. K. and S. Krishnamurthy (2021). "Development and treatment of cognitive inflexibility in sub-chronic stress–re-stress (SRS) model of PTSD." Pharmacological Reports **73**: 464-479.

Pratten, J., et al. (2004). "In vitro attachment of Staphylococcus epidermidis to surgical sutures with and without Ag-containing bioactive glass coating." Journal of Biomaterials Applications **19**(1): 47-57.

Program, N. T. (1994). "NTP toxicology and carcinogenesis studies of barium chloride dihydrate (CAS No. 10326-27-9) in F344/N rats and B6C3F1 mice (drinking water studies)." National Toxicology Program technical report series **432**: 1-285.

Qazi, T. H., et al. (2018). "Dosage and composition of bioactive glasses differentially regulate angiogenic and osteogenic response of human MSCs." Journal of Biomedical Materials Research Part A **106**(11): 2827-2837.

Qi, Q., et al. (2020). "Local intramyocardial delivery of bioglass with alginate hydrogels for post-infarct myocardial regeneration." Biomedicine and Pharmacotherapy **129**: 110382.

Rahaman, M. N., et al. (2011). "Bioactive glass in tissue engineering." Acta Biomater **7**(6): 2355-2373.

Raja, S. N., et al. (2020). "The revised International Association for the Study of Pain definition of pain: concepts, challenges, and compromises." Pain **161**(9): 1976-1982.

Randall, L. O. (1957). "A method for measurement of analgesic activity of inflamed tissue." Archives Internationales de Pharmacodynamie et de Therapie **111**: 409-411.

Rathinam, K., et al. (1994). "In vivo andin vitro evaluation of a biomachinable glassceramic." Bulletin of Materials Science **17**(2): 171-179.

Ravarian, R., et al. (2010). "Synthesis, characterization and bioactivity investigation of bioglass/hydroxyapatite composite." Ceramics International **36**(1): 291-297.

Reddy, D. S. and S. K. Kulkarni (1998). "Possible role of nitric oxide in the nootropic and antiamnesic effects of neurosteroids on aging-and dizocilpine-induced learning impairment." Brain Research **799**(2): 215-229.

Ripamonti, U., et al. (1992). "The critical role of geometry of porous hydroxyapatite delivery system in induction of bone by osteogenin, a bone morphogenetic protein." Matrix **12**(3): 202-212.

Rivadeneira, J., et al. (2015). "Novel antibacterial bioactive glass nanocomposite functionalized with tetracycline hydrochloride." Biomedical Glasses **1**(1).

Romero-Sandoval, A., et al. (2008). "A comparison of spinal Iba1 and GFAP expression in rodent models of acute and chronic pain." Brain Research **1219**: 116-126.

Ross, A., et al. (2012). "Overview of calcium—dietary reference intakes for calcium and vitamin D—NCBI bookshelf." Pediatrics **130**(1427): 10.1542.

Rozas, G., et al. (1997). "An automated rotarod method for quantitative drug-free evaluation of overall motor deficits in rat models of parkinsonism." Brain Research Protocols **2**(1): 75-84.

Sá, K. N., et al. (2019). "Prevalence of chronic pain in developing countries: systematic review and meta-analysis." Pain Reports **4**(6): e779.

Sabbatini, M., et al. (2014). "Adhesion and differentiation of neuronal cells on Zn-doped bioactive glasses." Journal of Biomaterials Applications **28**(5): 708-718.

Saegusa, H., et al. (2002). "Effects of ablation of N-and R-type Ca2+ channels on pain transmission." Neuroscience Research **43**(1): 1-7.

Saini, A. K., et al. (2007). "Preventive and curative effect of edaravone on nerve functions and oxidative stress in experimental diabetic neuropathy." European Journal of Pharmacology **568**(1-3): 164-172.

Saravanapavan, P., et al. (2004). A549 lung carcinoma cells: Binary vs. ternary bioactive gel-glasses. Key Engineering Materials, Trans Tech Publ.

Sathe, K., et al. (2012). "S100B is increased in Parkinson's disease and ablation protects against MPTP-induced toxicity through the RAGE and TNF-α pathway." Brain **135**(11): 3336-3347.

Satoh, S., et al. (1987). "Mechanisms of the Ba2+-induced contraction in smooth muscle cells of the rabbit mesenteric artery." The Journal of general physiology **89**(2): 215-237.

Saxena, A. K., et al. (2018). "Pharmacological management of neuropathic pain in India: A consensus statement from Indian experts." Indian Journal of Pain **32**(3): 132-144.

Saxena, A. K., et al. (2018). "The prevalence of chronic pain among adults in India." Indian journal of palliative care **24**(4): 472.

Schaf, D. V., et al. (2005). "S100B and NSE serum levels in patients with Parkinson's disease." Parkinsonism & related disorders **11**(1): 39-43.

Schepers, E. J., et al. (1993). "Bioactive glass particles of narrow size range: a new material for the repair of bone defects." Implant Dentistry **2**(3): 151-157.

Schmittgen, T. D. and K. J. Livak (2008). "Analyzing real-time PCR data by the comparative CT method." Nature protocols **3**(6): 1101-1108.

Schroeder, H. A., et al. (1972). "Trace metals in man: strontium and barium." Journal of Chronic Diseases **25**(9): 491-517.

Schwartz, S. and T. Pateman (2021). Pre-clinical pharmacokinetics. A Handbook of Bioanalysis and Drug Metabolism, CRC Press**:** 113-131.

Schwotzer, D., et al. (2017). "Effects from a 90-day inhalation toxicity study with cerium oxide and barium sulfate nanoparticles in rats." Particle and fibre toxicology **14**(1): 1-20.

Scripture, C. D., et al. (2006). "Peripheral neuropathy induced by paclitaxel: recent insights and future perspectives." Current Neuropharmacology **4**(2): 165-172.

Seyfert, U. T., et al. (2002). "In vitro hemocompatibility testing of biomaterials according to the ISO 10993-4." Biomolecular engineering **19**(2-6): 91-96.

Shahrbabak, M. S. N., et al. (2019). "A Comparative Investigation on Bioactivity and Antibacterial Properties of Sol-Gel Derived 58S Bioactive Glass Substituted by Ag and Zn." Silicon **11**(6): 2741-2751.

Shin, D. W., et al. (2022). "Global, regional, and national neck pain burden in the general population, 1990–2019: An analysis of the global burden of disease study 2019." Frontiers in neurology **13**: 955367.

Siau, C. and G. J. Bennett (2006). "Dysregulation of cellular calcium homeostasis in chemotherapy-evoked painful peripheral neuropathy." Anesthesia and Analgesia **102**(5): 1485-1490.

Silva, T. A., et al. (2022). "Detection of barium in the atmospheres of the ultra-hot gas giants WASP-76b and WASP-121b-Together with new detections of Co and Sr+ on WASP-121b." Astronomy & Astrophysics **666**: L10.

Sims, G. P., et al. (2009). "HMGB1 and RAGE in inflammation and cancer." Annual review of immunology **28**: 367-388.

Singh, P. and S. A. Ali (2022). "Multifunctional role of S100 protein family in the immune system: an update." Cells **11**(15): 2274.

Skouen, J. S., et al. (1999). "Protein markers in cerebrospinal fluid in experimental nerve root injury: a study of slow-onset chronic compression effects or the biochemical effects of nucleus pulposus on sacral nerve roots." Spine **24**(21): 2195.

Smith, B. H., et al. (2020). "Neuropathic pain in the community: prevalence, impact, and risk factors." Pain **161**: S127-S137.

Smith, J. A., et al. (2012). "Role of pro-inflammatory cytokines released from microglia in neurodegenerative diseases." Brain Research Bulletin **87**(1): 10-20.

Smith, M. T., et al. (2002). "The novel N-type calcium channel blocker, AM336, produces potent dose-dependent antinociception after intrathecal dosing in rats and inhibits substance P release in rat spinal cord slices." Pain **96**(1): 119-127.

Souza Monteiro de Araujo, D., et al. (2020). "TRPA1 as a therapeutic target for nociceptive pain." Expert opinion on therapeutic targets **24**(10): 997-1008.

Stanley, H. R., et al. (1997). "Using 45S5 bioglass cones as endosseous ridge maintenance implants to prevent alveolar ridge resorption: a 5-year evaluation." International Journal of Oral and Maxillofacial Implants **12**(1).

Stefani, L. C., et al. (2019). "BDNF and serum S100B levels according the spectrum of structural pathology in chronic pain patients." Neuroscience Letters **706**: 105-109.

Stoewsand, G., et al. (1988). "Deposition of barium in the skeleton of rats fed Brazil nuts." Nutrition reports international **38**(2): 259-262.

Sui, B., et al. (2016). "Drug-loadable Mesoporous Bioactive Glass Nanospheres: Biodistribution, Clearance, BRL Cellular Location and Systemic Risk Assessment via 45 Ca Labelling and Histological Analysis." Scientific reports **6**(1): 1-12.

Sui, B., et al. (2016). "Drug-loadable mesoporous bioactive glass nanospheres: biodistribution, clearance, BRL cellular location and systemic risk assessment via 45Ca labelling and histological analysis." Scientific reports **6**(1): 1-12.

Sun, L., et al. (2022). "Targeted ubiquitination of sensory neuron calcium channels reduces the development of neuropathic pain." Proceedings of the National Academy of Sciences **119**(20): e2118129119.

Taherkhani, S. and F. Moztarzadeh (2016). "Influence of strontium on the structure and biological properties of sol–gel-derived mesoporous bioactive glass (MBG) powder." Journal of Sol-Gel Science and Technology **78**(3): 539-549.

Takasusuki, T. and T. L. Yaksh (2011). "Regulation of spinal substance p release by intrathecal calcium channel blockade." The Journal of the American Society of Anesthesiologists **115**(1): 153-164.

Tan, A., et al. (2003). The effect of 58S bioactive sol-gel derived foams on the growth of murine lung epithelial cells. Key Engineering Materials, Trans Tech Publ.

Tan, A. M., et al. (2008). "Neuropathic pain memory is maintained by Rac1-regulated dendritic spine remodeling after spinal cord injury." Journal of Neuroscience **28**(49): 13173-13183.

Tang, L., et al. (2016). "Structural basis for inhibition of a voltage-gated Ca2+ channel by Ca2+ antagonist drugs." Nature **537**(7618): 117-121.

Tanga, F., et al. (2006). "Role of astrocytic S100β in behavioral hypersensitivity in rodent models of neuropathic pain." Neuroscience **140**(3): 1003-1010.

Taye, M. B. (2022). "Biomedical applications of ion-doped bioactive glass: A review." Applied Nanoscience **12**(12): 3797-3812.

Teixeira-Santos, L., et al. (2020). "Neuroinflammation, oxidative stress and their interplay in neuropathic pain: Focus on specialized pro-resolving mediators and NADPH oxidase inhibitors as potential therapeutic strategies." Pharmacological Research **162**: 105280.

Tibbs, G. R., et al. (2016). "Voltage-gated ion channels in the PNS: novel therapies for neuropathic pain?" Trends in Pharmacological Sciences **37**(7): 522-542.

Tilley, D. M., et al. (2022). "Differential target multiplexed spinal cord stimulation programming modulates proteins involved in ion regulation in an animal model of neuropathic pain." Molecular pain **18**: 17448069211060181.

Timofeev, I., et al. (2012). "Decompressive craniectomy—operative technique and perioperative care." Advances and technical standards in neurosurgery: 115-136.

Todorovic, S. M. and V. Jevtovic-Todorovic (2014). "Targeting of Ca v 3.2 T-type calcium channels in peripheral sensory neurons for the treatment of painful diabetic neuropathy." Pflügers Archiv-European Journal of Physiology **466**: 701-706.

Tong, C., et al. (2021). "Pregabalin and gabapentin in patients with spinal cord injury-related neuropathic pain: a network meta-analysis." Pain and therapy **10**: 1497-1509.

Tracey, I. and P. W. Mantyh (2007). "The cerebral signature for pain perception and its modulation." Neuron **55**(3): 377-391.

Tripathi, H., et al. (2015). "Structural characterization and in vitro bioactivity assessment of SiO2–CaO–P2O5–K2O–Al2O3 glass as bioactive ceramic material." Ceramics International **41**(9): 11756-11769.

Tripathi, H., et al. (2016). "Preparation and characterization of Li 2 O–CaO–Al 2 O 3–P 2 O 5–SiO 2 glasses as bioactive material." Bulletin of Materials Science **39**(2): 365-376.

Tripathi, H., et al. (2016). "Preparation and characterization of Li 2 O–CaO–Al 2 O 3–P 2 O 5–SiO 2 glasses as bioactive material." Bulletin of Materials Science **39**(2): 365-376.

Tripathi, H., et al. (2019). "Structural, physico-mechanical and in-vitro bioactivity studies on SiO2–CaO–P2O5–SrO–Al2O3 bioactive glasses." Materials Science and Engineering: C **94**: 279-290.

Tulyaganov, D. U., et al. (2013). "Synthesis, processing and characterization of a bioactive glass composition for bone regeneration." Ceramics International **39**(3): 2519-2526.

Tuusa, S. M. R., et al. (2008). "Reconstruction of critical size calvarial bone defects in rabbits with glass–fiber- reinforced composite with bioactive glass granule coating." Journal of Biomedical Materials Research Part B: Applied Biomaterials: An Official Journal of The Society for Biomaterials, The Japanese Society for Biomaterials, and The Australian Society for Biomaterials and the Korean Society for Biomaterials **84**(2): 510-519.

Van Hecke, O., et al. (2014). "Neuropathic pain in the general population: a systematic review of epidemiological studies." PAIN® **155**(4): 654-662.

Vassort, G. (1975). "Voltage- clamp analysis of transmembrane ionic currents in guinea- pig myometrium: evidence for an initial potassium activation triggered by calcium influx." The Journal of physiology **252**(3): 713-734.

Verma, M., et al. (2018). "Excitatory dendritic mitochondrial calcium toxicity: implications for Parkinson's and other neurodegenerative diseases." Frontiers in neuroscience **12**: 523.

Verma, V., et al. (2014). "Pregabalin in neuropathic pain: evidences and possible mechanisms." Current Neuropharmacology **12**(1): 44-56.

Verrier, S., et al. (2004). "PDLLA/Bioglass® composites for soft-tissue and hard-tissue engineering: an in vitro cell biology assessment." Biomaterials **25**(15): 3013-3021.

Vicario, N., et al. (2020). "Intercellular communication and ion channels in neuropathic pain chronicization." Inflammation Research **69**: 841-850.

Vizuete, A. F. K., et al. (2019). "GABA A modulation of S100B secretion in acute hippocampal slices and astrocyte cultures." Neurochemical Research **44**: 301-311.

Vo, T., et al. (2009). "Non-steroidal anti-inflammatory drugs for neuropathic pain: how do we explain continued widespread use?" PAIN® **143**(3): 169-171.

Walsh Jr, J. V. and J. J. Singer (1980). "Calcium action potentials in single freshly isolated smooth muscle cells." American Journal of Physiology-Cell Physiology **239**(5): C162-C174.

Wan, C., et al. (2008). "Activation of the hypoxia-inducible factor-1α pathway accelerates bone regeneration." Proceedings of the National Academy of Sciences **105**(2): 686-691.

Wang, C., et al. (2021). "Effects of varying degrees of ligation in a neuropathic pain model induced by chronic constriction injury." Life Sciences **276**: 119441.

Wang, H., et al. (2006). "Bradykinin and peripheral sensitization."

Wang, T. W., et al. (2007). "The development of magnetic degradable DP- Bioglass for hyperthermia cancer therapy." Journal of Biomedical Materials Research Part A: An Official Journal of The Society for Biomaterials, The Japanese Society for

Biomaterials, and The Australian Society for Biomaterials and the Korean Society for Biomaterials **83**(3): 828-837.

Wanner, M., et al. (1991). "Influence of dietary citric acid and calcium on the bioavailability of orally administered chlortetracycline in piglets." Journal of Veterinary Medicine Series A **38**(1- 10): 755-762.

Wasner, G., et al. (2004). "Topical menthol—a human model for cold pain by activation and sensitization of C nociceptors." Brain **127**(5): 1159-1171.

Watanabe, M., et al. (2015). "Expression and regulation of Cav3. 2 T-type calcium channels during inflammatory hyperalgesia in mouse dorsal root ganglion neurons." PLoS ONE **10**(5): e0127572.

Waxman, S. G., et al. (2014). "Sodium channel genes in pain-related disorders: phenotype–genotype associations and recommendations for clinical use." The Lancet Neurology **13**(11): 1152-1160.

Whiteside, G., et al. (2008). "Predictive validity of animal pain models? A comparison of the pharmacokinetic–pharmacodynamic relationship for pain drugs in rats and humans." Neuropharmacology **54**(5): 767-775.

Widerström-Noga, E. (2017). "Neuropathic pain and spinal cord injury: phenotypes and pharmacological management." Drugs **77**(9): 967-984.

Widyadharma, I. P. E. and E. H. Tedyanto (2022). "Serum neurofilament light chain: A potential biomarker for peripheral neuropathy." Siriraj Medical Journal **74**(10): 714-720.

Wilson, J., et al. (1994). Clinical applications of bioglass implants. Bioceramics, Elsevier**:** 415-422.

Wilson, J., et al. (1981). "Toxicology and biocompatibility of bioglasses." Journal of Biomedical Materials Research **15**(6): 805-817.

Wiltrout, R., et al. (1978). "Isotope-release cytotoxicity assay with the use of indium-111: advantage over chromium-51 in long-term assays." Journal of the National Cancer Institute **61**(1): 183-188.

Wood, J. N. (2020). The Oxford handbook of the neurobiology of pain, Oxford University Press.

Woolf, C. J. (2007). "Central sensitization: uncovering the relation between pain and plasticity." The Journal of the American Society of Anesthesiologists **106**(4): 864-867.

Woolf, C. J. and R. J. Mannion (1999). "Neuropathic pain: aetiology, symptoms, mechanisms, and management." The Lancet **353**(9168): 1959-1964.

Wu, C., et al. (2012). "Hypoxia-mimicking mesoporous bioactive glass scaffolds with controllable cobalt ion release for bone tissue engineering." Biomaterials **33**(7): 2076-2085.

Wu, Z., et al. (2019). "Sedentary time, metabolic abnormalities, and all-cause mortality after myocardial infarction: A mediation analysis." European journal of preventive cardiology **26**(1): 96-104.

Xia, C., et al. (2018). "S100 proteins as an important regulator of macrophage inflammation." Frontiers in immunology **8**: 1908.

Xing, H., et al. (2007). "TRPM8 mechanism of cold allodynia after chronic nerve injury." Journal of Neuroscience **27**(50): 13680-13690.

Xing, Z., et al. (2018). "Ameliorative effects and possible molecular mechanisms of action of fibrauretine from Fibraurea recisa Pierre on d-galactose/AlCl 3-mediated Alzheimer's disease." RSC advances **8**(55): 31646-31657.

Yadav, S., et al. (2020). "Synthesis, characterization, mechanical and biological properties of biocomposite based on zirconia containing 1393 bioactive glass with hydroxyapatite." Ceramics International **46**: 10442-10451.

Yajima, I., et al. (2012). "Barium inhibits arsenic-mediated apoptotic cell death in human squamous cell carcinoma cells." Archives of Toxicology **86**(6): 961-973.

Yaksh, T. L. (2006). "Calcium channels as therapeutic targets in neuropathic pain." The Journal of Pain **7**(1): S13-S30.

Yamaguchi‐Ueda, K., et al. (2019). "Combination of ions promotes cell migration via extracellular signal‐regulated kinase 1/2 signaling pathway in human gingival fibroblasts." Molecular medicine reports **19**(6): 5039-5045.

Yang, M., et al. (2019). "Acute and subacute toxicity evaluation of ethanol extract from aerial parts of Epigynum auritum in mice." Food and Chemical Toxicology **131**: 110534.

Yang, Y., et al. (2004). "Mutations in SCN9A, encoding a sodium channel alpha subunit, in patients with primary erythermalgia." Journal of Medical Genetics **41**(3): 171-174.

Yesudhas, D., et al. (2014). "Multiple roles of toll-like receptor 4 in colorectal cancer." Frontiers in immunology **5**: 334.

Yinhua, Y., et al. (1993). "Effects of barium chloride on the immune functions in mice." Di 3 jun yi da xue xue bao= Disanjunyidaxue Xuebao= Acta Acadiemiae [ie Academiae] Medicinae Militaris Tertiae **15**(1): 25-28.

Yu, H., et al. (2016). "Bioglass activated skin tissue engineering constructs for wound healing." ACS applied materials & interfaces **8**(1): 703-715.

Yu, Y., et al. (2013). "Acute toxicity of amorphous silica nanoparticles in intravenously exposed ICR mice." PLoS ONE **8**(4): e61346.

Yun, J. W., et al. (2015). "Comparative toxicity of silicon dioxide, silver and iron oxide nanoparticles after repeated oral administration to rats." Journal of Applied Toxicology **35**(6): 681-693.

Zamponi, G. W., et al. (2009). "Role of voltage-gated calcium channels in ascending pain pathways." Brain research reviews **60**(1): 84-89.

Zaqout, S. and A. M. Kaindl (2016). "Golgi-Cox staining step by step." Frontiers in neuroanatomy **10**: 38.

Zeng, Q., et al. (2015). "Design of a thermosensitive bioglass/agarose–alginate composite hydrogel for chronic wound healing." Journal of Materials Chemistry B **3**(45): 8856-8864.

Zhang, J., et al. (2015). "Effects of bioactive cements incorporating zinc-bioglass nanoparticles on odontogenic and angiogenic potential of human dental pulp cells." Journal of Biomaterials Applications **29**(7): 954-964.

Zhang, Y., et al. (2010). "PKSolver: An add-in program for pharmacokinetic and pharmacodynamic data analysis in Microsoft Excel." Computer Methods and Programs in Biomedicine **99**(3): 306-314.

Zhang, Y., et al. (2018). "Bioglass enhanced wound healing ability of urine- derived stem cells through promoting paracrine effects between stem cells and recipient cells." Journal of tissue engineering and regenerative medicine **12**(3): e1609-e1622.

Zheng, K. and A. R. Boccaccini (2017). "Sol-gel processing of bioactive glass nanoparticles: A review." Advances in Colloid and Interface Science **249**: 363-373.

Zheng, K., et al. (2019). "Protein interactions with bioactive glass surfaces: a review." Applied Materials Today **15**: 350-371.

Zhu, D.-Y., et al. (2019). "Gadolinium-doped bioglass scaffolds promote osteogenic differentiation of hBMsc via the akt/gsK3β pathway and facilitate bone repair in vivo." Int J Nanomedicine **14**: 1085.

Zhuo, M., et al. (2011). "Neuronal and microglial mechanisms of neuropathic pain." Molecular brain **4**: 1-12.

Zilliox, L. A. (2017). "Neuropathic pain." CONTINUUM: Lifelong Learning in Neurology **23**(2): 512-532.

List of Publications

List of Publications from the Thesis

- **Majumdar S**, Tiwari A, Mallick D, Patel DK, Trigun SK, Krishnamurthy S. Oral Release Kinetics, Biodistribution, and Excretion of Dopants from Barium-Containing Bioactive Glass in Rats. ACS omega. 2024 Jan 31.
- **Majumdar S**, Krishnamurthy S. In vivo toxicological evaluation of barium-doped bioactive glass in rats. Ceramics International. 2022 Nov 15;48(22):33288-305.
- **Majumdar S**, Hira SK, Tripathi H, Kumar AS, Manna PP, Singh SP, Krishnamurthy S. Synthesis and characterization of barium-doped bioactive glass with potential anti-inflammatory activity. Ceramics International. 2021 Mar 1;47(5):7143-58.